The Hemispherical Magnetic Field of Ancient Mars: Numerical Simulations and Geophysical Constraints

Dissertation
zur Erlangung des mathematisch-naturwissenschaftlichen Doktorgrades
"Doctor rerum naturalium"
der Georg-August-Universität Göttingen

im Promotionsprogramm ProPhys
der Georg-August University School of Science (GAUSS)

vorgelegt von
Wieland Dietrich
aus Weimar

Göttingen, 2012

Betreuungsausschuss

Prof. Dr. Ulrich Christensen, Max-Planck-Institut für Sonnensystemforschung

Prof. Dr. Andreas Tilgner, Institut für Geophysik, Universität Göttingen

Dr. Johannes Wicht, Max-Planck-Institut für Sonnensystemforschung

Mitglieder der Prüfungskommision

Referen: Prof. Dr. Andreas Tilgner, Institut für Geophysik, Universität Göttingen

Korreferent: Prof. Dr. Ulrich Christensen, Max-Planck-Institut für Sonnensystemforschung

Weitere Mitglieder der Prüfungskommision:

Prof. Dr. Wolfgang Glatzel, Institut für Astrophysik, Universität Göttingen

Prof. Dr. Manfred Schüssler, Max-Planck-Institut für Sonnensystemforschung

Prof. Dr. Laurent Gizon, Institut für Astrophysik, Universität Göttingen, Max-Planck-Institut für Sonnensystemforschung

Prof. Dr. Ansgar Reiners, Institut für Astrophysik, Universität Göttingen

Tag der mündlichen Prüfung: 7. 11. 2012

Bibliografische Information der Deutschen Nationalbibliothek

Die Deutsche Nationalbibliothek verzeichnet diese Publikation in der Deutschen Nationalbibliografie; detaillierte bibliografische Daten sind im Internet über `http://dnb.d-nb.de` abrufbar.

ISBN 978-3-942171-70-0

uni-edition GmbH 2012
http://www.uni-edition.de

Printed in Germany

Contents

Abstract

Although the planet Mars shows no global magnetic field today, the amplitude of the crustal magnetization excludes any external origin (Acuña et al. 1999). Therefore Mars must have had a period of generating actively an intrinsic magnetic field. Hydrodynamic instabilities, such as convection due to thermal or compositional buoyancy, are thought to drive complex flows of the liquid iron inside the planetary core which allow for self-sustained induction of a magnetic field. Studies on the thermal evolution of Mars (Morschhauser et al. 2011) suggest that only during the first 500 Myrs of the planetary evolution the cooling rate of the core was sufficiently high to enforce a dynamo process driven by thermal convection. Ferromagnetic minerals such as magnetite, formed and cooled under the Curie temperature during this dynamo period, will preserve the strength and orientation of the ambient magnetic field. From the year 1997, the Mars Global Surveyor (MGS) spacecraft delivered the pattern and amplitude of the crustal magnetization. One of the surprising results is the strong equatorial asymmetric (or more specific 'hemispherical') distribution, where most of the magnetic anomalies are located south of the Martian equator. However, the amplitude of the magnetic moment of the crustal magnetization was measured to be comparable to the one of Earth (Acuña et al. 1999), what can be explained by either a thicker layer of magnetized crust (Langlais et al. 2004), a higher density of magnetic carriers or a much stronger internal magnetic field.

The simplest end-member scenarios for the origin of such a magnetization pattern might be either an internal one due to a hemispherical magnetizing field or an external characterized by heterogeneous demagnetization of the crust in the northern hemisphere. The latter scenario assumes an ancient field of strong dipolar morphology, which will magnetize the crust more or less homogeneously. After the global magnetization was acquired and the dynamo ceased impacts, volcanoes, plate tectonics and any other kind of resurfacing event need then to appear in a heterogeneous way such that the remaining crustal magnetization matches it's present day hemispherical pattern. However, it remains unclear how to justify a hemispherical preference of these quite statistical resurfacing processes.

Dynamo models for planetary interiors describe the conducting, rotating and convecting liquid iron with the MHD (Magnetohydrodynamics) approach. Researchers investigating the first (internal) magnetization scenario adopt their numerical MHD models to the characteristics of the early Martian interior (Stanley et al. 2008, Amit et al. 2011). Within the limitations of today's knowledge about the ancient Mars, a non-homogeneous core mantle boundary (CMB) heat flux pattern and core convection driven exclusively by thermal buoyancy are the expected key features. Since Mars is substantially smaller than the Earth, the mantle convection is thought to be dominated by very few or only a single hot upwelling (Keller and Tackley 2009), its large scale thermal footpoint can be trans-

lated into a heat flux anomaly at the CMB. The convection in the Earth's core is supported by strong buoyancy contributions due to chemical convection, where the iron of the core melt freezes at the surface of the solid inner core and buoyant light elements are released. The Martian core is thought to be entirely liquid, therefore only thermal convection can power an early dynamo process (Sohl and Spohn 1997).

The magnetic field achieved from the MHD simulations needs to fulfill several criteria in order to serve as proper model to the problem of a hemispherical magnetization at the surface. Besides the appropriate hemisphericity of the surface field these are long time stability without polarity inversions and a surface magnetic field strength matching the suggestions for the surface field strength of ancient Mars. In this study, we test the hypothesis of an internal origin of the dichotomy in the crustal magnetization by conducting numerical experiments for a hemispherical dynamo while solving numerically for the MHD equations and applying a setup characterizing early Mars (Amit et al. 2011). We enforce hemispherical dynamos in a similar way as reported by Stanley et al. (2008) and Amit et al. (2011). If they reach the appropriate hemisphericity at the surface fast oscillations including polarity reversals set in what seems inconsistent with the required magnetization depth and amplitude. A rough comparison between the time scales typical for crustal cooling and magnetization and the magnetic cycle period yields the conclusion, that there might be no signal detectable on the surface of Mars. As the main result, we suggest that a reversing hemispherical dynamo model does not fit to the observations of strong and heterogeneous crustal magnetization. Furthermore we suggest a simplified scaling law evaluating the possibility of such a boundary driven hemispherical dynamo in a realistic planetary core.

As one of the key features of the hemispherical dynamos studied here, the convection and magnetic field induction, show a special symmetric behavior making the model applicable to the mean field theory. The mean field theory successfully explained the 22-year magnetic cycle of the sun where plane dynamo waves evolve in its convection zone. We adopt and apply this theory to our model and compare the oscillation frequencies of the hemispherical dynamo to the predictions from mean field theory, where we find a surprisingly good agreement.

1 Introduction

The investigation of global planetary magnetic fields generated from a prosperous dynamo process bares an approach to infer the present and past state of the interior. As we will see, the induction of a self-sustained magnetic field in the interior of a planet yields constraints on the thermal evolution, composition and the planets interior structure. It is thought that the induction of a magnetic field is caused by complex motions of conducting liquids, e.g. the liquid iron in the core of terrestrial planets. For the Earth, it was proposed that such a dynamic process can explain the variation of the geomagnetic field on time scales from several hundreds of years for the secular variation up to reversal time scales of several hundreds of millions years (Glatzmaier and Coe 2007, Jones 2007). In this study we focus on the historical dynamo process on the planet Mars. Even though, Mars has today no global magnetic field, crustal magnetization might attest an active dynamo during the time of generating the crust (Acuña et al. 1999). If the crustal magnetization pattern can be interpreted as the fingerprint of the ancient Martian dynamo, it might show some remarkable differences to the present day magnetic field of Earth. For example, it is reasonable (Sohl and Spohn 1997) that the Martian dynamo was powered exclusively by thermal convection and thus might mimic as well the dynamo process on Earth roughly 2 billion years ago, before the solid inner core of the Earth nucleated. Therefore understanding the dynamics and the induction process of the ancient Martian dynamo might not only explain the acquisition of a hemispherical crustal magnetization pattern, but also yield information about the early evolution of the Earth and its dynamo process.

1.1 Planetary Magnetism

A recent review of the scientific history of magnetism and its application to the Earth is discussed extensively by Stern (2002) or Kono (2007). Here we overview the main steps of the historical evolution of magnetism and its origin. It was already known to the ancient Greek, that special stones (loadstones) attract iron dust (Kono 2007), but the nature of the responsible attraction remained enigmatic. The more systematic investigation of magnetism on Earth dates back roughly 1000 years, when the Chinese noted that pivoted loadstones are subject to a preferred north-south alignment. This can be seen as the first technical application of Earth's magnetic field. Loadstone are a remanently magnetized pieces of magnetite, thus contain iron oxides and therefore can carry a permanent magnetic moment. During the 12th century (Stern 2002) it was also known, that a compass needle as an instrument for navigation on sea and land, typically shows an inclination and deviations from the exact north-south direction (declination), but the origin of the magnetic force field itself remain unclear. In the year 1600, William Gilbert proposed the Earth itself being a big magnet and as such being responsible for the force applied to compass needles (Gilbert 1600). It was thought that the interior of the Earth is remanently magnetized and thus forms a huge bar magnet. But in 1634, Henry Gellibrand noted the time dependence of the declination (Stern 2002), today known as secular variation, what contradicts the remanent magnetization theory. Gellibrand explained that the Earth interior is built up by several concentric shells hosting magnetization and with a motion relative to each other (Busse and Simitev 2007). It was Gauss in 1828 developing a method to measure the magnetic field intensity, not only the direction. Later (1834) he derived the spherical harmonics analysis in describing the magnetic field as a scalar potential field originated from inside the Earth. Once it was known, that the temperature inside the Earth increases with depth such fast, that the Curie depth as the natural border for remanent magnetization is reached at 30 km, the idea of a permanent and deep magnetization of the Earth's interior was ruled out (Busse and Simitev 2007). In 1919 Joseph Larmor devised the idea, that rotating bodies such as Sun and Earth can become magnets due to self-sustained dynamo action caused by convective motions of a conducting fluid (Larmor 1919). As the next step theories of coupling magnetic induction and rotating convection start to develop. The full physical description is rather complex, therefore the first successful mathematical treatment dealed with the simplified kinematic dynamo problem (only solving the induction equation) and dates back to Braginsky (1964). The first numerical model of the full dynamo problem including the Navier-Stokes equation and the conservation of thermal energy, was given by Glatzmaier and Roberts (1997). Since then a vast amount of numerical studies adressed various aspects of planetary and stellar dynamos and enlighted the details of the induction mechanism.

The magnetic properties of other solar system planets and the Earth moon was discovered by space missions. The Apollo missions 15 and 16 found crustal magnetization on the Earth's Moon in 1971 and 1972, Jupiter's magnetosphere was crossed by Pioneer 10 in 1973, Mariner 10 observed the magnetic field of Mercury in 1974, Pioneer 11 passed the magnetosphere of Saturn in 1979 and Voyager 2 found magnetospheres on Uranus (1986) and Neptune (1989) (Stern 2002). Although Mars was visited by a series of space crafts before, no global magnetic field was detected. But from 1997 the Mars Global Surveyor spacecraft found a magnetic field due to crustal magnetization and mapped its surprisingly heterogeneous pattern (Acuña et al. 2001).

Today it seems an exception that a solar system planet lacks a global magnetic field of internal origin. Probably all of the solar system planets have or had, as inferred from magnetized rocks on the surface, an evolutionary period with an intrinsic magnetic field generation. It is thought, that a magneto-hydrodynamical dynamo process in the interiors is responsible for the generation of a global magnetic field. Today active dynamos can be found in Mercury, Earth, Jupiter, Saturn, Neptune and Uranus, additionally in the Jovian Moon Ganymede. A special case is the planet Venus, which is quite similar to Earth in size and chemistry. But Venus probably lacks plate tectonics and the mantle cools slower under the stagnant lid crust (Spohn 2007). So the planetary cooling process might not be fast enough to drive a dynamo. Besides that, any crustal magnetization as the fingerprint of a hypothetical early Venusian dynamo might have been removed at surface temperatures of roughly 450 °C exceeding the Curie temperature of some ferromagnetic minerals and the extreme conditions due to the large atmospheric pressure and acidity. Interestingly, each of the solar system planets hosting a dynamo today reveals some distinctions from a hypothetical standard dynamo model of a stationary dipole dominated field elongated with the axis of rotation. For example Mercury has a peculiar weak but actively generated field, Mars' field was probably quite confined to the southern hemisphere, Saturn's is extremely axisymmetric, whereas the dynamos of Uranus and Neptune show exceptional strong dipole tilting angles. For the time dependence of the dynamo of the Earth, statistical reversals of the field on time scales of several hundreds of millions of years are also a possible state of a planetary dynamo process (Glatzmaier and Coe 2007). The magnetic field of the sun has a strong time dependence too, but with remarkable differences. A magnetic cycle of the solar dynamo takes as long as 22 years, and the oscillations are strongly periodic (Rüdiger and Hollerbach 2004).

In this study we focus on the dynamo process in terrestrial planets. The four terrestrial planet Mercury, Venus, Earth and Mars, are structured roughly in the same way. On the surface of the planet a brittle crust of low-density material like basalts or silicates form the upper solid boundary of the planet. Under this so called lithosphere (solid) with a thickness of tens of km a convecting or non convecting mantle reaches typically down to a large fraction of the total planetary radius (Schubert et al. 2001). Underneath resides the planet's core. It mainly consists of iron, but usually also a lighter element such as sulphur or oxygen is part of the core melt. Temperature and pressure increase with depth and are such high in the core, that the core material can be fully or partially liquid. In some planets there is also a solid inner core of pure iron, which nucleates when the iron in the core melt solidifies at the center of the planet.

All the geophysical activity, such as mantle convection and a possible core dynamo is controlled by the thermal evolution of the planet. The initial thermal structure of a planet depends on the accretional heat during the planetary formation and distribution and concentration of radioactive elements. Temperature and pressure increase with depth inside the planetary interior and thus there is (to first order) radial outward directed temperature gradient. The simplest mechanism to transport heat towards the planetary surface is heat conduction. If the temperature contrast across the mantle or the core exceeds a critical value (adiabatic temperature gradient), it becomes energetically more efficient to support the heat conduction with a convective transport of hot material towards the cool surface. Convection in the mantle gives rise to sluggish large scale up- and downwellings, what translates to the observable plate tectonics, sea floor spreading or other geologic activity. The presence of a global magnetic field generated by an internal dynamo might attest convective motions in the core.

1.2 Dynamos in Terrestrial Planets

The phrase 'dynamo process' means the production of a self-sustained magnetic field via continuous transformation of kinetic into magnetic energy, such that the induction mechanism overwhelms the ohmic decay of the magnetic field. The main ingredients are on the one hand a sufficiently complex motion driven, e.g. by the interplay of convection and the action of the Coriolis force. And on the other hand the presence of a conducting fluid, such as liquid iron in terrestrial or metallic hydrogen in gas planets or liquid sodium in dynamo experiments.

The evolution of a magnetic field is described by the induction equation, which is

Quantity	symbol	value	Reference
planetary radius	r_{tot}	3390 km	3
planetary mass	m	6.41×10^{23} kg	
radius cmb	r_o	1550 km	3
gravitational accel. surface	g_0	3.25 $\mathrm{m/s^2}$	1
gravitational accel. CMB	g_0	2.5 $\mathrm{m/s^2}$	1
density CMB	ρ_0	7200 $\mathrm{kg/m^3}$	3
pressure CMB	p_o	40 GPa	2
adiabatic CMB heat flux	q_0	5-19 $\mathrm{mW/m^2}$	2
heat capacity	C	840 J/kgK	3
temperature CMB	T_0	2000 K	1
kinematic viscosity	ν	5×10^{-7} $\mathrm{m^2/s}$	4
thermal expansivity	α	2.5×10^{-5}	2
thermal conductivity	k	45 W/mK	2
electric conductivity	σ	4×10^5 S/m	4

Table 1.1: Typical core values for the Ancient Martian core. References 1 - (Sohl and Spohn 1997), 2 - (Nimmo and Stevenson 2000), 3 - (Morschhauser et al. 2011) and 4 - Jones (2007)

function of the magnetic field $\boldsymbol{B}$ and the velocity of the conducting fluid $\boldsymbol{u}$. Here we anticipate the induction equation, whereas the derivation and deeper discussion can be found in section 2.5:

$$\frac{\partial \boldsymbol{B}}{\partial t} = \nabla \times (\boldsymbol{u} \times \boldsymbol{B}) + \lambda \nabla^2 \boldsymbol{B} \ . \tag{1.1}$$

Here $\lambda = 1/\sigma\mu_0$ is the magnetic diffusivity, given by the conductivity σ and the vacuum permeability μ_0. The first term on the right hand side is the dynamo term converting kinetic energy into magnetic energy, the second term is the ohmic decay dissipating magnetic energy. A small magnetic seed field will amplify, if the first term exceeds the second one (Roberts 2007) in amplitude. The ratio between both is given by the magnetic Reynolds number Rm:

$$Rm = \left| \frac{\nabla \times (\boldsymbol{u} \times \boldsymbol{B})}{\lambda \nabla^2 \boldsymbol{B}} \right| \approx \frac{UB/L}{\lambda B/L^2} = \frac{UL}{\lambda} = U\, L\, \sigma \mu_0 \ . \tag{1.2}$$

Therefore Rm needs to be larger than unity, to allow for dynamo action. A typical value for the velocities $\boldsymbol{u}$ in the core are of the order of 10^{-3} m/s (Jones 2007), the electrical conductivity of the core melt is nearly metallic ($\sigma = 4 \times 10^5$ S/m). The other parameters can be taken from the table 1.1. Then we find for the core of a terrestrial planet such as Mars, $Rm \approx 800$, therefore a dynamo is possible.

The metallic conductivity σ is given by the large contribution of iron in the core melt. A terrestrial planet needs be chemically differentiated, thus heavy iron has accumulated in the center of the planet forming an iron core. For such a process a significant fraction of the planet volume needs to be molten (Weiss et al. 2010). Planets of sufficient radius (more than 2000 km) gain enough gravitational energy during formation to melt the planet body completely (Wetherill 1990, Weiss et al. 2010). Then the heavy iron migrates to the center of the planet thus forming a core enriched in iron. There might be minor contributions of light elements. Given the large cosmochemical abundance, sulphur is the most likely candidate (Schubert and Spohn 1990). Depending on size, composition and pressure of the core melt, the large iron fraction can remain entirely or partially liquid for several billions of years.

The characteristic velocity used for calculating the magnetic Reynolds number Rm (eq. 1.2), is thought to represent a typical amplitude of convective motions in the core, therefore core convection might be needed to enforce a core dynamo. However, there are also other sources of hydrodynamic instabilities possible, such as precession (Tilgner 2007) or superrotation (Guervilly and Cardin 2010). For thermal convection the amount of heat escaping from the core into the mantle is the crucial quantity. If this heat flux exceeds the so called adiabatic temperature gradient, convective motions support the heat conduction. We will later derive and calculate this adiabatic gradient (see section 2.3). Besides the thermal driving, also compositional convection can occur in terrestrial cores (Jones 2007), since the core melt contains minor contributions from lighter elements. During cooling of the core, the melt can cross the core solidus, thus iron freezes out and form a solid inner core of pure iron. The release of light elements at the CMB additionally drives then chemical or compositional convection, while the solid inner core grows. This flux of light elements serves as an additional buoyancy source. An excellent review of the theory of chemical and thermal convection can be found in Jones (2007). To sustain a convective dynamo process, the core material thus needs to be at least partially liquid and the buoyancy gradients must be steep enough. If the core is entirely solidified due to runaway inner core solidification or the CMB heat flux drops under the adiabatic gradient, the dynamo process can not be maintained again the ohmic losses and thus the magnetic field ceases.

Planets are fast rotating objects, they spin around their figure axis and additionally around the central star. The typical time scales τ_{rot} of the daily rotation $\tau_{rot} = 1/\Omega$, where Ω is the rotation rate. For Mars $\tau_{rot} = 2.8 \times 10^{-3}$ yr. We want to relate this time with the time scale of viscous diffusion. The dynamic viscosity $\eta = \nu\rho$ of the core melt $\eta \approx 7 \times 10^{-3}\,\mathrm{kgm^{-1}s^{-1}}$ (Jones 2007) and thus comparable to the viscosity of liquid water ($\eta \approx 1.5 \times 10^{-3}\,\mathrm{kgm^{-1}s^{-1}}$). The density of the core melt is $\rho \approx 7 \times 10^3\,\mathrm{kg/m^3}$. The appropriate viscous diffusion time scale is given by D^2/ν. When assuming a core thickness of 1550 km, this yields $\tau_{vis} = 1.8 \times 10^{11}$ yr. Therefore the rotational time scale is by far shorter than the viscous diffusion, thus the rotation of the planet dominates the evolution of the flow and viscous effects play only a minor role. On the other hand, such a small viscosity is needed to reach sufficiently high core flow velocities. The ratio of the two time scales is named Ekman number, and we will re-find this number during the discussion of the MHD equations.

The theoretical investigation of fast rotating and convecting fluids in spherical shells is well established (Busse 1970, Jones 2007). We define a coordinate system such that the rotation vector points to $\mathbf{\Omega} = \Omega \boldsymbol{e}_z$. The large Coriolis force ($2\rho\mathbf{\Omega}\times\boldsymbol{u}$) breaks the spherical symmetric properties of the core and thus defines an preferred axis (z-direction here). If the large Coriolis force would not be balanced in some way, very fast variations of the core flow would occur and thus the magnetic field would vary on similar short time scales, what does not seem to be the case (Jones 2007). In the absence of buoyancy and Lorentz force, the main force balance is between the Coriolis force and the pressure gradient (Jones 2007). Albeit, we discuss the force balance or the conservation of momentum (Navier-Stokes equation) and its simplifications extensively in section 2.1, we anticipate the force balance given by only the two terms of the Navier-Stokes equation representing pressure gradient and Coriolis force:

$$0 = -\nabla p + 2\rho\mathbf{\Omega} \times \boldsymbol{u} \, . \tag{1.3}$$

The pressure gradient term ∇p is a conservative term, since it can be describe as the gradient of a scalar potential (the pressure). The Coriolis force is in general not a conservative force, since it does not vanish when applying a curl operator. If now the main force balance is supposed to be established between pressure gradient and Coriolis force, the velocity field has to organize in way such that the curl of the Coriolis force vanishes or at least becomes small:

$$\nabla \times (\mathbf{\Omega} \times \boldsymbol{u}) = 0 \ \text{ if } \ \frac{\partial \boldsymbol{u}}{\partial z} = 0 \tag{1.4}$$

This is known as the Taylor-Proudman theorem and will lead to so called 'geostrophic flows'. Core flows have then the requirement for not changing along any axis parallel to the rotation axis. The buoyancy introduced by thermal or compositional convection is directed radially outward, and might then counteract the Taylor-Proudman theorem, which tries to constraint motions to be independent of z-direction. Close to the onset of convection, Busse (1970) showed that the convection sets in a geometry of convective columns. The convective columns are parallel to the rotation axis, and therefore do not violate the Taylor-Proudman constraint. Close to the inclined outer boundaries and (if present) inner boundaries, the Taylor-Proudman theorem will be not valid anymore and the other forces such as viscosity play a large role there.

If the flow is also subject to a Lorentz force, introduced by the magnetic field, the main force balances will be altered. The ratio of the Coriolis and Lorentz force, known as the Elsasser number Λ, is of order unity (Christensen and Wicht 2007) and therefore the Lorentz force is significant for the 'magnetostrophic' force balance. The convective columns elongated with the axis of rotation host the main induction effect, therefore the magnetic field also has the preferred direction along the rotation axis.

1.3 Thermal Evolution of Mars

The planet Mars is the fourth planet of our solar system and accompanied by two moons, Phobos and Deimos. Planetary radius and mass are significantly smaller than for the Earth (see table 1.1 for details), but the chemical composition is very similar (Spohn et al. 2001). Together with Mercury, Venus and Earth Mars forms the group of the terrestrial planets. But there are major differences between Mars and Earth, such as the absence of a global magnetic field or the thin atmosphere. Today, the atmosphere has an extremely low pressure of only a few millibars (Zolotov 2007), containing mainly carbon dioxide CO_2. Mars might have lost most of its volatile atmosphere constituents during its history, most probably due to the lack of a planetary magnetosphere protecting the atmosphere from erosion (Barabash et al. 2007). Observed from Earth or space, Mars shows a distinct reddish or brown color. This color is due to more abundant iron oxides on the surface (Spohn et al. 2001). A closer look reveals the remarkable geological features, such as the huge volcanic area of the Tharsis bulge, the crustal dichotomy or the Hellas basin. Especially the Tharsis region was found to be geological active in terms of volcanism during the very recent past, maybe even today (Hartmann et al. 1999).

One of the striking features of Mars is the hemispherical dichotomy in the crust. It was found that the northern crust is relatively thin (roughly 10 km), whereas the southern crust is thick (roughly 60 km) and old (Zuber et al. 2000). As one of the findings of the MGS (Mars Global Surveyor) mission, the two hemispheres also differ in the type of crustal rocks there are covered with (Bandfield et al. 2000). Crustal rocks on the northern hemisphere are mainly silica-rich, whereas in the southern hemisphere the rocks are more basaltic and therefore of volcanic origin. Laser altimetry from MGS space craft yields an elevation level of several thousands of meters (on average) of the southern highlands, where as the northern plains are below the zero line (Smith et al. 1999). The ticker southern crust is so more massive than the northern, the center of mass deviates by 3 km southwards from the center of figure (Smith et al. 2001). The origin of the crustal dichotomy is still under great debate (Breuer and Moore 2007), and may have been formed either externally by one mega-impact (Marinova et al. 2008), series of large impacts (Frey and Schultz 1988) or internally by low degree mantle convection (Keller and Tackley 2009) an thus dichotomous crustal growth.

All of these features and findings are the consequenceses of several billions of years of planetary evolution. As a first step, we adopt the partition of the Martian evolution into three main epochs. The methods of crater chronology yields a division of the history of Mars into geochrons (or better areochrons). Details for the geochronology can be found in Tanaka (1986) and Hartmann and Neukum (2001).

- Noachian : 4.5 - 3.7 Gyrs of age
- Hesperian : 3.7 - 3.0 Gyrs of age
- Amazonian : 3.0 - present

The border between Noachian and Hesperian is given by the end of Late Heavy Bombardement (Hartmann and Neukum 2001). Noachis, Hesperia Planitia and Amazonia Planitia are geologic features showing a typical terrain created during that epoch. During the noachian epoch, thus in the first several hundred million years after accretion, Mars was a geophysically very active planet hosting mantle convection, volcanism and (most probably) the generation of a strong internal magnetic field.

The crustal magnetization observed by the MGS space craft reflects the dichotomy in the crust to a large extend. Therefore it is an interesting question when and how the crustal dichotomy was formed. The precise age of the crustal dichotomy is still under debate. In older studies, it was assumed, that the northern plains created during the end of Hesperian are significantly younger than the southern highlands formed during the Noachian (Banerdt et al. 1992). Then the northern crust was formed without the presence of a global magnetic field. However the more recent studies contradict this conjecture. Breuer and Moore (2007) pointed out that the dichotomy is probably one of the oldest features on Mars, whereas Nimmo and Tanaka (2005) suggest an age of 3.9 Gyrs (late Noachian) thus coinciding with the end of the Martian dynamo. Frey et al. (2002) concluded from Laser Altimeter data, that the Martian northern lowlands have been stable throughout the entire history of Mars. The numerous detection of impact craters buried by a thin and plain layer (northern plains), gives rise the conclusion that the bulk of the northern crust is much older than the plains covering them (Frey et al. 2002). In any case a precise dating of the dynamo period can yield some constraints on the crustal evolution.

After the accretion Mars was entirely molten, the iron migrate towards the center of the planet and form an iron core (Spohn et al. 2001). The differentiation into crust, mantle and core might not have taken longer than 20 Myrs, as suggested by Lee and Halliday (1997). The fraction of light elements in the core is thought to be roughly 15% of (most probably) sulphur. The fact that the crust is (compared to Earth) more enriched in iron oxides, the larger light element abundance in the core and studies on isotopic measurements of SNC meteorites suggest the differentiation process and mixing by mantle convection throughout the Martian evolution was much less efficient or incomplete (Spohn et al. 2001). Here our specific interest is on the evolution of the mantle convection. Mantle convection controls the thermal evolution and the amount of heat extracted from the underlying core. A significantly high CMB heat flux is a crucial ingredient for a magnetic dynamo driven exclusively by thermal convection. In opposite to the Earth there is no observation of the total heat flux emerging from the surface of Mars. Knowledge of today's surface heat flux might not be sufficient to decide about the supercriticality of a possible ancient dynamo. Radiogenic heating in the mantle typically exceeds the heat flux originated from the secular cooling of the core by an order of magnitude (Spohn et al. 2001, Breuer and Moore 2007). The core mantle boundary heat flux is basically given as the sum of the adiabatic secular cooling, the convective cooling and a possible, but minor, contribution from radiactive decay. Since the Martian core did likely not start to nucleate an inner iron core the additional solidificational heat is zero. We will discuss the state of the Martian core in greater detail in section 1.7. One hint for the timing of the dynamo comes from magnetized and unmagnetizd impact craters and their ages, where the magnetized ones are formed during the presence of an ambient magnetic field. Lillis et al. (2008b) proposed a strong decay of the magnetic field strength during the Noachian at roughly 4.1 Gyrs ago due to unmagnetized large craters, such as the Hellas basin. Langlais et al. (2012) analyzed impact basins and volcanoes for setting the end of the Martian dynamo at 3.77 Gyrs, so between late Noachian and Early Hesperian. Besides this approach the analysis of rock samples from Martian meteorites (if magnetized) can also yield contraints on the timing and magnetic field strength. Further details on the SNC meteorites and their magnetic properties are discussed in section 1.4.2.

The magnetic history of Mars is closely related to its thermal evolution. Estimates from modeling of the thermal evolution of the planet suggests an active dynamo only during the Noachian period (Breuer and Spohn 2003), where the CMB heat flux was superadiabatic. Most probably the crustal rocks showing thermoremanent magnetization today, were generated during this early phase of the planetary evolution. Although the mixing efficiency of the mantle was not very strong as mentioned above, mantle convection was most probably active during the entire history of the Martian evolution (Spohn et al. 2001). Satisfying the argument of an incomplete mixing of the mantle and the permanent mantle convective motions, it was suggested that the mantle convection develops with only a few or even one single upwelling (Breuer and Moore 2007). There have been several attempts to apply mantle convection models to the characteristic setup of early Mars, such as phase transitions (Harder and Christensen 1996, Roberts and Zhong 2006) introducing a viscosity jump, different rheology (Yoshida and Kageyama 2006) or initial temperatures to achieve a low-degree mantle convection, see Breuer and Spohn (2003), Roberts and Zhong (2006), Spohn et al. (2001), or Morschhauser et al. (2011) for the most recent study. Also the relation to the crustal thickness dichotomy was used to link a probable single plume mantle convection to the different crustal production rates in the two hemispheres (Breuer et al. 1993). We will make use of the single plume convection, when assuming that the thermal footpoint of such a large scale upwelling will dehomogenize the lateral CMB heat flux pattern.

Plate tectonics as present on Earth are one of the states of mantle convection. It is very likely (Breuer and Spohn 2003), that during an early phase in the Martian history plate tectonics was present and mantle convection was much more energetic (Spohn et al. 2001). As a consequence, the mantle cooled more efficiently and the heat flow through the CMB exceeded the critical value necessary to drive a dynamo. On today's Mars, the entire crust forms one single plate which significantly limits the vigor of mantle convection and thus the heat transport through the mantle. An hypothetical early phase of tectonic activity (Breuer and Spohn 2003) during the Early Noachian, requires a change in the style of the mantle convection from plate tectonics to the (now present) stagnant lid regime. Morschhauser et al. (2011) pointed out that besides a phase of plate tectonics alternatively an initially superheated core is possible to allow for a thermally driven dynamo process in the core.

1.4 Crustal Magnetization

The bulk of the Martian crust (100 km depth) is thought to be formed during the Noachian (Breuer and Spohn 2003), what coincides the active dynamo period. Albeit a phase of early plate tectonics allows for an efficient cooling of the mantle and thus a core dynamo to operate, the (magnetized) crust will remain thin due to the fast recycling. As a comparison, the subductable oceanic crust of the Earth has an average thickness of only 8 km. Morschhauser et al. (2011) found a crustal thickness of 50 km for the now present stagnant lid regime. Magnetized crust needs to be created during the period of an active core dynamo, where a magnetization depth of at least 20 km (Langlais et al. 2004) is required to match the measurements of the magnetic moment. It therefore remain an open question to what extend early plate tectonics on Mars are compatible with the crustal magnetization pattern and amplitude.

Crustal magnetization is a magnetic fingerprint acquired during one or several periods of active dynamo action during the evolution of the planet. Rocks formed and cooled under the Curie temperature conserve the ambient field orientation and (to some extent) the magnetic field strength. If no altering or reheating process occurs, this Thermoremanent

Magnetization (TRM) can survive for billions of years. The oldest magnetized rock samples on Earth date back to 3.5 Gyrs (Hulot et al. 2010) and are located in unsubductable continental crust. Oceanic crust on the other hand is permanently created and recycled into the mantle, therefore it can only reaches ages of several hundred million years. It is created in crustal spreading zones at divergent plate boundaries, where it then moves outwards due to the mantle convective motions. In the presence of an ambient magnetic field, ferromagnetic minerals allow to imprint the actual direction and strength of this field. If the magnetic field changes polarity the typical stripe pattern of crustal magnetization, e.g. starting at the mid-atlantic ridge, emerges. The width of one individual stripe then gives the time of a stable polarity assuming knowledge about the plate divergence speed. These measurements were the first hint for the reversing nature of Earth's magnetic field. Crustal magnetization was also found in rocks on the lunar surface during the Apollo 11 missions and interpreted being of thermoremanent origin (Runcorn et al. 1970). However, the famous 'Runcorn Theorem' appeared in the course of the discussion of an ancient lunar dynamo. Runcorn (1975a) calculated, that a homogeneously magnetized spherical shell will not show any external field outside the shell, if the magnetizing field was of dipolar morphology. Therefore all magnetic anomalies measured in the crust are only deviations from a homogeneously magnetized crust (Runcorn 1975b). In a more recent study by Leweling and Spohn (1997) this ideas were applied to Martian crustal magnetization as well. That means it is indeed possible that besides the detectable anomalies, as measured by the MGS space craft (Acuña et al. 1999), a homogeneous crustal magnetization of unknown magnetic moment is present in the crust. Of course, it might be rather unlikely to magnetize crust homogeneously because magnetization events appear more statistically and the magnetization depth is in general strongly inhomogeneous.

1.4.1 Crustal Genesis and Chemistry

A crustal rock conserving magnetic signals needs to be ferromagnetic. In such materials the microscopic magnetic moments rearrange to a macroscopic magnetization in the direction of the ambient field. In opposite to paramagnetic materials, the magnetization remains after the removal of the ambient field. To first order, the relation of induced magnetization and the ambient field is parallel and linear, given by the magnetic susceptibility χ (Langlais et al. 2010). Ferromagnetic rocks gain this ability from the iron, cobalt or nickel contribution (Langlais et al. 2010), where on Mars iron is by far the most abundant of them. In its ferromagnetic phase it can be found in minerals such as magnetite Fe_3O_4 or hematite Fe_2O_3 or in combination with sulphur in iron sulfides FeS or oxyhydroxides such as goethite FeO(OH). The iron is sometimes replaced by titanium. Once a rock is formed and reaches the Curie temperature while cooling, it imprints the direction and strength of the ambient field. This critical temperature defines the point, from which the thermal fluctuations of the individual magnetic spins are exceeded by the ordering force due to ferromagnetism. The Curie temperature ranges from 700°C for magnetite and hematite down to 150°C for minerals with strong titanium abundance (Langlais et al. 2010). Note, that most of the upper mantle and crustal rocks are silicates $(\mathrm{Mg}, \mathrm{FeSiO_4})$, not oxides. Silicates do not contribute to the crustal magnetization even if they contain iron, because the iron atoms in the crystal lattice are spatially not close enough for a ferromagnetic interaction. Another source of magnetization in rocks is the process of serpentinization or hydrothermal alteration of iron bearing silicates, where they are transformed in the presence of water into magnetite Fe_3O_4 (Langlais et al. 2010). Since magnetite is ferromagnetic, it will imprint the direction and strength of the ambient field at the moment this process takes place. Hood et al. (2005) suggested that hydrothermal alteration of silicates are the main source of the strong magnetic anomalies. However, the composition and mineralogy of the crustal rocks remains an open question, and it is unclear to what extend different rocks serve as carriers of the crustal magnetic field.

1.4.2 Measurements and Satellite Data

A very successful way to study the early evolution of the solar system and its planets, is the analysis of meteorites as witnesses of early solar system composition or paleomagnetic data. A detailed discussion of this subject is beyond the scope of this work, but an excellent review can be found in Weiss et al. (2010). There are roughly 50 meteorite samples, which have been identified sampling the crust of Mars (Weiss et al. 2008). They are called SNC[1] meteorites, and only a few of them carry magnetic signals (Rochette et al. 2001). There is only one meteorite sample containing both, thermoremanent magnetization and an age old enough to be magnetized during the period of an active dynamo (Noachian), namely the meteorite ALH84001 (Weiss et al. 2002). This meteorite shows strong natural remanent magnetization acquired during cooling under the Curie temperature in an ambient planetary magnetic field. Analysis of bulk grains suggested an ambient field strength ranging from $5 - 50\,\mu$T (Weiss et al. 2002), whereas studies on much smaller samples suggest stronger fields of $38 - 64\,\mu$T (Weiss et al. 2008). It should be mentioned that this estimate only reflects the local field strength at a given spot in space and time when this piece of rock was formed. Analysis of this meteorite brought up the major finding that comparing to Earth's concentration of ferromagnetic minerals, a 10 times larger ferromagnetic density is needed to achieve the global magnetic moment of the crustal magnetization on Mars (Weiss et al. 2008). Or as another possibility, the volume of magnetized material needs to much larger. However, Langlais et al. (2010) argued that the maximal magnetization depth of the Martian crust during the Noachian period is restricted in depth by the Curie temperature and might not exceed 40 km.

Meteorites found on Earth allow for analysis in the lab, but the in situ measurements can only be conducted by space crafts or rovers. There have been 24 missions to Mars, where 14 of them were successful (Ness 2010). The search for the present or past existence of liquid water as a possible potential habitat of extraterrestrial life made Mars the most studied planet of the solar system besides Earth. A few space crafts studied the magnetic properties of Mars as well. It was known that solar wind and an internal magnetic field do not form a large magnetosphere as on Earth (Balogh 2010), but the thin ionosphere of Mars being an obstacle for the solar wind. It lasted until the Mars Global Surveyor orbiting phase in 1997 to map the magnetic field of the Martian crust (Ness et al. 1999). A combination of fluxgate magnetometer and electron reflectometer was used to measure the magnetic vector field during the aerobreaking phases. These phases are used to slow down the space craft using the friction of the atmosphere and circularize the space crafts orbit. After the initially highly elliptical aerobraking phase, the

[1]SNC stands for Shergottite, Nakhlatite, Chassignytite

scientific measurements began at an altitude of 400 km, whereas MGS approaches Mars during the aerobraking as close as 100 km Langlais et al. (2010). The further away the space craft is from the surface of the planet, the more the magnetic signal is biased by the solar wind-ionospheric interaction. The aerobraking phase revealed for the first time the crustal magnetization (Acuña et al. 1999), because MGS reaches altitudes smaller than the bow shock of the ionosphere.

The MGS conducted map of crustal anomalies (figure 1.1) shows several distinct features, the most surprising is the strong equatorial asymmetry. Most of the magnetized rocks are south of the equator in the old and heavily cratered terrain. There is also a significant dependence on azimuthal direction. The strength of the NRM (natural remanent magnetization) excludes any external origin Acuña et al. (1999). The magnetic lineations observed in the patterns of the crustal magnetization were interpreted as the fingerprint of a reversing magnetic field magnetizing fresh crustal rocks in a divergent crustal spreading zone (Connerney et al. 1999). During the Noachian period (4.4 – 3.9 Gyrs ago) most probably the Martian crust was formed and magnetized in the presence of an ambient magnetic field of internal origin. The end of the active dynamo period is inferred from the ages of unmagnetized impacts basins in the southern hemisphere. We will discuss the possible magnetization and demagnetization scenarios in section 1.4.3.

The magnetic moment of some sources are of the order of $10^{16}-10^{17}$ Am^2 (Acuña et al. 1999), (Connerney 2007), requiring a very large magnetization volume (3.6×10^{15} m^3, Langlais et al. (2004)). The thickness of the magnetized layer is thereby a crucial information needed to infer the remanent magnetization density of the crustal rocks, since only the product of magnetization density and magnetized volume is constrained. An upper limit of the crustal magnetization thickness is given by the depth of the Curie temperature. Assuming a temperature gradient of roughly 10 K/km in the crust of ancient Mars leading to a maximum Curie depth of 50 km. Since the Curie temperature of ferromagnetic rocks depend strongly on the content of titanium, thinner layers are usually assumed. Langlais et al. (2004) obtained a magnetization of ±12 A/m and ±25 A/m, for a 40 km and 20 km magnetized crust, respectively. An even thinner magnetized crust would require a much higher magnetization, what is unlikely.

There are basically two methods how to translate a magnetic vector field measurement from a space craft at different altitudes to a map of crustal magnetism. Either an expansion in spherical harmonics (Cain et al. 2003) or a carpet of equivalent dipole sources (Langlais et al. 2004) are used to reconstruct the observed field at space craft altitude. The expansion in spherical harmonics is intensively used to describe the large scale magnetic field of the Earth, but brings mathematical difficulties if the anomalies are rather small scale and of crustal origin or if the data coverage is non-homogeneous or sparse (Langlais et al. 2004). The amplitudes of the magnetic anomalies needed are up to ±200 nT at 400 km to match the observation. The anomalies at the surface (or within the first tens of km crust) reach 1500 nT (Connerney et al. 1999) or even exceed 5000 nT (Langlais et al. 2004). It will need then a substantial amount of spherical harmonics modes (Cain et al. (2003) used $n = 90$ modes), to properly describe the field. Therefore the equivalent dipole source is the better approach.

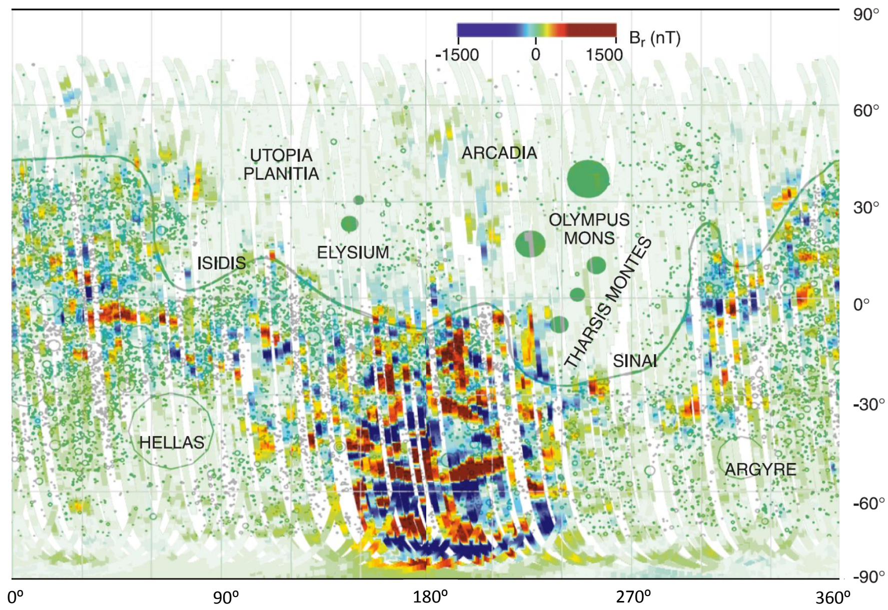

Figure 1.1: Map of the radial magnetic anomalies measured by the MGS space craft (Acuña et al. 1999). The green line denotes the 'border' between the chemically distinct hemispheres.

1.4.3 Magnetization and Demagnetization

Different magnetization scenarios were discussed as alternatives to explain the dichotomy in crustal magnetization. The distinct hemisphericity in the crustal magnetization, puts some constraints on the magnetizing and demagnetizing history. The simplest model would assume a stable dipole dominated magnetic field, what would magnetize all rocks reaching (cooling) the curie temperature as long as the dynamo runs. This will lead to a more or less homogeneous distribution of magnetized sites. Then after the cessation of the dynamo the demagnetization process needs to be of sufficient equatorial asymmetry. Large impacts, e.g. in the northern hemisphere then have to demagnetize the crust due to shock demagnetization and supercurie thermal heating (Lillis et al. 2008a, Mohit and Arkani-Hamed 2004). Other geological activity such as volcanoes, would need to demagnetize and heat up the underlying crust in sufficient depth and width. However it remains statistically quite unlikely, only to demagnetize the northern hemisphere by impacts or other resurfacing events. Several work has been done to relate the absence of magnetic signatures and the crustal dichotomy (Marinova et al. 2008, Keller and Tackley 2009). We discussed already the possibilities of the different ages of the crust in both hemispheres, where the more recent work suggested that both crustal hemispheres are older than the end of the dynamo (Breuer and Moore 2007).

Note, that today's magnetization pattern might not reflect the original positions of the magnetizations. A source of bias are plate tectonics which would rearrange the magnetized sites around the globe. Of course it might be also possible, that the rotation axis of planet in its orientation today differs strongly from the orientation when the crust was magnetized. Different studies tried to fit a simple dipolar magnetic mode to the observed magnetization, where the typical outcome of these studies suggest a true polar wander event (Hood et al. 2005, Sprenke and Baker 2000). There it assumed that the magnetic field consists only of a dipolar mode, which is elongated with the rotation axis. The rise of the Tharsis bulge is thought to lead into such a global reorientation of the spin axis (Melosh 1980).

Here the possibility of a magnetizing field is investigated, which has already intrinsically the same equatorial asymmetry as the measurements of the crustal magnetization pattern. An admissible model for such a dynamo should be able to recover the strong crustal magnetization (or at least exceed the magnitude of the thermal remanent magnetization), and persist over time long enough to magnetize several tens of kilometers of crust. In section 5 the translating step from time scales typical of the dynamo towards a magnetization time is discussed in detail. It is shown there that the crustal field will in any case reflect the time averaged dynamo field. Dynamo solutions with fast polarity reversals are then ruled out, since they can not provide a stationary field over the time scales typical for the magnetization process. Such a hemispherical dynamo model does not need any hemispherical demagnetizing resurfacing or a true polar wander event in order to explain the hemispherical magnetization on the Martian crust.

1.5 Core Mantle Interactions

For our purposes the thermal interaction between mantle and core is crucial. Between mantle and core a layer boundary (CMB) controls the outward transport of heat. It is assumed, the this heat transport is only via heat conduction thus there is no material exchange between mantle and core. The thermal properties of the CMB are determined by the convection in the mantle and by the convection in the core. In comparison, convective motions in the mantle are rather sluggish and large scale, whereas core convection is much faster and vigorous. A typical convective time scale is the convective turn over time τ_{con} given by the ratio of a typical length to a typical velocity. Assuming 5×10^{-4} m/s (Bloxham and Gubbins 1987), and 5×10^{-7} m/s (Schubert et al. 2001) as typical convective velocities for core and mantle, yields a factor of 10^3 between the two when assuming comparable convective length scales in the core and the mantle. Due to this faster convective stirring in the core, the CMB will provide an isothermal boundary for the mantle. Bloxham and Gubbins (1987) estimated the temperature anomaly introduced by core convection at the bottom of the mantle to be as small as 5×10^{-4} K as seen from the mantle. But for the core, the large lateral heterogeneities at the bottom of the mantle due to hot upwellings, cold downwellings or subducted (and cold) slabs (Schubert et al. 2001) will affect the amount of heat conducted through the CMB. As a consequence the CMB translate the thermal variations introduced by mantle structures into a heterogeneous pattern defining the upper thermal boundary for the core. The appropriate thermal CMB boundary condition for the core is then a heat flux condition, whereas the core provides an isothermal lower boundary for the mantle (Bloxham and Gubbins 1987).

Several studies investigated the effect of non-homogeneous core mantle boundary heat flux on core convection and dynamo action. Since most of the studies are related to the Earth, the typical shape of the anomaly is the sectorial Y_2^2-pattern. Y_l^m is the spherical harmonic of degree l and order m. This pattern is determined by the analysis of seismic velocity anomalies. The PREM model, as a seismic reference model (e.g. in Dziewonski and Anderson (1981)), suggests seismic anomalies at the base of the mantle shaped to first order like a spherical harmonic mode of degree and order $l = m = 2$. Assuming a linear relationship between seismic velocity and temperature yields the same pattern for a CMB heat flux map. It has been shown, that such a pattern may affect dynamo secular variation (Christensen and Olson 2003), the reversal rate (Glatzmaier et al. 1999, Olson et al. 2010), the amplitude (Olson and Christensen 2002) or morphology of the core field (Takahashi et al. 2008, Bloxham and Gubbins 1987, Bloxham 2000), Earth's inner core boundary (Sreenivasan and Gubbins 2011) and inner core anisotropy (Aubert et al. 2008a).

Also for the ancient Mars during the period of an active dynamo process, the mantle will have the control over the core convection. Whilst the thermal structure of the mantle of Earth was measured using seismic tomography and revealed the dominant Y_2^2 pattern, the pattern for Mars remained unconstrained. However, since Mars is significantly smaller than the Earth, it is expected that the mantle convection planform develops in large scales. Numerical modeling of the Martian mantle convections typically show a few or even only one single plume (Keller and Tackley 2009, Harder and Christensen 1996, Roberts and Zhong 2006, Yoshida and Kageyama 2006). Besides the thermal impact at the CMB of such a mantle plume, also the crustal production rate will be enhanced, therefore a thicker crust is expected (Keller and Tackley 2009). Also the geologically active Tharsis region is thought to be heated from an equatorial giant mantle plume. Probably even the same plume, if there was a true polar wander event. Here some contradictions appear. The study of Keller and Tackley (2009) locate a single mantle plume underneath the southern crust since it enhanced the crustal production rate, whereas strong volcanic activity of the Tharsis region coincides with an equatorial plume (Breuer and Moore 2007). Other studies see the position of this hot mantle upwelling located in the northern hemisphere, where it creates basaltic crust in the northern hemisphere (Bandfield et al. 2000). It remains an open question if and when a global reorientation of the planetary rotation axis (true polar wander) had happened during the evolution of the planet.

Besides the large scale mantle convection, also impacts of sufficient size will dehomogenize the CMB heat flux. However, the effect of large impacts on planets is currently under great debate. Roberts et al. (2008) argued that impacts can dehomogenize the CMB heat flux since they create temperature anomalies in the underlying mantle. Furthermore, upwelling or hot plumes will arise under the impact region and, as a consequence, also lower the CMB heat flux underneath the impact site. Recently it was reported that globally distributed temperature anomalies due to the dissipation of shock waves triggered by the impact, as reported by Arkani-Hamed and Olson (2010), can effect mantle and core. Note, that large impacts are also thought to cease dynamos due to subcriticality (Roberts et al. 2009) or shock heating (Arkani-Hamed and Olson 2010). If the iron content of the impactor is large enough, impacts can also trigger a dynamo (Reese and Solomatov 2010).

We will simplify the effect of the impacts such that only the effect of a laterally varying CMB heat flux is taken into account. Therefore both, single-plume mantle convection and giant impacts lead to first order into a spherical harmonic degree-1 CMB heat flux anomaly.

1.6 CMB Heat Flux and Amplitude of Anomalies

Studies on planetary thermal evolution provide estimates of the amount of heat evacuated from the core into the mantle (Sohl and Spohn 1997, Morschhauser et al. 2011) during the evolution of the planet. The recent study by Morschhauser et al. (2011) addressed the thermal evolution of Mars and found a CMB heat flux decreasing from 140 to 10 $\mathrm{mW/m^2}$ during the first 500 Myrs of planetary evolution. The adiabatic gradient is estimated by Nimmo and Stevenson (2000) to be between 5 and 19 $\mathrm{mW/m^2}$ thus defining the amount of heat conducted down the adiabate. Since the excess over the adiabatic heat flux is rather large, thermal core convection and thus a thermally driven dynamo might be present during that time. As an example, a CMB heat flux of 100 $\mathrm{mW/m^2}$ translates into a temperature gradient of 2.2×10^{-3} K/m, when using a thermal conductivity k of 45 W/mK (Jones 2007). The adiabatic temperature gradient in the core is then less than one Millikelvin per meter. A hot mantle plume or convective upwelling will decrease, at least locally, the heat flux from the core, since the temperature difference between mantle and core shrinks. On the other hand a cooler mantle downwelling can increase the core heat flux. As a rough estimate, that total temperature anomaly of mantle convective features might be 80% of the heat flux, as suggested by Elkins-Tanton et al. (2005). The authors investigate the dynamics and thermal properties of convective magma ocean overturns and the foot points of thermal up- and downwellings. Assuming a mean $q_{cmb} = 50\,\mathrm{mW/m^2}$ the local heat flux density then varies maximal between 10 and 90 $\mathrm{mW/m^2}$. When the adiabatic temperature gradient is 10 $\mathrm{mW/m^2}$, the relative change on the superadiabatic heat flux seen by the core can raise up to several 100%. Note, if an anomaly of the superadiabatic CMB heat flux has an relative amplitude of larger than 100%, the anomaly exceeds the mean superadiabatic heat flux. This might introduce some shortcomings, what we will discuss further in the conclusion section. Giant impacts can introduced temperature anomaly of several 100 to 1000 K at the core mantle boundary and will thus cause CMB heat flux anomalies of even larger scale and amplitude. The main problem for our numerical model is that the quantity we perturb with anomalies is the superadiabatic temperature or its gradient. This temperature is defined as the excess over the adiabatic temperature, which characterizes heat conduction along the adiabate. But, of course also the adiabate will be affected by thermal disturbances. This is not covered by the frequently used Boussinesq models.

1.7 Status of the Martian Core

Another debated point is the thermal state of the ancient Martian core in the stage of dynamo action (Breuer and Moore 2007). Here we are following the arguments of Schubert and Spohn (1990), where the authors used thermal evolution models to predict or exclude from the sulphur content in the Martian core a possible solidification of an inner core, thus driving compositional convection. Sulphur does have strong impact on the melting temperature of the core iron/light element mixture (Dehant et al. 2003). The amount of sulphur critical for chemical convection depends strongly on the viscosity of the mantle and the size of the inner core (Schubert and Spohn 1990). Williams and Nimmo (2004) found in a similar study, that a sulphur content of at least 5 wt% allows for an entirely molton core, whereas Schubert and Spohn (1990) and Dehant et al. (2003) provide 15 wt% of sulphur. However studies on SNC meteorites, as reported by Longhi et al. (1992), suggest an core sulphur content of around 14 wt% of sulphur, what is quite at the border of the maximum estimates for the critical sulphur content. It might then be reasonable, that the core has no solid inner part and thus no compositional convection has contributed to the buoyancy. Since this value is fairly close to the critical sulphur content, chemical convection could start at some point in the future. When the core was driven by thermal convection only, then it might have stopped during an early stage of planetary evolution (Schubert and Spohn 1990) once the CMB heat flux dropped under the adiabatic gradient, what seems to be consistent with the age of of unmagnetized impact basins (Lillis et al. 2008b). If on the other hand, chemical convection would have set in and thus an inner core would have grown, an additional and long-lived convective driving mechanism could have sustained the Martian dynamo for a far longer period (Breuer and Moore 2007). Other evidence for a liquid core even today might come from investigations of core nutations and other normal modes of the planet Mars (Dehant et al. 2003); seismic measurements would also help. Due to the lack of such data, the best way to infer the state of the Martian core are still the SNC meteorites. In our study we assume an entirely liquid core hosting thermal convection only.

1.8 Related Studies

There are several studies addressing the challenge of how to enforce and sustain a magnetic field of appropriate equatorial field asymmetry and field strength to match the magnetization measurements in the Martian crust.

Stanley et al. (2008) firstly introduced the model of a boundary modulated dynamo in the interior of the ancient Mars. In that study a fairly strong degree-1 CMB heat flux anomaly amplitude of three times the superadiabatic heat flow was used to successfully turn a dipolar into a hemispherical dynamo. The anomaly was orientated at the axis of rotation, such that the largest heat flux is at the southern pole. The flow structure showed the emergence of strong azimuthal zonal flows and the confinement of the convective motions close to the southern pole. Stable hemispherical dynamos were found, which are compatible with the requirements for the crustal magnetization. Mechanical and thermal boundary conditions are taken as free slip and fixed flux at the inner and outer core boundary.

Amit et al. (2011) improved the model using rigid walls and internal heating finding that, much smaller amplitudes of thermal boundary forcing are sufficient to drive a hemispherical dynamo. The authors directly relate the numerical results to the crustal magnetization and its acquisition, while using different time averages to bridge the short dynamo time scales to the much longer time scales of crustal genesis. Amit et al. (2011) also investigated orientations other than axial for the boundary anomaly. They report stronger hemispherical fields, when applying a north/south aligned anomaly than applying an east/west aligned anomaly. The influence of the passive inner core size, the relative amplitude of the anomaly and other nondimensional parameters reflecting the rotation rate (Ekman number) or the vigor of the convection (Rayleigh number) are studied as well. The temporal stability of the hemispherical fields is only given for lower (and more realistic) Ekman number cases. Cases with higher Ekman number showed polarity inversions.

Landeau and Aubert (2011) more closely examined the axisymmetric and equatorially antisymmetric (EAA) convection responsible for hemispherical dynamo action. The convective mode consists of an equatorial antisymmetric zonal flow and a dichotomy for radial flows regarding southern and northern hemisphere. We will discuss the convective properties, symmetries and the difference to the more classical columnar convection extensively in section 3. In their model, internal heating, a homogeneous CMB heat flux and a negligible size of the inner core was used. Investigating pure hydrodynamical and dynamo cases as well, lead to the conclusion that EAA convection can occur without forcing through boundary anomalies of the heat flux. They showed the natural occurrence of the hemispherical mode when increasing the vigor of the convection, thus leading to a superposition of both, the columnar and EAA convection. Additionally the induction of hemispherical dynamos was linked to the enforced convective mode and arises as a natural consequence of the convection. Landeau and Aubert (2011) also predicted scaling laws for the relative strength of EAA convection as function Rayleigh and Ekman number. Increasing the Rayleigh number leads to a transformation of the magnetic field from a dipole dominated towards a hemispherical field, where in between them a regime with strongly varying magnetic energy is reported (Landeau and Aubert 2011). We propose an explanation for this behavior in section 3.4.1. This model does not need a heat flux anomaly to enforce hemispherical dynamos, but they can also emerge on both hemispheres.

Aurnou and Aubert (2011) tested the convective dynamics and induction of purely boundary driven flows in the absence of an underlying thermal convection. Here anomalies of different spherical harmonic modes, such as Y_{10}, Y_{20}, Y_{22} were tested. For the Mars-equivalent degree-1 anomaly, they report the induction of hemispherical fields, which involve polarity reversals and estimated the time scales of the oscillations to be roughly 15 kyrs. The authors already suggest the incompatibility of the oscillating solutions and the crustal magnetization of Mars (Aurnou and Aubert 2011).

Our study tries to create a more complete picture of the hemispherical dynamos and its applicability for the ancient Mars. We use the same heating mode as Amit et al. (2011), but provide much broader coverage of the relative amplitude of the heat flux anomaly, its tilting angles and the important model parameter such as Ekman E, Rayleigh Ra and magnetic Prandtl number Pm. We are suggesting that the emergence and typical symmetries of the hemispherical convection are due to (ageostrophic) thermal winds, where the thermal wind balance seems to hold for all tested cases. Also the mechanical and thermal boundary conditions are tested for affecting the emergence and time variability of the hemispherical solution. We investigate the induction mechanism in much more detail, finding a very strong contribution of shear induced magnetic field and relate the results to a mean field dynamo model. We link the appearance of dynamo waves, which are quite similar to the Parker waves (Parker 1955), with the strong shear in the zonal flow. Due to the broad data coverage, we can quite conclusively rule out a hemispherical dynamo for the ancient Mars. We can not support the approach of Amit et al. (2011) of different time averages to relate the dynamo results to crustal magnetization. Either the equatorial asymmetry of the surface field does not match the measurements (Langlais et al. 2004), or the dynamo shows fast and regular polarity reversal thus not allowing a thick magnetized crust to serve as a magnetic carrier of the crustal magnetization anomaly. For further details the reader is referred to the discussion and conclusion in chapter 6.

2 MHD Dynamos

Magnetohydrodynamics (MHD) describe the dynamic evolution of a liquid or a gas, whose constituents are subject to the electromagnetic Lorentz force (plasma). These constituents are charges or charge currents, where we investigate their continuum counterparts. However, it might be an adventurous task, to describe the motion of each individual charged particle in a planetary core of a volume of roughly 2×10^{10} km^3. Therefore MHD describes the mean of the individual flows of each particle as vector field of ensemble flow velocity and the sum of the individual electromagnetic effects as an ensemble magnetic field. MHD can not provide information of how a single particle evolves, but the major aim is a description of flow and magnetic field on time and length scales much larger than the gyro radius and time as characteristic scales for the single charged particle evolution. Shortly, MHD is the continuum description of kinetic plasma theory.

The theory of plasma physics in general with application to fusion and space plasmas is described in the book of Piel (2010), whereas the application to astrophysical plasmas including the single particle and fluid picture of plasma can be found in Kulsrud (2005). A detailed introduction the theory of Magnetohydrodynamics (MHD) is given in Goedbloed and Poedts (2004). Whereas Rüdiger and Hollerbach (2004) concentrated on dynamo theory for planets and stars as a special application of the MHD, the specific application to planetary dynamos is reviewed in, e.g. Roberts (2007), Jones (2007) or Jones (2011).

2.1 Hydrodynamics

The melt in the core of a terrestrial planet can be described as a convecting, rotating and conducting fluid, what allows for self-sustained magnetic induction. We first discuss the hydrodynamical evolution equations and the applied simplifications. The confinement of the core does not allow for mass to escape from the core. Therefore the mass density ρ is conserved, what is described by the continuity equation:

$$\frac{\partial \rho}{\partial t} + \boldsymbol{\nabla} \cdot (\rho \boldsymbol{u}) = 0 \tag{2.1}$$

$$\frac{\partial \rho}{\partial t} + \rho \boldsymbol{\nabla} \cdot \boldsymbol{u} + \boldsymbol{u} \cdot \boldsymbol{\nabla} \rho = 0 \tag{2.2}$$

$$\frac{d\rho}{dt} + \rho \boldsymbol{\nabla} \cdot \boldsymbol{u} = 0\,. \tag{2.3}$$

Here we introduced the convective derivative: $d/dt = (\partial/\partial t + \boldsymbol{u} \cdot \boldsymbol{\nabla})$. The second term in equation 2.2 describes the compressibility, where the third is the advection of mass density. The density then changes locally if there are sources or sinks of mass density if the fluid is advected to concentrate or dispersed.

The conservation of momentum $\rho\boldsymbol{u}$ is given in general by the Navier-Stokes equation

$$\rho\left(\frac{\partial \boldsymbol{u}}{\partial t} + \boldsymbol{u}\cdot\boldsymbol{\nabla}\boldsymbol{u}\right) = -\boldsymbol{\nabla}P - \rho\boldsymbol{g} + \boldsymbol{f} \tag{2.4}$$

$$= -\boldsymbol{\nabla}p + \eta\boldsymbol{\nabla}^2\boldsymbol{u} + \frac{\eta}{3}\boldsymbol{\nabla}(\boldsymbol{\nabla}\cdot\boldsymbol{u}) - \rho\boldsymbol{g} + \boldsymbol{f}\,, \tag{2.5}$$

where $\boldsymbol{u}$ is the vector field of the fluid velocity, ρ the density, $\boldsymbol{\nabla}P$ the gradient of the pressure tensor (or sometimes called momentum flux density tensor), μ the dynamic viscosity, $-\rho\boldsymbol{g}$ the gravitational force and $\boldsymbol{f}$ are other forces, which will be introduced later. The gradient of pressure tensor P be written as $\boldsymbol{\nabla}P = \boldsymbol{\nabla}p + \eta\boldsymbol{\nabla}^2\boldsymbol{u} + \frac{\eta}{3}\boldsymbol{\nabla}(\boldsymbol{\nabla}\cdot\boldsymbol{u})$ when assuming a Newtonian fluid, thus a linear relation between stress and strain rate. Here we introduce the scalar pressure p as the diagonal elements of P. Details on this point can be found in the fluid mechanics book of Landau and Lifshitz (1959). In the equation 2.5 the term $\rho\boldsymbol{u}\cdot\boldsymbol{\nabla}\boldsymbol{u}$ describes the advection of momentum, $\eta\boldsymbol{\nabla}^2\boldsymbol{u}$ the diffusion or viscous drag and $\eta/3\boldsymbol{\nabla}(\boldsymbol{\nabla}\cdot\boldsymbol{u})$ is the compressibility. This equation describes the evolution of the velocity field of a viscous fluid being subject to different forces.

One of the key properties of planetary dynamos is the presence of convection. For Mars it might be a valid approximation to restrict the discussion to thermal convection. Therefore an equation for the conservation of (thermal) energy is needed. As we will see, the energy budget of the core dynamo powered by thermal convection is exclusively given by the thermal energy. There are many books and review articles regarding the conservation of energy in MHD, e.g. Desjardins and Dormy (2007), Jones (2007), Braginsky and Roberts (1995). The conservation of internal energy E is described by the second law of thermodynamics

$$dE = \delta Q + \delta W = TdS - pdV\,, \tag{2.6}$$

hence the internal energy can be affected by change of heat δQ or work $\delta W = -pdV$. The change of heat δQ can be reformulated in terms of entropy S, thus $\delta Q = TdS$. The entropy for thermal convection is a function of temperature T and pressure p, hence expanding yields

$$\delta Q = TdS(T,p) = T\left(\frac{\partial S}{\partial T}\right)_p dT + T\left(\frac{\partial S}{\partial p}\right)_T dp\,. \tag{2.7}$$

The first term ($T(\partial S/\partial T)_p dT$) on the right hand side can be rewritten introducing the heat capacity c_p at constant pressure

$$c_p = T\left(\frac{\partial S}{\partial T}\right)_p\,. \tag{2.8}$$

The second term can be rewritten using one of the thermodynamic Maxwell relations and make use of the relation between the volume V and the density ρ, such that $dV = -d\rho/\rho^2$ when using a unit mass $m = 1$:

$$\left(\frac{\partial S}{\partial p}\right)_T = \left(\frac{\partial V}{\partial T}\right)_p = -\frac{1}{\rho^2}\left(\frac{\partial \rho}{\partial T}\right)_p\,. \tag{2.9}$$

We find the definition of the thermal expansion coefficient α

$$\alpha = -\frac{1}{\rho}\left(\frac{\partial \rho}{\partial T}\right)_p \ . \tag{2.10}$$

Hence we find for the entropy

$$TdS(T,p) = c_p dT - \frac{\alpha T}{\rho} dp \ . \tag{2.11}$$

Applying the time derivative and the multiplying with the density to reach specific quantities yields

$$\rho T \frac{dS}{dt} = \rho c_p \frac{dT}{dt} - \alpha T \frac{dp}{dt} \ . \tag{2.12}$$

The heat budget $\delta Q/dt = TdS/dt$ is affected by either heat flux $-\boldsymbol{\nabla q}$ or heat sources H. The heat flux is proportional to temperature differences, where the proportionality constant is the thermal conductivity, k as stated by Fourier's law of heat conduction $\boldsymbol{q} = -k\boldsymbol{\nabla}T$. For simplicity we assume the thermal conductivity being constant. Inserting this yields

$$\rho T \frac{dS}{dt} = \rho c_p \frac{dT}{dt} - T\alpha \frac{dp}{dt} = k\boldsymbol{\nabla}^2 T + H \ , \tag{2.13}$$

where H contains all heat sources. These might be $H = H_i + H_{vis} + H_{ohm} + H_{com}$, where

- H_i are internal heat sources due to radioactivity or simple secular cooling. If the core is cooling through thermal convection, this is a homogeneously distributed and positive heat source (Jones 2007).
- $H_{vis} = \eta \boldsymbol{\nabla} \cdot (\boldsymbol{u} \cdot \boldsymbol{\nabla u})$ is the heating due to viscous friction.
- $H_{ohm} = \eta\mu_0(\boldsymbol{\nabla} \times \boldsymbol{B})^2$ is the ohmic heating. μ is the kinematic viscosity and μ_0 the vacuum permeability. This term is thought to be of minor importance in the here studies Boussinesq systems (Anufriev et al. 2005).
- $H_{com} = \frac{2}{3}\eta(\boldsymbol{\nabla} \cdot \boldsymbol{u})^2$ is the square of stress tensor and creates heat due to compression and expansion.

If one considers also chemical convection to occur in the core, the heat budget becomes more complicated. Discussion of the full heat equation can be found in Jones (2007) or Nimmo (2007).

To close the system of equations an equation of state is needed. The dependence of the density on its natural variables such as pressure and temperature gives the equation of state. This equation will have the general form

$$\rho = \rho(T,p) \tag{2.14}$$

and will be examined while discussing the onset of convection and the Boussinesq approximation. We collect the conservation equations for mass density ρ, momentum $\boldsymbol{u}$ and entropy S:

$$\frac{\partial \rho}{\partial t} + \boldsymbol{\nabla} \cdot (\rho \boldsymbol{u}) = 0 \tag{2.15}$$

$$\rho \left(\frac{\partial \boldsymbol{u}}{\partial t} + \boldsymbol{u} \cdot \boldsymbol{\nabla} \boldsymbol{u} \right) = -\boldsymbol{\nabla} p + \eta \boldsymbol{\nabla}^2 \boldsymbol{u} + \frac{\eta}{3} \boldsymbol{\nabla} (\boldsymbol{\nabla} \cdot \boldsymbol{u}) - \rho \boldsymbol{g} + \boldsymbol{f} \tag{2.16}$$

$$\rho T \frac{dS}{dt} = \rho c_p \frac{dT}{dt} - \frac{\alpha T}{\rho} \frac{dp}{dt} = k \boldsymbol{\nabla}^2 T - \frac{2}{3} \eta (\boldsymbol{\nabla} \cdot \boldsymbol{u})^2 + H \tag{2.17}$$

$$\rho = \rho(T, p) \; . \tag{2.18}$$

2.2 Boussinesq Approximation and the Adiabatic Background State

The Boussinesq approximation is one of the major simplifications to the above introduced system of equations. The systematic investigation of this approximation can be found in Spiegel and Veronis (1960). To obtain and justify this approximation we first need to distinguish between the stationary adiabatic background state and the convective perturbations. The background state is given by the large fraction of the thermal energy transported via heat conduction, where no convective motions are involved. It is useful to further separate the background state into a mean background (index *m*) and the variation due to the adiabatic heat conduction (index *ad*). The perturbations (primed quantities) refer to variations on top of the adiabatic state due to the convective instability. We separate density ρ, temperature T and pressure p into the mean background, another part related to the heat conduction and a part to the additional thermal convection. Thus we write

$$\rho(\boldsymbol{r}, t) = \rho_0^m + \rho_0^{ad}(\boldsymbol{r}) + \rho'(\boldsymbol{r}, t) \tag{2.19}$$

$$T(\boldsymbol{r}, t) = T_0^m + T_0^{ad}(\boldsymbol{r}) + T'(\boldsymbol{r}, t) \tag{2.20}$$

$$p(\boldsymbol{r}, t) = p_0^m + p_0^{ad}(\boldsymbol{r}) + p'(\boldsymbol{r}, t) \; . \tag{2.21}$$

The background state as the value averaged over the core shell is independent of space and time. The adiabatic variation changes with radius but is time independent, whereas the convective contributions can vary with both, space and time. We firstly concentrate on the two contributions of the background state. Solving the equations in the absence of motion ($\boldsymbol{u} = 0$) and thus all convective perturbations are zero, yields the definition of the background state.

$$-\boldsymbol{\nabla} p_0^{ad} - \rho_0^m \boldsymbol{g} - \rho_0^{ad} \boldsymbol{g} = 0 \tag{2.22}$$

$$k \boldsymbol{\nabla}^2 T^{ad} = H_0^{ad} \tag{2.23}$$

This describes a state of heat conduction, where the pressure is due to hydrostatic layering, the density is constant and the temperature profile is given by heat conduction feed from either a heat source H_0^{ad} within the core shell or from the boundaries. As a next step, we want to estimate the size of the variations of the mean background state due to the adiabatic heat transport, since the major claim of the Boussinesq approximation is that all quantities vary on much larger length scales than the thickness of the core. This is sometimes called the 'thin-shell-approximation' (Spiegel and Veronis 1960). To evaluate this, we calculate the scale heights D_f for density, temperature and pressure, D_ρ, D_T, D_p, respectively. We name the core thickness as d.

$$D_f = f_0^m \frac{d}{f_0^{ad}} \tag{2.24}$$

The scale height defines the thickness of an hypothetical layer, in which the quantity f varies from zero to its maximal value. Table 2.1 shows the scale heights of temperature T, pressure p and density ρ, where we take the values at the center of the Martian core (r_i) and the core mantle boundary (r_{cmb}) for the calculating the resulting scale heights. We approximate f_0^m and f_0^{ad} such that,

$$f_0^m = \frac{f(r_i) + f(r_{cmb})}{2} \tag{2.25}$$

$$f_0^{ad} = f(r_i) - f(r_{cmb}) \, . \tag{2.26}$$

Additionally, we calculate $D^* = D/d$ as the normalization to the thickness of the core (1700 km). In general, table 2.1 shows that all scale heights exceed the thickness of the core, therefore the thin-shell-approximation is (at least marginally) satisfied.

However, the scale height for the density and temperature are much larger than for the pressure. This yields the conclusion, that the density variations are due to variations in the temperature and the influence of the pressure fluctuations is minor, and therefore effects of compressibility are negligible. Otherwise the density should change on length scales of the pressure. However, it can be seen that $\rho_0^m >> \rho_0^{ad}$, $T_0^m >> T_0^{ad}$ and $p_0^m >> p_0^{ad}$, thus the adiabatic variations are small compared the values of the mean background state.

Now we add perturbations of the adiabatic state according to the convective motions. Table 2.1 also lists the size of the convective perturbations, where it can be seen that they are very small compared to the adiabatic variation. King et al. (2010) estimated the relative density change introduced by core convection to be as small as $\rho'/\rho_0^{ad} = 10^{-7}$ and Jones (2007) stated for the temperature perturbations $T'/T_0^{ad} = 10^{-7}$. A density change of $\rho' = 10^{-4}\,\mathrm{kg/m^3}$ is seismically not detectable (King et al. 2010), the same is true for temperature anomaly like 10^{-4} K. We define a small quantity ϵ, such that $\epsilon := f_0^{ad}/f_0^m$. Note, that the convective perturbations are much smaller ($f'/f_0^m << \epsilon$) for core convection. In general the relative size of f'/f_0^{ad} can only by evaluated experimentally (Spiegel and Veronis 1960), where we show in table 2.1 that f_0^{ad} indeed exceeds f'. We state that the size of convective perturbations are maximal equal to the adiabatic variations, thus

$$O(f'/f_0^m) \leq O(f_0^{ad}/f_0^m) \, . \tag{2.27}$$

The density and the other material properties such as thermal diffusivity are assumed to be constant in the Boussinesq approximation, where only the temperature dependence of the density is taken into account. Using the separation $\rho = \rho_0^m + \rho_0^{ad} + \rho'$ yields a

f	$f(i)$	$f(o)$	f_0^m	f_0^{ad}	f'	D	D^*
ρ	$7200\,\mathrm{kg/m^3}$	$6800\,\mathrm{kg/m^3}$	$400\,\mathrm{kg/m^3}$	$7000\,\mathrm{kg/m^3}$	$10^{-4}\,\mathrm{kg/m^3}$	$2.98 \cdot 10^7\,\mathrm{m}$	17.5
T	2000 K	1800 K	200 K	1900 K	$10^{-4}\,\mathrm{K}$	$1.65 \cdot 10^7\,\mathrm{m}$	9.5
p	40 GPa	25 GPa	15 GPa	32.5 GPa	?	$3.66 \cdot 10^6\,\mathrm{m}$	2.17

Table 2.1: Scale heights for density ρ, temperature T and pressure p. All values are taken from Sohl and Spohn (1997). Instead of calculating the scale height for the pressure, one could also use the hydrostatic relation resulting from the Navier-Stokes-Equation in the absence of motion. The values for the primed quantities are suggestions from Jones (2007) and King et al. (2010).

continuity equation 2.15 like:

$$\frac{d(\rho_0^m + \rho_0^{ad} + \rho')}{dt} + \rho \boldsymbol{\nabla} \cdot \boldsymbol{u} = 0 \tag{2.28}$$

$$\boldsymbol{\nabla} \cdot \boldsymbol{u} = \frac{1}{\rho} \frac{d(\rho_0^m + \rho_0^{ad} + \rho')}{dt} \; . \tag{2.29}$$

Now we make use of the time independence of the mean and adiabatic background state and find

$$\boldsymbol{\nabla} \cdot \boldsymbol{u} = \frac{1}{\rho} \frac{d\rho'}{dt} = O(\epsilon) \approx 0 \; , \tag{2.30}$$

thus to order ϵ the flow divergence vanishes and thus the fluid can be treated as incompressible.

The equation of state for the density can be expanded in a Taylor series in the small perturbations ϵ around the mean background state (Spiegel and Veronis 1960), where we stop after the first term.

$$\rho(T, p) = \rho_0^m \left[1 + \frac{1}{\rho_0^m} \left(\frac{\partial \rho}{\partial T} \right)_p (T - T_0^m) + \frac{1}{\rho_0^m} \left(\frac{\partial \rho}{\partial p} \right)_T (p - p_0^m) \right] \tag{2.31}$$

$$\rho(T, p) = \rho_0^m \left[1 - \alpha (T - T_0^m) + k(p - p_0^m) \right] \; , \tag{2.32}$$

where we can neglect the influence of the compressibility k because the compressible effects do not play a major role here as mentioned above and hence the fluid is incompressible. This is here a quantitative argument, what might not be entirely true, we refer to the more sophisticated work in the Boussinesq approximation by Spiegel and Veronis (1960). Because of the time independence of the adiabatic variation of the mean background, the last equation can be further modified for the adiabatic background ρ_0^{ad}, T_0^{ad} and the convective perturbations ρ', T' separately such that

$$\frac{\rho_0^{ad}}{\rho_0^m} = -\alpha T_0^{ad} = O(\epsilon) \tag{2.33}$$

$$\frac{\rho'}{\rho_0^m} = -\alpha T' = O(\epsilon) \tag{2.34}$$

$$\rho' = -\rho_0^m \alpha T' \; , \tag{2.35}$$

where both sides of the equations 2.33 and 2.34 are of the order ϵ, thus small. The constraint $\alpha T' = \alpha T_0^{ad} = \epsilon << 1$ is usually used as the core of the Boussinesq-approximation (Jones 2007). The thermal expansion coefficient is as small as $\alpha = 1.5 \times 10^{-5}\,\mathrm{K}^{-1}$ (Jones 2007) and temperature fluctuations due to the convection are on the order of 10^{-4} K, where even the total temperature contrast associated with the adiabatic variation through the core does not exceed 200 K (Sohl and Spohn 1997). Then the product of the two is indeed rather small.

Secondly we want to show the implications for the momentum equation. Inserting the separation of density and pressure into the large mean background part, the small adiabatic variations and the small convective perturbations gives:

$$\rho\left(\frac{\partial \boldsymbol{u}}{\partial t} + \boldsymbol{u}\cdot\boldsymbol{\nabla}\boldsymbol{u}\right) = -\boldsymbol{\nabla}(p_0^m + p_0^{ad} + p') - (\rho_0^m + \rho_0^{ad} + \rho')\boldsymbol{g} + \eta\boldsymbol{\nabla}^2\boldsymbol{u} \tag{2.36}$$

$$\rho\left(\frac{\partial \boldsymbol{u}}{\partial t} + \boldsymbol{u}\cdot\boldsymbol{\nabla}\boldsymbol{u}\right) = -\boldsymbol{\nabla}p' - \rho'\boldsymbol{g} + \eta\boldsymbol{\nabla}^2\boldsymbol{u}\ . \tag{2.37}$$

The hydrostatic pressure of the adiabatic background ($\boldsymbol{\nabla}p_0^{ad}$) dropped out with the background gravity of mean and adiabatic state ($\rho_0^m\boldsymbol{g} + \rho_0^{ad}\boldsymbol{g}$) as this is the definition of the background state. The remaining density perturbation $\rho' = -\rho_0^m\alpha T'$ is a small (ϵ) quantity. But it is kept since it is multiplied with the gravitational acceleration $\boldsymbol{g}$. The typical acceleration $\partial\boldsymbol{u}/\partial t$ gives the time scale of motions in the fluid and is much smaller than $\boldsymbol{g}$. Or in other words, the gravitation needs to be multiplied with a small quantity, what is represented with ϵ here. Otherwise large forces would occur introducing much shorter timescales on the order of the gravitational acceleration. Using a viscous diffusion time scale ($\hat{t} = \rho d^2/\eta$), the scale of the acceleration a is then $\hat{a} = \rho^2 d^3/\eta^2$. The ratio between the scale of flow acceleration and gravity is given by $G = gL^3/\nu^2$ (Lyubimov et al. 1998). There the authors pointed out, that the Boussinesq-limit is given, when $G \to \infty$ and $\epsilon \to 0$, but the product remains finite (Lyubimov et al. 1998). As a consequence all density variations besides those multiplied with the gravitation can be neglected. Note, this is a constraint for the flow acceleration, not the amplitude of the gravity (Spiegel and Veronis 1960).

As the last step we simplify the energy equation.

$$\begin{aligned}\rho c_p\frac{d(T_0^m + T_0^{ad} + T')}{dt} - (T_0^m + T_0^{ad} + T')\frac{\alpha}{\rho}\frac{d(p_0^m + p_0^{ad} + p')}{dt}&\\ = k\boldsymbol{\nabla}^2(T_0^m + T_0^{ad} + T') + H_0^{ad} + H'&\end{aligned} \tag{2.38}$$

The term proportional to the pressure changes dp contains αT, what is to order ϵ equal zero (Jones 2007). Additionally the dp/dt can be reformulated such that

$$\frac{dp}{dt} = \frac{dp}{d\rho}\frac{d\rho}{dt} \propto p\boldsymbol{\nabla}\cdot\boldsymbol{u}\ , \tag{2.39}$$

thus this term is also proportional to the divergence of the flow, what is zero for an incompressible fluid.

If the heat source H is large enough, it contributes for the convection too, therefore

$H = H_0^{ad} + H'$. Then we rewrite the equation such that,

$$\rho c_p \frac{dT'}{dt} = k\nabla^2 T_0^{ad} + k\nabla^2 T' + H_0^{ad} + H' \tag{2.40}$$

$$\rho c_p \frac{dT'}{dt} = k\nabla^2 T' + H' \, . \tag{2.41}$$

Here the diffusive term of the adiabatic background temperature is exactly balanced with the heat source contribution for the adiabatic background state, as suggested when we derived the equations for the background state. As the major advantage of the Boussinesq approximation, it is possible to decouple the equations for the conductive background state and the convective perturbations and we found the incompressibility of the flow. Therefore we can treat the velocity field same as the magnetic field, for which $\nabla \cdot \boldsymbol{B} = 0$ always holds. Also several terms of the heat budget, which are proportional to $\nabla \cdot \boldsymbol{u}$, can be neglected.

Note, that the Boussinesq-approximation is only marginally satisfied as we had seen when calculating the scale heights for the density, temperature and especially pressure (see table 2.1). Anufriev et al. (2005) estimated the errors introduced by the Boussinesq-simplification. The authors show, that the heating terms due to viscous dissipation and ohmic dissipation entering the energy budget are not negligible. However, we restrict our model to the simpler and intensively studied Boussinesq-system.

2.3 Adiabatic Temperature Gradient

We proposed that a sufficiently high CMB heat flux is needed to allow for thermal convection. Here we want to calculate this critical heat flux. Heat can be transported either exclusively via conduction or due to supportive convection. As we had seen, the temperature declines from the center of the core towards the CMB. The discussion of the equation of state yielded an increase of density with decreasing temperature. Therefore the fluid is heaviest (largest density), where the temperature is smallest thus close to the CMB and rather light (small density), where the temperature is large deeper inside. Thus even in the heat conducting background state heavier fluid is layered on top of lighter, what is a potentially instable situation. The mechanical stability of such a layering is given by the entropy, or more specific by the entropy gradient. Therefore the radial gradient of the entropy controls whether convection sets in. If the temperature contrast is small, the entropy gradient is negative and the fluid is stably stratified. Once a critical temperature contrast is exceeded, the entropy gradient changes the sign, thus the fluid is unstable and convective motions set in. The maximum temperature contrast along which heat is exclusively transported via heat conduction and $dS/dr = 0$, is the so called adiabatic gradient. From the vast amount of literature regarding the onset of thermal convection, we refer here only to Chandrasekhar (1961), Landau and Lifshitz (1959) or Faber (1995) for further reading about the theoretical background. As an application besides the core convection, Schubert et al. (2001) embeds the onset of thermal instabilities in the context of mantle motions.

As an illustration, we track a small fluid volume V of entropy S what is lifted up from a hotter layer and is placed into a cooler (less dense) layer. It then start to buoyantly rise up, if its density due to thermal expansion is smaller then the density of the fluid volume it replaced. In other words, if the destabilizing buoyancy exceeds the ordering force of the hydrostatic pressure gradient, convection sets in (Chandrasekhar 1961). The adiabatic entropy gradient ($dS/dr = 0$) is a function of temperature T and the pressure p, and serves as condition for the onset of convection:

$$\frac{dS}{dr} = \left(\frac{\partial S}{\partial T}\right)_p \frac{dT}{dr} + \left(\frac{\partial S}{\partial p}\right)_T \frac{dp}{dr} = 0 \,. \tag{2.42}$$

The pressure gradient term dp/dr is the hydrostatic pressure $dp/dr = -g\rho$, as found from equation 2.5 in the absence of motion. Then we find

$$\frac{dT}{dr} = -g\rho \left(\frac{\partial S}{\partial p}\right)_T \left(\frac{\partial S}{\partial T}\right)_p^{-1} \,. \tag{2.43}$$

Using one of Maxwell relations of thermodynamics, such as

$$-\left(\frac{\partial S}{\partial p}\right)_T = \left(\frac{\partial V}{\partial T}\right)_p \tag{2.44}$$

gives

$$\frac{dT}{dr} = g\rho \left(\frac{\partial V}{\partial T}\right)_p \left(\frac{\partial S}{\partial T}\right)_p^{-1} \,. \tag{2.45}$$

Using the definitions of thermal expansivity α and specific heat for constant pressure c_p:

$$\alpha = \frac{1}{V}\left(\frac{\partial V}{\partial T}\right)_p \tag{2.46}$$

$$c_p = T\left(\frac{\partial S}{\partial T}\right)_p \tag{2.47}$$

yields the definition of the critical temperature gradient

$$\frac{dT}{dz} = \frac{g\rho\alpha T}{c_p} \,. \tag{2.48}$$

The right hand side defines the adiabatic entropy gradient translated in terms of temperature. As a consequence, once the temperature contrast exceeds this so called adiabatic temperature gradient, convection sets in. These motions transport hot material from the bottom or interior of the core towards the core mantle boundary. Calculating the adiabatic temperature gradient close to the CMB using $\rho = 6800\,\mathrm{kg/m^3}$, $\alpha = 3 \cdot 10^{-5}\,1/\mathrm{m}$, $T = 2000\,\mathrm{K}$ and $C_p = c_p/\rho = 1000\,\mathrm{J/kgK}$ yields $\partial T/\partial z = 15 \cdot 10^{-5}\,\mathrm{K/m}$ (numbers from Morschhauser et al. (2011), Sohl and Spohn (1997)). Assuming a core shell thickness of 1550 km leads to a adiabatic temperature contrast of roughly 230 K. This is consistent with the findings for the total temperature contrast (see table 2.1). From such a simple calculation, it can not be decided whether convection is present in the core or not. Because on the one hand the material properties and the thermodynamics quantities characterizing the core state are only poorly constrained (Jones 2007). On the other hand the convective perturbations are minor contributions of the temperature. As another source of bias, the adiabatic temperature gradient is function of core radius (especially because of the increasing gravity), thus it increases with radius. It might be possible, that the core is superadiabatic only for a given fraction of its radius (Jones 2007).

2.4 Coriolis Force

As a reminder, the Boussinesq equations describing the conservation of momentum and thermal energy for the convective perturbations read

$$\rho\left(\frac{\partial \boldsymbol{u}}{\partial t} + \boldsymbol{u}\cdot\boldsymbol{\nabla}\boldsymbol{u}\right) = -\boldsymbol{\nabla}\Pi + \eta\boldsymbol{\nabla}^2\boldsymbol{u} + \boldsymbol{g}\rho\alpha T + \boldsymbol{f} \tag{2.49}$$

$$\rho c_p\left(\frac{\partial T}{\partial t} + \boldsymbol{u}\cdot\boldsymbol{\nabla}T\right) = -k\boldsymbol{\nabla}^2 T + H_i\,, \tag{2.50}$$

where we dropped the primes of the fluctuations and rename the nonhydrostatic pressure as Π for consistency with the literature. As we mentioned in the section 1.2 the rotation of the core and thus the action of the Coriolis force is an essential ingredient for prosperous dynamo action in terrestrial planets. This force appears due to the transformation of the Navier-Stokes-equation into a reference frame, that co-rotates with the planetary rotation $\boldsymbol{\Omega}$. Since this is an accelerated frame of reference, additional forces emerge. Denoting the rotating frame with a prime, the transformation equation is given by

$$\boldsymbol{u}' = \frac{\partial \boldsymbol{r}'}{\partial t'} = \frac{\partial \boldsymbol{r}}{\partial t} + \boldsymbol{\Omega}\times\boldsymbol{r} = \boldsymbol{u} + \boldsymbol{\Omega}\times\boldsymbol{r}\,. \tag{2.51}$$

Applying this rule twice yields the additional terms:

$$\frac{\partial \boldsymbol{u}'}{\partial t'} = \frac{\partial^2 \boldsymbol{r}'}{\partial t'^2} = \frac{\partial^2 \boldsymbol{r}}{\partial t^2} + \boldsymbol{\Omega}\times\frac{\partial \boldsymbol{r}}{\partial t} + \dot{\boldsymbol{\Omega}}\times\boldsymbol{r} + \boldsymbol{\Omega}\times\frac{\partial \boldsymbol{r}}{\partial t} + \boldsymbol{\Omega}\times\boldsymbol{\Omega}\times\boldsymbol{r}\,. \tag{2.52}$$

Since the rotation rate and axis is assumed to be constant, the Poincare force term proportional to $\dot{\boldsymbol{\Omega}}$ drops out. This force describes, e.g. the effect of precession and can serve also as a source for hydrodynamical instabilities. A recent review can be found in Tilgner (2007). The other terms can be rewritten such that

$$\frac{\partial \boldsymbol{u}'}{\partial t'} = \frac{\partial \boldsymbol{u}}{\partial t} + 2\boldsymbol{\Omega}\times\boldsymbol{u} + \boldsymbol{\Omega}\times\boldsymbol{\Omega}\times\boldsymbol{r}\,. \tag{2.53}$$

The first term entering the Navier-Stokes-equation is the Coriolis force, the other the centrifugal force, what is either added to the pressure term or to the gravitational acceleration. This treatment is allowed since the centrifugal force can be as well expressed as a potential. The Navier-Stokes-equation for an incompressible, rotating and convecting fluid is then given by

$$\rho\left(\frac{\partial \boldsymbol{u}}{\partial t} + \boldsymbol{u}\cdot\boldsymbol{\nabla}\boldsymbol{u}\right) = -\boldsymbol{\nabla}\Pi + 2\boldsymbol{\Omega}\times\boldsymbol{u} + \boldsymbol{g}\rho\alpha T + \eta\boldsymbol{\nabla}^2\boldsymbol{u}\,. \tag{2.54}$$

2.5 Induction Equation

Since the proposal of Larmor (1919) that the sun or a planet can create an internal magnetic field due to a dynamo process, this idea was applied to magnetic fields and their generation inside stars, planets and even galaxies (Rüdiger and Hollerbach 2004). The dynamo theory mainly concerns the induction and evolution of magnetic fields. Electromagnetic fields follow the description according to the Maxwell equations:

$$\operatorname{div} \boldsymbol{B} = 0 \tag{2.55}$$

$$\operatorname{div} \boldsymbol{E} = \frac{\rho_c}{\epsilon_0} \qquad \text{Gauss' law} \tag{2.56}$$

$$\boldsymbol{\nabla} \times \boldsymbol{B} = \mu_0 \boldsymbol{j} + \left(\mu_0 \epsilon_0 \frac{\partial E}{\partial t} \right) \qquad \text{Faraday's law} \tag{2.57}$$

$$\boldsymbol{\nabla} \times \boldsymbol{E} = -\frac{\partial \boldsymbol{B}}{\partial t} \qquad \text{Ampere's law} \tag{2.58}$$

with the electrical field $\boldsymbol{E}$, the magnetic field $\boldsymbol{B}$, the charge and current density ρ_c and $\boldsymbol{j}$, the electric vacuum permittivity ϵ_0, the magnetic permeability of free space μ_0 and the conductivity σ. We denoted Maxwell's correction of Faraday's law with parenthesis, because it is negligible here. The prefactor $\mu_0 \epsilon_0 = 1/c^2$, with c is the speed of light. The time derivative of the electric field can be estimated with a typical velocity amplitude. Then size of that term is proportional to the ratio of a typical velocity and the speed of light. Since the velocities in the core are small (few mm/s) compared to speed of light the displacement current term ($\epsilon_0 \dot{\boldsymbol{E}} = \dot{\boldsymbol{D}}$) in Faraday's law can be neglected. Electric and magnetic fields are defined due to the forces they execute on electric charges ρ_c or currents $\boldsymbol{j}$. The relation between such a current density and electromagnetic fields is given by Ohm's law. For a conductor moving with the velocity $\boldsymbol{u}$, Ohm's law is given as

$$\boldsymbol{j} = \sigma \left[\boldsymbol{E} + (\boldsymbol{u} \times \boldsymbol{B}) \right] \ . \tag{2.59}$$

Using Faraday's law (the Maxwell equation 2.57), gives

$$\boldsymbol{\nabla} \times \boldsymbol{B} = \mu_0 \sigma \left[\boldsymbol{E} + (\boldsymbol{u} \times \boldsymbol{B}) \right] \ . \tag{2.60}$$

Applying the curl operator ($\boldsymbol{\nabla} \times$) on this equation and using the relation $\boldsymbol{\nabla} \times \boldsymbol{\nabla} \times \boldsymbol{B} = (\boldsymbol{\nabla} \cdot \boldsymbol{\nabla} - \boldsymbol{\nabla}^2)\boldsymbol{B}$ gives

$$-\boldsymbol{\nabla}^2 \boldsymbol{B} = \mu_0 \sigma \left[\boldsymbol{\nabla} \times \boldsymbol{E} + \boldsymbol{\nabla} \times (\boldsymbol{u} \times \boldsymbol{B}) \right] \ . \tag{2.61}$$

Using Ampere's law (equation 2.58) yields the induction equation:

$$\frac{\partial \boldsymbol{B}}{\partial t} = \boldsymbol{\nabla} \times (\boldsymbol{u} \times \boldsymbol{B}) + \lambda \boldsymbol{\nabla}^2 \boldsymbol{B} \ , \tag{2.62}$$

where $\lambda = (\sigma \mu_0)^{-1}$ is the magnetic diffusivity. These equation is linked to the hydrodynamics over the velocity field, what controls the dynamo term.

As mentioned in the introduction (section 1.2), an estimate of the ratio between the first term (induction) and the second (ohmic decay) is defined by the magnetic Reynolds number Rm:

$$Rm = \frac{\boldsymbol{\nabla} \times (\boldsymbol{u} \times \boldsymbol{B})}{\lambda \Delta \boldsymbol{B}} \approx \frac{UB/L}{\lambda B/L^2} = \frac{UL}{\lambda} \tag{2.63}$$

A magnetic Reynolds number bigger than unity would mean, that the induction of magnetic field is larger than the diffusion of magnetic field, therefore offering a criterion for dynamo action. In planetary, numerical or experimental dynamos the critical magnetic Reynolds number needs to be higher reflecting the additionally required complexity of the flow. Values of $Rm \approx 50$ seem to be sufficient to drive a dynamo. Note, that the induction term has two contributions, the advection and the induction of the magnetic field. Only the latter one can create (or destroy) mean magnetic field, where the first one simply transports the field. If a velocity field is given or can be parameterized, one can only solve the induction equation and study the magnetic field. This might introduce some shortcomings. The induction equation is a linear equation of the magnetic field. Thus a dynamo with sufficiently high Rm would exponentially grow from a small seed field. But the backreaction on the flow in terms of the Lorentz force, leads to a nonlinear equation and to a saturation of the magnetic field growth.

If Rm is not sufficiently high, the magnetic field decays on the magnetic diffusion time scale $\tau_\lambda = D^2/\lambda$. Say, for a magnetic field whose length scale is comparable to the thickness of the core and the magnetic diffusivity $\lambda = 2\,\mathrm{m}^2/\mathrm{s}$ (Jones 2007), the magnetic diffusion time is roughly 50 kyrs. This estimate gives a hint for the presence of a successful dynamo process, simply because unsuccessful dynamos diminish that fast. This might not be true for other objects, such as the sun or galaxies hosting a dynamo since the magnetic diffusivities are quite different. For further reading on this issue, we refer to Rüdiger and Hollerbach (2004).

The backreaction of the induced magnetic field on the conducting fluid is given by the Lorentz force $\boldsymbol{j} \times \boldsymbol{B}$. The Maxwell equation (2.57) yields $\mu_0 \boldsymbol{j} = \boldsymbol{\nabla} \times \boldsymbol{B}$. Finally the conservation of momentum can be expressed as

$$\rho\left(\frac{\partial \boldsymbol{u}}{\partial t} + \boldsymbol{u}\cdot\boldsymbol{\nabla}\boldsymbol{u}\right) = -\boldsymbol{\nabla}\Pi + 2\boldsymbol{\Omega}\times\boldsymbol{u} + \boldsymbol{g}\rho\alpha T + \eta\boldsymbol{\nabla}^2\boldsymbol{u} + \frac{1}{\mu_0}(\boldsymbol{\nabla}\times\boldsymbol{B})\times\boldsymbol{B}\,. \tag{2.64}$$

2.6 Nondimensionalization, Scaling

It is useful to translate the system of equations into a nondimensional form, because two systems are 'dynamical equivalent' if they are consistent within the nondimensional numbers we introduce here (Faber 1995). That means, even if two systems differ in several length, time etc. scales, they can be equivalent as long as the nondimensional numbers agree. Here we will show, how to translate the MHD equation from their dimensional into the nondimensional form and introduce the important control parameters characterizing our core model.

Here we use the nondimensionalization as given by Christensen and Wicht (2007), others are possible. The units or scales are separated from the quantities, using a notation like $x = x'\hat{x}$, where x is the scaled quantity, x' the nondimensional quantity and $\hat{x}$ the scale/unit of the quantity. The choice of length and time scale is crucial. The thickness of the spherical shell $\hat{D} = \hat{r}_{cmb} - \hat{r}_{icb}$ is used as length scale, viscous diffusion time $\hat{t} = \hat{D}^2/\hat{\nu}$, with $\hat{\nu} = \hat{\eta}/\hat{\rho}$ the kinematic viscosity, as time scale, and $\hat{B} = \sqrt{\hat{\rho}\hat{\lambda}\hat{\mu}_0\hat{\Omega}}$ as magnetic scale. The source term $H = H'\hat{H}$ has the dimension of temperature per time. Then the velocity scales as $\boldsymbol{u} = \boldsymbol{u}'\hat{\nu}/\hat{D}$. The differentiation operator $\boldsymbol{\nabla} = \boldsymbol{\nabla}'/\hat{D}$.

The temperature contrast between the inner core and the core mantle boundary is usually used as temperature scale. Since we apply fixed flux temperature boundary conditions, the temperature at the borders is not fixed. We make use of Fourier's law of heat conduction ($\boldsymbol{q} = -k\boldsymbol{\nabla}T$). The mean superadiabatic heat flux serves then as a scale for the superadiabatic temperature $\hat{T} = \hat{q}_0\hat{D}/\hat{k}$.

As a first application the heat transfer equation is scaled. Using the above introduced temperature, time and velocity scales gives.

$$\hat{\rho}\hat{c_p}\left(\frac{\partial T'}{\partial t'}\frac{\hat{q}_0\hat{D}}{\hat{k}}\frac{\hat{\nu}}{\hat{D}^2} + \boldsymbol{u'}\boldsymbol{\nabla'}T'\frac{\hat{\nu}}{\hat{D}}\frac{1}{\hat{D}}\frac{\hat{q}_0\hat{D}}{\hat{k}}\right) = \boldsymbol{\nabla'}\boldsymbol{\nabla'}T'\frac{1}{\hat{D}}\frac{1}{\hat{D}}\hat{k}\frac{\hat{q}_0\hat{D}}{\hat{k}} + H'\frac{\hat{q}_0\hat{D}}{\hat{k}}\frac{\hat{\nu}}{\hat{D}^2}, \tag{2.65}$$

where $\hat{H}$ is scale of the heat source density. When introducing the heat diffusivity $\hat{\kappa} = \hat{k}/(\hat{\rho}\hat{c_p})$ instead of the heat conductivity $\hat{k}$, this leads

$$\frac{\partial T'}{\partial t'} + \boldsymbol{u'}\boldsymbol{\nabla'}T' = Pr\boldsymbol{\nabla'^2}T' + H*' \ , \tag{2.66}$$

with the hydrodynamic Prandtl number $Pr = \hat{\kappa}/\hat{\nu}$ measuring the ratio between the diffusion of heat and momentum. For the heat source $H*' = H'/(\hat{\rho}\hat{c_p})$.

As second step the induction equation is scaled:

$$\frac{\partial \boldsymbol{B'}}{\partial t'}\sqrt{\hat{\rho}\hat{\lambda}\hat{\mu}_0\hat{\Omega}}\frac{\hat{\nu}}{\hat{D}^2} = \boldsymbol{\nabla'}\times(\boldsymbol{u'}\times\boldsymbol{B'})\frac{1}{\hat{D}}\frac{\hat{\nu}}{\hat{D}}\sqrt{\hat{\rho}\hat{\lambda}\hat{\mu}_0\hat{\Omega}} + \boldsymbol{\nabla'^2}\boldsymbol{B'}\frac{1}{\hat{D}^2}\sqrt{\hat{\rho}\hat{\lambda}\hat{\mu}_0\hat{\Omega}}\hat{\lambda} \ . \tag{2.67}$$

Which can be simplified to

$$\frac{\partial \boldsymbol{B'}}{\partial t'} = \boldsymbol{\nabla'}\times(\boldsymbol{u'}\times\boldsymbol{B'}) + \frac{1}{Pm}\boldsymbol{\nabla'}^2\boldsymbol{B'} \ , \tag{2.68}$$

with the magnetic Prandtl number $Pm = \nu/\lambda$ measuring the ratio between the diffusion of magnetic field and momentum.

As a last step the Navier-Stokes-equation is scaled. Using $\boldsymbol{g} = \boldsymbol{e'_r}\hat{g}$, $\boldsymbol{\Omega} = \boldsymbol{e'_z}\hat{\Omega}$, $\rho = \hat{\rho}$ and $\alpha = \hat{\alpha}$ allows to separate all scales from the quantities. The Lorentz force $\boldsymbol{j}\times\boldsymbol{B}$ can be formulated as $\mu_0^{-1}(\boldsymbol{\nabla}\times\boldsymbol{B})\times\boldsymbol{B}$. The scale for the non-hydrostatic pressure is $\boldsymbol{\nabla}\Pi = \boldsymbol{\nabla'}\Pi'\hat{D}/\hat{\rho}\hat{\Omega}\hat{\nu}$, thus same as for the Coriolis force. Inserting delivers:

$$\begin{aligned}\hat{\rho}\left(\frac{\partial \boldsymbol{u'}}{\partial t'}\frac{\hat{\nu}}{\hat{D}}\frac{\hat{\nu}}{\hat{D}^2} + \boldsymbol{u'}\boldsymbol{\nabla'}\boldsymbol{u'}\frac{\hat{\nu}}{\hat{D}}\frac{1}{\hat{D}}\frac{\hat{\nu}}{\hat{D}}\right) &= -\boldsymbol{\nabla'}\Pi'\frac{\hat{D}}{\hat{\rho}\hat{\Omega}\hat{\nu}} \\ +\boldsymbol{\nabla'^2}\boldsymbol{u'}\nu\frac{1}{\hat{D}^2}\frac{\hat{\nu}}{\hat{D}} + 2\boldsymbol{e'_z}\times\boldsymbol{u'}\hat{\Omega}\frac{\hat{\nu}}{\hat{D}} - \boldsymbol{e'_r}T'\hat{\alpha}\frac{\hat{q}_0\hat{D}}{\hat{\kappa}}\hat{\rho}\hat{g} &+ \boldsymbol{\nabla'}\times\boldsymbol{B'}\times\boldsymbol{B'}\frac{1}{\hat{\mu}_0}\frac{1}{\hat{D}}\hat{\rho}\hat{\mu}_0\hat{\lambda}\hat{\Omega}\end{aligned} \tag{2.69}$$

Multiplying the whole equation with $\hat{D}/\hat{\rho}\hat{\Omega}\hat{\nu}$ leads to:

$$\begin{aligned}\frac{\partial \boldsymbol{u'}}{\partial t'}\frac{\hat{\nu}}{\hat{\Omega}\hat{D}^2} + \boldsymbol{u'}\boldsymbol{\nabla'}\boldsymbol{u'}\frac{\hat{\nu}}{\hat{\Omega}\hat{D}^2} &= -\boldsymbol{\nabla'}\Pi' + \boldsymbol{\nabla'^2}\boldsymbol{u'}\nu\frac{\hat{\nu}}{\hat{\Omega}\hat{D}^2} + 2\boldsymbol{\Omega'}\times\boldsymbol{u'} \\ &\quad - \boldsymbol{e'_r}\frac{\hat{q}_0\hat{\alpha}\hat{g}\hat{D}^2}{\hat{\nu}\hat{\kappa}\hat{\Omega}} + \boldsymbol{\nabla'}\times\boldsymbol{B'}\times\boldsymbol{B'}\frac{\hat{\lambda}}{\hat{\nu}}\end{aligned} \tag{2.70}$$

The first remaining factor $\hat{\nu}/\hat{\Omega}\hat{D}^2$ is the ratio between the time scale of viscous diffusion and the rotation, which has been named Ekman number $E = \hat{\nu}/\hat{\Omega}\hat{D}^2$. It measures the ratio between viscous drag (momentum diffusion) and the Coriolis force. Its planetary value is as small as $E = 10^{-15}$. Therefore viscous diffusion does not play a major role in the dynamics of planetary cores. Core dynamics are dominated by the Coriolis force. We discussed that issue in the section 1.2. The second factor is the modified Rayleigh number $Ra^* = \hat{\alpha}\hat{q}_0\hat{g}\hat{D}^2/\hat{\nu}\hat{\kappa}\hat{\Omega}$. It relates to the more general flux based Rayleigh number Ra as

$$Ra^* = \frac{RaE}{Pr} = \frac{\hat{\alpha}\hat{g}\hat{q}_0\hat{D}^4}{\hat{\nu}\hat{\kappa}^2}\frac{\hat{\nu}}{\hat{\Omega}\hat{D}^2}\frac{\hat{\kappa}}{\hat{\nu}}\,. \tag{2.71}$$

The Rayleigh number measures the vigor of the convection. The higher Ra the faster and more turbulent is the convection. Even though we describe here fluctuations on top of adiabatic state, the Rayleigh number still needs to be sufficiently high for convection to set in. The critical Rayleigh number is, depending on Ekman number, much larger than unity since the buoyancy also has to overwhelm the viscosity or/and the Coriolis force. The last factor in front of the Lorentz force is again the inverse magnetic Prandtl number Pm. The table 2.2 gives an overview over all the nondimensional input and output parameters. Each of the nondimensional numbers defines the ratio of two time scales. Due to the limitations in computational power, most of the parameters can not be modeled with their realistic values. A realistic value of the Ekman number is roughly 10^{-15} for a terrestrial planet. This means the time scale introduced by the rotation ($\approx$ 1 day) is 15 orders of magnitude faster than the viscous time scale assuming a viscosity as given in table 1.1.

The magnetic Prandtl number Pm gives the ratio between the viscous and magnetic diffusivity. As shown in table 2.2, the realistic value is much smaller then unity. This means in our numerical dynamo model the magnetic diffusion is substantially weakened, otherwise no self-sustained magnetic field could be maintained against magnetic diffusion (ohmic decay). The time scale for magnetic diffusion is of the order fifty thousand years and thus much faster then the viscous time scale ($\approx 10^{11}$ yrs). The magnetic Reynolds number Rm, as the ratio between inertia and magnetic diffusion and the crucial condition for dynamo action provides realistic values (Christensen and Wicht 2007). As strong we overestimate the Pm, as strong we underestimate the hydrodynamical Reynolds number Re leading to a realistic $Rm = Re\ Pm = UD/\lambda$, where U is a typical flow velocity and D a typical length scale. The smaller Pm is chosen, the more vigorously the flow needs to be driven for providing a sufficiently high flow amplitude.

Table 2.2: Nondimensional numbers and control parameters

	Symbol	forces	time scales	model range	realistic value
Input					
Ekman	E	$\frac{\text{viscous diff.}}{\text{coriolis}}$	τ_{rot}/τ_{vis}	$10^{-3}\ldots 10^{-5}$	3×10^{-15}
Rayleigh	Ra	$\frac{\text{buoyancy}}{\text{viscous diff.}}$	$\tau_{vis}^2\tau_{diff}^T/\tau_{gra}$	$10^5\ldots 10^8$	10^{28}
Prandtl	Pr	$\frac{\text{viscous diff.}}{\text{thermal diff.}}$	τ_{diff}^T/τ_{vis}	1	1
magn Prandtl	Pm	$\frac{\text{viscous diff.}}{\text{magnetic diff.}}$	τ_{diff}^m/τ_{vis}	$2\ldots 10$	10^{-6}
Output					
Rossby	Ro	$\frac{\text{inertia}}{\text{coriolis}}$	τ_{rot}/τ_{ine}	10^{-2}	$10^{-5}\ldots 10^{-6}$
Elsasser	Λ	$\frac{\text{Lorentz}}{\text{coriolis}}$	τ_{rot}/τ_{alf}^2	$0.5\ldots 12$	≈ 1
Reynolds	Re	$\frac{\text{inertia}}{\text{viscous diff.}}$	τ_{vis}/τ_{ine}	$50\ldots 300$	$10^8\ldots 10^9$
magn. Reynolds	Rm	$\frac{\text{inertia}}{\text{magnetic diff.}}$	τ_{diff}^m/τ_{ine}	$50\ldots 1500$	$100\ldots 1000$

Table 2.3: The time scales are given by: rotation $\tau_{\mathrm{rot}} = 1/\Omega$, viscous diffusion $\tau_{\mathrm{vis}} = \mathrm{D}^2/\nu$, magnetic diffusion $\tau_{\mathrm{diff}}^{\mathrm{m}} = \mathrm{D}^2/\lambda$, thermal diffusion $\tau_{\mathrm{diff}}^{\mathrm{T}} = \mathrm{D}^2/\kappa$, convective turnover $\tau_{\mathrm{ine}} = \mathrm{D}/\mathrm{U}$, alfvenic $\tau_{\mathrm{alf}} = \mathrm{B}^{-1}\sqrt{\rho\mu_0\lambda}$ and the gravitational time scale $\tau_{\mathrm{gra}} = \mathrm{D}^2/\alpha\mathrm{gq}$. Compare also Christensen and Tilgner (2002).

2.7 Numerical Method

For simplicity we drop the again the primes for the nondimensional quantities, and the rename $H* = H$ as the heat source density. The MHD equations in their nondimensional form are:

$$E\left(\frac{\partial \boldsymbol{u}}{\partial t} + \boldsymbol{u}\cdot\boldsymbol{\nabla}\boldsymbol{u}\right) = -\boldsymbol{\nabla}\Pi + E\nabla^2\boldsymbol{u} - 2\boldsymbol{e}_z\times\boldsymbol{u} + Ra\boldsymbol{e}_r T + \frac{1}{Pm}(\boldsymbol{\nabla}\times\boldsymbol{B})\times\boldsymbol{B} \tag{2.72}$$

$$\frac{\partial T}{\partial t} + \boldsymbol{u}\cdot\boldsymbol{\nabla}T = \frac{1}{Pr}\nabla^2 T + H \tag{2.73}$$

$$\frac{\partial \boldsymbol{B}}{\partial t} = \boldsymbol{\nabla}\times(\boldsymbol{u}\times\boldsymbol{B}) + \frac{1}{Pm}\nabla^2\boldsymbol{B} \tag{2.74}$$

$$\boldsymbol{\nabla}\cdot\boldsymbol{u} = 0 \tag{2.75}$$

$$\boldsymbol{\nabla}\cdot\boldsymbol{B} = 0 \tag{2.76}$$

This set of equations of MHD is solved within a 3D numerical implementation. There numerous codes, which solve for the MHD equations. In the application for planetary dynamos, spectral or pseudo-spectral methods are widely used today (Christensen and Wicht 2007). As a comparison for a fraction of the codes available for this special MHD problem, the study by Christensen et al. (2001) conducted a benchmark including the most prominent of today's codes. Here we focus on the pseudo-spectral code MagIC3

(Wicht 2002), which is exclusively used and slightly modified for this project. A detailed description of the numerical method can be found in Christensen and Wicht (2007), Wicht (2002). This code is a further development of an older code by Glatzmaier and Roberts (1995), which is based on a solar model (Glatzmaier 1984).

The governing equations will provide nine equations for the eight unknown fields, namely three components of magnetic field (B_r, B_ϑ, B_ϕ) and flow (u_r, u_ϑ, u_ϕ), the temperature T and the pressure Π. The components of magnetic field and flow are linked to each other by vanishing of their divergence. Therefore a further simplification can be made. Both, the flow $\boldsymbol{u}$ and the magnetic field $\boldsymbol{B}$, can be described by two scalar fields, namely the poloidal $g(r, \vartheta, \phi)$ and toroidal field $h(r, \vartheta, \phi)$ contribution of the magnetic field. Analogously v and w are the poloidal and toroidal flow potentials, respectively.

$$\boldsymbol{B}(r, \vartheta, \phi) = \boldsymbol{\nabla} \times \boldsymbol{\nabla} \times [\boldsymbol{e_r} g(r, \vartheta, \phi)] + \boldsymbol{\nabla} \times [\boldsymbol{e_r} h(r, \vartheta, \phi)] \tag{2.77}$$

$$\boldsymbol{u}(r, \vartheta, \phi) = \boldsymbol{\nabla} \times \boldsymbol{\nabla} \times [\boldsymbol{e_r} v(r, \vartheta, \phi)] + \boldsymbol{\nabla} \times [\boldsymbol{e_r} w(r, \vartheta, \phi)] \,. \tag{2.78}$$

This decomposition automatically fulfills the incompressibility condition and $\boldsymbol{\nabla} \cdot \boldsymbol{B} = 0$, thus reduces the number of unknown independent fields from originally eight ($\boldsymbol{B}$, $\boldsymbol{u}$, T, Π) to six (g, h, v, w, T, Π).

The MagIC code is a pseudospectral code, thus solves the nonlinear terms on a spherical grid (r, ϑ, ϕ) and the remaining components in spectral space. For the spectral representation each of these six fields is represented by a series of spherical harmonics $Y_{lm}(\vartheta, \phi)$ for the horizontal and series of Chebyshev polynomials $C_n(r)$ for the radial direction. Therefore a single scalar field (v here) depending on the radius r, latitude ϑ and azimuth ϕ can be expanded as:

$$v(r, \vartheta, \phi) = \sum_{l=0}^{L} \sum_{m=-l}^{l} \sum_{n=0}^{N} v_{lmn} C_n(r) Y_{lm}(\vartheta, \phi) \,, \tag{2.79}$$

where

$$C_n(x) = \cos(n \arccos(x)) \tag{2.80}$$

are the Chebyshev polynomials. This choice of radial representation is motivated by denser radial grid point distribution at the inner and outer boundaries (Christensen and Wicht 2007). The spherical harmonics Y_{lm} in complex notation are defined by

$$Y_{lm}(\vartheta, \phi) = P_{lm}(\cos\vartheta) \, \exp(i\, m\, \phi) \,, \tag{2.81}$$

with P_{lm} being the associated Legendre polynomials of degree l and order m. A major advantage of the spherical representation is the simple treatment of the horizontal part of the Laplacian operator since $\Delta_h Y_{lm} = -l(l+1) Y_{lm}/r^2$, and derivatives in general. Six equations are needed to solve for the six unknown scalar fields (g_{lmn}, h_{lmn}, v_{lmn}, w_{lmn}, T_{lmn}, Π_{lmn}) in the spectral representation. They are derived by taking the radial component (poloidal component) and the radial component of the curl (toroidal) of the Navier-Stokes equation (flow potentials) and the induction equation (magnetic potentials). The equation for the pressure is obtained when taking the horizontal divergence of the Navier-Stokes equation. Thus the pressure is treated as an additional unknown in the Navier-Stokes equation.

The full spectral equations and their detailed discussion can be found in Glatzmaier (1984), Christensen and Wicht (2007), Wicht (2002). The nonlinear terms are not treated in spectral space due their ability to couple several spectral modes. Thus a forward and back transformation between spectral and grid space is needed. Here a Fast Fourier Transform is applied to transform the azimuthal and radial direction ($v(r, \phi, \vartheta)$ to $v(n, m, \vartheta)$) and a Gauss-Legendre transformation for the longitudinal direction ($v(n, m, \vartheta)$ to $v(n, m, l)$). The terms mixing spectral modes, namely the Coriolis force, Lorentz force, induction term and temperature advection are calculated on the grid and forwarded in time using an explicit second-order Adams-Bashfort scheme. The remaining components are time stepped with an implicit Crank-Nicholson algorithm (Christensen and Wicht 2007). The most severe limitation in terms of computational speed is the Gauss-Legendre-transformation. It would be possible to solve the full equations in spectral space, but unfortunately then different spectral modes will couple leading into larger loss in computational speed (Christensen and Wicht 2007).

While forwarding in time, the time step needs to be constrained to avoid numerical instabilities. In terms of spherical grid representation, each field is not allowed to be advected or diffused further than the size of a grid cell. The grid point resolution is homogeneously distributed in azimuthal direction, but inhomogeneously in radial and longitudinal direction. Implemented in the code is a time step controlled by a modified Courant criterion, that also takes the alfvenic velocity as a characteristic magnetic velocity into account.

We run the code mainly with $n_r = 49$ radial grid points, and $n_\phi = 288$ in azimuthal direction. The number of longitudinal grid points n_ϑ is then adjusted to be half of those in ϕ-direction. For avoiding alias effects, we limit the maximal number of spectral degrees l and orders m $l_{max} = m_{max} = 2n_\vartheta/3$, giving 96 for the above mentioned resolution. The code is parallelized in the radial direction to work on shared memory machines, where the maximal number of CPUs used is limited by the number of radial grid points. Thus we use either 16 or 24 cores. Given the limitations of the computational resources, several 10^5 until few 10^6 time integrations translate into several till tens of magnetic diffusion times depending on the control parameters. As we will see, we are bounded to use $Pm > 1$, thus the magnetic times scales are slower than the viscous time scales. We expect relaxation to a more or less statistical state, which is already independent of the initial condition, after one or two magnetic time scales.

2.8 From a Method to a Model

The code is able to implement different heating modes and boundary conditions. A careful choice of these parameters allow to modify the standard model to a more realistic model for Mars. We discussed already the characteristics of the ancient Martian interior in the introduction. The presence or absence of compositional convection will have an important effect for the choice of the thermal boundary conditions. Shortly, the two major characteristics are convective driving by only thermal convection in the absence of an inner core and a lateral varying CMB heat flux.

If chemical convection is present, the additional buoyancy source due to the release of light elements is located close the inner core boundary. An proper model approach is then either combining temperature and composition into one variable (co-density) or solve two separate diffusion equations for the two buoyancy sources (Manglik et al. 2010). The composition is fixed at the lower boundary since there pure iron freezes out there and acts as the buoyancy source. The released light element flux is assumed to mix into the core melt, thus the sink of the composition would be a negative homogeneous volumetric sink.

For the temperature the physically more correct fixed flux conditions at the CMB acts as the sink, where a volumetric heat source distributed homogeneously throughout the outer core, models best the secular cooling process. Hori et al. (2010) showed a larger sensitivity to CMB heat flux heterogeneities if internal heating and no flux from the inner core are used as thermal boundary conditions. The largest temperature gradients are in such a case much closer at to CMB. In opposite to the bottom driven standard model, a dynamo driven by internal heating should not have a solid inner core in the model setup since it is assumed that no chemical convection powers the dynamo. Hori et al. (2010) studied the effect of the presence of an inner core in internally heated dynamos and found only a minor influence. Following Hori et al. (2010) we have an inner core with $r_i/r_o = 0.35$ as a passive flow obstacle. We model the characteristic early Martian heating mode by setting the heat flux from the solid inner core to zero, while a volumetric heat source H is homogeneously distributed in the core shell to balance the superadiabatic heat flux q_{cmb} through the CMB. The total CMB heat flux integrated over the CMB area should then be equal to the volume integrated heat source density, thus

$$\int_0^{2\pi}\int_0^{\pi} q_{cmb}(\phi,\vartheta) r_{cmb}^2 \sin\vartheta \,\mathrm{d}\vartheta\,\mathrm{d}\phi = -Pr\,H \int_0^{2\pi}\int_0^{\pi}\int_{r_{icb}}^{r_{cmb}} r^2 \mathrm{d}\,r\,\mathrm{d}\phi \sin\vartheta\,\mathrm{d}\vartheta \tag{2.82}$$

Additionally, the code allows to impose any heat flux variation $\delta q(\vartheta,\phi)$ in terms of spherical harmonics Y_{lm}:

$$q_{cmb} = q_0 + \delta q(\vartheta,\phi) = q_0 + \sum_l \sum_{m=-l}^{m=l} q_{lm} Y_{lm} \quad , \tag{2.83}$$

where $q_{l-m} = q^{\star}_{lm}$ guarantees that q remains real, the star indicating the conjugate complex here. The heat flux anomaly and its relative strength are the crucial ingredients for our model. Since the heat flux anomaly δq is defined as a sinusoidal variation it does not change the mean heat balance

$$\int_0^{2\pi}\int_0^{\pi} \delta q(\phi,\vartheta)\ \sin\vartheta\,\mathrm{d}\vartheta\,\mathrm{d}\phi = 0\ . \tag{2.84}$$

The mean heat flux q_0 is independent of colatitude ϑ and longitude ϕ. The integration of the heat balance (equation 2.82) simplifies then to:

$$q_0 4\pi r_{cmb}^2 = -Pr\,H\frac{4}{3}\pi(r_{cmb}^3 - r_{icb}^3) \tag{2.85}$$

$$q_0 = -\frac{r_{cmb}^3 - r_{icb}^3}{3r_{cmb}^2} Pr\,H\ . \tag{2.86}$$

The CMB heat flux anomalies mimic giant impacts and mantle plumes. Those may have large scales at the CMB, but arbitrary positions and orientations with respect to the rotation axis. A linear combination of two spherical harmonics (l, m), a $(1, 0)$ and a $(1, 1)$-mode with total q_{10}, q_{11} and relative amplitudes g_{10},g_{11}:

$$g_{10} = q_{10}/q_{00} \tag{2.87}$$
$$g_{11} = q_{11}/q_{00} \; , \tag{2.88}$$

allows to define a tilting angle α and model arbitrary orientations of heat flux anomalies. The angle α between the orientation of the sinusoidal perturbation and the axis of rotation is then given by

$$\alpha = \arctan(g_{11}/g_{10}) \; . \tag{2.89}$$

By using this relation, we can define the relative amplitude of the heat flux anomaly g, such that

$$\Rightarrow g := g_{10} = g_{11}/\tan\alpha \; . \tag{2.90}$$

We will use g (given in percent) as one of the main study parameters where, e.g $g = 100\%$ and $\alpha = 0$ describes a sinusoidal heat flux anomaly, what reduces the superadiabatic heat flux at the northern pole exactly to zero, and doubles it at the southern pole. Using the relations 2.82 - 2.89 provides an expression for the heat flux at the core mantle boundary depending on the tilting angle α and the relative perturbation amplitude g

$$q_{cmb}(\phi, \vartheta) = q_0 + q_{10} + q_{11} \tag{2.91}$$
$$q_{cmb}(\phi, \vartheta) = q_0 Pr\, H \left[1 + g(\cos\vartheta + \tan\alpha \sin\vartheta \cos\phi)\right] \; . \tag{2.92}$$

Starting with small perturbations of the mean cmb heat flux of about $g = 5\%$ we investigate a broad range up to $g = 300\%$, which is used in Stanley et al. (2008). Note, that for perturbations equal or bigger 100% the heat flux becomes subadiabatic in the vicinity of the point of lowest heat flux. The tilt angle α covers the full range from $\alpha = 0°$, where the axis of perturbation is parallel to the rotation axis, up to the equatorial perturbation of $\alpha = 90°$.

The schematic numerical setup and the boundary conditions are clarified in figure 2.1. The temperature boundaries are given by the radial derivative at the outer and inner core shell boundary, and are therefore flux conditions.

$$\frac{\partial T}{\partial r} = 0 \;\text{ for }\; r = r_{icb} \tag{2.93}$$
$$\frac{\partial T}{\partial r} = Pr\,(q_{cmb} + \delta q(\vartheta, \phi)) \;\text{ for }\; r = r_{cmb} \; . \tag{2.94}$$

The fluid flow can not penetrate into the shell boundaries, therefore the radial velocity is set to zero at the boundaries. Additionally we model rigid walls, thus all velocity components are forced to be zero at both boundaries.

$$\boldsymbol{u} = 0 \;\text{ for }\; r = r_{icb} \tag{2.95}$$
$$\boldsymbol{u} = 0 \;\text{ for }\; r = r_{cmb} \tag{2.96}$$

The magnetic field is matched to a potential field at the outside of the shell under the assumption of an electrically isolating ($\nabla \times \boldsymbol{B} = \mu_0 \boldsymbol{j} = 0$) mantle. The toroidal field has no radial component and therefore vanishes at the boundary. The poloidal field needs to be continuous across the boundary. The inner core is assumed to be insulating as well, and we use the same conditions there.

$$[\boldsymbol{B}] = 0 \;\text{ for }\; r = r_{cmb} \;\text{ and }\; r = r_{icb} \,, \tag{2.97}$$

where the brackets denote the jump across the boundary. Wicht (2002) had shown, that conductivity of the inner core is of minor importance for homogeneous core dynamos. We also tested this hypothesis for the boundary forced hemispherical solution and confirm the findings of Wicht (2002).

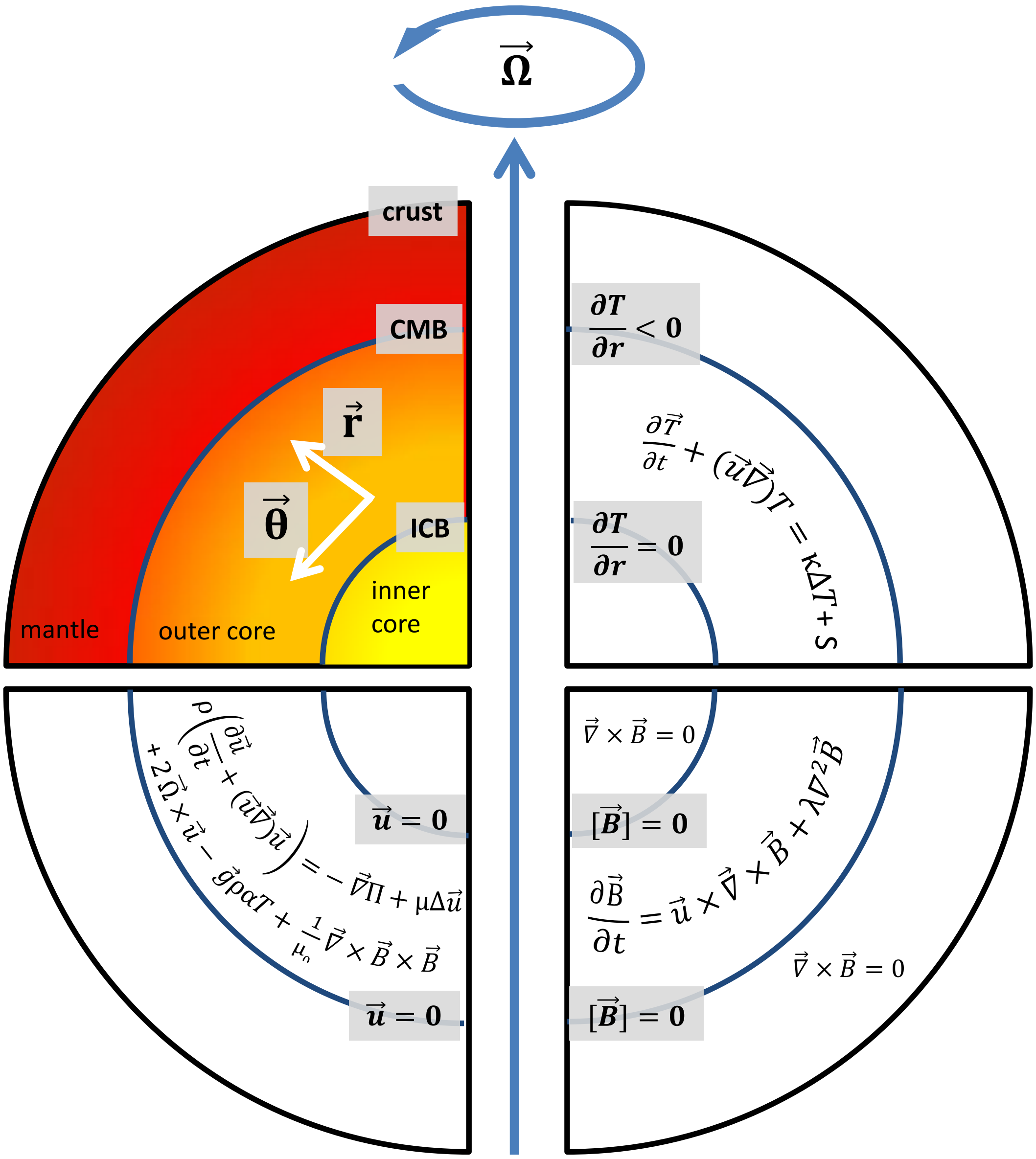

Figure 2.1: Schematic picture of the model setup and the boundary conditions. The left top sector names the spherical shells of Mars, the boundaries in between and the directions of the unit vectors. The right top sector explains the temperature equation solved in the outer core, and the appropriate boundary conditions. The right and left bottom sector is analogously, but for the magnetic field and the velocity field, respectively.

2.9 Symmetries

The rotation of the model system, or more specific the Coriolis force, breaks the spherical symmetry of the nonrotating problem. The buoyancy for example does have a radial direction, but the flow structure is more columnar due to the Coriolis force. However, the solutions of the MHD equations 2.72 - 2.76 for magnetic and flow vector field, $\boldsymbol{B}$ and $\boldsymbol{u}$, and the scalar temperature often show distinct symmetries closely related to the rotation axis. Figure 2.2 distinguishes the most important symmetries found in rotating convection and magnetic field induction. There two main groups of symmetries replacing the spherical symmetry. The first group is a mirror symmetry with respect to the equatorial plane (figure 2.2 left four plots), the second one the axial symmetry with respect to the axis of rotation (figure 2.2 right two plots).

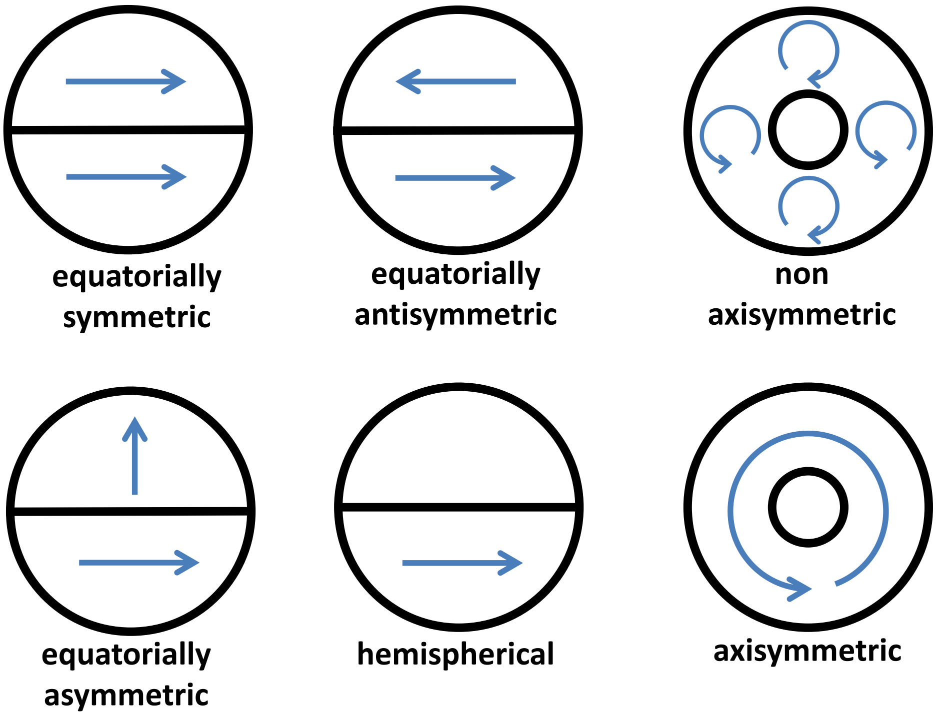

Figure 2.2: Symmetries: The left four plots show a front view with the equator separating northern and southern hemisphere, the right two the equatorial plane with inner and outer core boundary.

A symmetry operation σ is map of a general vector field $\boldsymbol{f}$ onto itself (Bronstein et al. 2005). In the spectral representation $\boldsymbol{f} = \sum_{lm} \boldsymbol{f_{lm}}(r)Y_{lm}$, the symmetries are reflected as characteristic distribution of degree l and order m of spherical harmonics Y_{lm}. We denote the mirror symmetry operation as σ_M and the symmetry operation describing a rotation around around the axis of rotation by σ_R.

- Equatorial Symmetry $\boldsymbol{f}^{es}$ is given by (figure 2.2, top left)

$$\boldsymbol{f}^{es} : \sigma_M(\boldsymbol{f}) = \boldsymbol{f} \qquad (2.98)$$
$$\text{all } Y_{lm} \text{ are restricted to } l + m = \text{even} \,,$$

thus a analogon of the vector field with the same amplitude and direction can be found on either side of the equator. The radial flow in a standard columnar dynamo, such as the benchmark model (Christensen et al. 2001), shows for example an equatorial symmetry. The group of magnetic modes symmetric with respect to the equator is named as the 'quadrupolar family', since the quadrupolar mode ($l = 1, m = 1$) has this parity.

- Equatorial Antisymmetry $\boldsymbol{f}^{ea}$ is given by (figure 2.2, top middle)

$$\boldsymbol{f}^{ea} : \sigma_M(\boldsymbol{f}) = -\boldsymbol{f} \qquad (2.99)$$
$$\text{all } Y_{lm} \text{ are restricted to } l + m = \text{odd} ,$$

thus an equivalent of the vector field with the same amplitude but opposing direction is present in the other hemisphere. A magnetic dipolar mode ($l = 1, m = 0$) is a prominent example of such a symmetry. Therefore modes having this parity belong to the 'dipole family'.

- Equatorial Asymmetry $\boldsymbol{f}^{ne}$ is given by (figure 2.2, bottom left)

$$\boldsymbol{f}^{ne} : \sigma_M(\boldsymbol{f}) = 0 , \qquad (2.100)$$

thus no analogon of the vector field with a matching direction is present in the other hemisphere, although there might be some vector field of finite amplitude. Such field contributions can be calculated by $\boldsymbol{f}^{ne} = \boldsymbol{f} - \boldsymbol{f}^{es}$ showing that any vector field can be separated into symmetric and asymmetric parts. All of the three so far discussed symmetry cases show equatorial symmetry when using the intensities $\boldsymbol{f}^2$ of the vector field.

- Equatorial Hemisphericity $\boldsymbol{f}^{eh}$ is given by (figure 2.2, bottom middle)

$$\boldsymbol{f}^{eh} : \sigma_M(\boldsymbol{f}^2) = 0 , \qquad (2.101)$$

thus one hemisphere is devoid of contributions of $\boldsymbol{f}$. This measure gives an information about the equatorial symmetry of the intensity. As we had seen, the distribution of the crustal magnetic field on Mars (Acuña et al. 1999) shows such a property and it therefore might be useful to examine the magnetic field obtained from the numerics with respect to this quantity. As can be seen from the figure 2.2 a combination of equatorially symmetric and equatorially antisymmetric with equal amplitude sums up to a stronger field in one hemisphere and weaker in the outer.

For the rotational symmetry, as shown in figure 2.2 (right plots), we only distinguish between axisymmetry and non axisymmetry. Axisymmetry here means, the rotational symmetry operator σ_R maps $\boldsymbol{f}$ on itself for any rotation angle ϕ. Dynamo solutions close to the onset, such as described by Christensen et al. (2001), do have an intrinsically symmetry. Therefore the axial symmetry in that case is given only for a special set of rotation angles ϕ. In our notation this would count as nonaxisymmetric.

- Nonaxisymmetry $\boldsymbol{f}^{na}$ is given by (figure 2.2, top right)

$$\boldsymbol{f}^{na} : \sigma_R(\boldsymbol{f}) = 0 \qquad (2.102)$$
$$\text{all } Y_{lm} \text{ are restricted to } m \neq 0 ,$$

thus if a rotation about at least on angle ϕ does not map $\boldsymbol{f}$ on itself. The sketch in the figure 2.2, top right might represent the equatorial cut of convective columns. Knowing the axial symmetric partition allows for calculating the nonaxisymmetric contribution ($\boldsymbol{f}^{na} = \boldsymbol{f} - \boldsymbol{f}^{as}$)

- Axisymmetry $\boldsymbol{f}^{as}$ is given by (figure 2.2, bottom right)

$$\begin{aligned} \boldsymbol{f}^{as} &: \sigma_R(\boldsymbol{f}) = \boldsymbol{f} \\ &\text{all } Y_{lm} \text{ are restricted to } m = 0 \, , \end{aligned} \tag{2.103}$$

thus if a rotation about about any angle ϕ does map $\boldsymbol{f}$ on itself. The spherical harmonics are axisymmetric, if the order $m = 0$. The magnetic axial dipole ($l = 1, m = 0$) or zonal flows are examples for axisymmetric mode.

3 Results I : Hemispherical Convection and Induction

The main research highlights of the this chapter are compiled in a publication named 'A hemispherical dynamo model: Implications for the Martian crustal magnetization' and re-submitted after moderate revision to the 'Physics of the Earth and Planetary Interiors' (PEPI).

The theory of rotating convection was established during the 1960s by Roberts (1965), Bisshopp and Niiler (1965), but their work concentrated on convective instabilities, which where symmetric with respect to the rotation axis (Landeau and Aubert 2011). Later work by Roberts (1968) investigated non-axisymmetric and equatorial antisymmetric convection, whereas it was (Busse 1970) to describe the well established columnar flow structures, which are non-axisymmetric, but equatorially symmetric. This result is basically confirmed by nearly all numerical experiments at the onset of thermal convection in such systems (see e.g. Christensen et al. (2001)). Recent numerical studies, such as Landeau and Aubert (2011) on vigorous convection driven by internal heat sources, brought back the attention to equatorially antisymmetric convection. There the authors found the emergence of such an axisymmetric and equatorially antisymmetric convective mode, if the convective driving in terms of the Rayleigh number is sufficiently high.

3.1 Defining a Reference Case

In order to clarify the transition from dipolar to a hemispherical dynamo due to CMB heat flux anomalies, a well chosen reference case with homogeneous heat flux needs to be defined. This state should have a non-reversing dipole dominated magnetic field and the convection should be dominated by the typical columnar structures. Then the changes in flow and field are easier to observe and might offer the chance to compare the features of the new convection and induction to a well studied system. The choice of Rayleigh number is a trade off between intrinsic symmetries at lower values (Christensen et al. 2001) and the natural occurrence of the hemispherical convection at higher values (Landeau and Aubert 2011). Of course, the parameters like magnetic Prandtl number Pm and Ekman number E should be taken as close as possible to real planetary values. However, there are bounded by the numerical power accessible. The lowest Ekman number used is $E = 1.0 \times 10^{-5}$, what is roughly nine orders of magnitude too large.

Christensen and Aubert (2006) introduced the concept of the local Rossby number Ro_l. The Rossby number gives the ratio of inertia over the strength of the Coriolis force. Instead of the classical definition $Ro = U/D\Omega$, a typical inertia length scale $D_{ini} = D\pi/\bar{l}_u$

is used. The factor $\bar{l}_u$ is the mean degree of the kinetic energy spectra. This definition attempts to consider the real length scale of the convection which decreases with increasing Rayleigh number and decreasing Ekman number. This measure was used to find a relationship between Ro_l and the dipole strength. Christensen and Aubert (2006) reported a transition from stable dipolar towards reversing multipolar magnetic field morphology, whenever the strength of the inertia term becomes significantly more important. The relative strength of the axial dipolar magnetic mode at the CMB is defined as

$$dip_{cmb} = \frac{B_{l=1,m=0}(r = r_{cmb})}{\sum_l \sum_m B_{l,m}(r = r_{cmb})} \,. \tag{3.1}$$

Whenever $Ro_l > 0.1$ the dipole strength is remarkably smaller. The general effect is thought to be independent of hydrodynamic and magnetic Prandtl numbers, Pm and Pr and Ekman numbers E (Christensen and Aubert 2006). All dynamo cases studied by Christensen and Aubert (2006) use fixed temperature conditions, rigid walls and no internal heat sources. Hori et al. (2010) investigated the strength of the axial dipole in internal heated dynamos for different thermal boundary conditions. It was found, that for fixed temperature conditions the solutions generally tend to be non-dipolar. However, for the combination of internal heating and fixed flux conditions the relation found by Christensen and Aubert (2006) still holds (Hori et al. 2010). For our tested cases with the same heating setup, figure 3.1 shows the strength of the axial dipole normalized with the total magnetic energy as a function of the local Rossby number Ro_l. Obviously there is a transition from dipole dominated towards multipolar magnetic morphologies. For higher Ekman numbers, such as $E = 10^{-3}$ (black crosses), all dynamo cases shows weaker dipolarity. For $E = 3.0 \times 10^{-4}$ (black triangles down) and $E = 10^{-4}$ (black squares) we have a data coverage what is broad enough, to cross the significant border at $Ro_l = 0.1$. At least for those the transition between dipolar dominated and multipolar is clearly visible. As a consequence we can confirm that the proposal of Christensen and Aubert (2006) still holds. For the dipole dominated side of $Ro_l < 0.1$, the gradual decrease of the dipolarity might be due to the smaller length scales introduced by the more vigorous convection. For the lower Ekman numbers (black circles and triangle up) we could not afford to increase the Rayleigh such high, that the local Rossby number exceeds 0.1. The blue symbols in figure 3.1 describe the situtation if a heat flux anomaly of different strength is applied to the outer boundary. Starting from $E = 10^{-4}, Ra = 4.1 \times 10^7, Pm = 2$ (black square), adding and increasing a heat flux heterogeneity with relative amplitude of $g = 10\%$ (first blue symbol) up to 400% (last blue symbol) shows the cease of dipolarity by a large scale heat flux anomaly even if the local Rossby number Ro_l remains smaller then 0.1. We will further analyse this behavior when discussing the effect of the boundary anomaly in greater detail.

The red symbols in figure 3.1 denote equivalent simulations, but using mechanical boundary conditions of stress-free type. Here the dipolarity at high Ekman numbers, such as $E = 10^{-3}$ (red crosses) is always significantly lower than for the comparable rigid wall cases (black crosses). The red squares describe the situation for $E = 10^{-4}$, where a bistability of dipole dominated and weakly dipolar cases can be found. This is consistent with Gastine et al. (2012). It then depends on the initial condition whether the dynamo settles in the dipolar dominated or in the weakly dipolar regime. Gastine et al. (2012) also reported a spontaneous dipole break down.

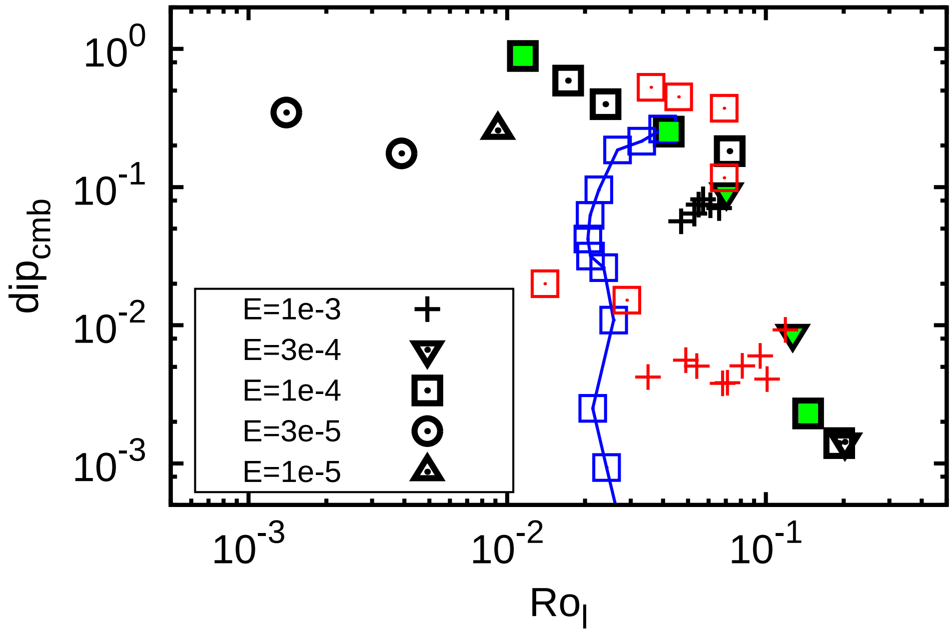

Figure 3.1: Relative strength of axial dipole mode at the CMB (dipolarity) as function of the local Rossby number Ro_l. The black symbols denote cases with rigid walls, the red symbols for the free slip boundary conditions. As suggested by Christensen and Aubert (2006), the dipolarity at the CMB is much weaker if $Ro_l > 0.1$. Blue symbols describe the dipolarity in the boundary forced dynamos. Those filled in green are further described and shown in figures 3.2 and 3.3. Different symbol types refer to different Ekman numbers used. For further details see text.

Here we want to restrict the main analysis to the rigid walls, and try to find a meaningful reference state for the study. For numerical reasons, we choose the Ekman number $E = 10^{-4}$ for the main analysis. The few symbols filled with green color in figure 3.1 represent those cases, whose convection and induction process are displayed in greater detail in figures 3.2 and 3.3. As suggested in figure 3.1 the first, third and fourth case are dipole dominated, what can clearly be seen in the plots of the radial field in the right plots of figure 3.2. The magnetic field is strongly antisymmetric with respect to the equator. In opposite to that, the second and last case are only weakly dipolar. The magnetic field shows equatorial asymmetry and stronger time dependence in terms of irregular reversals. Although the magnetic field changes its time dependence and equatorial symmetry when increasing the Rayleigh number, the convection in terms of the radial flow (figure 3.2, left plots) seems similar for all cases. It is organized in equatorial symmetric convective columns, which are non-axisymmetric (figure 3.2), left plots. The exceptional third case ($E = 10^{-4}$ and $Ra = 7.0 \times 10^6$) is very close to onset of dynamo action and therefore shows the typical drifting symmetric ($m = 2$)-solution. The dynamo benchmark (Christensen et al. 2001) differs in the heating mode, but also shows a solution with an intrinsic

(m = 4)-symmetry.

However, the zonal averages and equatorial slices shown in figure 3.3 reveals differences in the flow structure for the dipolar and non-dipolar cases. At first, the equatorial slices of temperature and z-vorticity (5th and 6th column in figure 3.3) reflect the structure of the convective columns. For the dipolar cases (first, third and fourth row) the radial extend of the convective cells match roughly with the thickness of the convective shell, as can be seen in the z-vorticity (figure 3.3, right column). The z-vorticity is chosen here, because it mimics the ability of the flow to induce magnetic field via helical flows or an α-effect. The nondipolar cases show shorter convective length scales, and therefore larger local Rossby numbers.

The plots of the zonal averaged quantities, such as temperature, flow and magnetic field in figure 3.3 clearly visualizes differences in the convection and its symmetries, when comparing dipolar and non-dipolar dynamo cases. Those solutions possessing a stable dipolar dynamo solution (first, third and fourth) have an equatorial symmetry in the temperature (first column in figure 3.3), the zonal flow (second column) and poloidal field line structure (fourth column). Merely the azimuthal field (third column in figure 3.3) is equatorially antisymmetric. This is the frequently reported structure of a stable and dipolar dominated field (Christensen and Wicht 2007, Wicht and Aubert 2005). The zonal flow shows a strong equatorially symmetric westward drift patch surrounding the equator, a weaker inside the tangent cylinder and eastward drift patches at high latitudes. The nondipolar cases (second and last row in figure 3.3) show the emergence of an equatorially asymmetric temperature anomaly (first column), which turn seems to drive thermal winds. These thermal wind are equatorially antisymmetric, and show westward drift in the northern hemisphere and eastward in the southern. Coinciding with the change in azimuthal flow pattern and symmetry, the azimuthal field becomes more irregular (figure 3.3, third column) and the dipolarity decreases significantly (figure 3.1). All of the dynamos found with $Ro_l > 0.1$ show dynamo reversals without any clear periodicity. Even though, the radial flow does not show strong deviations from the equatorial symmetry, the radial field is significantly hemispherical (figure 3.2, last plots). These findings are consistent with the results of Landeau and Aubert (2011), where it was shown that a critical Rayleigh number Ra_c for the natural onset of the EAA mode can be estimated such that $Ra_c = 21.2E^{-1.49}$ giving $Ra_c = 2 \times 10^7$ in our nondimensionalization. Our case with $Ra = 2 \times 10^8$ is then far beyond this border and expected to show a significant EAA contribution. For $Ra = 4 \times 10^7$ the natural EAA strength is still negligible, since EAA strength grows linearly with the distance from Ra_c (Landeau and Aubert 2011).

Since the temperature anomaly in the case $Ra = 2 \times 10^8$ by chance emerges such that the northern hemisphere remains hotter than the southern, the cooling in the latter one would be more efficient and hence allow for more efficient dynamo action. Interestingly, the hemisphere of stronger unsigned magnetic flux (here north for $E = 10^{-4}$) or more intense magnetic field, does not coincide with the cooler hemisphere. The placement of the hemispherical magnetic field seem to be independently of the arbitrary orientation of the temperature anomaly. Later we will see, that this does not hold for the boundary forced dynamos anymore.

As a conclusion, we choose $Ra = 4.1 \times 10^7$ (fourth plot in 3.2 and 3.3) as the base for the bulk of the numerical analysis. It does not show intrinsic symmstries, as the case for a lower Rayleigh number, but is still sufficiently far away from the $Ro_l = 0.1$ border the possess a stationary and strong dipolar magnetic field and leading equatorial symmetry in the zonal temperature and zonal flow.

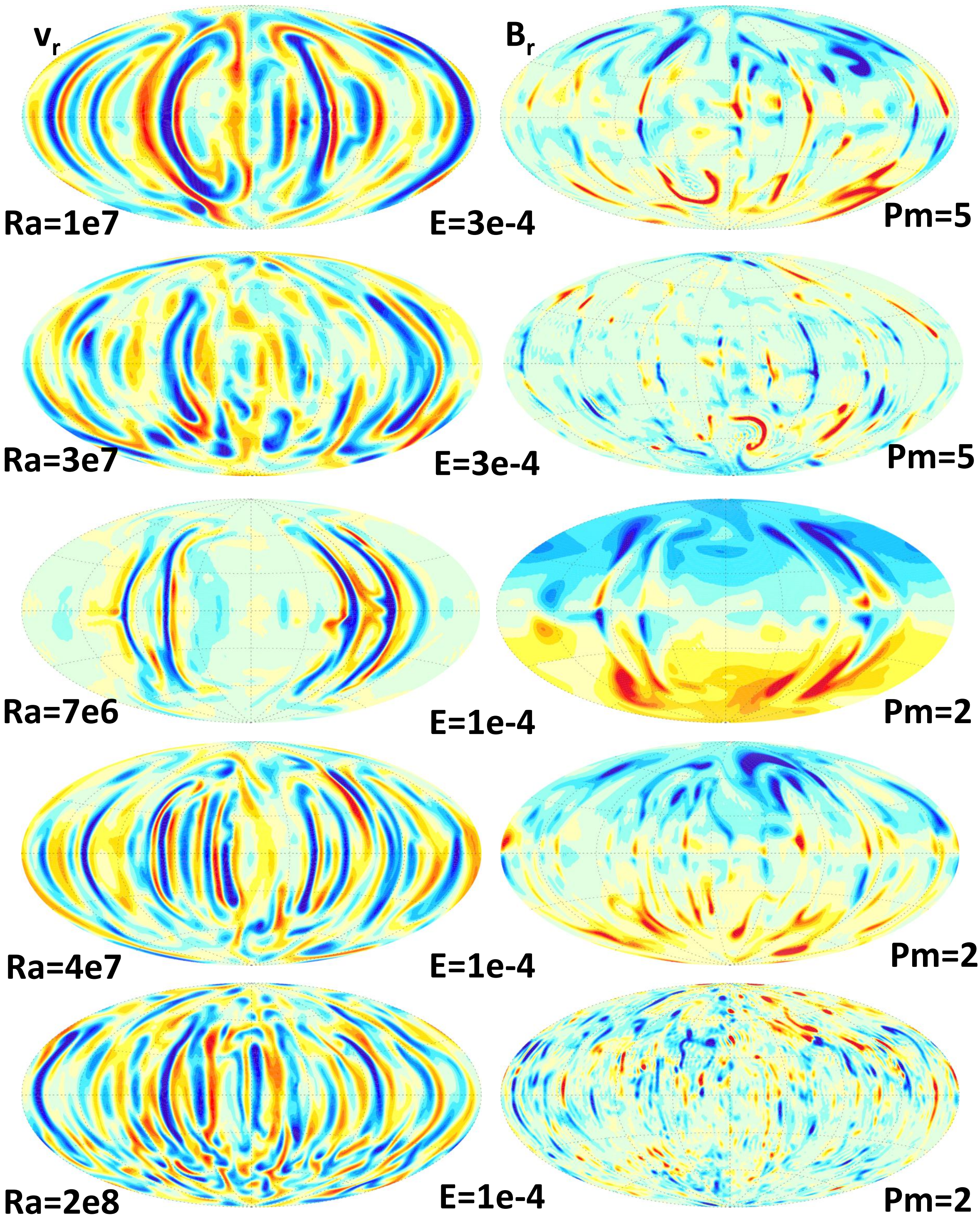

Figure 3.2: Radial velocity at mid-depth in the left column and radial magnetic field at the CMB in the right column. The two case on the top are calculated for $E = 3.0 \times 10^{-4}$ and for two different Rayleigh numbers chosen such that each case falls on either side of the $Ro_l = 0.1$ boundary in figure 3.1 (black outlined/green filled triangles down). The lower three cases are calculated for $E = 10^{-4}$ and three different Rayleigh numbers. They refer to the three black squares filled with green color in figure 3.1. All plots are snapshots, no time-averages. The color scales are chose to maximize the visibility of symmetries and structure and therefore do not contain information about the amplitudes.

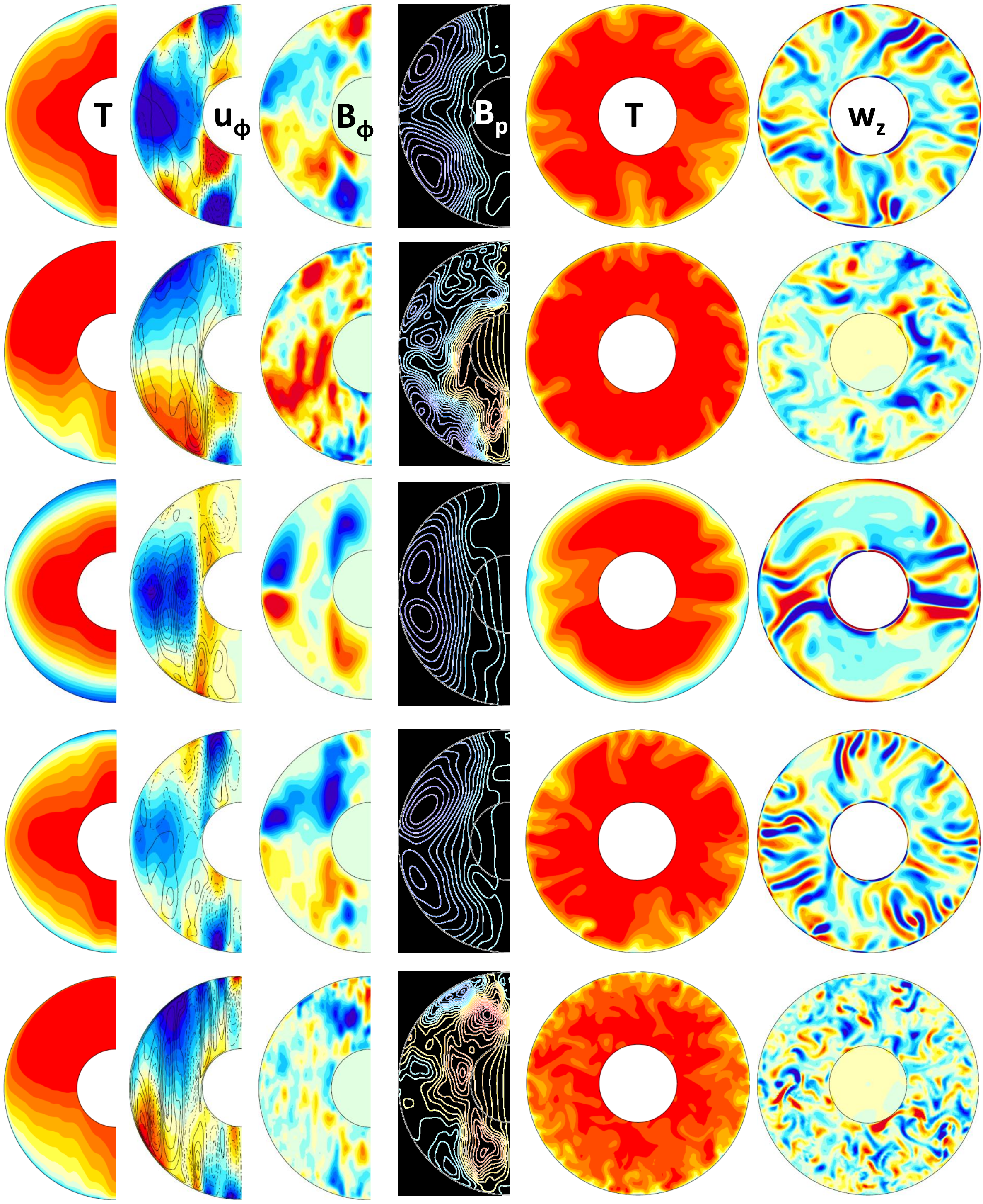

Figure 3.3: Shown is (from left to right) the zonal averaged temperature, the zonal flow with meridional flow as contours, the azimuthal magnetic field, the poloidal field lines, equatorial cut of the temperature and z-vorticity. The ordering is equivalent to figure 3.2.

3.2 Dynamo Action at $Ra = 4 \times 10^7$, $E = 10^{-4}$ and $Pm = 2$

The well defined reference case induces a stable magnetic field that is dominated by the axial dipole. As a criteria for dynamo action the magnetic Reynolds number Rm needs to be sufficiently high. Calculating Rm for this case we find $Rm = 157$. Obviously the flow has enough amplitude and complexity to permanently convert kinetic into magnetic energy. Here we want to investigate the induction mechanism in more detail. Figure 3.4 shows 3D visualizations of the flow and magnetic field lines. The upper plot mimics the convective columns as isocontours of the vertical (z-direction) vorticity for the benchmark dynamo, whereas the lower plot of figure 3.4 describes the situation for the reference case with isocontours of the radial flow. Both cases show well the induction mechanism, but differ in the details of the numerical setup. The benchmark dynamo uses fixed temperature conditions and no internal heat sources, whereas the reference case is driven by flux conditions and uses a heat source distribution as buoyancy source. We choose the benchmark dynamo (Christensen et al. 2001) here, because it hosts an stationary (but drifting) convective state with a simple $m = 4$ azimuthal symmetry. The reference case is by far more time dependent and contains much smaller convective length scales. We assume that the induction of magnetic field is based on the same convective features and thus we describe the induction on the somewhat simpler benchmark dynamo. The convection of the benchmark dynamo contains of four pairs of columns, where each column pair has a retrograde rotating and a prograde rotating column. This columns are called then anticyclones and cyclones, respectively. In figure 3.4 we colored the anticyclones in blue and the cyclones in red. In each convective column a secondary flow along the column is present. This is an effect of the boundary curvature Jones (2011) and as we will see, an important ingredient for the dynamo. The secondary flow is directed poleward in cyclones and equatorwards in the anticyclones, so both are parallel to the axis of rotation. Both flows together define vortex or a helical motion. Jones (2011) showed in detail how individual convective columns interchange flow and field, because the secondary flows converge at the equator and thus needs to be deflected into the next poleward pumping column. Instead of the flow $\boldsymbol{u}$, the vorticity $\boldsymbol{w} = \nabla \times \boldsymbol{u}$ is typically used to describe the potential of induction (Wicht and Aubert 2005). Isocontours of the vertical component of the vorticity $\boldsymbol{w}$ then visualizes the columnar structure of cyclones and anticyclones. Note, in the lower plot of figure 3.4 for the reference case of the internal heated dynamos the radial component of the flow velocity is used to characterize the convection. Although not as sophisticated as the z-vorticity, the columnar structure of the convection can be seen easily. Compared to the benchmark dynamo, the reference case has a smaller Ekman number and larger supercritical driving. Both translate into thinner and more turbulent convective columns (Jones 2007). Due to the different heating mode, one might expect that the columns are expelled further out to the CMB in the internal heated case as suggested by Jones (2007). The equatorial slices of the z-vorticity are shown in the fourth row of figure 3.3. Stronger temperature gradients and thus the convection are more attached to the CMB rather than to the inner core. This is expected from the results of Hori et al. (2010), where it was mentioned that in internally driven dynamos the largest temperature contrasts will be located close to the CMB.

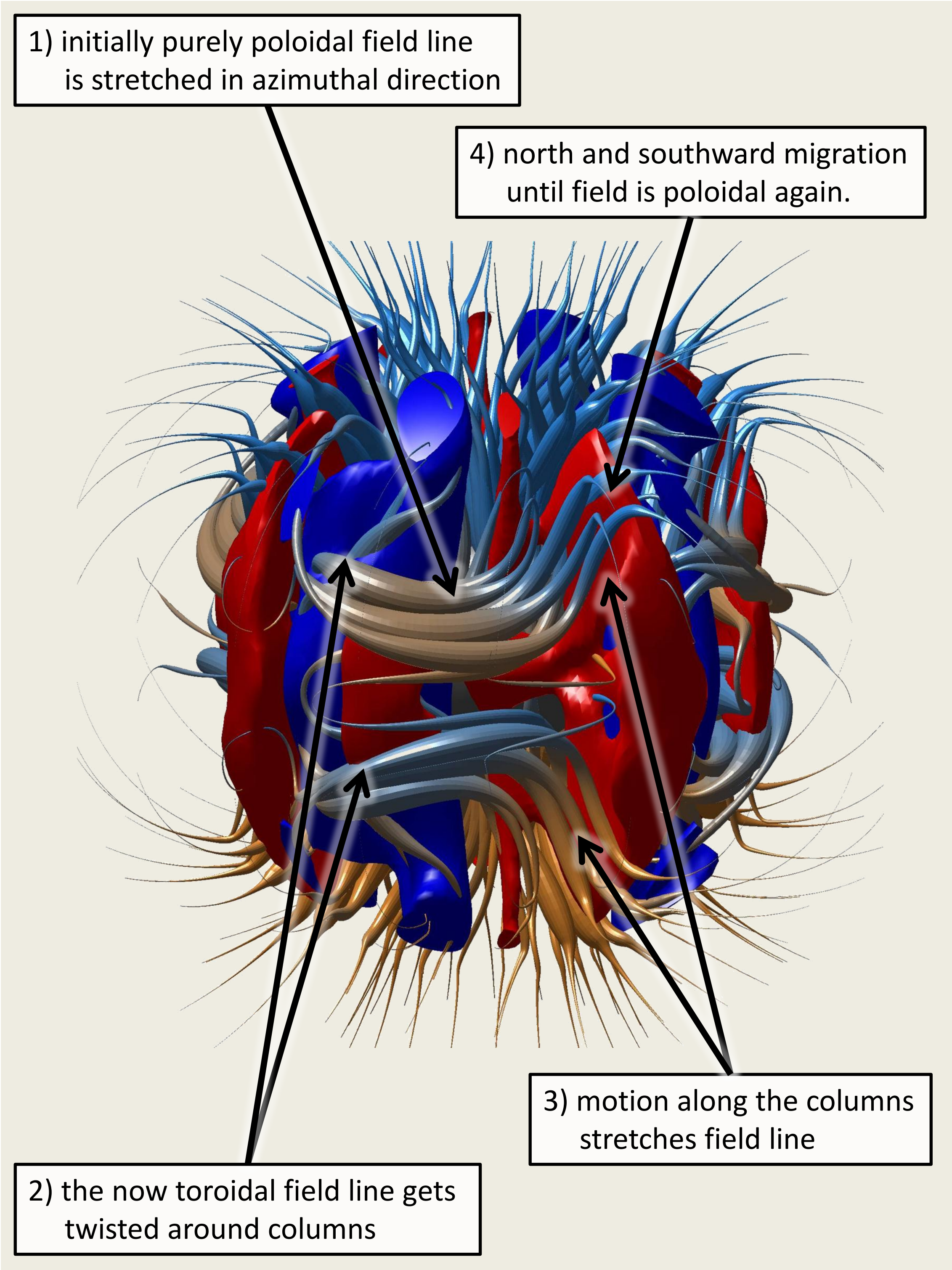

Figure 3.4: 3D visualization of the induction mechanism. The benchmark (Christensen et al. 2001) dynamo with isocontours of z-vorticity is used here. Blue (red) columns rotate retrograde (prograde) and are named anticyclones (cyclones). The thickness of the magnetic field lines is scaled with the local field strength, where red/blue fieldlines are directed outward/inward. Figure based on a 3D rendering by J. Wicht.

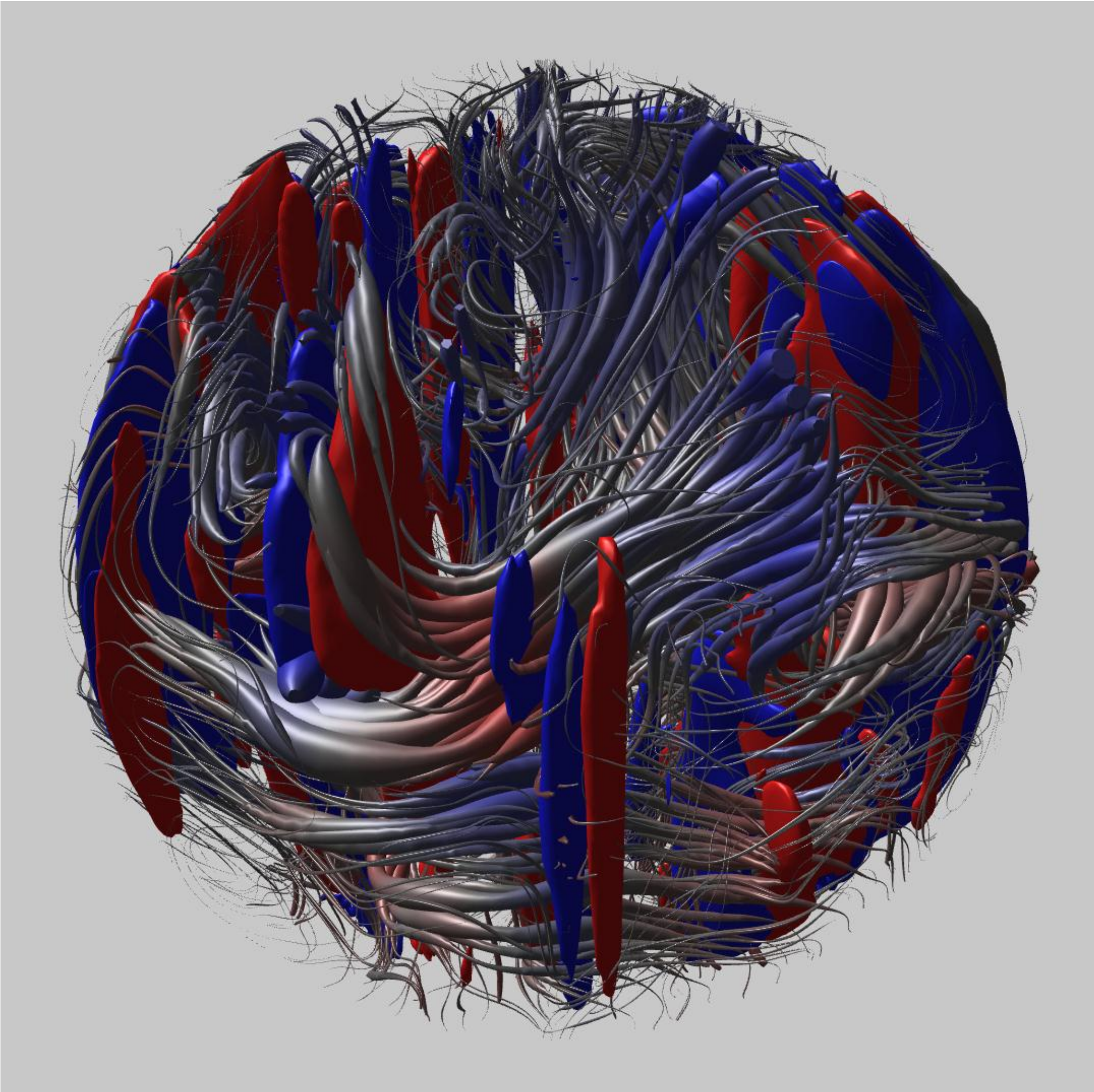

Figure 3.5: 3D visualization of the induction mechanism for the homogeneous reference case with $\mathrm{Ra} = 4 \times 10^7$, $\mathrm{E} = 10^{-4}$ and $\mathrm{Pm} = 2$. Red/blue isocontours show radial outward/inward flow. Compare also figure 3.4. The 3D rendering is made with VMagic tool by M. Meyer.

The details on the standard induction process is reviewed in Wicht and Aubert (2005), Aubert et al. (2008b), Christensen and Wicht (2007), Jones (2011). We start with a initially purely poloidal field line orientated along the rotation axis but placed into core shell such that it does not touch the inner core. This vertical field line is picked up by an anticyclonic column and thus advected in azimuthal direction (see figure 3.4). The field lines has now a strong azimuthal and retrograde toroidal contribution (Wicht and Aubert 2005). Along with the motion of the anticyclone the toroidal magnetic field line gets twisted around the column. Depending on the direction of the secondary flow in an individual convective column, the toroidal field is also advected either towards the pole or towards the equator where it is subject to firm stretching. This stretching and advection re-creates a stronger poloidal field line. For the cyclones the magnetic field is pushed towards the poles. Once the magnetic field lines reaches the CMB there, the magnetic cycle starts over again. The cyclones transport the field towards the CMB and thus should be reflected in intense flux patches of radial field (Jones 2011) at the CMB. The horizontal field is collected at the equator (see figure 3.4). For figure 3.5 denoting the reference case of our study of the internal heated dynamo, the induction mechanism works similar. Although the flow is far more complex, the main features such as the collection of horizontal field at the equator or the advection of poloidal field into the polewards can be seen there as well. Note, a single convective column contains both, inward (blue isocontours of figure 3.5) and outward (red) radial flow.

We want to fix two major conclusions from that analysis. Firstly, a helical flow is needed to enforce a prosperous dynamo process (Wicht and Aubert 2005). The helicity h is quantified as the scalar product of flow velocity $\boldsymbol{u}$ and vorticity $\boldsymbol{w}$, such that

$$h = \boldsymbol{u} \cdot \boldsymbol{w} = \boldsymbol{u} \cdot (\boldsymbol{\nabla} \times \boldsymbol{u}) \,. \tag{3.2}$$

As we will see later, this quantity is measure for the strength of the so called α-effect. Secondly, a successful dynamo permanently converts toroidal field into poloidal and poloidal into toroidal field (Jones 2011). Therefore no pure poloidal or pure toroidal dynamo is possible. Here in the benchmark (Christensen et al. 2001) the conversion into both directions is given by helical motions. In the boundary driven dynamos this will not be true anymore. Shortly, a successful dynamo needs a three-dimensional helical flow to induce a self-sustained magnetic field.

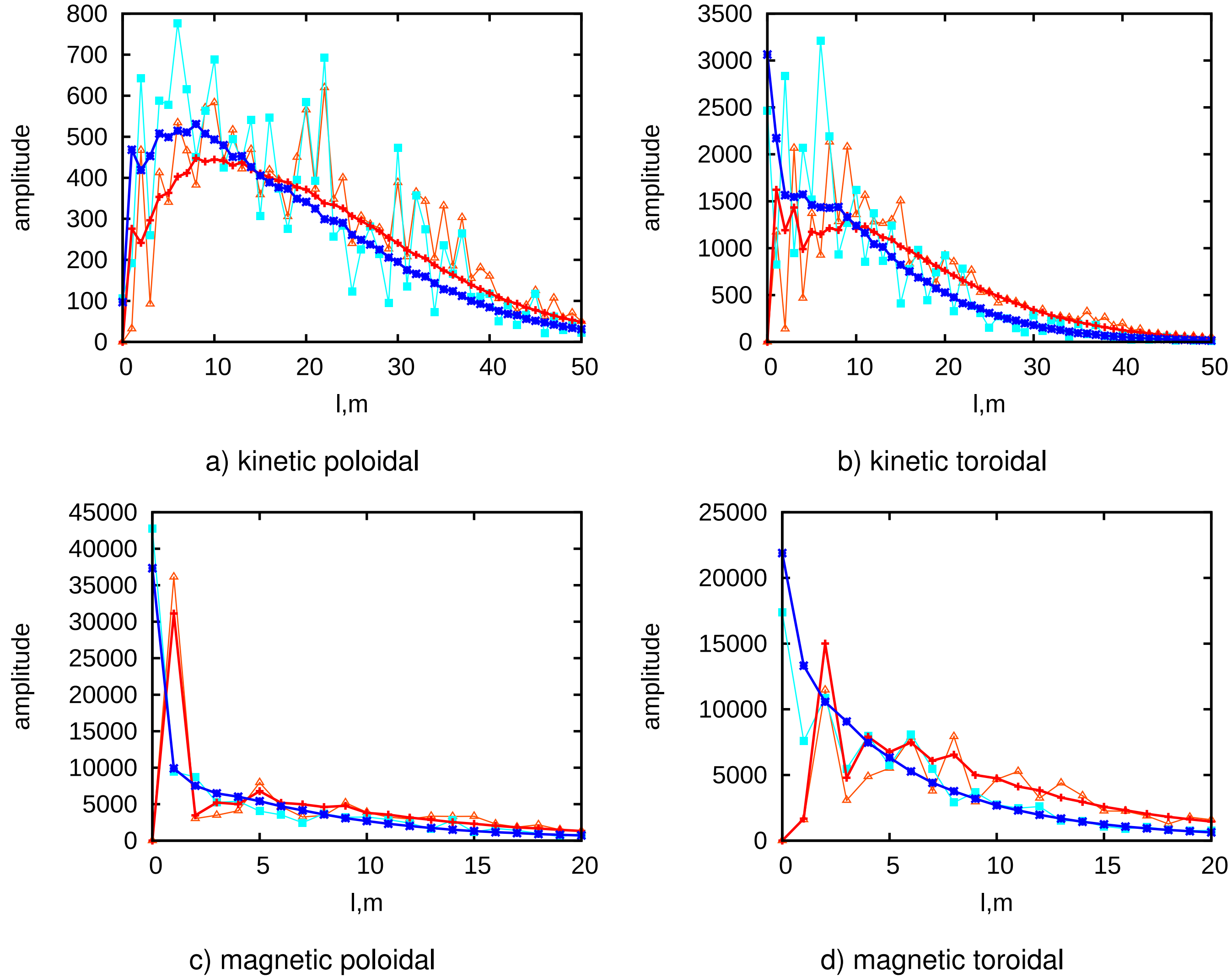

Figure 3.6: Spectra of kinetic (upper) and magnetic energy (lower) energy. The plots on the left side show the poloidal contribution, whereas those at the right side describe the toroidal energy. In each plot, the snapshot spectra are given in the thin faint lines (light blue order m, orange degree l) and the time averaged energy spectra thick lines (dark blue order m, red degree l).

We further analyze the structure and morphology the magnetic field gains during the induction process. The reference case with homogeneous heat flux boundary conditions and internal heating shows the typical convective structure, where the flow is mainly organized in convective columns. The dominating symmetry of these columns are equatorial symmetry and non-axisymmetry. Figure 3.6 describes flow (upper plots) and magnetic field (lower plots) in the spectral representation. We separate poloidal (left plots) and toroidal (right plots) contributions of the respective fields. We combine both, degree l (red/orange) and order m (blue/light blue) for snapshots (faint lines) and time averages (thick lines) in the plots. Both, poloidal and toroidal spectra show a strong time dependence as the snapshot spectra differ significantly from the time average energy spectra. The poloidal kinetic energy (figure 3.6, left top plot) shows broad distribution in degree l and order m, what reflects the typical convective length scales. The toroidal kinetic energy has a rather strong axisymmetry ($m = 0$) in the time average energy spectra (dark blue line in figure 3.6, top right), corresponding to zonal flow and meridional circulation contributions to the flow. Note, that spectra plots (figure 3.6) only show the large scale contributions and do not cover the full spectral resolution.

The magnetic field is dominated by larger scales than the flow, as shown in figure 3.6 lower plots. The number of modes displayed in the spectra plot is limited to $l_{max} = m_{max} =$ 50 for the kinetic energy, but only to 20 for the magnetic energy. Especially the poloidal energy (figure 3.6, left bottom) is dominated by the stationary axial dipole ($l = 1, m = 0$), with weaker contribution of the $l = 5$ mode. The weak time dependence is reflected in the magnetic spectra since the time average and snapshot spectra are quite similar. In the spectra of the toroidal field (figure 3.6, right bottom) the dipole is visible as $l = 2$ mode. The toroidal field of the equatorial antisymmetric dipole mode is equatorially symmetric.

3.3 An axial CMB Heat Flux Anomaly

We had seen, that the reference case with homogeneous heat flux induces a dominantly equatorially antisymmetric magnetic field what is created by the columnar structures of the equatorial symmetric and nonaxisymmetric convection. As mentioned during the introduction, one of the main characteristics of the early Martian interior dynamos might be the presence of single plume mantle convection (see section 1.5). This plume mantle plume is reflected in a CMB heat flow pattern, since it introduces large scale heat flux anomalies on top of the core. Also giant impacts might dehomogenized the CMB heat flow. Thus we study the influence of a simplified CMB heat anomaly, by using a sinusoidal perturbation pattern of spherical harmonic degree $l = 1$, what is simply a cosine of colatitude. The amplitude of the CMB heat flux anomaly and the orientation angle of the anomaly with respect to the rotation axis are study parameters here. Starting with an axial perturbation, the anomaly amplitude relative to the mean superadiabatic heat flux is systematically increased from $g = 0\%$ up to $g = 300\%$, three times the mean superadiabatic heat flux as used in the study of Stanley et al. (2008). Because the knowledge about realistic perturbation amplitudes is rather limited we start from weakly perturbed dynamos and extend our models then to strongly boundary driven setups.

3.3.1 Symmetries, Styles of Convection

We start with the parameters of the reference case, such as $E = 10^{-4}$, $Ra = 4 \times 10^{7}$, $Pm = 2$ and $Pr = 1$, but adding a CMB heat flux anomaly of $l = 1, m = 0$-shape with an amplitude of $g = 100\%$ relative to the mean heat flux. With this setup, the total heat flux at the northern pole is exactly zero and increases with colatidude until it reaches the double value of the mean heat flux at the southern pole. Then the heat flux at the equator remains unchanged, and the orientation angle is $\alpha = 0°$. We compare the convection and induction for perturbed case with the findings of the reference case with homogeneous heat flux.

One interesting observation is the onset of an equatorially antisymmetric and axisymmetric convective mode. This has been recently reported for models for the ancient Martian dynamo with homogeneous thermal boundaries (Landeau and Aubert 2011) and with heat flux anomalies (Stanley et al. 2008, Amit et al. 2011). The new mode of convection was named after its symmetry properties by Landeau and Aubert (2011), equatorially antisymmetric and axisymmetric convection (EAA). We measure the relative importance of the EAA convective mode by the relative amount of axisymmetric and equatorially antisymmetric kinetic energy:

$$EAA = \frac{(E_{kin}^{rms})^{as} - (E_{kin}^{rms})^{eqa}}{E_{kin}^{rms}} = \frac{\sum_{l_{odd},m=0} E_{lm}}{\sum_{lm} E_{lm}} , \tag{3.3}$$

where as denotes the axisymmetric and ea the equatorially antisymmetric contribution of the root-mean-square kinetic energy and E_{lm} is the rms kinetic energy carried by a flow mode of spherical harmonic degree l and order m. We introduced different kinds of symmetries and their spectral analogons in section 2.9. Therefore the spectral equivalent will be $m = 0$ for the axisymmetry and all equatorial antisymmetric energy modes (l =odd). Note, that poloidal and toroidal modes will have equatorial antisymmetric (l =odd) and equatorial symmetric modes (l =even), respectively. The sum of the curl of toroidal and double curl of the poloidal field defines the magnetic energy, where the curl operator changes the equatorial symmetry. Thus the poloidal scalar field has the same equatorial parity as the kinetic energy, whereas the toroidal scalar field is has the inverse equatorial symmetry.

The heat flux anomaly with an amplitude of $g = 100\%$ relative to the mean superadiabatic heat flux, alters the pattern and symmetries of the convection significantly. In the northern hemisphere the efficiency to cool the core is reduced due to smaller heat flux, while the southern hemisphere is cooled more efficiently. As a consequence, the northern hemisphere remains hot, while the southern can be cooled efficiently by more vigorous convection. Large scale temperature differences between the northern and southern hemisphere, and therefore a latitudinal temperature gradient emerges. This gradient breaks the typical equatorial symmetry in the temperature in the reference case. Figure 3.7 shows in left plots the axisymmetric temperature for the homogeneous reference case (top) and in the perturbed system (bottom). Single cell meridional circulation from north to south seek to equilibrate the temperature anomaly. Figure 3.7 shows in the middle plots the contours of the meridional circulation. For the reference case (top) the meridional circulation does not cross the equatorial plane and shows equatorial antisymmetry. The lower plot for the perturbed system shows the large scale meridional transport across the equator without any clear symmetry (see figure 3.7 middle bottom). The strong coriolis force due the fast rotation of the system will deflect the meridional flows into azimuthal direction. This so called thermal wind is a consequence of latitudinal temperature gradients and the action of the Coriolis force. When we derived the geostrophic force balance between pressure gradient and Coriolis force we assumed that the buoyancy has no influence (see section 1.2). If the buoyancy is taken into account and viscous terms and the Lorentz force are neglected, we find as force balance

$$-2\boldsymbol{z} \times \boldsymbol{u} + \frac{Ra\,E}{Pr}\hat{\boldsymbol{e}}_r T - \boldsymbol{\nabla}\Pi = 0\,. \tag{3.4}$$

If we apply a curl operator we can further neglect the conservative forces, such as the pressure gradient

$$-2\boldsymbol{\nabla} \times \boldsymbol{z} \times \boldsymbol{u} + \frac{Ra\,E}{Pr}\boldsymbol{\nabla} \times \hat{\boldsymbol{e}}_r T = 0\,. \tag{3.5}$$

The buoyancy is purely radial, thus in components for the spherical coordinates we find

$$2\boldsymbol{\nabla} \times \boldsymbol{z} \times \boldsymbol{u} = \frac{Ra\,E}{Pr}\left[\frac{1}{r}\frac{1}{\sin\vartheta}\frac{\partial T}{\partial \phi}\hat{\boldsymbol{e}}_\vartheta - \frac{1}{r}\frac{\partial T}{\partial \vartheta}\hat{\boldsymbol{e}}_\phi\right], \tag{3.6}$$

where the geostrophic force balance follows if the temperature has no gradients in ϕ or ϑ-direction and thus can be neglected. But we had seen, that the heat flux anomaly creates a large scale temperature gradient in latitudinal (ϑ-) direction. This will then drive a flow in ϕ-direction. For the left hand side, thus the ϕ-component of the curl of the Coriolis force we find

$$2\frac{1}{r}\left(\frac{\partial}{\partial r}\left(r(\boldsymbol{z} \times \boldsymbol{u})_\vartheta\right) - \frac{\partial}{\partial \vartheta}(\boldsymbol{z} \times \boldsymbol{u})_r\right) = \frac{Ra\,E}{Pr}\frac{1}{r}\frac{\partial T}{\partial \vartheta}\,. \tag{3.7}$$

Next, we express the cylindrical z component in spherical coordinates and examine the $(\boldsymbol{z} \times \boldsymbol{u})$

$$\boldsymbol{z} \times \boldsymbol{u} = \begin{pmatrix} \cos\vartheta \\ -\sin\vartheta u_\phi \\ 0 \end{pmatrix} \times \begin{pmatrix} u_r \\ u_\vartheta \\ u_\phi \end{pmatrix} = \begin{pmatrix} \sin\vartheta u_\phi \\ -\cos\vartheta u_\phi \\ \cos\vartheta u_\vartheta - \sin\vartheta u_r \end{pmatrix}. \tag{3.8}$$

The left hand-side of equation 3.26 is then

$$\frac{2}{r}\left[\frac{\partial}{\partial r}\left(r(\cos\vartheta u_\phi)\right) - \frac{\partial}{\partial \vartheta}\left(\sin\vartheta u_\phi\right)\right] \tag{3.9}$$

$$=\frac{2}{r}\left[r\cos\vartheta\frac{\partial u_\phi}{\partial r} - \sin\vartheta\frac{\partial u_\phi}{\partial \vartheta}\right]. \tag{3.10}$$

The variable $z = r\cos\vartheta$ and thus we can replace the partial derivatives with $\partial_r = (\cos\vartheta)^{-1}\partial_z$ and $\partial_t heta = -(r\sin\vartheta)^{-1}\partial_z$:

$$\frac{2}{r}\left[r\cos^2\vartheta\frac{\partial u_\phi}{\partial z} + r\sin^2\vartheta\frac{\partial u_\phi}{\partial z}\right] = 2\frac{\partial u_\phi}{\partial z}\,. \tag{3.11}$$

	E_{pol}				E_{tor}			
g	total	as	ea	eaa	total	as	ea	eaa
0	13910	96.6	2409	45.92	31210	3126	8296	248.2
100	10540	2375	6055	2076	199800	187200	178700	172400

Table 3.1: Comparison of the poloidal and toroidal kinetic energy contributions, and their symmetries (as-axisymmetric, ea-equatorially antisymmetric, eaa-equatorially antisymmetric and axisymmetric) for the reference case (g = 0%) and the (g = 100%) boundary forced case.

This yields then the thermal wind balance:

$$\frac{2}{E}\frac{\partial u_\phi}{\partial z} = \frac{Ra}{Pr}\frac{1}{r_0}\frac{\partial T}{\partial \vartheta}\,, \tag{3.12}$$

which shows the emergence of zonal flow gradients if there is large a latitudinal temperature gradient. Note, the thermal wind balance serves as a measure for the deviation from a geostrophic force balance. The dynamic consequence of this effect is the onset of two strong zonal flow cells. In the middle plot of figure 3.7 we can see the emergence of these thermal winds, where for the perturbed case they show equatorially antisymmetric parity. In the co-rotating reference frame, the northern cell rotates eastward and the southern westward.

Although both cases show axisymmetric zonal flows, their amplitudes relative to total kinetic energy are significantly different. In table 3.1 we collected the amplitudes of the poloidal and toroidal energy for the homogeneous reference cases ($g = 0\%$) and the strongly perturbed case with $g = 100\%$. Besides the total amplitude, table 3.1 lists also the contribution to the axisymmetry (as), equatorial antisymmetry (ea) and the combined equatorial antisymmetry and axisymmetry (eaa). The table shows several distinct effects. Concentrating on the reference case (first line) shows that the total toroidal energy is larger than the poloidal by factor two or three, whereas the axisymmetric and equatorial antisymmetric contributions are rather minor. The zonal flow is given by the axisymmetric contribution of the toroidal energy and the meridional circulation by the axisymmetric poloidal energy. Zonal flows contribute to roughly ten percent to the toroidal energy, whereas the meridional circulation is neglegible. This reflects the situation for the classical columnar convection. For the boundary forced case characterized in the second line of table 3.1, the toroidal energy exceeds the poloidal by factor of almost 20. The change in the ratio is largely due to much stronger toroidal energy, but also the poloidal energy is slightly weaker. The vast majority of the toroidal energy is now stored in axisymmetric and equatorially antisymmetric zonal flows (compare also figure 3.7), where even the combination of the two symmetries, thus the relative strength of the EAA convective mode ranges up to 85% of the total kinetic energy. As noted above, the thermal wind balance (equation 3.12) introduces gradients of axisymmetric zonal flows and thus zonal flows of large amplitude. We see here, that the vast majority of the kinetic energy is driven by ageostrophic thermal winds. Besides the strong thermal winds, also the convective flows or poloidal energy will be affected by the thermal anomaly. We investigate

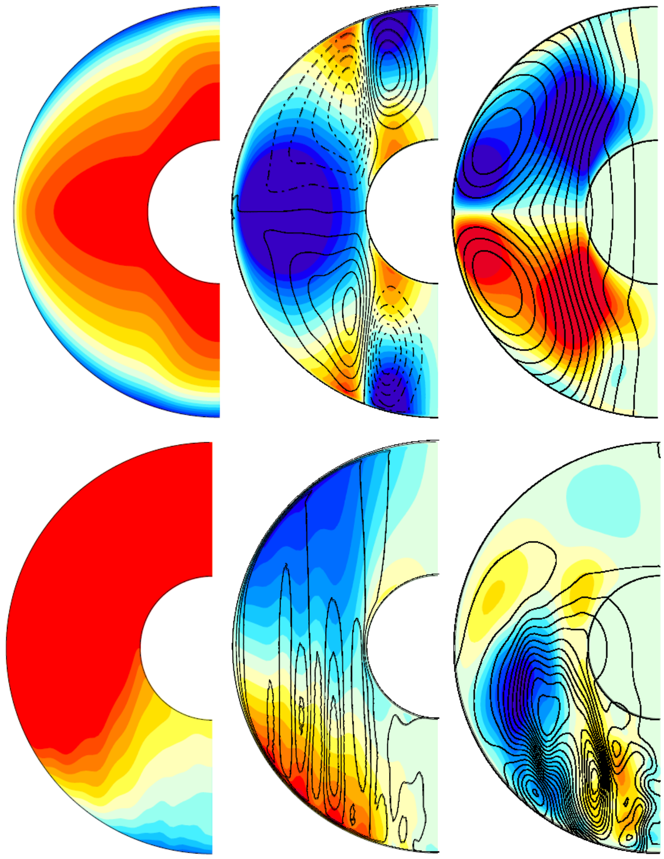

Figure 3.7: Zonal average of the temperature (left plots), zonal flow with meridional circulation as contour (middle plots) and toroidal field with poloidal field lines as contour (right plots) for columnar convection dominated and magnetic dipolar reference case (left) and a typical hemispherical dynamo solution with the strong EAA symmetry in the flow (right).

in figure 3.8 the radial flow at mid-depth (top row) and radial magnetic field at the CMB (bottom row) for the reference cases and the pertured dynamo. For the reference case, the equatorial symmetric convective columns extend from one hemisphere to the other. But for the boundary forced convection they are weakened, since the spatially most efficient cooling location is then close to the southern pole (compare also the azimuthal temperature in figure 3.7). The convection in terms of meridional circulation and radial upwellings are predominantly located at a cusp of high heat flux (fig. 3.7). Therefore the typical equatorial symmetry is broken as well and the convection becomes hemispherical, thus mainly constrained to the southern hemisphere. Table 3.1 suggested already that the poloidal flow is weaker in the heterogeneous dynamo but contains more axisymmetric meridional circulation. To summarize, the symmetry properties of the new hemispherical solution are fundamentaly different from the classical columnar convection. Columnar convection is predomimantly equatorial symmetric and non-axisymmetric (at least when

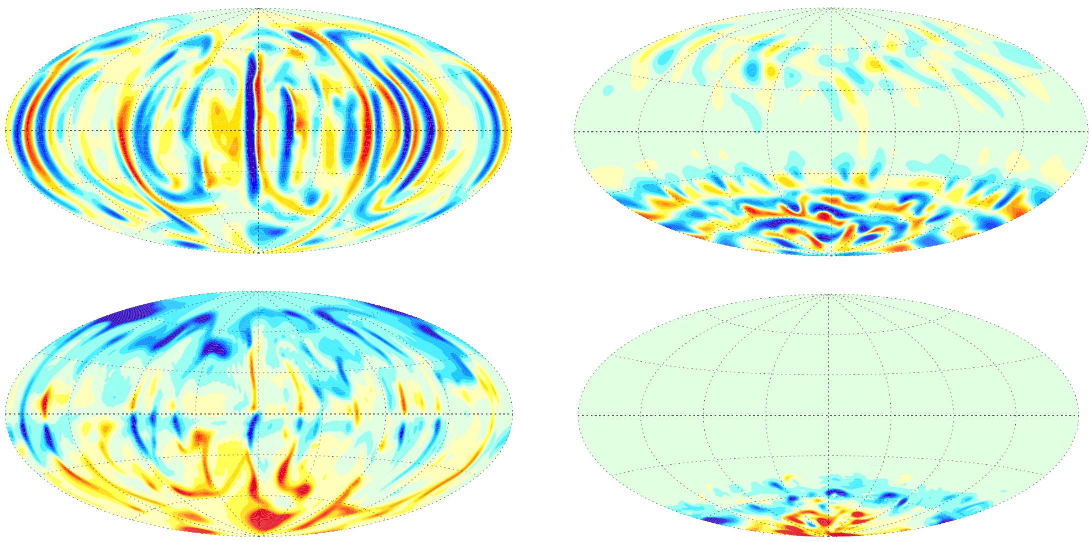

Figure 3.8: Radial flow (top row) at mid-depth and radial field at CMB (lower row) for the columnar reference case (left) and the hemispherical dynamo (right), indicates the reduction of the magnetic signature at the CMB if the radial motions are limited to the southern polar cusp of high heat flux.

the Rayleigh number is not too large). The hemispherical convection is dominated by equatorial antisymmetric and axisymmetric (EAA) thermal winds.

The poloidal flows are essential for the magnetic field induction process. On the one hand they provide helical flows and thus can perform magnetic induction. On the other hand, radial upwellings carry the magnetic field towards the CMB. Figure 3.8 relates the radial flow at mid core shell depth with the radial CMB field. A hemispherical induction process leads to a hemispherical field. Figure 3.7 (right plots) shows the poloidal magnetic field lines and color-coded the toroidal field for the homogeneous dynamo (top) as well as for the heterogeneous dynamo (bottom). The poloidal field is confined to the radial flows of the convection, thus strongly hemispherical. This translates also into hemispherical radial field at the CMB, as shown in figure 3.8. Note, that the radial field is more hemispherical than the radial flow. While the reference case has a rather stable magnetic field that never reverses, a CMB heat flux variation of $g = 100\%$ induces strong magnetic field oscillations that involve polarity reversals. The time dependence will be discussed in more detail in section 3.4.2.

The differences in flow structure and symmetry is well reflected in the kinetic and magnetic spectra. Figure 3.9 provides the same compilation of spectra for kinetic and magnetic energy as the figure 3.6 for the unperturbed reference case. The equatorially antisymmetry of the flow is visible in the figure 3.9, upper plots, in the toroidal flow. Since the kinetic energy is dominated by axisymmetric, but equatorially antisymmetric zonal flow, the dominating mode in the toroidal energy is given by $(l = 2, m = 0)$. Note a toroidal $l = 2$ modes corresponds to an equatorial antisymmetric mode of the kinetic energy. The poloidal energy, shows a clear dominance of the axisymmetry (figure 3.9, right top), even though it is much weaker than in the toroidal energy. This corresponds to the large scale meridional circulation cells. The sharp peaks for $l = 1, 3, 5$ shows again an equatorial antisymmetry. The broad peak around $l, m = 10..15$ corresponds to the remaining small convective plumes close to the southern hemisphere. These flows are hemispherical, not equatorially antisymmetric since there is not much corresponding convection on the northern hemisphere. For hemispherical symmetry, a superposition of the equatorial symmetric and equatorial antisymmetric modes are needed to achieve strong hemisphericity. Thus the spectral response of such small scale and hemispherical convective features will be represented by a broad peak in the degrees l within the poloidal energy without equal contributions of even and odd modes. The contributions are rather weak in amplitude compared to zonal flows ($m = 0$), but they are crucial for the dynamo to operate.

The radial magnetic field (figure 3.8) shows the same hemispherical configuration as the radial flow, both are more or less confined to the southern hemisphere. This is reflected in the magnetic energy spectra (figure 3.9, lower plots). The poloidal energy shows a rather flat spectral distribution of the degrees l, leading to a hemispherical magnetic field. The unperturbed reference case with $g = 0\%$ (figure 3.6, bottom left) is clearly dominated by the axial dipole mode, therefore it is equatorially antisymmetric. The toroidal energy of the hemispherical dynamo (figure 3.9, bottom right) shows the clear axisymmetry ($m = 0$), and also the hemisphericity is depicted in the flat l-distribution. We refer here again to figure 3.7, for zonal averaged plots of the poloidal field lines and toroidal field.

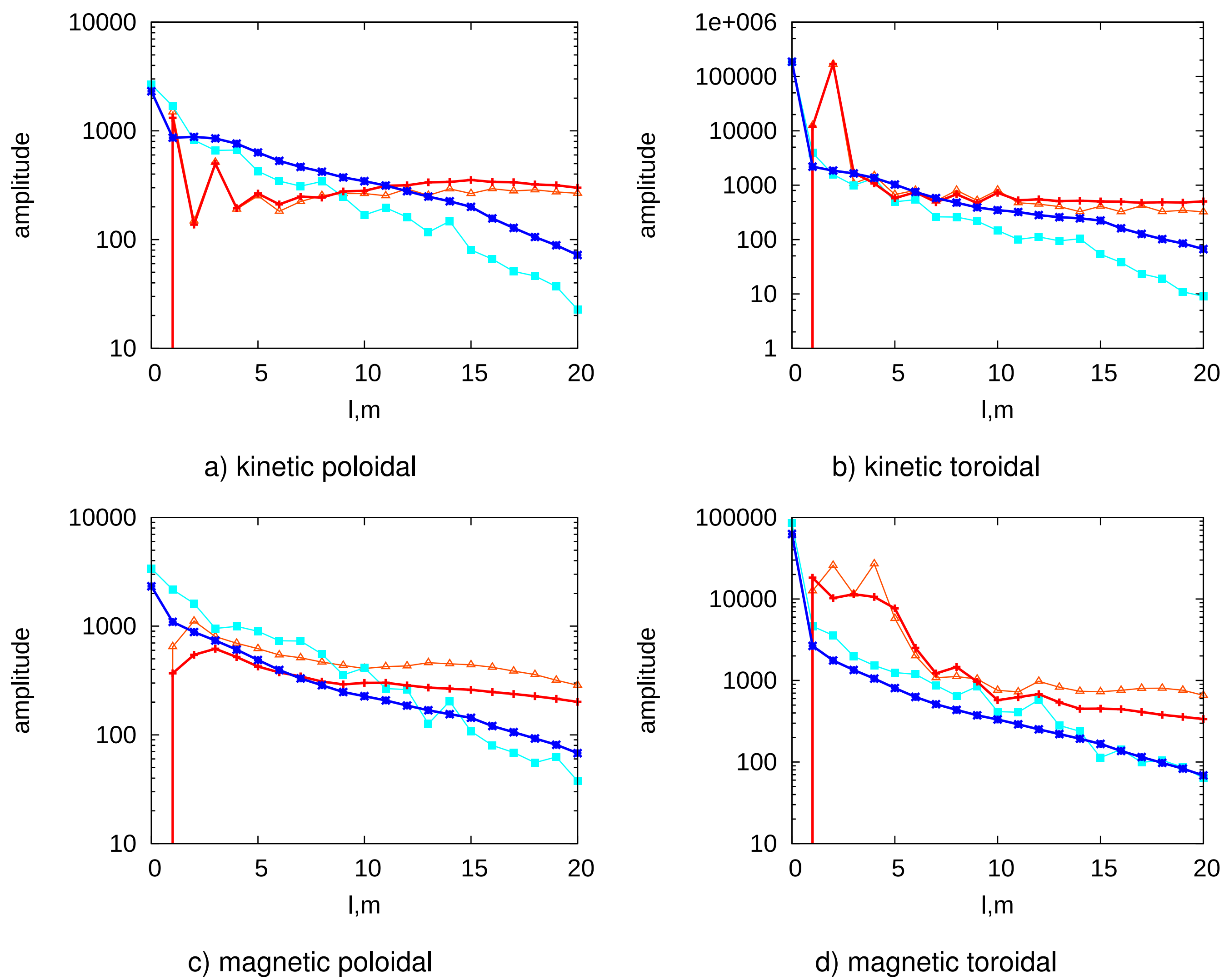

Figure 3.9: Spectra of kinetic (upper) and magnetic energy (lower) energy. The plots on the left side show the poloidal contribution, whereas those at the right side describe the toroidal energy. In each plot, the snapshot spectra are given in the thin faint lines (light blue order m, orange degree l) and the time averaged energy spectra thick lines (dark blue order m, red degree l).

3.3.2 Variable Heat Flux Anomaly Amplitude

Here we want to address the question what is the response of the dynamo for CMB heat flux anomalies of different amplitudes g. It is of special interest to what extent smaller values of g effect the system. Increasing the perturbation from $g = 0\%$ up to 300% as used in Stanley et al. (2008), shows a clear transition from the columnar towards the EAA convective state. We had seen, that investigating the symmetries of the convection yields a measure for the relative strength of the EAA convection.

Figure 3.10 tries to compile our findings for amplitude of the EAA convection as function of the anomaly amplitude g. In the first plot we distinguish the symmetries of axisymmetry (as, red), equatorial antisymmetry (eas, green) and equatorially antisymmetric and axisymmetric parity (eaa, blue). Furthermore we test how the total kinetic (top panel), toroidal (middle) and poloidal (bottom) energy are affected. All curves are normalized to the total kinetic/toroidal/poloidal energy. In the $g = 0\%$-reference state the EAA symmetry contributes only little to the kinetic energy. Nearly all the kinetic energy is nonaxisymmetric and equatorial symmetric, what is typical for the convective columns. Adding the perturbation increases the equatorial antisymmetry and axisymmetry in toroidal and total kinetic energy more or less linearly. The effect on the poloidal energy is much weaker, even though the equatorial antisymmetry rises. At a perturbation amplitude of around $g = 60\%$, the system is saturated at $EAA = 0.8$ in the new convective mode. The relative strength of the EAA mode can not reach one, since there is always non-axisymmetric (convective) poloidal motions involved. The system is remarkably axisymmetric due the dominance of the strong thermal winds. At higher g the axisymmetry remains strong at 90% of the total energy, but the equatorial antisymmetry decrease and thus the EAA contribution as well. The shear layer between the two zonal flow cells moves southward at higher g and thus reduces the equatorial antisymmetry. The effect on the poloidal energy is minor, although the equatorial antisymmetry reaches roughly 55%.

The absolute amplitudes of the kinetic energy (red - total, green - toroidal, blue - poloidal) and symmetries (as in the upper plot) are shown in the lower plot of figure 3.10. It shows the onset of very strong zonal flows (axisymmetric toroidal flows), thus most of the energy added to the system due to boundary forcing is translated into thermal winds. The axisymmetric toroidal kinetic energy exceeds the poloidal by far and seem not to saturate for high g.

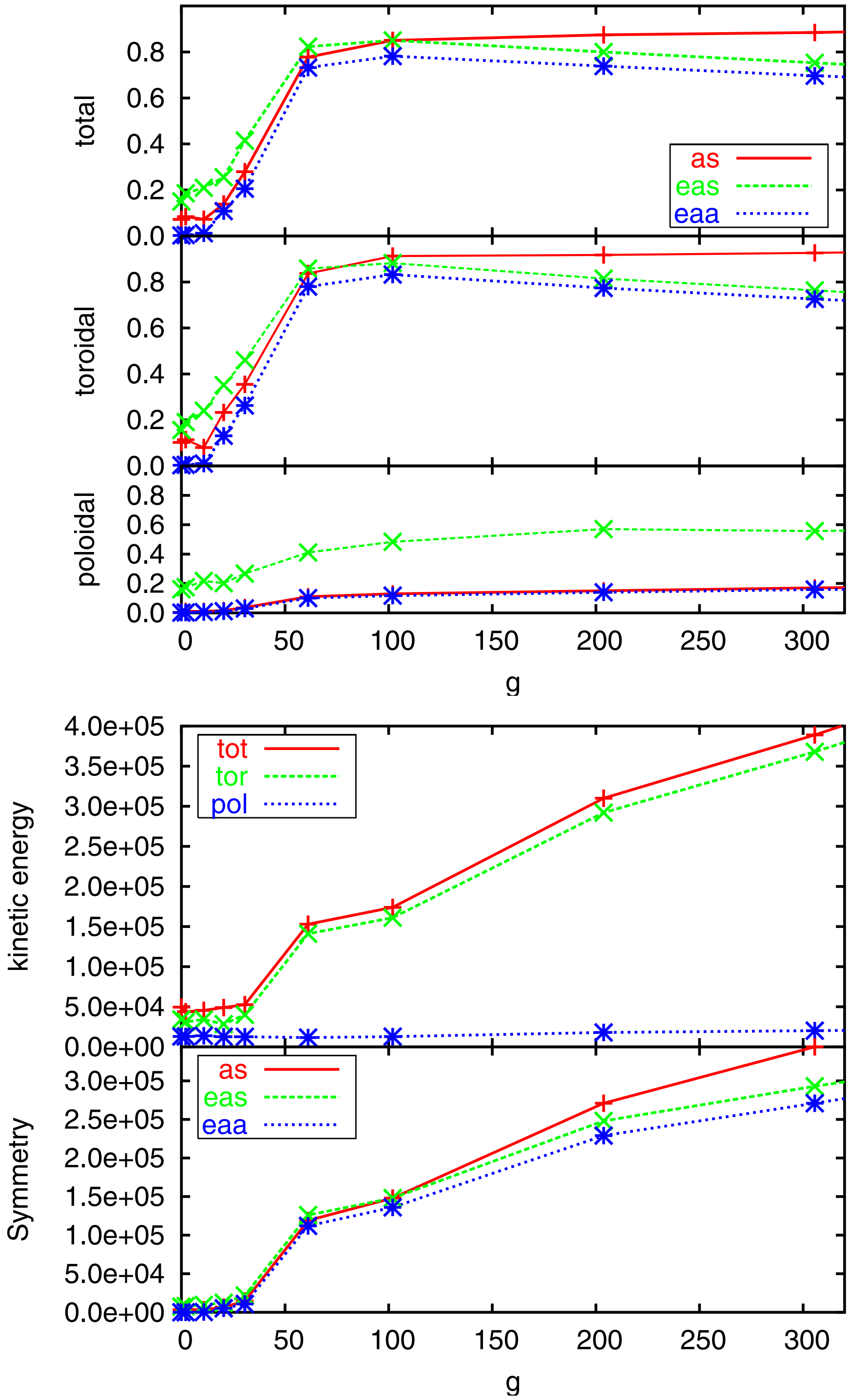

Figure 3.10: Symmetries and amplitude of total kinetic energy and toroidal/poloidal contributions as a function of g. In the upper compilation of plots, the relative amount of axisymmetry (red), equatorial antisymmetry (green) and the combined symmetry (EAA, blue) for the full kinetic energy (first panel), the toroidal and poloidal contributions (second and third panel), whereas in the lower plot the total kinetic energy (top panel, red), toroidal (green) and poloidal (blue) and the symmetries (as in the upper plot) are given. Details see text.

3.4 Dynamo Mechanism

The two distinct modes of convection are inducing magnetic fields of different magnetic field strength and morphology. We defined the magnetic Reynolds number $Rm = UD/\lambda$ as the crucial quantity for dynamo action. Thus $Rm = Re\,Pm$ serves as measure for the flow amplitude and we use the Elsasser number $\Lambda = B^2/\mu_0\lambda\rho\Omega$ as measure for the rms magnetic field amplitude. See section 2.6 for details on the nondimensional control and output quantities. Figure 3.11 shows that the rise in the magnetic Reynolds number Rm, that goes along with toroidal flow amplitude, does not necessarily lead to higher Elsasser numbers. Hemispherical convection yields a less efficient dynamo. The rms Elsasser number Λ increases at small perturbation amplitudes g, but decreases from $\Lambda = 10$ at $g = 25\%$ to $\Lambda < 1.5$ at $g < 200\%$, where the EAA convection is isolated.

The discussion of the EAA convection showed that poloidal flows, which are important for the magnetic field induction, are confined to the southern hemisphere and thus concentrate the poloidal magnetic field there. When we discussed the induction process in the benchmark or reference dynamo (see section 3.2), we linked the presence of helical flows to the induction of magnetic field. Helical flows are exclusively poloidal flows, but also the toroidal flow can create magnetic field. Here we will compare the induction process in the hemispherical convection, with a classical columnar dynamo from our reference case. Typically rotation dominated spherical convective flow motions are organized in columns parallel to the rotation axis. The flow motion around and along the convective columns leads to a helical (spiraling) flow, and is therefore the main source of magnetic field. These helical motions twist magnetic field lines and increase the magnetic energy due to electromagnetic induction. This process is called α-effect (Rüdiger and Hollerbach 2004) and converts poloidal into toroidal field and vice versa. But the toroidal has exclusively another source, that is differential rotation or shearing. A poloidal field line is stretched into the direction of the zonal flow, where azimuthal toroidal field is created via this so called ω-effect if there are strong gradients in the zonal flow. This is thought to be the main driver of the toroidal magnetic field of the sun (Rüdiger and Hollerbach 2004), where strong differential rotation shears the poloidal field. For our hemispherical convection, we found strong equatorially antisymmetric zonal flow, thus strong gradients between them. Actually the thermal wind balance translates latitudinal temperature gradients into zonal flow gradients. Therefore it is quite useful to distinguish the magnetic field components of toroidal and poloidal field here. A successful dynamo permanently converts poloidal into toroidal magnetic energy and vice versa. The helical flows, in terms of the α-effect, are capable of create both field components. In systems with strong zonal flow, the toroidal field can be additionally created in axisymmetric flow shear, known as the ω-effect. Typically the α-effect (helical flow) dominates when the convection is columnar (Wicht and Aubert 2005). We measure the relative importance of the ω-effect by calculating the relative production of axisymmetric toroidal field in axisymmetric shear layers in terms of

$$\omega^* = \frac{\left[(\boldsymbol{B}\boldsymbol{\nabla})u_\phi^{as}\right]_{tor}^{rms}}{\left[(\boldsymbol{B}\boldsymbol{\nabla})\boldsymbol{u}\right]_{tor}^{rms}} \,. \tag{3.13}$$

Parallel to the emergence of the zonal flows as the main effect of the heat flux anomalies, the induction of axisymmetric toroidal field via shear is enhanced. We compiled

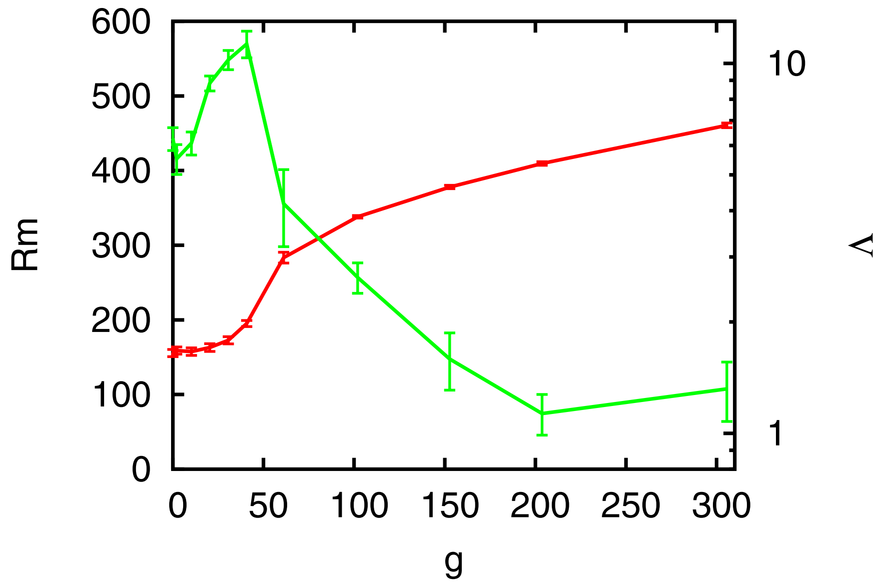

Figure 3.11: Flow amplitude in terms of the magnetic Reynolds number (red) and magnetic field strength in terms of Elsasser number (green) as function of the CMB heat flux anomaly amplitude g, shows the difference between both dynamo regimes in the efficiency of inducing a dynamo. The hemispherical solution contains large amounts of axisymmetric zonal flows created by the Coriolis force, therefore the kinetic energy is drastically larger than in the columnar regime (g = 08). The magnetic energy decreases, the more the g increases. The error bars correspond to the standard deviation due to time variability.

figure 3.12 similar as figure 3.10, thus showing the symmetries and amplitudes of the different magnetic field contributions. Figure 3.12, top plot shows the relative axisymmetry of the total (top panel) and toroidal magnetic field (2nd panel). The axisymmetry reaches 80% at an perturbation amplitude of $g = 100\%$. Even higher perturbations introduce more non-axisymmetric field contributions due to the enhanced small scale irregular convective motions close to the southern pole. Like for the kinetic energy the poloidal contribution of the magnetic energy is much less affected, but the equatorial antisymmetry nevertheless nearly doubles (figure 3.12 upper plot, lower panel, green). This is expected, since the convection and thus the radial upwellings are confined to one hemisphere. Besides, the poloidal field does not show strong axisymmetry (same plot, blue), what is again the impact of the small scale convection in the south polar cusp. The increase of magnetic field energy at small g is due to the supportive ω-induced toroidal field. Interestingly the magnetic fied is dominated by axisymmetric toroidal field, in analogy to the kinetic energy, where the main contribution are the axisymmetric thermal winds.

Since the classical (equatorial symmetric) convective columns are weakened and pushed towards the pole of higher heat flux, the efficiency of inducing poloidal and toroidal field via an α-effect is reduced. Therefore both magnetic field contributions decrease simultaneously as the perturbation amplitude g and thus the hemispherical convection increases.

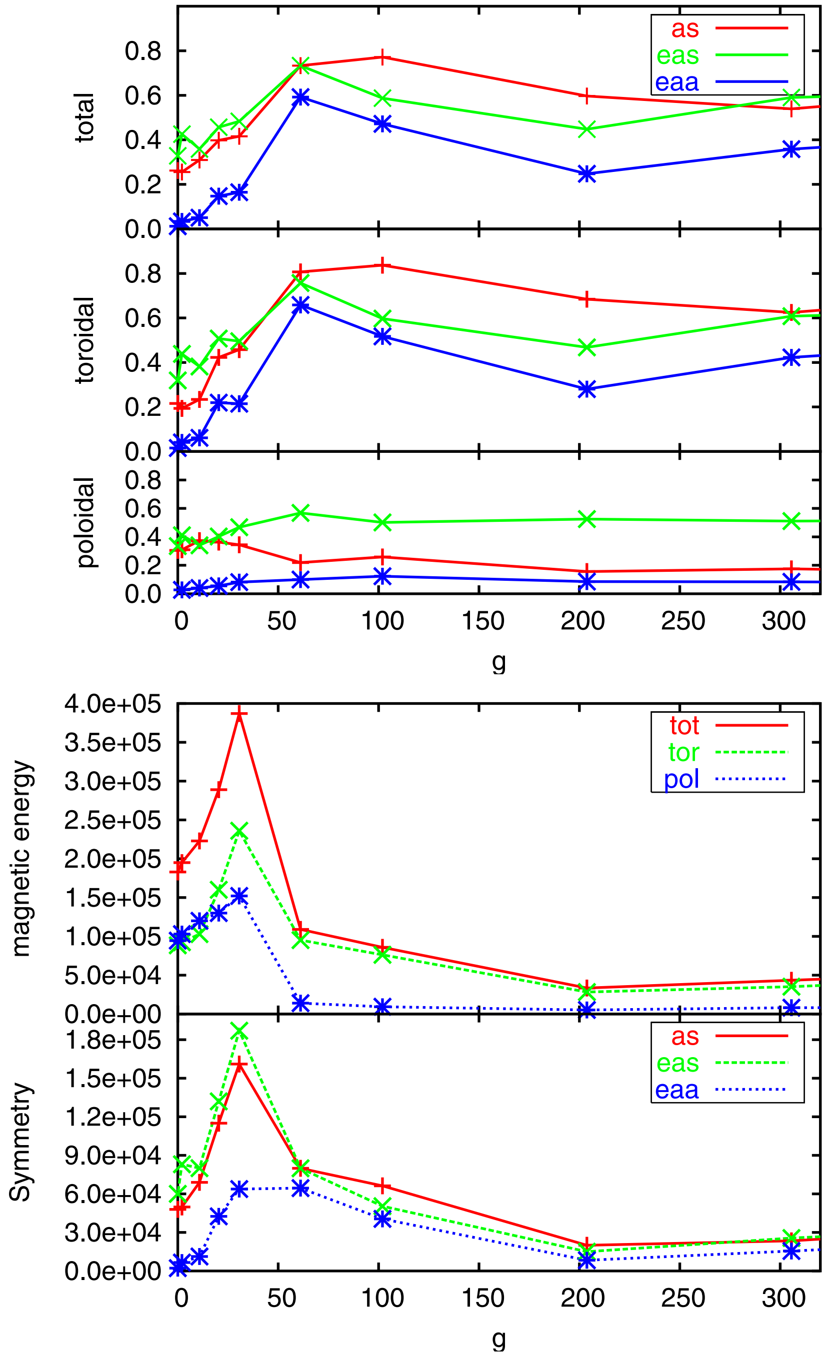

Figure 3.12: Symmetries and amplitude of total magnetic energy and toroidal/poloidal contributions as a function of g. In the upper compilation of plots, the relative amount of axisymmetry (red), equatorial antisymmetry (green) and the combined symmetry (EAA, blue) for the full kinetic energy (first panel), the toroidal and poloidal contributions (second and third panel), whereas in the lower plot the total kinetic energy (top panel, red), toroidal (green) and poloidal (blue) and the symmetries (as in the upper plot) are given. Details see text.

The supportive induction of toroidal field via shear between the two zonal flow cells helps to promote a strong axisymmetric toroidal field. Figure 3.12 shows the dependence of the magnetic energy contributions (top plot) as a function of g. When the hemispherical convection dominates at larger g, toroidal (green) and poloidal (blue) fields are weaker than in the columnar convection. At mild g up to 40% the coexistence of columnar and hemispherical convection effects lead to a rise in magnetic energies, which is accompanied by strong variations of the magnetic energy we further discuss below. The main effect of the hemispherical solution is a growth of the axisymmetric toroidal magnetic energy, see figure 3.12, as a function of g. The relative equatorial antisymmetry also increase, but to a smaller degree. It might be a better measure to investigate the hemisphericity of radial flow and field, instead of the equatorial antisymmetry. The latter one is dominant in the toroidal flow and field, thus the minor contributions of poloidal flow and field do not affect the strength of EAA convection and induction to a large extent. However, we will later analyse the hemisphericity of the radial magnetic field in greater detail, when applying the magnetic field solutions to the crustal magnetization of Mars.

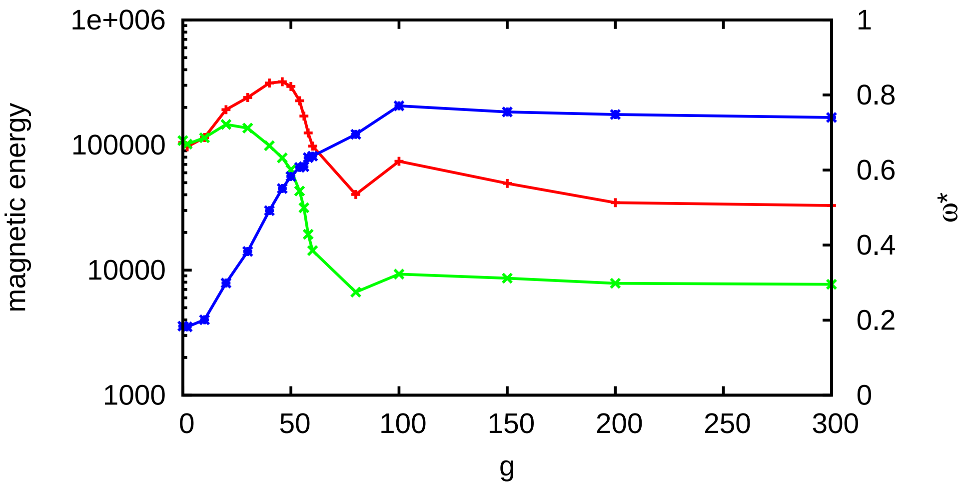

Figure 3.13: Toroidal (dashed) and poloidal (solid) magnetic field in nondimensional units and the relative ω-effect in terms of ω^* (dotted) as a function of g demonstrates the transformation of induction characteristic from an α^2-dynamo at g = 0 (columnar dynamo) towards an $\alpha\omega$-type from g = 60 (hemispherical solution).

Dynamos are classified as α^2 and $\alpha\omega$ type according to main induction process for the toroidal field (Rüdiger and Hollerbach 2004). Figure 3.13 illustrates how ω-field-induction changes with the heat flux perturbation amplitude g. To measure that effect, we calculate the induction of toroidal magnetic field due to zonal winds and normalize it with the total toroidal field induction (equation 3.13). This resulting relative omega effect ω^* is shown in figure 3.13. The figure shows, that dynamos with columnar convection are mainly of α^2-type since the ω-effect is rather small. The reference case, $g = 0\%$, here was chosen to be a good example of that α^2 induction, as described in Olson et al. (1999). Note, both poloidal and toroidal magnetic field are crucially dependent on each other since the dynamo permantly converts one to the other. Figure 3.7 showed both field contributions are closely aligned. The induced toroidal magnetic field can not grow further even if there is such an extremely efficient induction mechanism. The growth of the toroidal field is limited by the amount of poloidal field feed into the shear zone around the equator. As the thermal winds increase for larger g the associated ω-effect starts to dominate toroidal field production (see figure 3.13) and the dynamo is predominantly of an $\alpha\omega$-type. Since there is always toroidal field created by the supporting α-effect, some toroidal field induced by α-effect always remains. For the further analysis it might be useful to distinguish between $\alpha\omega$ and $\alpha^2\omega$ dynamo types. We will discuss that issue while discussing the Parker waves (see section 4).

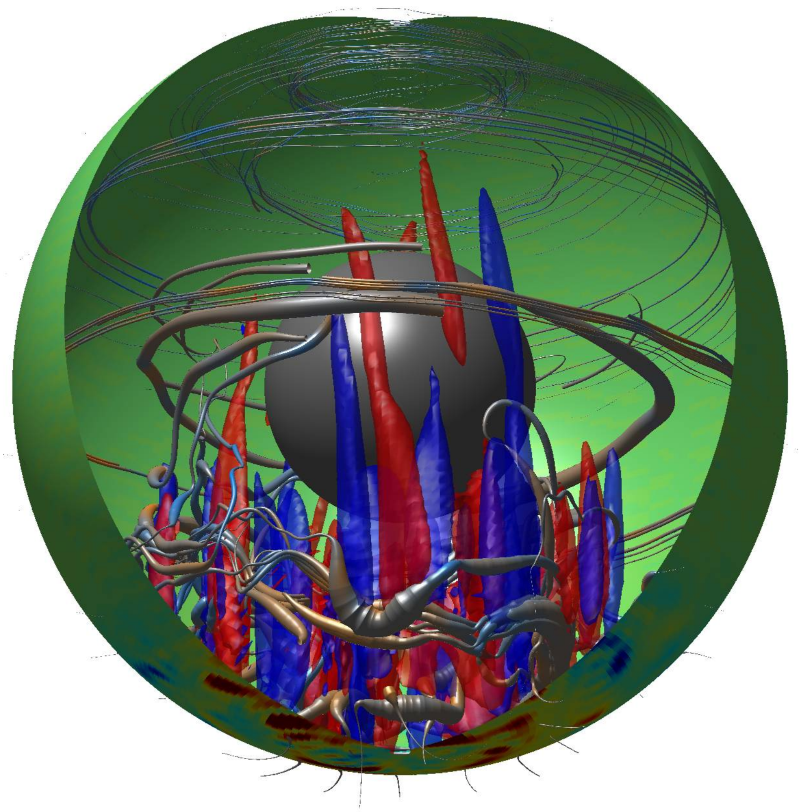

Figure 3.14: 3D visualization of the induction process. Blue/red isocontours of the radial flow (inward/outward), magnetic field lines scaled by the magnetic energy. Furthermore the radial CMB field is shown color coded on the green spherical shell. Rendering by J. Wicht, based on the VMagic tool by M. Meyer.

Figure 3.14 clarifies the dynamo mechanism in a 3D rendering. Magnetic field lines illustrate the magnetic field configuration, their thickness is scaled with the local magnetic energy. Red and blue color intensities indicate the relative inward and outward radial field contribution. Plain gray lines are purely horizontal. Red and blue transparent surfaces are isosurfaces and show inward and outward directed radial plume-like motions. Note, how strong axisymmetric field is produced by zonal flow shear somewhat below the equatorial plane. The northern hemisphere is dominated by axisymmetric toroidal magnetic field, while radial field is associated to plume-like up- and downwellings dominating the southern hemisphere.

3.4.1 Influence of the Lorentz Force

In this section we will investigate the influence of the Lorentz force on the EAA convection. The saturation of the magnetic field growth is given by the action of the Lorentz force on the convection (Roberts 2007). As the main feature of the hemispherical convection and induction, the axisymmetric toroidal contribution of flow and field dominate the energies. Hence both are mainly parallel one would expect the Lorentz force not to have a strong influence on the dynamics. In figure 3.11 we compared the amplitude of the kinetic energy in terms of the magnetic Reynolds number *Rm* and the magnetic energy in terms of the Elsasser number Λ. Additionally we added the standard deviation as error bars reflecting the time dependence of flow and field. Interestingly, the hemispherical magnetic field does show much stronger time variability. The kinetic energy is mainly time invariant. We track the time evolution of the magnetic and kinetic energy in figure 3.15. The top plot refers to moderately perturbed case with $g = 60\%$, where as the lower plot shows $g = 100\%$. In each plot the top panel shows the relative strength of the *EAA* convection (red) and relative shear induced toroidal field production ω^* in blue. The panels for the magnetic (2nd) and kinetic energy (3rd) give the total (red), toroidal (blue) and poloidal (green) contribution to the respective energy. If in the upper plot of figure 3.15, the magnetic energy is low the EAA strength and ω^* is reduced, whereas the kinetic energy increases for both the poloidal and the toroidal contribution. The two magnetic contributions (same figure, middle panel of upper plot) are aligned during the variation cycle. This reflects that the total magnetic energy simply goes up and down. If the magnetic energy is large, the flow is more EAA dominated and ω^* is larger. We interpret this behavior, such that the strong (and mainly toroidal) magnetic field suppresses the convective columns. Thus a strong magnetic energy leads to weaker convection, hence to weaker magnetic field. If the magnetic field is weak, the stronger columnar convection provides more magnetic field. EAA strength and ω^* increase linearly, where the systems tends to be more in the hemispherical solution. Thus the azimuthal magnetic field is again stronger in suppressing the radial flow in the equatorial region and cycle starts over again. For the stronger perturbation of $g = 100\%$ (figure 3.15, lower plot) the variations in kinetic and especially magnetic energy are not anymore visible. The EAA mode remains constant, whereas the ω^* varies faster. The total magnetic energy is also rather constant, therefore the effect on the flow is minor.

To proof the hypothesis of the Lorentz force reducing the strength of the convective columns, we compare in figure 3.16 radial flows in mid-depth for states of weak and strong magnetic field energy to a nonmagnetic run. Figure 3.16 shows the solution at maximal (top row) and minimal (middle row) magnetic energy. At the minimum columnar convection is still significant, while it seems to be suppressed by the Lorentz force at the maximum of magnetic energy. The equatorial slices of z-vorticity (2nd column of the same figure), azimuthal field (3rd column) and axisymmetric azimuthal field show how the Lorentz forces weakens the convective columns. By suppressing columnar convection the Lorentz force promotes the relative importance of the hemispherical mode. Note, we

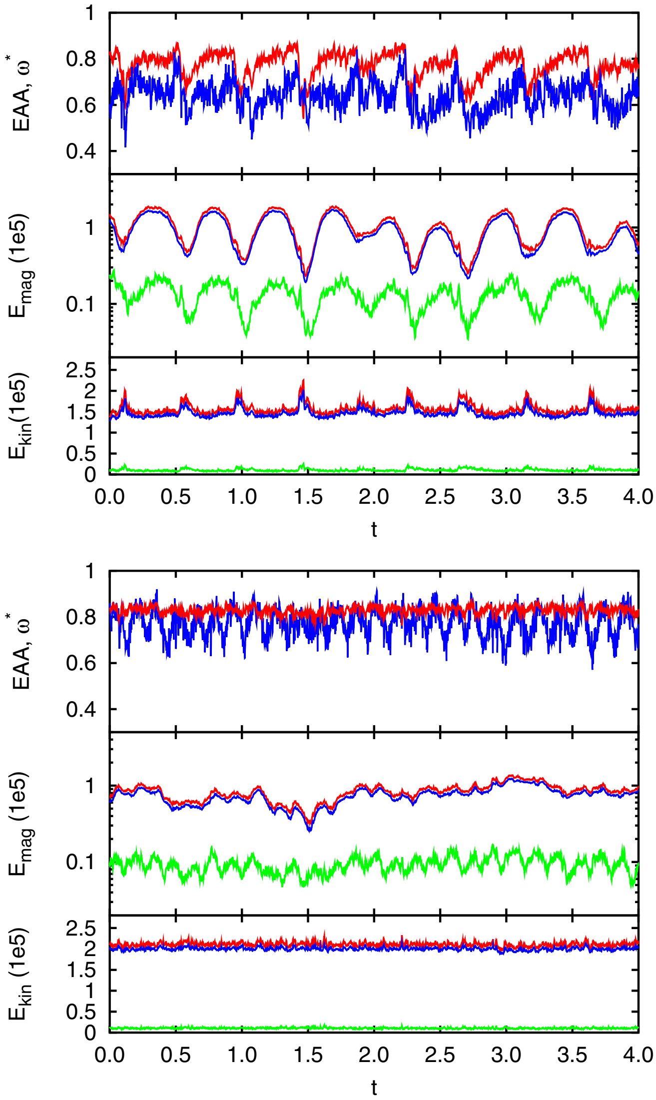

Figure 3.15: Time evolution of the oscillatory regime. Shown is the in the top panel the relative amount of EAA symmetry (red) and the relative amount of ω-induced toroidal field (blue). Middle and bottom panel, show the total amount (red), toroidal (blue) and poloidal (green) contributions for the magnetic and kinetic energy, respectively. The first plot shows the oscillations for g = 60% case, whereas the lower plot describes the g = 100% case.

can see here already that the toroidal field changes polarity during one of magnetic cycle. Toroidal field of one polarity diminishes, and toroidal field of inverse polarity is created. This effect becomes more apparently when comparing the relative importance of the EAA mode in magnetic and non-magnetic simulations.

Figure 3.17 shows the time average of the EAA strength and illustrates that this relative importance is around 35% higher for the magnetic case (red) than in the nonmagnetic (green). The difference reduces for perturbations stronger than $g = 150\%$, where the magnetic energy is anyway weaker. The fact, that these oscillations are not found in the

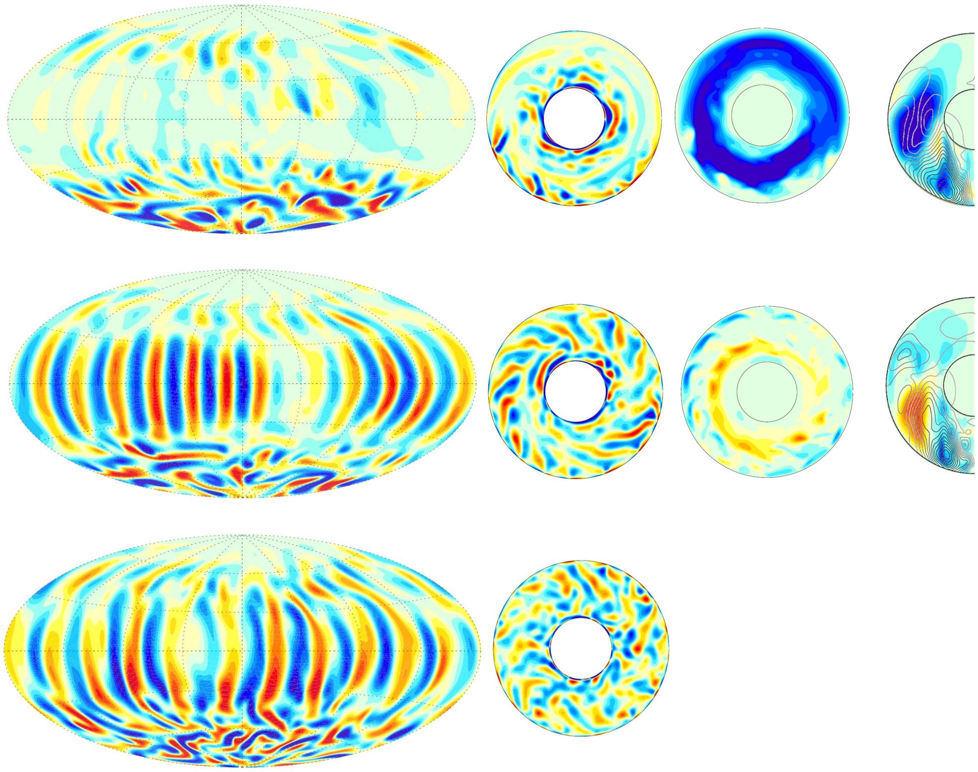

Figure 3.16: Radial flow at mid-depth (first column) for a case of strong (top row) and weak magnetic field amplitude (middle row) and the non magnetic (bottom) case. Additionally, the z-vorticity and the azimuthal field at equator (middle columns) and the zonal average toroidal field (right column) is plotted.

non-magnetic case highlights their magnetic origin. The variations in the flow are then mainly due to variations in the Lorentz force. Landeau and Aubert (2011) mentioned the emergence of magnetic energy variations for intermediate strength of EAA convection. Note, they used no boundary forcing in terms of CMB heat flux pattern. We can confirm their findings, even though we will interpret them differently in the next section.

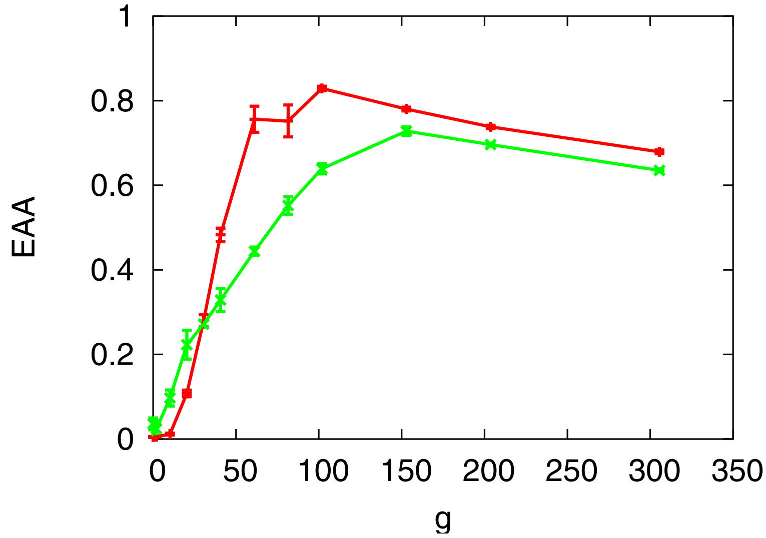

Figure 3.17: Effect of the Lorentz force on the relative strength of the axisymmetry and equatorial antisymmetry of the kinetic energy shows a clear support of the EAA mode if the Lorentz force is present (Pm=2, red line) in comparison to a non-magnetic case (Pm=0, green). The time variability is given as standard deviation.

3.4.2 Oscillations

We had seen in figure 3.16 that the toroidal field might change its polarity. If so, also the poloidal field has to reverse. Therefore we track the time evolution of the amplitudes of the axisymmetric modes of the poloidal field at the CMB. Figure 3.18 illustrates the changes of the temporal evolution for the poloidal magnetic field when the CMB heat flux perturbation is increased. The decomposition of the magnetic field is motivated by the Gauss coefficients, since we will make further use of them while extrapolating the field radially outwards towards the planetary surface in order to apply the hemispherical dynamo to the crustal magnetization. The Gauss coefficients are proportional to the amplitude of spherical harmonics mode. The derivation and discussion of the Gauss coefficients can be found in section 5.1. We concentrate on axisymmetric Gaussian coefficients here due to highlight the evolution of hemisphericity. The nonaxisymmetric part of the poloidal CMB field does not show the cyclic oscillations. In the reference case (top plot of figure 3.18) the axial dipole dominates, varies chaotically in time and never reverses. At the perturbation amplitude of $g = 50\%$ (second plot) the relative importance of the axial quadrupole component has increased significantly, which indicates the emergence of a hemispherical magnetic field.

Another small increase of the perturbation amplitude to $g = 60\%$ (third plot), where the hemispherical convective mode is now dominant, all magnetic field harmonics oscillate in time with a period of roughly half a magnetic diffusion time. Interestingly at this perturbation amplitude the first five axisymmetric poloidal modes are equal in amplitude. When further increasing the perturbation amplitude, the frequency of this oscillations increases and the relative importance of higher harmonics increase as well. Considering the

$g = 60\%$ case, the coefficients oscillate roughly in phase, which implies that the magnetic energy varies significantly. Figure 3.15 demonstrates, that these oscillations correlate with variations in the importance of the EAA mode and the magnetic energy. We now understand why the absolute magnetic energy reaches a maximum around $g = 40\%$. The combination of the efficient poloidal field production by columnar convection and the toroidal field production by zonal wind shear leads to particularly high magnetic energy and increased time average amplitude (see figure 3.12).

At $g = 60\%$, the production of toroidal field in the zonal wind shear dominates. The associated Lorentz forces then suppress the columnar convection and thereby an important contribution of poloidal field production. At higher perturbation amplitudes the magnetic oscillation is still recognizeable but has a smaller period of roughly one eighth of the magnetic diffusion time and is blurred by other time dependencies. The variation in magnetic energy, in kinetic energy and relative EAA importance are less affected than for the moderate $g = 60\%$ case, as shown in figure 3.15, bottom plot.

To sum up, the stationary dipole dominated dynamo turned into a regularly reversing hemispherical dynamo if a CMB heat flux anomaly of sufficient amplitude is applied. Dynamos with strong ω-effect tend to be oscillatory (Rüdiger and Hollerbach 2004), so it might be expected that the increasing importance of a shear induced toroidal field leads into a oscillatory dynamo with regular magnetic polarity inversions.

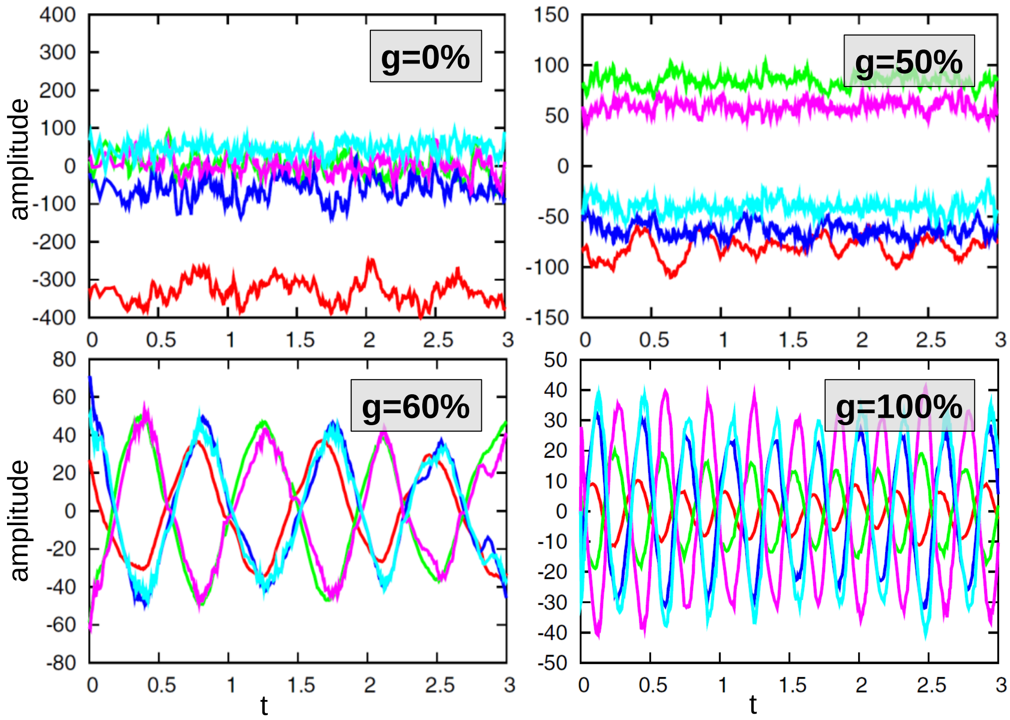

Figure 3.18: Time evolution of the first axisymmetric Gauss coefficients taken at the CMB for the dipole dominated (g = 0%, 50%) (first two plot in upper row), the oscillatory (g = 60%, bottom left) and the reversing hemispherical regime (g = 100% bottom right). The more hemispherical the dynamo becomes, the more equal are the amplitudes of the higher modes with respect to the weakened dipole mode. This is a typical spectral behavior for a hemispherical dynamo. Surprisingly all coefficients do oscillate with a slight phase shift in the hemisperical regime. Red - l = 1, green - l = 2, blue - l = 3, pink - l = 4, light blue - l = 5, yellow - l = 6, black - l = 7.

3.5 Equatorial and Inclined Anomalies

The heat budget of the core is entirely controlled by the overlying mantle. The CMB heat flux pattern is shaped by convective mantle processes or impacts. Until now, we always assumed that the simplified degree-one CMB heat flux anomaly is aligned with the axis of rotation. The position or orientation of thermal anomalies in the mantle, such as due to low-degree mantle convection or impacts, is rather unconstrained. Therefore we have to test the influence of inclined CMB heat flux anomalies. In the related study of Amit et al. (2011) the heat flux anomaly was tilted away from the axis of rotation. The authors compared a 45° inclined and an equatorial anomaly. They find that for the inclined anomaly the hemispherical convection emerges same as for the axial perturbation (Amit et al. 2011). Here we will systematically tilt the anomaly from a orientation aligned with the axis of rotation up to an equatorial heat flux anomaly.

3.5.1 Arbitrary Tilting Angles

Since a degree (l=1, m=0) shaped anomaly is a rather special case, we systematically vary the tilting angle α (see eq. 2.89) of the perturbation up to 90 degrees. In terms of spherical harmonics, different tilting angles are prescribed as a linear combination of (l=1, m=0) and (l=1, m=1) modes according to equation 2.92. The equatorial perturbation of $\alpha = 90°$ corresponds then to the pure (l=1, m=1) pattern. Note, that the axial perturbation with $\alpha = 0°$ is still axisymmetric, but equatorial antisymmetric. But the equatorial perturbation of $\alpha = 90°$ is equatorial symmetric, but axisymmetric. All anomalies with tilting angles smaller than 90° and larger than 0° are nonaxisymmetric and equatorial asymmetric.

The figure 3.19 shows the relative strength of the EAA symmetry as a function of the perturbation amplitude for various tested tilt angles. It demonstrates that the hemispherical mode dominates up to $\alpha = 80°$. Only the $\alpha = 90°$ shows a new behavior where the strength of the EAA mode remains negligible. Also the magnetic energy (figure 3.19, bottom plot) shows the similar behavior as for an axial perturbation. Note, that there was no dynamo solution found for a tilting angle of $\alpha = 60°$ and $g = 60\%$. Slight breaking of north-south symmetry obviously suffices to strongly excite the new hemispherical convective mode prescribed above. Consequently, a breaking of equatorial symmetry of the CMB heat flux affects the systems more severely than breaking the axisymmetry. Only the purely equatorial (l=1, m=1) perturbation forms a rather special case, that we describe in the following section.

3.5.2 Equatorial Anomaly

Increasing the relative perturbation amplitude g for the equatorial anomaly leads to a rise in the flow amplitude (see figure 3.20, red). Like in the (l=1, m=0) case the kinetic energy increases with growing perturbation amplitude. And once more the rise is mainly carried by growth of toroidal energy. The magnetic energy has a distinct minimum around $g = 50\%$ and $g = 100\%$. Interestingly there the magnetic field reverses rather periodically with a period of half the magnetic diffusion time. This oscillation might have the same origin as the oscillations observed for the axial perturbations, at least the frequencies are rather similar and increase with the perturbation amplitude. Surprisingly the magnetic field oscillations disappear for perturbation amplitudes larger than $g = 100\%$. Therefore the time averaged magnetic energy in terms of the Elsasser number (figure 3.20, green) is significantly higher at $g = 200\%$. In case of the oscillations found for the axial perturbations we could relate the onset of their onset with the increasing amount of toroidal field induced by an ω-effect thus with the presence of flow gradients. This does not seem to be true here, since the $g = 200\%$-case has a larger ω^* of roughly 24%, whereas for the two reversing cases we find $\omega^*(g = 50\%) \approx \omega^*(g = 100\%) = 21\%$. Additionally the oscillations on the axial perturbation case set in when ω^* reached 60%, hence a much larger value. It remains unclear, why the oscillations set in for moderate perturbation amplitudes and disappear again for strong perturbation.

For convenience, we name the more and less efficiently cooled hemispheres western and eastern, respectively. As expected, the imposed heat flux pattern leaves the eastern hemisphere hotter than the western. This difference drives a large scale westward directed flow and a more confined eastward flow in the equatorial region of the outer part of the

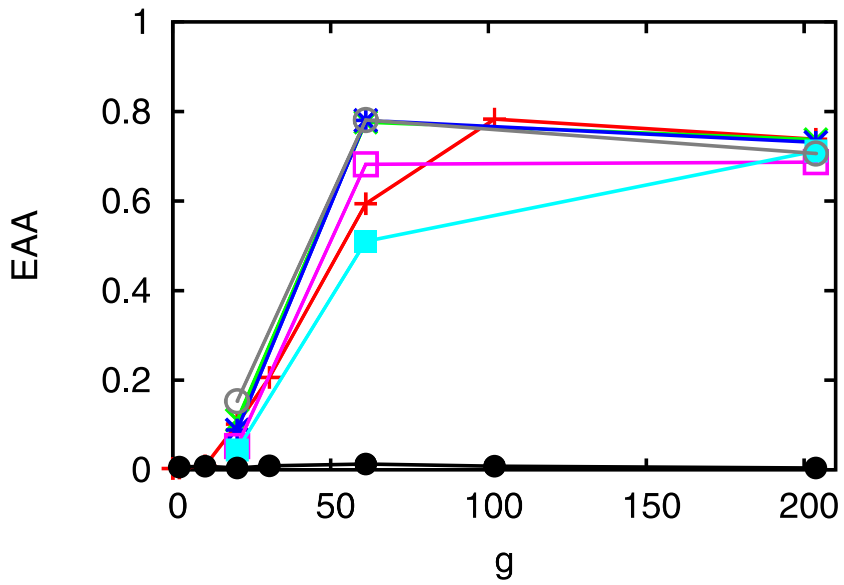

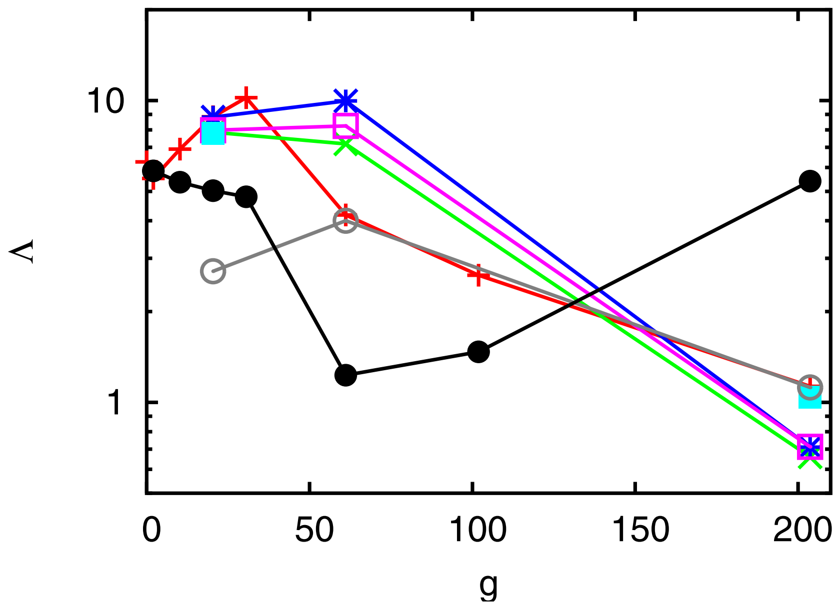

Figure 3.19: The relative equatorial antisymmetric axisymmetric energy for different tilting angles follows the onset of EAA convective mode in the axial perturbation case (red). For the equatorial perturbation (black) the EAA contribution to total kinetic energy remains Zero. Green - 10°, blue - 30°, Pink - 45°, light blue - 60°, gray - 80°

shell (figure 3.21). Coriolis forces divert the westward directed flow poleward and inward, and lead to the confinement of the eastward directed flow. Consequently, the westward flow plays the more important role here.

Figure 3.22 illustrates the solution in a snapshot (left column) and time averaged (right

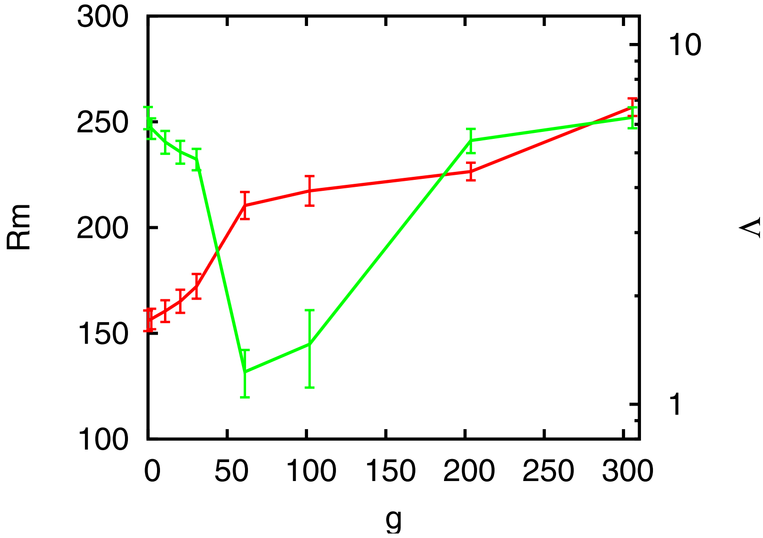

Figure 3.20: As figure 3.11 but for the equatorial perturbation.

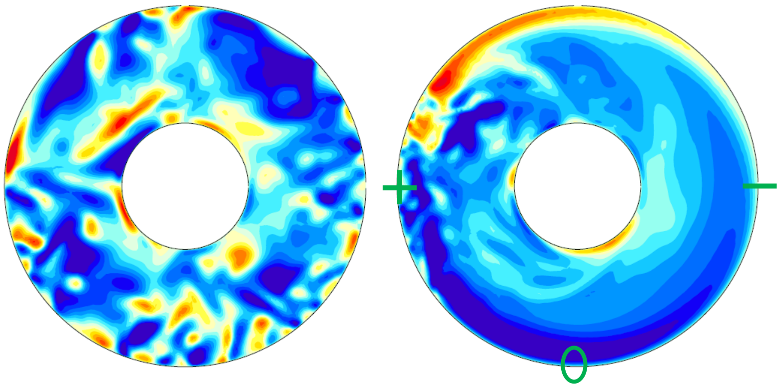

Figure 3.21: Equatorial slice of u_ϕ for the homogeneous reference case (left) and the equatorial heat flux anomaly (right). The marks '+', '-' and '0' denote maximal, minimal and zero perturbation amplitude.

column) over roughly a magnetic diffusion time for a perturbation amplitude of 200%. We collect spherical surfaces of the radial and temperature at the CMB in the top plots, and the three components u_r, u_ϕ, u_ϑ and z-vorticity at mid-depth (see figure 3.22). The diverted flows feed two distinct downwelling features, which are best identified in the time average flow and correlate with the coldest temperatures. Right at the latitude of zero heat flux disturbance a pair of downwelling forms close to the tangent cylinder. The second important downwelling region is located close the to maximum heat flux. Eastward directed backflows connect the second and the first feature at higher latitudes and additionally feed the downwellings close to the tangent cylinder. The time averaged flows form two main cyclonic structures illustrated with the z-vorticity in figure 3.22.

A long anticylonic structure associated to the strong equatorial westward flow stretches nearly around the globe and connects the equator with high latitudes inside the tangent cylinder. A smaller cyclonic feature is owed to the eastward equatorial flow.

The comparison of snapshots and the time averages (see figure 3.22) shows that at any instance in time the flow is significantly more complex than the time average. Several classical convective columns are located beneath the region of increased heat flux but are absent in the opposite hemisphere, where up- and downwellings are mainly located at higher latitudes. These smaller scale features vary strongly and therefore average out over time.

The snapshot and time averaged radial magnetic fields shown in figure 3.22 are rather similar which demonstrates that the time dependent small scale convective features are not very efficient in creating larger scale coherent magnetic field. The radial field is strongly concentrated in patches above flow downwellings where the associate inflows concentrate the background field (Olson et al. 1999). Like in the study for dynamos with homogeneous CMB heat flux by Aubert et al. (2008b) the anticyclone is the main player in poloidal magnetic field production. The cyclone gives the field another twist and thereby is responsible for the pair of inverse (outward directed here) field patches located at mid latitudes in the western hemisphere. The exceptional strength of the high latitude normal flux patches suggests that additional field line stretching further intensified the field here.

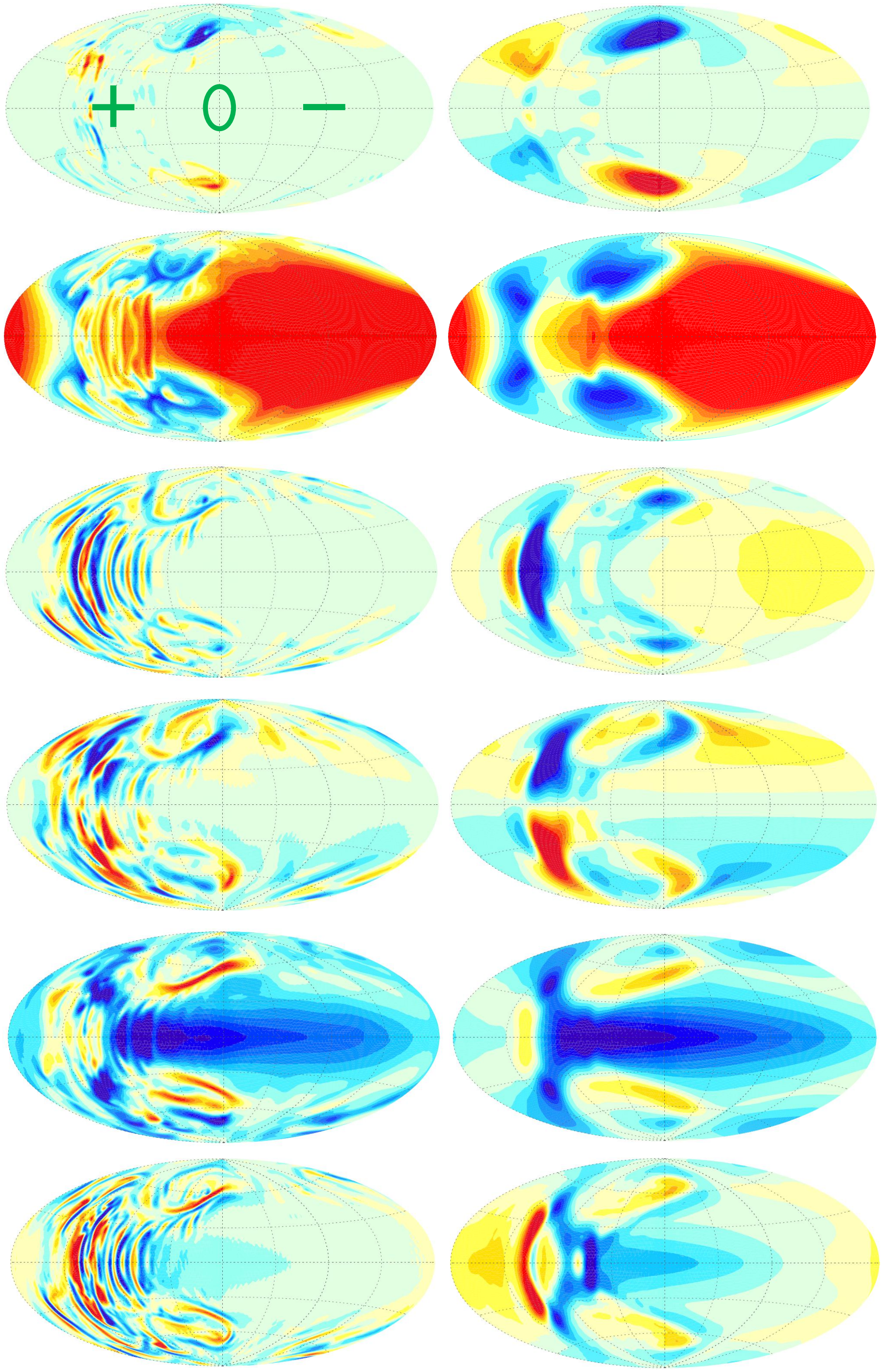

Figure 3.22: Aitoff projections of spherical surfaces of (from top to bottom) radial field, temperature (both at the CMB), u_r, u_ϑ, u_ϕ and z-vorticity at $r/r_{cmb} = 0.8$ for a snapshot (left plots) and the time average (right).

3.6 Dependence on Boundary Conditions and Model Parameters

Unfortunately a parameter regime realistic for planet can not be reached with the available computational power. Analyzing many model cases might allow to compile a scaling law for extrapolating the results to realistic planetary parameters. Here the dependence on heating mode, the mechanical boundary conditions, the Rayleigh and the Ekman number is investigated. The special characteristics of the Martian interior such as secular cooling as heating mode and the heterogeneous CMB heat flux pattern allow the hemispherical convection to emerge more easily. Thus a hemispherical magnetic field might be the favored mode of magnetic induction.

3.6.1 Heating Mode

The core of Mars might be entirely liquid even today (Dehant 2003), therefore the dynamo was driven by secular cooling. The Earth, on the other hand, started to nucleate an inner solid iron core at a given point in its thermal evolution. After which core convection was supported by the chemical buoyancy due to light element release from the inner core boundary. Here we compare the reaction of core convection driven either by internal or bottom heating to a heat flux anomaly at the CMB. We set up the bottom heated case in prescribing a heat flux at the inner core boundary and set the amplitude of the heat source density to zero. Even though Mars most probably never nucleate an inner core, the question whether the strong sensitivity to heat flux anomalies is a unique property of the internal heated dynamos needs to be clarified. Figure 3.23 shows the strength of the EAA convective mode for unperturbed core convection (lower lines) and the $g = 100\%$ case (upper lines) for both heating modes.

The unperturbed cases show higher EAA contribution if the system is driven from the bottom, even though both are fairly low. But the heat flux anomaly does have a much greater effect on the internal heated dynamo. For $g = 100\%$ the hemispherical convection dominates by far and columnar convection seems entirely removed from the system. In the bottom driven dynamos, the relative strength does not exceed 15% of the total kinetic energy. The cause for this beavior might be the radial distribution of the temperature, where in the internal heated case the strongest temperature gradients are close to the outer boundary (Hori et al. 2012). Therefore it is much more sensitive to CMB heat flux anomalies. In the bottom heated core convection, the largest temperature gradients are located close to the inner boundary, therefore it reacts only weakly to a heterogeneity on the outer boundary. The study of Hori et al. (2012) investigated that issue in closer detail. Their findings, that internally driven dynamos are more sensitive to the outer boundary, whereas the dynamos driven from the bottom are more sensitive to the inner boundary indeed confirms our results.

3.6.2 Mechanical Boundary Conditions

Here also the influence of the mechanical boundary conditions is investigated. Stanley et al. (2008) used free slip walls, whereas in our study we impose rigid walls. This choice

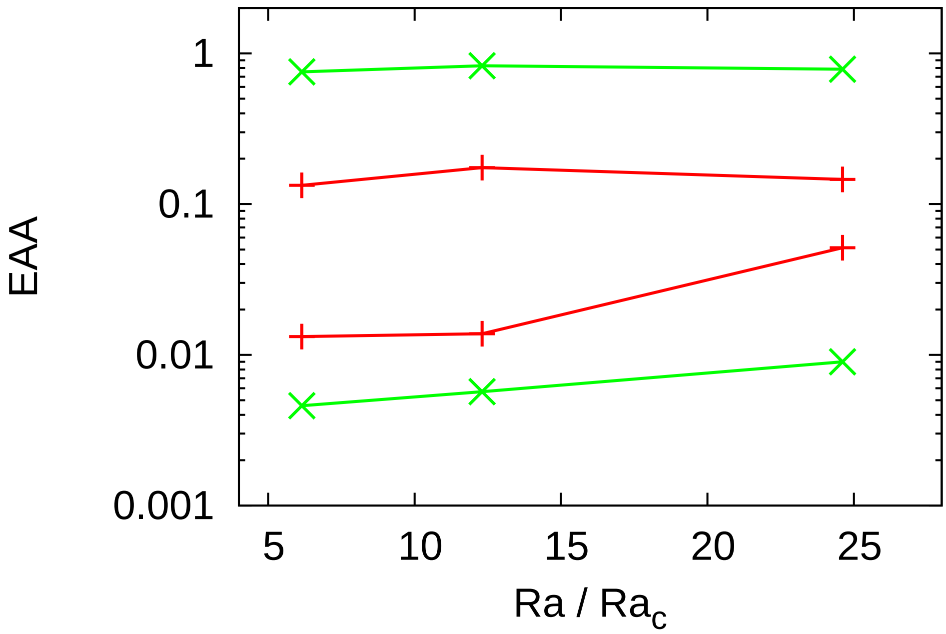

Figure 3.23: Natural onset and forced emergence of the hemispherical convection measured by its equatorial asymmetry and axisymmetry (EAA) for different heating modes (green - internal heated, red - bottom driven) for the homogeneous (lower lines) and perturbed system (upper lines).

is based on the fact, that the thickness of the mechanical boundary layers scales with the square root of the Ekman number (Soward and Dormy 2007). Therefore the effect of the mechanical walls is very minor at realistic Ekman numbers or inside a planetary core. But the numerical reachable Ekman numbers or far too large in comparison to a realistic Ekman number, thus the mechanical boundary conditions have a stronger influence. Hence we consider a realistic confinement with rigid walls, what is the physically more accurate choice for simulating a highly viscous model of the core.

Stanley et al. (2008) reported that they could find a hemispherical solution for stress free but not for rigid mechanical boundaries. We propose, that it is even easier for rigid walls to enforce a dominant EAA mode and thus a hemispherical dynamo. To proof or disproof this hypothesis a series of runs was made for the identical parameters but different mechanical boundary conditions. Here we concentrate on the onset and strength of the hemispherical convection. In figure 3.24 the response of the convection to heat flux anomalies of different strength is shown, where the left plot shows the behavior for the free slip walls and the right for the rigid walls. The total kinetic energy is given in red color, the kinetic energy contained in the EAA mode in green and the ratio of the two giving the relative strength of the EAA in blue (right axis, in figure 3.24).

The amplitude of the total kinetic energy as well as the EAA energy is significantly higher in the free slip cases with an axial perturbation. The rigid wall cases store a significant amount of kinetic energy, here especially zonal flows, in the boundary layers (Jones

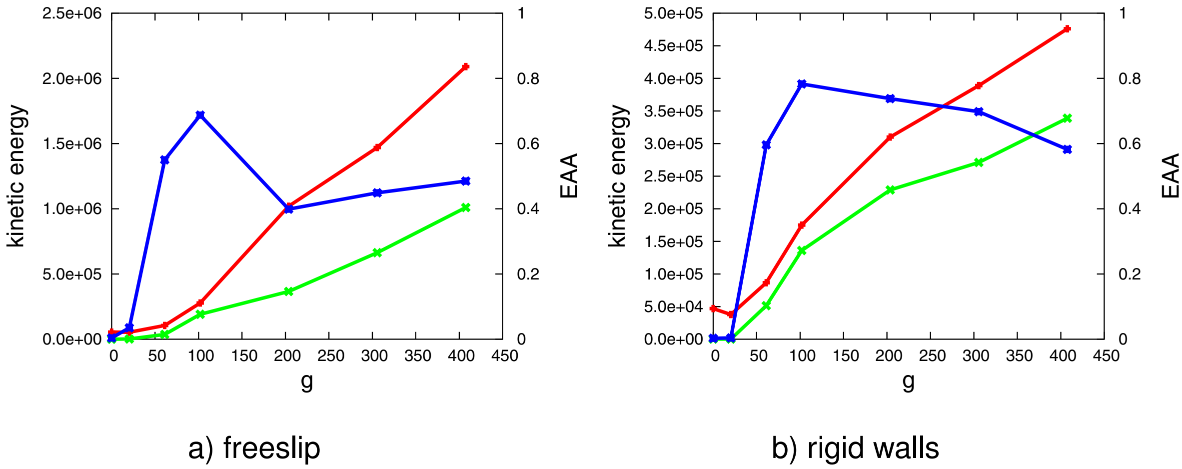

Figure 3.24: Onset of the EAA mode and symmetry of the kinetic energy for free-slip (left) and rigid (rigid) mechanical boundaries. The total kinetic energy is colored red, the kinetic energy contained in the EAA mode in green, whereas the blue curve is the relative strength of the EAA mode.

2011) since also the tangential part of the kinetic energy has to vanish at the boundary. The tangential velocity is mainly given by the axisymmetric toroidal energy of the zonal flows, thus their amplitudes are weaker for rigid walls. The difference in total kinetic energy can also originate from different magnetic field strengths.

The contributions and symmetries of poloidal and toroidal kinetic energy, listed in table 3.2, show also that the amplitude of axisymmetric poloidal energy (meridional circulation) is significantly higher in the rigid wall cases although the total kinetic energy is smaller. This is a hint on the Ekman pumping mechanism driven by the rigid mechanical boundaries. Ekman pumping and Ekman suction appears only for no slip boundary, where a flow into to the boundary layer (suction) or outwards (pumping) emerges. Soward and Dormy (2007) pointed out that Ekman suction (pumping) appears if the vorticity of the flow is antiparallel (parallel) to the rotation. Since we find an eastward zonal flow cell in the northern hemisphere, and the westward directed in the southern, the rigid walls will pump fluid from north to south. In the recent review by Soward and Dormy (2007) it is mentioned, that the amplitude of Ekman suction/pumping decrease with increasing colatitude. As a consequence a large scale meridional circulation downward close the inner core and upward close to the outer boundary emerges. This results was recently discussed by Landeau and Aubert (2011), where the authors already suggested the Ekman pumping mechanism for supporting the zonal flows. We thus find besides the temperature anomaly in the Ekman pumping mechanism another source of meridional circulation. Both kinds of meridional flow will transport hotter fluid from the northern into the southern hemisphere closer to the rotation axis and colder fluid backwards closer to the CMB. Note, that meridional circulation is deflected by the Coriolis force into zonal flows independently of the source of the meridional circulation. In any case, the following zonal flow gradients are ageostrophic. In the free slip simulations, no Ekman pumping can emerge, thus the ageostrophic zonal is entirely driven by the temperature anomaly emerging from

g	E_{pol} total	as	ea	eaa	E_{tor} total	as	ea	eaa
0	13910	96.6	2409	45.92	31210	3126	8296	248.2
	13390	72.8	2511	37.7	41310	8256	6990	200.2
20	12170	300.5	3018	219.5	35150	774.3	12470	4911
	12350	146.8	2860	86.33	41220	9751	10620	1790.4
60	11010	1324	4731	1210	144300	123600	126400	116300
	11350	389.6	3571	273.5	115400	80820	74520	62450
100	10540	2375	6055	2076	199800	187200	178700	172400
	15190	475.7	5492	322.1	263500	219200	208100	191000
200	17370	2995	9860	2705	289100	266800	234100	223600
	65250	995.1	17940	632.4	950300	770600	489700	404300

Table 3.2: Comparison of the impact of a heat flux anomaly on the amplitude and symmetry of the kinetic energy for different mechanical boundaries. The upper value is calculated for rigid walls, whereas the lower one corresponds to stress free mechanical boundaries.

the heat flux anomaly.

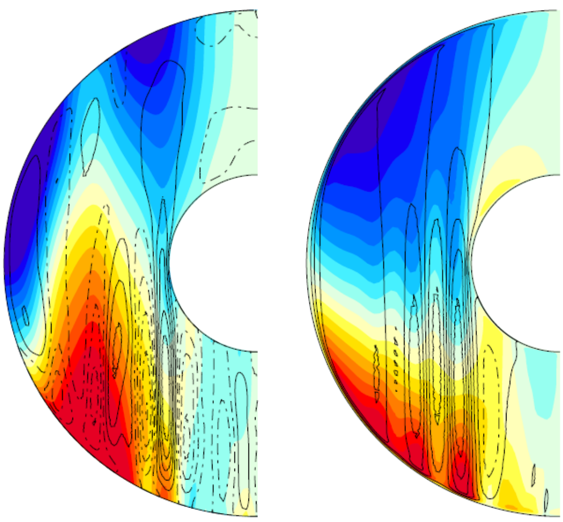

Figure 3.25: Snapshot of the axisymmetric zonal flow free slip (left) and rigid walls (right), with meridional circulation as contour. In the free slip case there is a geostrophic and an ageostrophic zonal flow visible, where as in the rigid wall case only the ageostrophic thermal wind is present. Parameters: $\mathrm{Ra} = 4.0 \times 10^4, \mathrm{E} = 10^{-4}, \mathrm{Pm} = 2, \mathrm{g} = 200\%$

The relative strength of the EAA mode reaches a maximum around $g = 100\%$ in the free slip case. For higher perturbations the total kinetic energy increases much faster than the equatorial antisymmetric zonal contribution (see also last line in table 3.2) driven by the temperature anomaly. This means that equatorially symmetric zonal flows contribute more significantly than for rigid boundaries. Figure 3.25 show the emergence of a geostrophic contribution that opposes the thermal winds in the northern hemisphere. Thermal winds can not be geostrophic, Reynolds stresses seem to become increasingly important. Typically they emerge if there is a clear correlation between the cylindrical-s and ϕ velocity component. Christensen (2002) showed this relation, when proposing Reynolds stresses as the main source of the zonal flows on gas giants.

3.6.3 Thermal Wind Balance

The main driver of the strong zonal flows are the latitudinal temperature gradients. Meridional flows seek to equilibrate them and are diverted into strong zonal flows by the strong Coriolis force. The thermal wind balance yielded (see equation 3.12)an equation for the strength of the zonal flows as function of latitudinal temperature gradients.

$$\frac{2}{E}\frac{\partial u_\phi}{\partial z} = \frac{Ra}{Pr}\frac{1}{r_o}\frac{\partial T}{\partial \vartheta} \tag{3.14}$$

We showed in section 3.4.1 that the Lorentz force associated to the azimuthal field suppresses the convective columns. Therefore the thermal wind balance is tested explicitly for a magnetic and non-magnetic case with a moderately perturbation amplitude of $g = 60\%$. Due to the strong time variability of magnetic and kinetic energy, snapshots as well as time averages are used. The figure 3.26 shows left- and right-hand side of the thermal wind balance for a snapshot and as a time average for the four different scenarios mentioned. It can be seen, that in the nonmagnetic cases (a and b), the zonal shear is entirely driven by the temperature anomaly. The mechanical boundary conditions are rigid, therefore strong velocity gradients appear in the plots of the shear, which do originated from the temperature anomaly. The Lorentz force, on the other hand, shows only minor influence on the thermal wind balance. Since both, the main contribution of flow and field, are azimuthal the resulting Lorentz force is zero. This can be seen, if we assume the magnetic field $\boldsymbol{B} = B\hat{\boldsymbol{e}}_{\boldsymbol{\phi}}$ has only an azimuthal component. The azimuthal component of the Lorentz force is then

$$\begin{aligned}
[(\boldsymbol{\nabla}\times\boldsymbol{B})\times\boldsymbol{B}]_\phi = \\
&\frac{1}{\sin\vartheta}\left(\frac{\partial}{\partial\vartheta}(\sin\vartheta B_\phi) - \frac{\partial}{\partial\phi}B_\vartheta\right)B_\vartheta \\
&-\frac{1}{r}\left(\frac{1}{\sin\vartheta}\frac{\partial}{\partial\vartheta}B_r - \frac{\partial}{\partial r}(rB_\phi)\right)B_r\,.
\end{aligned} \tag{3.15}$$

If B_r and B_ϑ are zero, the azimuthal Lorentz force is zero as well. Of course, in the southern hemisphere, where field and flow are much more variable, the Lorentz force is responsible for small deviations from the thermal wind balance (compare figure 3.26. Because of the good agreement other sources, such as Reynolds stresses, driving zonal flows can be ruled out.

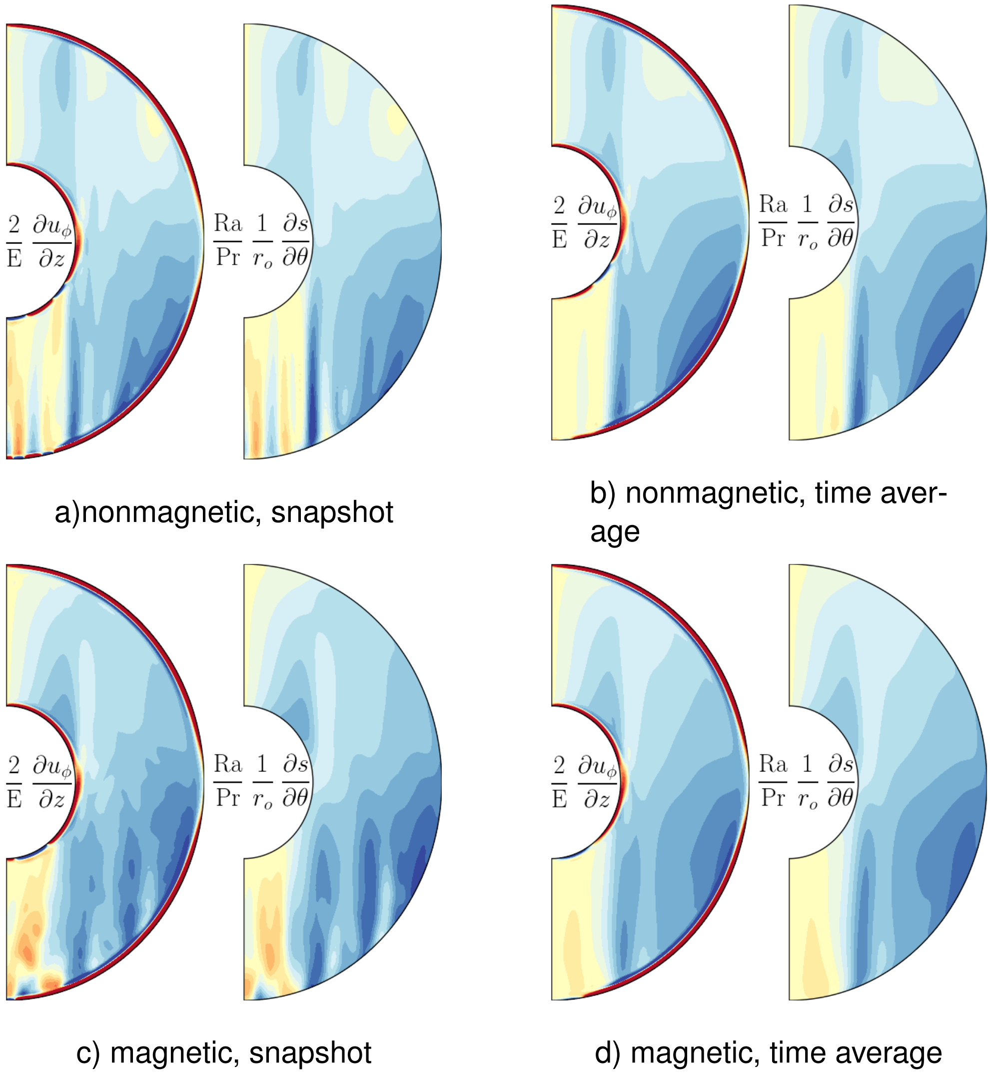

Figure 3.26: Plots the left and right hand side of the thermal balance equation 3.14 for pure hydrodynamic cases (a and b) and including the Lorentz force (c and d). Figure provided by T. Gastine.

The thermal wind balance can be simplified to find an order-of-magnitude estimate. The Reynolds number $Re = UD/\nu$ contains the rms kinetic energy and thus serves as measure for a characteristic flow amplitude. We construct a special Reynolds number Re^* such that the involved flow amplitude is calculated exclusively from the strength of the axisymmetric toroidal flows. The z-derivative of the zonal flow is approximated with the ratio ($\partial u_\phi / \partial z \approx Re^*/l_z$), where l_z is the typical variation length scale of the zonal flow. Assuming the hydrodynamic Prandtl number $Pr = 1$ yields

$$Re^* = \frac{RaE}{2}\frac{l_z}{r_o}\left[\frac{\partial \overline{T}}{\partial \vartheta}\right]^{rms} . \tag{3.16}$$

The temperature anomaly is estimated as the root mean square of the latitudinal gradient of the time averaged axisymmetric temperature, therefore zonal flow Re^* and $[\partial\overline{T}/\partial\vartheta]^{rms}$ are output quantities. We set the variation length of the zonal flow $l_z = 1$ and use $r_o = 1.55$ for the nondimensional outer core radius. Figure 3.27 compares the observed zonal flow Re^* with the value predicted by the thermal wind balance (the right hand side of equation 3.16). Figure 3.27 shows that the agreement is surprisingly good. Hence the thermal wind balance is also valid for different Ekman numbers (colors in the figure) and Rayleigh numbers (symbols). The axisymmetric toroidal flow dominating the kinetic energy is exclusively driven thermal winds.

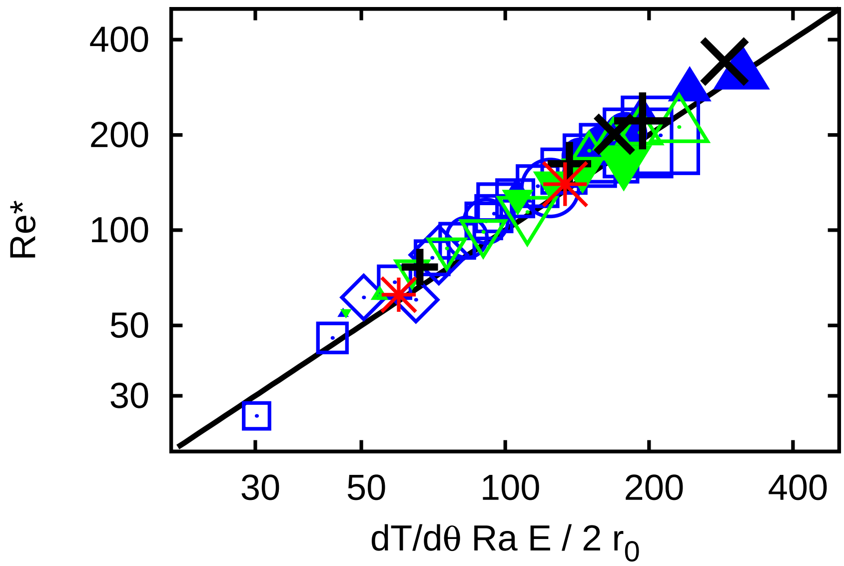

Figure 3.27: Approximated thermal wind balance for different Ekman numbers (green - $3.0 \cdot 10^{-4}$, blue - $1.0 \cdot 10^{-4}$, black - $3.0 \cdot 10^{-5}$, red - $1.0 \cdot 10^{-5}$) and Rayleigh numbers (symbols). The size of the symbols is scaled proportional to the square root of the perturbation amplitude g. See table 3.3 on page 100 for details.

To predict the importance of the EAA zonal flows and thus hemispherical dynamo action in a simulation or a planet one would have to know how the temperature anomaly $[\partial\overline{T}/\partial\vartheta]^{rms}$ depends on the system parameters Ra, E and g. Intuitively, one might aspect increasing the perturbation amplitude g will lead to an increase of the temperature anomaly, whereas an increase of the vigor of convective motions in terms of an increasing Rayleigh number will lead to faster mixing and stirring thus to a weaker temperature anomaly. For a realistic Ekman number, the Taylor-Proudman constraint becomes increasingly more important.

Figure 3.28 shows the temperature anomaly calculated for all our model runs. It can be seen, that an increase of g indeed leads to higher temperature anomalies, but the more crucial parameter seems to be the Rayleigh number. As an example the low Ekman number case: $E = 3.0 \times 10^{-4}$ (green symbols), the closer to the onset (triangles down - weakly

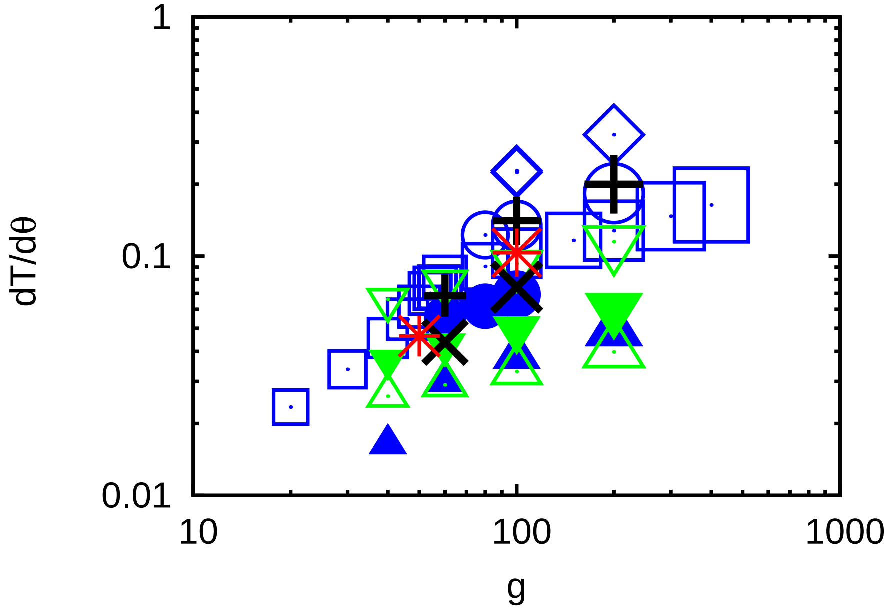

Figure 3.28: Amplitude of the temperature anomaly as function of the perturbation amplitude g for all our model runs. Colors indicate Ekman numbers, symbols the Rayleigh numbers, the symbol size increases with g. See table 3.3 on page 100 for details.

supercritical, triangles up - strongly supercritical) the stronger is the latitudinal temperature contrast. The Ekman number itself, seem to be of minor importance. The blue squares denoting $E = 10^{-4}$ and $Ra = 4 \times 10^7$ show another difficulty arising here. For weaker perturbations up to $g = 60\%$, the slope in figure 3.28 is much stronger, whereas it flattens for higher g. Obviously, for the weak perturbation, the EAA mode is activated more and more, whereas for $g > 60\%$ a saturation appears. This saturation is given if the convection is dominated by the EAA mode. Thus further increase of g leads to a weaker increase of the temperature anomaly. We will focus for the scaling attempt on cases where the EAA mode is saturated.

We restrict the amount of data to $g = 100\%$ and plot the temperature anomaly as function of supercriticality Ra/Ra_c in figure 3.29 as log-log plot. We fit further the decrease of temperature anomaly $[\partial\overline{T}/\partial\vartheta]^{rms}$ with increasing supercriticality Ra/Ra_c with power laws of the form

$$\left[\frac{\partial\overline{T}}{\partial\vartheta}\right]^{rms} = m\left(\frac{Ra}{Ra_c}\right)^n \ . \tag{3.17}$$

and find

$$\begin{array}{ccc} \mathrm{E} & m & n \\ 3.0 \times 10^{-4} & 0.5319 & -0.5728 \\ 1.0 \times 10^{-4} & 0.3679 & -0.5262 \\ 3.0 \times 10^{-5} & 0.3725 & -0.5396 \end{array} \tag{3.18}$$

These exponents are fairly close to those predicted by King et al. (2010) in a somewhat different context (gray lines in figure 3.29). There the authors studies scaling laws for the convective heat transfer in planetary dynamos measured by the Nusselt number Nu

$$Nu = \frac{q_0 D}{k \Delta T} \ . \tag{3.19}$$

The Nusselt number measures the ratio between superadiabatic heat transport and the convective part of this heat transport. The thickness of the thermal boundary layers δ_κ scales as inverse of the Nusselt number (Spiegel 1971). The study by King et al. (2010) inspected the radial temperature gradient distribution for small Ekman E and large temperature contrast based Rayleigh numbers R. They proofed that the Nusselt number scales with supercriticality such that $Nu = (R/R_c)^{6/5}$. Our main interest is in the temperature gradients in latitudinal direction. If we assume now, the thickness of the thermal boundary layer $\delta_\kappa \approx [\partial\overline{T}/\partial\vartheta]^{rms}$ is representing the amplitude of the latitudinal temperature anomaly, we should be able to reconcile the findings of King et al. (2010). Note, that in this study a Rayleigh number R based on the temperature contrast, rather than the heat flux was used. The two relate like $R = Ra * Nu^{-1}$. We find then

$$Nu \propto \left(\frac{RaNu}{Ra_c} \right)^{6/5} \tag{3.20}$$

$$Nu^{11/5} \propto \left(\frac{Ra}{Ra_c} \right)^{6/5} \tag{3.21}$$

$$Nu^{-1} \propto \delta_\kappa \approx \left(\frac{\partial\overline{T}}{\partial\vartheta} \right)^{rms} \propto \left(\frac{Ra}{Ra_c} \right)^{-6/11} \ . \tag{3.22}$$

We added the slope of $n = -6/11$ as gray lines in figure 3.29 showing a good agreement. Note, our calculated slopes for the different Ekman numbers are only constraint by a few, sometime only two points. However, the striking agreement suggests, that the temperature anomaly introduced by a CMB heat flux anomaly scales very similarly as the radial temperature contrast given by the vigor of the convection as suggested by King et al. (2010). We can go one step further and try to suggest the amplitude of thermally driven zonal winds presumably this scaling law holds. Landeau and Aubert (2011) used $Ra_c \propto E^{-4/3}$ for scaling the critical Rayleigh number. Thus we find for the estimate of the thermal wind according to equation 3.16

$$
\begin{aligned}
Re^* &= \frac{Ra\,E}{2}\frac{1}{r_0}\left(\frac{\partial\overline{T}}{\partial\vartheta}\right)^{rms} \\
Re^* &= \frac{Ra\,E}{2}\frac{1}{r_0}\left(\frac{Ra}{Ra_c}\right)^{-6/11} \\
Re^* &= \frac{Ra^{1-6/11}\,E^{1-6/11\;4/3}}{2r_0} \\
Re^* &= \frac{Ra^{5/11}\,E^{3/11}}{2r_0}\;.
\end{aligned}
\tag{3.23}
$$

The flux based Rayleigh number Ra and the Ekman number for the ancient Mars are given by

$$
Ra = \frac{\alpha\rho c_p g q D^4}{\nu\kappa^2} = 2\times 10^{28} \tag{3.24}
$$

$$
E = \frac{\nu}{\Omega D^2} = 3\times 10^{-15}\;, \tag{3.25}
$$

when using the values given in the introduction section 1.3 and by table 1.1. We find $Re^* \approx 2.66\times 10^8$, thus a significant fraction of the total flow amplitude of a planetary core ($Re = 10^8...10^9$). Note, that we have neglected an additional Ekman number dependence. We will further discuss this result in the discussion section 6.

3.6.4 Parameter Dependence I - General Trends

In this section we collect the results of all numerical runs and show general dependencies on the governing parameters. The data used for this study cover four different Ekman numbers ($E = 3.0\times10^{-4}, 1.0\times10^{-4}, 3.0\times10^{-5}, 1.0\times10^{-5}$), several Rayleigh numbers ($Ra = 7.0\times10^6$ up to 4.0×10^8) and magnetic Prandtl numbers ($Pm = 1.0$ up to 5.0). The heat flux variation g is bordered by $g = 0$ and $g = 600\%$. Only the hydrodynamic Prandtl number is kept constant ($Pr = 1$). The table 3.3 lists the different symbols (different Rayleigh numbers and magnetic Prandtl numbers) and colors (Ekman numbers) used to distinguish the parameters in the figures. If not described differently, the perturbation amplitude scales the size of the symbols.

We had seen, the thermal wind balance holds for all our studied cases. The source of the thermal wind is the latitudinal temperature anomaly, for which we suggest a scaling law. The consequence of the strong thermal winds is a switch in the convective structure from equatorially symmetric, but nonaxisymmetric columnar convection, to the equatorial antisymmetric and axisymmetric EAA mode. It has been reported by Landeau and Aubert (2011), that the EAA mode can emerge naturally from strong supercritical convection in internal heated dynamos. We test this hypothesis in comparing the relative EAA strength for unperturbed dynamos and such with a $g = 100\%$ CMB heat flux anomaly in figure 3.30. The colors are again given by the Ekman number and according to table 3.3. The unperturbed cases show (lower curves in the figure) the natural emergence of the EAA mode, thus being consistent with the results of Landeau and Aubert (2011). For the lowest Ekman number used here ($E = 3\times10^{-4}$) we see, that the growth of EAA mode

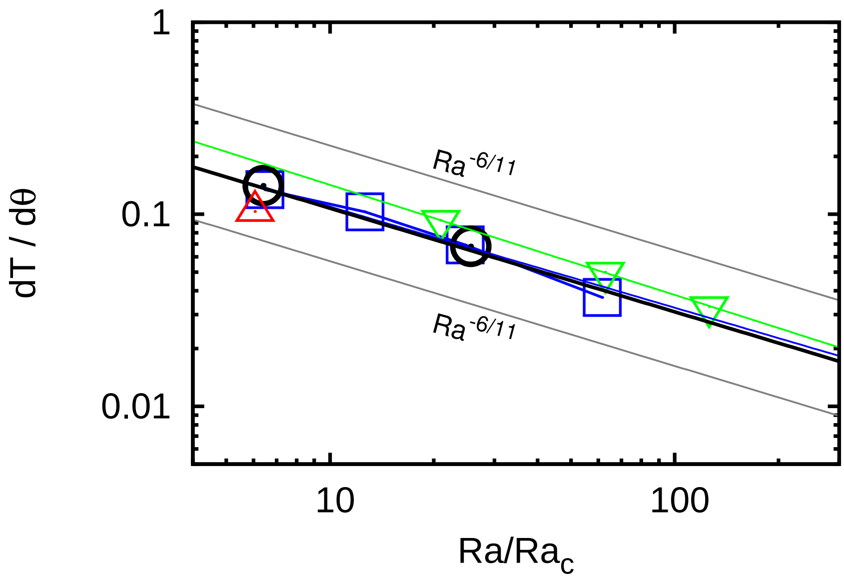

Figure 3.29: Amplitude of the temperature anomaly as function of supercriticality for a subset of our model runs where g = 100%. Colors of the symbols and linear functions indicate Ekman numbers. The symbols refer the cases, whereas the colorish straight lines are least mean square fits calculated seperately for each Ekman number. The grey lines indicate the prediction fom theory. For details see text.

with increasing supercriticality Ra/Ra_c is limited and turns into a decrease of the EAA mode when the convection is strongly supercritical. We interpret this as the effect of the increasing stirring and mixing efficiency according to the more and more vigorous convection overwhelming the intrinsic temperature anomalies given by the onset of EAA flows. In other words, once the mixing is fast enough, the source of the EAA mode (temperature anomalies) dissappear faster than the EAA mode can establish and further promote them. The lower Ekman number curves (blue, black, red) in figure 3.30 do not show this effect, but are not driven that far into supercriticality neither. The upper curves denote the according $g = 100\%$-cases, and show the same effect. The higher the supercriticality, the weaker is the EAA mode.

As a second important feature, we investigated how the EAA mode grows if the amplitude of the boundary anomaly is increased. We studied this transition for $E = 10^{-4}$ and $Ra = 4 \times 10^7$ in section 3.3. In figure 3.31 we investigate the strength of the EAA mode as function of the perturbation amplitude, while covering the whole data set. The different colors in figure 3.3 relate to the different Ekman numbers, where the curves for $E = 3 \times 10^{-4}$ (green) and $E = 3 \times 10^{-5}$ (black) match the curve for $E = 10^{-4}$ (blue). At a perturbation amplitude of $g = 100\%$, all cases exceed (besides the low Ekman number case, red stars in the plot) in EAA strength 0.6, thus the EAA mode dominates or at least contributes significantly to the convection. Note, the blue squares reflecting the intensively studied runs ($E = 10^{-4}$, $Ra = 4 \times 10^7$ and with a broad coverage in pertur-

E	Ra	Pm	Symbol
3.0×10^{-4}	1.0×10^{7}	5	▽
3.0×10^{-4}	3.0×10^{7}	5	▼
3.0×10^{-4}	6.0×10^{7}	5	△
1.0×10^{-4}	7.0×10^{6}	2	◇
1.0×10^{-4}	2.1×10^{7}	2	○
1.0×10^{-4}	4.1×10^{7}	2	□
1.0×10^{-4}	8.0×10^{7}	2	●
1.0×10^{-4}	2.0×10^{8}	1	▲
3.0×10^{-5}	1.0×10^{8}	2	+
3.0×10^{-5}	4.0×10^{8}	2	×
1.0×10^{-5}	4.0×10^{8}	2	*

Table 3.3: Overview of the symbols and colors used for some of the upcoming plots. The color always refers to the Ekman number.

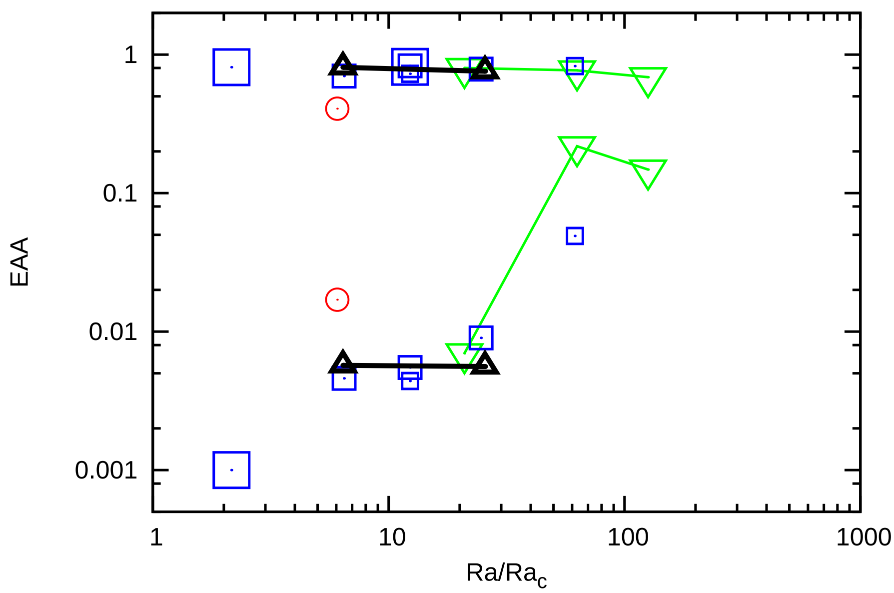

Figure 3.30: Natural onset of the EAA mode (lower curves) and forced EAA mode (upper) for different Ekman numbers and convective supercriticality. Details are in the text.

bation amplitude g) shows the decline of the EAA mode once g exceeds 200%. As we had seen during section 3.3 this is due to the southward migration of the shear zone between the zonal flow cells. As a consequence, the equatorial antisymmetry decreases and whereas the axisymmetry remains strong, thus the combined symmetry in the EAA mode decreases as well. Interestingly, the red symbols denoting the few cases for $E = 10^{-5}$ seem to have a much shallower onset curve for the EAA strength. This is indeed also visible in the figure 3.30, where we limit the plots to $g = 0$ and $g = 100\%$ cases. It might reflect the increasing importance of the Taylor-Proudman theorem, which does not allow for z-gradients in axisymmetric flows to emerge.

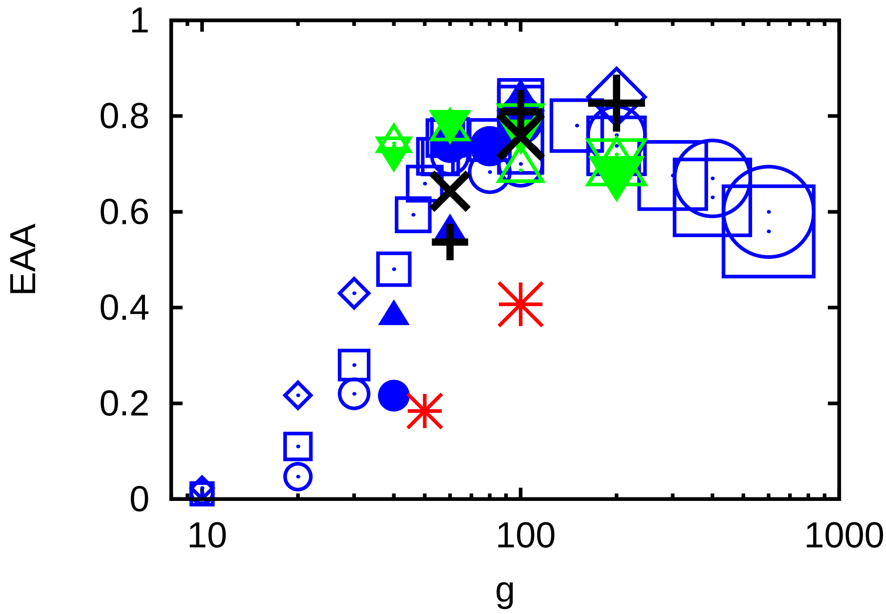

Figure 3.31: Relative strength of the EAA convective mode as function of the perturbation amplitude g. Colors refer to Ekman numbers, the symbols to different Rayleigh numbers. See table 3.3 for the full legend, and details in the text.

The induction mechanism is shown to be affected by the EAA mode, whereas the major contribution of the toroidal field is created by an ω-effect associated with the shear between the zonal flow cells (see section 3.4). Figure 3.32 extends this proposal to the whole data set in cross-correlating the EAA strength with the relative ω-effect ω^* (see equation 3.13 for the definition). The colors and symbols are again similar to the previous plots and summarized in table 3.3 on page 100. The figure 3.32 shows, that whenever the EAA mode is strong, the toroidal field is mainly induced by the shear of the zonal flows. Even in the unperturbed cases (small symbols) the ω-effect amounts roughly 20%. The relative ω-effect increases more or less linearly with the EAA mode and saturates around $\omega^* = 0.8$ thus 80% of the toroidal field is ω-induced. Both, EAA mode and ω^* can not reach unity. For the EAA there is neccessarily always non-axisymmetric poloidal (and toroidal as well) energy due to the convection, what is not coverd by the EAA symmetry. The induction, on the other hand, has always a contribution of α-effect associated with helical flows thus creates both, toroidal and poloidal field. Without the α-effect the dynamo will not work, since there wouldn't be any poloidal field being subject to shear thus creating toroidal field. Again the red symbols in figure 3.32 refering to the low Ekman number simulations seem to be somewhat exceptional. Even though the $g = 100\%$-case (upper red symbol) hosts an EAA strength of roughly 0.4, it does not show an strongly increased ω-effect compared to the $g = 0\%$ reference case (lowest red symbol in figure 3.32). A lower Ekman number also reflects smaller viscosity and thus smaller flow length scales. This smaller and faster convective length scales give stronger helical flow, thus a more efficient α effect. Therefore the extra induction of toroidal magnetic field via the ω-effect does not have a strong effect.

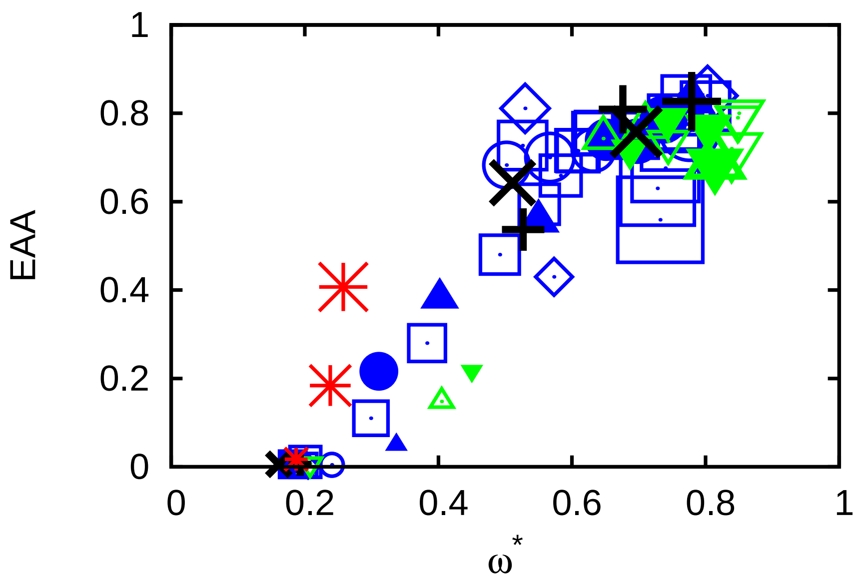

Figure 3.32: Relative shear flow induced toroidal field measured by the relative ω-effect ω^* cross-correlated with the strength if the EAA mode.

3.6.5 Parameter Study II - Peculiar Points

Here we collect special cases, which typically appear close to the onset of dynamo action. Interestingly, close to the onset of dynamo action the imposed heat flux variation can help to maintain magnetic field generation. For example, at $E = 10^{-4}$, $Ra = 7 \times 10^6$ and $Pm = 2$, no dynamo can be found for $g = 0\%$ with a magnetic Reynolds number at the small side with $Rm = 55$ (table A.1 first line). For $g = 100\%$, however, a rather weak field with $\Lambda = 0.1$ is sustained. The small extra Ω-effect promoted by the thermal wind seems to help here. The Lorentz forces are too weak to suppress columnar convection and the resulting field is a peculiar mixture of hemispherical and columnar dynamo action. We find a relative EAA strength of 0.85, but the relative ω-effect remains small like $\omega^* = 0.32$. Figure 3.33 shows the radial flow and field for that case. The solution is stationary in time, but drifting and shows a $m = 8$ azimuthal symmetry.

A similar case can be found for $E = 10^{-4}$, $Ra = 4 \times 10^7$, $Pm = 1$ and $g = 100\%$ although here the homogeneous boundary case already shows weak dynamo action. When increasing g further to 200%, however, the dynamo ceases because the still necessary columnar dynamo action becomes incompatible with the stronger ω-effect.

At $E = 10^{-4}$, $Ra = 2 \times 10^8$ and $Pm = 1$ we find another case were the homogeneous case fails but dynamo action is maintained for $g \geq 60\%$. Here the $g = 0$ is likely located in the cusp region between dipole dominated and quadrupolar dynamos where somewhat higher magnetic Prandtl numbers are required to guarantee dynamo action (see fig. 2 in Kutzner and Christensen (2002)).

For $E = 10^{-4}$, $Ra = 7 \times 10^6$ and $Ra = 4 \times 10^7$ we also varied the magnetic Prandtl number. A rise of Pm leads to a larger relative ω-effect ω^* due to the stronger magnetic field and therefore stronger suppression of convective columns and more dominant zonal flows. The magnetic Prandtl number provides a rough measure for the ratio of convective to magnetic length scales on the diffusive end of the spectrum.

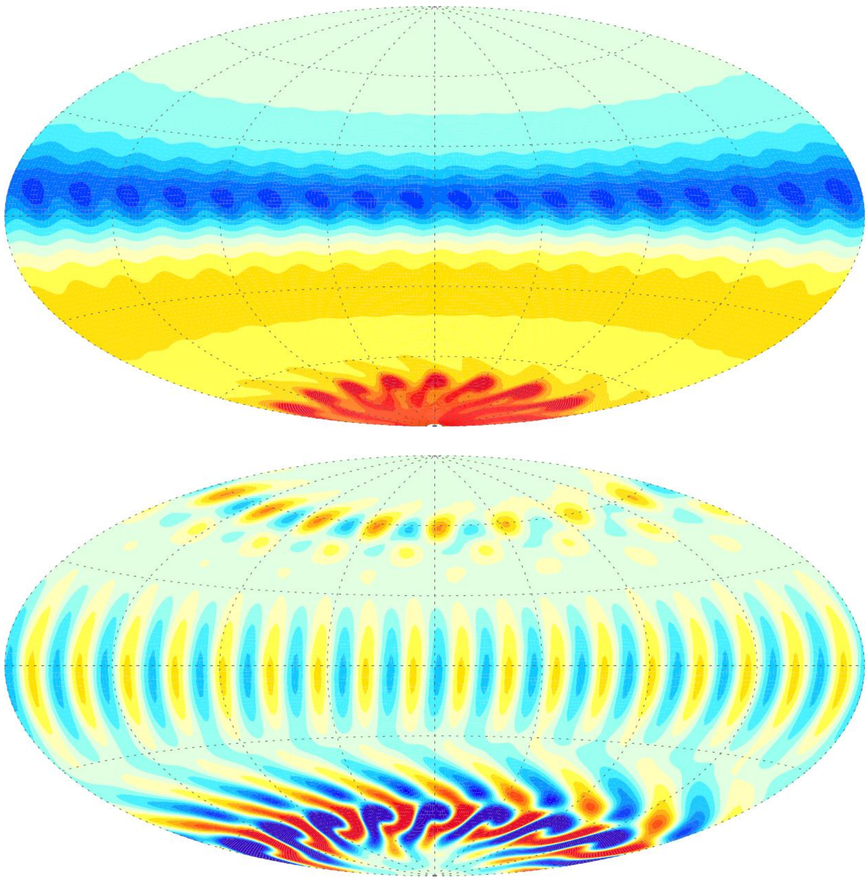

Figure 3.33: Radial magnetic field (top plot) at the CMB and radial flow at mid-depth (bottom plot) for the peculiar case of $E = 10^{-4}$, $Ra = 7 \times 10^6$ and $Pm = 2$ with $g = 100\%$ perturbation amplitude.

4 Results II : Periodic Oscillations – Parker Waves?

The transition from α^2 to $\alpha\omega$ dynamos seems to coincide with the onset of the magnetic oscillations, described in section 3.4.2. The convection in planetary cores is typically dominated by the fast rotation, thus subject to a strong Coriolis force. The main force balance is then geostrophic or magnetostrophic, depending on the strength and morphology of the magnetic field. As a consequence of the strong Coriolis force, it is thought that terrestrial planets do not show large ageostrophic zonal flows or differential rotation. Therefore the core dynamo of a terrestrial planet is usually, in terms of the mean-field theory, to first order an α^2-dynamo (Olson et al. 1999, Aubert et al. 2008b, Wicht and Aubert 2005). It would need a strong mechanism to enforce zonal flows yielding an efficient ω-effect. As shown above (section 3.4) the thermal winds promoted by the strong latitudinal temperature anomalies provide strong zonal flow shear, where axisymmetric toroidal field is induced by an ω-effect. This thermal wind is ageostrophic, since it shows large variations of the zonal flow along the latitude.

A model for oscillating dynamo waves in an $\alpha\omega$-dynamo was introduced by Parker (1955) in order to explain the solar cycle. The solar dynamo is maintained by large scale differential rotation at the bottom of the convection zone, where a substantial ω-effect is inducing the toroidal field of the Sun and helical convection within the convection zone. Here we test, by using a simplified dispersion relation, whether the observed magnetic oscillations in our simulations are of the same origin as the Parker waves.

4.1 Introduction to Mean-Field Dynamos

The Parker model (Parker 1955) is based on the theory of kinematic or mean-field dynamos. In the theory of mean-field dynamos (Krause and Rädler 1980), or kinematic dynamos in general, the effect of the Lorentz force on the flow structure is typically neglected and only the induction equation is analyzed with a prescribed or parametrized velocity field. This approach was very successful for investigating the cyclic solar magnetic field, see e.g. Proctor (2006), Ossendrijver (2003), Charbonneau (2010) for recent reviews. The main aim of these theories is the analysis and understanding of the first unstable modes, the onset of dynamo waves under the influence of shear flows, MHD turbulence or different geometries. The dimensional induction equations was given by (see eq. 2.62)

$$\frac{\partial \boldsymbol{B}}{\partial t} = \boldsymbol{\nabla} \times (\boldsymbol{u} \times \boldsymbol{B}) - \lambda \boldsymbol{\nabla} \times \boldsymbol{\nabla} \times \boldsymbol{B} \, , \tag{4.1}$$

where we assumed the magnetic diffusivity λ to be a constant. In the mean-field dynamo theory the magnetic and velocity field are separated into a mean part $\overline{\boldsymbol{u}}, \overline{\boldsymbol{B}}$ and a fluctuating or turbulent part $\boldsymbol{u}', \boldsymbol{B}'$. The fluctuating contributions vanish when applying the averaging method used to define the mean contributions. Then only the evolution of the mean field is investigated while the action of the fluctuating field is parametrized. The derivation of the mean field equations and the underlying average process can be found, e.g. in Krause and Rädler (1980). The choice of the averaging method, typically with respect to time, length scales or ensemble, needs to be defined according to the specific application. Here we propose to use a separation via the length scales, and assume the mean field $\overline{\boldsymbol{B}}$ and the mean flow $\overline{\boldsymbol{u}}$ to be axisymmetric, and the fluctuating contributions represent the nonaxisymmetric flow and magnetic field. The special convective and inductive dynamics in the hemispherical dynamos matches the requirements of such a treatment to a large extend. The major contribution of kinetic energy is indeed axisymmetric. Our results in section 3.3 shows, that the kinetic energy consists to roughly $\approx 80\%$ of azimuthal flow, but with smaller contributions of convective kinetic energy. The same is true for the magnetic field, since it consists mainly of axisymmetric azimuthal toroidal field ($\approx 80\%$) plus an additional small-scale (and hemispherical) poloidal field.

Providing the separation as described above, the induction equation reads:

$$\frac{\partial(\overline{\boldsymbol{B}} + \boldsymbol{B}')}{\partial t} = \nabla \times \left[(\overline{\boldsymbol{u}} + \boldsymbol{u}') \times (\overline{\boldsymbol{B}} + \boldsymbol{B}')\right] - \lambda \nabla \times \nabla \times (\overline{\boldsymbol{B}} + \boldsymbol{B}') \tag{4.2}$$

$$\begin{aligned}\frac{\partial \overline{\boldsymbol{B}}}{\partial t} + \frac{\partial \boldsymbol{B}'}{\partial t} &= \nabla \times \left[(\overline{\boldsymbol{u}} \times \overline{\boldsymbol{B}}) + (\boldsymbol{u}' \times \overline{\boldsymbol{B}}) + (\overline{\boldsymbol{u}} \times \boldsymbol{B}') + (\boldsymbol{u}' \times \boldsymbol{B}')\right] \\ &\quad - \lambda \nabla \times \nabla \times \overline{\boldsymbol{B}} - \lambda \nabla \times \nabla \times \boldsymbol{B}' \,. \end{aligned} \tag{4.3}$$

Now we make use of the averaging properties. The general rules for the averaging, such as commutability with derivatives or double averages are called 'Reynolds rules' (Krause and Rädler 1980). The average of the fluctuating contributions is by definition zero, thus $\overline{\boldsymbol{u}'} = \overline{\boldsymbol{B}'} = 0$. Applying the averaging to the induction equation yields:

$$\frac{\partial \overline{\boldsymbol{B}}}{\partial t} = \nabla \times \left[(\overline{\boldsymbol{u}} \times \overline{\boldsymbol{B}}) + \overline{(\boldsymbol{u}' \times \boldsymbol{B}')}\right] - \lambda \nabla \times \nabla \times \overline{\boldsymbol{B}} \,, \tag{4.4}$$

which describes the induction of the mean field. To find an equation for the fluctuating field, we subtract the full from the averaged equation and obtain

$$\frac{\partial \boldsymbol{B}'}{\partial t} = \nabla \times \left[(\boldsymbol{u}' \times \overline{\boldsymbol{B}}) + (\overline{\boldsymbol{u}} \times \boldsymbol{B}') + (\boldsymbol{u}' \times \boldsymbol{B}') - \overline{(\boldsymbol{u}' \times \boldsymbol{B}')}\right] - \lambda \nabla \times \nabla \times \boldsymbol{B}' \,. \tag{4.5}$$

It is of advantage to neglect the second order contributions of the fluctuating field, thus the terms $(\boldsymbol{u}' \times \boldsymbol{B}')$ and $\overline{(\boldsymbol{u}' \times \boldsymbol{B}')}$ are both neglected here. This is called the 'first order smoothing approximation' (FOSA) or 'second order correlation approximation' (see e.g., Stix (2002), Krause and Rädler (1980)).

In the equation for the mean field (equation 4.4), the term $\overline{(\boldsymbol{u}' \times \boldsymbol{B}')} = \mathcal{E}$ appears, this is the so called 'mean electromotive force'. It induces mean field from the fluctuating or turbulent flow and field. We consider the induction equation with FOSA approximation for the fluctuating field $\boldsymbol{B}'$

$$\frac{\partial \boldsymbol{B}'}{\partial t} = \nabla \times \left[(\boldsymbol{u}' \times \overline{\boldsymbol{B}}) + (\overline{\boldsymbol{u}} \times \boldsymbol{B}')\right] - \lambda \nabla \times \nabla \times \boldsymbol{B}' \,, \tag{4.6}$$

and integrate this equation to find an expression for $\boldsymbol{B}'$. Again, some simplifications are applied. For simplicity, the mean flow $\overline{\boldsymbol{u}}$ is assumed not to influence the turbulent field, thus the term $(\overline{\boldsymbol{u}} \times \boldsymbol{B}')$ drops out. Additionally we drop the diffusive term, requiring the magnetic diffusivity λ to be small. This is the widely used high conductivity limit (Krause and Rädler 1980), for which the magnetic Reynolds number Rm of the turbulent flow should be much larger then unity. As a test, we calculate $Rm = Re\, Pm \approx 70$ (Parameters: $E = 10^{-4}, Ra = 4{\times}10^7, Pm = 2$), where Re is a typical nondimensional velocity amplitude of the non-axisymmetric poloidal flow. Then the equation reduces to

$$\frac{\partial \boldsymbol{B}'}{\partial t} = \nabla \times (\boldsymbol{u}' \times \overline{\boldsymbol{B}}) \tag{4.7}$$

$$= \boldsymbol{u}' \cdot \nabla\overline{\boldsymbol{B}} + \overline{\boldsymbol{B}} \cdot \nabla\boldsymbol{u}' \,, \tag{4.8}$$

where two additional terms proportional to either $\nabla \cdot \boldsymbol{u}'$ or $\nabla \cdot \overline{\boldsymbol{B}}$ drop out due to the incompressibility of the flow and the non-existence of magnetic monopoles, respectively. The turbulent magnetic field $\boldsymbol{B}'$ is then a function of the turbulent flow $\boldsymbol{u}'$ and the mean magnetic field $\overline{\boldsymbol{B}}$. To find an expression for the mean electromotive force $\mathcal{E}$ depending on $\boldsymbol{u}'$ and $\overline{\boldsymbol{B}}$, a Taylor expansion of the turbulent field with respect the turbulent flow and the mean field is applied. The details of this expansion can be found in Krause and Rädler (1980) or Rüdiger and Hollerbach (2004).

$$\mathcal{E} = \overline{(\boldsymbol{u}' \times \boldsymbol{B}')} = \boldsymbol{\alpha} \cdot \overline{\boldsymbol{B}} - \boldsymbol{\beta} : \nabla\overline{\boldsymbol{B}} + \text{h.o.t.} \,, \tag{4.9}$$

where $\boldsymbol{\alpha}$ and $\boldsymbol{\beta}$ are tensors of 2nd and 3rd rank and depend on the turbulent velocity $\boldsymbol{u}'$. If the turbulence $\boldsymbol{u}'$ is homogeneous, i.e. independent on the spatial position, and isotropic, i.e. independent of direction, both $\boldsymbol{\alpha}$ and $\boldsymbol{\beta}$ contract to pseudo-scalars, such that:

$$\alpha_{ij} = \alpha\delta_{ij} \tag{4.10}$$

$$\beta_{ijk} = \beta\epsilon_{ijk}. \tag{4.11}$$

Inserting this approximation ($\mathcal{E} = \alpha\overline{\boldsymbol{B}} - \beta\nabla \times \overline{\boldsymbol{B}}$) into the mean field induction equation (eq. 4.4) leads to

$$\frac{\partial \overline{\boldsymbol{B}}}{\partial t} = \nabla \times \left[(\overline{\boldsymbol{u}} \times \overline{\boldsymbol{B}}) + (\alpha\overline{\boldsymbol{B}} - \beta\nabla \times \overline{\boldsymbol{B}})\right] - \lambda\nabla \times \nabla \times \overline{\boldsymbol{B}} \tag{4.12}$$

$$= \nabla \times (\overline{\boldsymbol{u}} \times \overline{\boldsymbol{B}}) + \nabla \times \alpha\overline{\boldsymbol{B}} - (\beta + \lambda)\nabla \times \nabla \times \overline{\boldsymbol{B}} \,. \tag{4.13}$$

Therefore the β-term is acting as an additional diffusion and we combine both into the turbulent diffusivity $\lambda_T = \beta + \lambda$. This is already a useful equation, as long as knowledge of α is either provided or not needed, depending on the application. Attempts to directly evaluate the coefficients of the α-tensor from 3D numerical simulations were made by Schrinner (2011), Schrinner et al. (2005, 2007), where the studies compare the applicability of the mean field approach to direct numerical simulations. However, we want to derive a dispersion relation for the dynamo waves and therefore describe the α-effect in more detail. Even though it would be possible to use this so called 'test field method' (Schrinner 2011) and explicitly calculate the components of the α-tensor, we restrict us to a simpler procedure. If isotropic turbulence is assumed α is a pseudo-scalar field

$$\alpha = -\frac{\tau}{3}\,\overline{\boldsymbol{u}' \cdot \nabla \times \boldsymbol{u}'} \tag{4.14}$$

and is thus proportional to the azimuthally averaged helicity of the turbulent velocity field. The graphical interpretation of this induction mechanism, was given by Parker (1955). This 'Parker Loop' mechanism, assumes that a horizontal field line is bended by the convection into the vertical direction, twisted around a vertical axis and thus forms magnetic field perpendicular to the initial horizontal field line (Proctor 2006). A new unknown, the correlation time τ appeared. It reflects the time for which the mean field does still depend on the (or 'memorizes') its state during an earlier time. We estimate τ as the ratio of a convective length scale and a typical convective flow amplitude.

For the further analysis of the mean induction equation, we introduce the separation into poloidal and toroidal field. If we assume axisymmetry, the toroidal field only has an azimuthal component. The poloidal field is described as the curl of the magnetic vector potential $\boldsymbol{a}$, what also has only an azimuthal component.

$$\overline{\boldsymbol{B}} = \boldsymbol{b} + \boldsymbol{\nabla} \times \boldsymbol{a} = b\hat{\boldsymbol{e}}_{\boldsymbol{\phi}} + \boldsymbol{\nabla} \times (a\hat{\boldsymbol{e}}_{\boldsymbol{\phi}}) \tag{4.15}$$

The curl of a toroidal (poloidal) field is then purely poloidal (toroidal), where the cross product of two toroidal (poloidal) fields vanishes. The induction equation for the mean field reads then:

$$\begin{aligned}\frac{\partial(\boldsymbol{b} + \boldsymbol{\nabla} \times \boldsymbol{a})}{\partial t} &= \boldsymbol{\nabla} \times [(\overline{\boldsymbol{u}} \times \boldsymbol{b}) + (\overline{\boldsymbol{u}} \times \boldsymbol{\nabla} \times \boldsymbol{a}) + \alpha\boldsymbol{b} + \alpha(\boldsymbol{\nabla} \times \boldsymbol{a})] - \lambda_T \boldsymbol{\nabla} \times \boldsymbol{\nabla} \times \boldsymbol{b} \\ &- \lambda_T \boldsymbol{\nabla} \times \boldsymbol{\nabla} \times \boldsymbol{\nabla} \times \boldsymbol{a} \, .\end{aligned} \tag{4.16}$$

We separate terms which contribute to the poloidal and toroidal field, respectively. The induction for the two fields are obtained as:

$$\frac{\partial(\boldsymbol{\nabla} \times \boldsymbol{a})}{\partial t} = \alpha\boldsymbol{b} - \lambda_T \boldsymbol{\nabla} \times \boldsymbol{\nabla} \times \boldsymbol{a} \tag{4.17}$$

$$\frac{\partial \boldsymbol{b}}{\partial t} = (\boldsymbol{\nabla} \times \boldsymbol{a}) \cdot \boldsymbol{\nabla}\overline{\boldsymbol{u}} + \boldsymbol{\nabla} \times (\alpha\boldsymbol{\nabla} \times \boldsymbol{a}) - \lambda_T \boldsymbol{\nabla} \times \boldsymbol{\nabla} \times \boldsymbol{b} \tag{4.18}$$

A constant α was used, and we neglected the advection terms ($\overline{\boldsymbol{u}} \cdot \boldsymbol{\nabla}(\boldsymbol{\nabla} \times \boldsymbol{a})$). As we will show later, the magnetic oscillations found during section 3.4.2 are not influenced by the advection.

In the famous work of Parker (1955), he investigated the behavior of the solutions of the mean field induction equation on a plane layer, known as 'Parker model'. Similar to Parker (1955) and Schrinner et al. (2011) we introduce a cartesian coordinate system (x, y, z) corresponding to the spherical coordinates (ϕ, ϑ, r). Further, we write the toroidal and poloidal field $\boldsymbol{b}$, $\boldsymbol{\nabla} \times \boldsymbol{a}$ as scalar fields, since they depend only on x-direction (ϕ before), such that $\boldsymbol{b} = b\ \boldsymbol{e_x}$ and $\boldsymbol{\nabla} \times \boldsymbol{a} = \boldsymbol{\nabla} \times a\ \boldsymbol{e_x}$. The mean velocity is simplified to $\overline{\boldsymbol{u}} = u\ \boldsymbol{e_x}$. The shearing term corresponding to an ω-effect has then two contributions, namely

$$\boldsymbol{\nabla}\overline{\boldsymbol{u}} \cdot (\boldsymbol{\nabla} \times \boldsymbol{a}) = \frac{\partial u}{\partial y}\frac{\partial a}{\partial z} + \frac{\partial u}{\partial z}\frac{\partial a}{\partial y} \tag{4.19}$$

The first describes the shearing due to variation in the zonal flow along the colatitudinal direction y (ϑ before), whereas the second describes the shear due to variations in the radial direction z (r before), what is rather small (see section 3.3.1). Similar to the nondimensionalization of the full MHD induction equation (see section 2.6 and equation 2.68), we introduce a magnetic Prandtl number, but here the turbulent magnetic diffusivity λ_T is used. The final set of equations describing our simplified mean field dynamo are then:

$$\frac{\partial a}{\partial t} = \alpha b + \frac{1}{Pm}\Delta a \tag{4.20}$$

$$\frac{\partial b}{\partial t} = - \underbrace{\alpha \Delta a}_{\alpha} + \underbrace{\frac{\partial u}{\partial y}\frac{\partial a}{\partial z}}_{\omega} + \frac{1}{Pm}\Delta b \tag{4.21}$$

This set of equations yield direct insights into the induction mechanism. The induction of poloidal field is exclusively done by the α-effect, the creation of toroidal field can be done by either α-effect (first term) or via shearing (ω-effect, second term). Parker (1955), Busse and Simitev (2006), Schrinner et al. (2011) used a pure $\alpha\omega$-dynamo model to describe the emergence of dynamo waves. Dropping the α-effect from the induction of toroidal field might not be applicable for our model. Even though up to 80% of the toroidal field is induced by the shear, the additional α-induced contributions might still have an effect on the observed frequencies. Therefore we follow both possibilities.

4.2 Parker Waves and Dispersion Relations

Plane waves can be used to derive an eigenvalue equation. We use the notation of Schrinner et al. (2011) for consistency:

$$a = \hat{a} \exp\left(i\boldsymbol{k} \cdot \boldsymbol{r} + \sigma t\right) \tag{4.22}$$

$$b = \hat{b} \exp\left(i\boldsymbol{k} \cdot \boldsymbol{r} + \sigma t\right) \ , \tag{4.23}$$

where $\sigma = \gamma + i\nu$ is the complex growth rate and $\boldsymbol{k} = (k_x, 0, k_z)$ is the wave number. Firstly we solve for the pure $\alpha\omega$-dynamo (equation 4.21), thus dropping the α-term in the equation for the toroidal field. Inserting the plane wave ansatz gives

$$\sigma\hat{a} = \alpha\hat{b} - \frac{k^2}{Pm}\hat{a} \tag{4.24}$$

$$\sigma\hat{b} = ik_z\frac{\partial u}{\partial y}\hat{a} - \frac{k^2}{Pm}\hat{b} \ . \tag{4.25}$$

To combine both equations into one, we first bring the diffusive part on the left hand side.

$$\left(\sigma + \frac{k^2}{Pm}\right)\hat{a} = \alpha\hat{b} \tag{4.26}$$

$$\left(\sigma + \frac{k^2}{Pm}\right)\hat{b} = ik_z\frac{\partial u}{\partial y}\hat{a} \ , \tag{4.27}$$

which then leads to the dispersion relation

$$\left(\sigma + \frac{k^2}{Pm}\right) = \sqrt{\alpha}\sqrt{ik_z\frac{\partial u}{\partial y}} \ . \tag{4.28}$$

The square root of a complex number $(m + in)$ is in general given by

$$\sqrt{m+in} = \frac{1}{\sqrt{2}}\left[\sqrt{\sqrt{m^2+n^2}+m} + i\,\mathrm{sgn}(n)\sqrt{\sqrt{m^2+n^2}-m}\right] . \tag{4.29}$$

Then we find for the growth rate γ and the frequency ν as the real and imaginary part of this root:

$$\gamma_{\alpha\omega} = -\frac{k^2}{Pm} + \sqrt{\frac{\alpha}{2}}\sqrt{k_z\frac{\partial u}{\partial y}} \tag{4.30}$$

$$\nu_{\alpha\omega} = \sqrt{\frac{\alpha}{2}}\sqrt{k_z\frac{\partial u}{\partial y}} . \tag{4.31}$$

This shows that the frequency increases like the square root of the zonal flow shear. Furthermore, we derive a second dispersion relation while keeping the second α-term. Inserting the plane wave ansatz into the full equation 4.21, gives

$$\sigma\hat{a} = \alpha\hat{b} - \frac{k^2}{Pm}\hat{a} \tag{4.32}$$

$$\sigma\hat{b} = \left(\alpha k^2 + ik_z\frac{\partial u}{\partial y}\right)\hat{a} - \frac{k^2}{Pm}\hat{b} . \tag{4.33}$$

Similar to the pure $\alpha\omega$ model, we derive a dispersion relation

$$\left(\sigma + \frac{k^2}{Pm}\right) = \sqrt{\alpha}\sqrt{\alpha k^2 + ik_z\frac{\partial u}{\partial y}} \tag{4.34}$$

The above introduced relation for the root of complex numbers (equation 4.29) is applied. This yields:

$$\gamma_{\alpha^2\omega} = -\frac{k^2}{Pm} + \sqrt{\frac{\alpha}{2}}\sqrt{\sqrt{(\alpha k^2)^2 + \left(k_z\frac{\partial u}{\partial y}\right)^2} + \alpha k^2} \tag{4.35}$$

$$\nu_{\alpha^2\omega} = \sqrt{\frac{\alpha}{2}}\sqrt{\sqrt{(\alpha k^2)^2 + \left(k_z\frac{\partial u}{\partial y}\right)^2} - \alpha k^2} . \tag{4.36}$$

The mathematical differences 4.31 shows already that this $\alpha^2\omega$-approach predicts smaller frequencies. The difference depend on the relative amplitude of zonal shear and the α-effect.

4.3 Evaluating the Helicity

Before we compare the frequencies measured from the time evolution of Gauss coefficients with the prediction from the two dispersion relations, we have to quantify how to calculate the helicity h. The α-effect is proportional to the kinetic helicity, thus estimating the potential of inducing magnetic field via helical flows. The MagIC code (Wicht 2002, Christensen and Wicht 2007) calculates the azimuthally averaged helicity out of the full flow velocity

$$h(r,\vartheta) = \overline{\boldsymbol{u} \times (\boldsymbol{\nabla} \times \boldsymbol{u})}\ , \tag{4.37}$$

and integrates h over a single hemisphere. This method works fine, if the axisymmetric flows do not contribute. Typically zonal flows are expected to be small for planetary dynamo models. But here very strong zonal flows are induced by the CMB heat flux anomaly in the form of thermal winds. The divergence of this thermal winds at the rigid walls will create a significantly amount of additional vorticity perpendicular to the flow, thus helicity. In the boundary driven models we study here, the helicity should be constrained to the southern hemisphere along with the convective motions and explicitly being hemispherical. To analyze the interplay of zonal flows and the rigid mechanical boundary conditions, we investigate radial profiles of the helicity averaged over a single hemisphere such that

$$h(r) = \int \overline{\boldsymbol{u} \times (\boldsymbol{\nabla} \times \boldsymbol{u})} \sin\vartheta \, d\vartheta\ , \tag{4.38}$$

where the integral is taken either over the northern or the southern hemisphere. Figure 4.1 shows the radial helicity profile for the northern (red) and southern hemisphere (blue) as function of the radius for a standard boundary forced case with $E = 10^{-4}$, $Ra = 4 \times 10^7$, $Pm = 2$ and $g = 100\%$. The large peaks close to the outer boundary are visible in both hemispheres and comparable in amplitude hence suggesting the influence of the zonal flows. The sign is opposite in both hemisphere, since the zonal flow is eastward in the north and westward in the south. The large zonal flows will have to vanish at the rigid boundaries. This obviuosly introduces large amounts of helicity which does not contribute to the α-effect. To avoid this problem, we use only the nonaxisymmetric flow

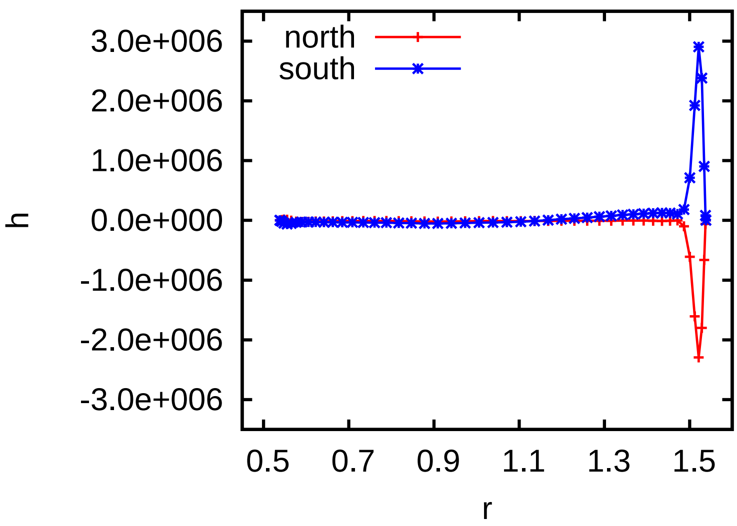

Figure 4.1: Radial profile of the helicity for northern (red) and the southern hemisphere (blue).

contributions and recalculate the helicity

$$h(r) = \int \overline{\boldsymbol{u}' \times (\boldsymbol{\nabla} \times \boldsymbol{u}')} \sin\vartheta \, d\vartheta \, . \tag{4.39}$$

The avoid problems with the mechanical boundaries, we further cut out the double thickness of the Ekman layers δ_E from the radial profiles. The Ekman layer gives the thickness of the mechanical boundaries, if the motion is dominated by Coriolis force and its thickness is of the order of $\delta_E = E^{1/2}$ (Soward and Dormy 2007). Figure 4.2 shows the radial profiles of the azimuthal averaged helicity calculated from the non-axisymmetric flow for the northern (light blue) and southern (orange) hemispheres and profiles (blue/red) if we cut the points being inside the double thickness of the Ekman layer. The usage of the nonaxisymmetric flow decreased the helicity dramatically and brought in the expected hemispherical asymmetry as shown by the light blue and orange curve in figure 4.2. Cutting the boundaries might be a valid approximation, since the potential to create magnetic field close to the boundaries is only given when there is magnetic field. Toroidal field has to decay to zero at the inner and outer boundaries. Hence the thickness of magnetic and flow boundaries are comparable, because the magnetic and viscous diffusivity in terms of the magnetic Prandtl number is of order unity, the helicity introduced by the rigid walls might not create poloidal field simply because the toroidal needed for such a process is not present there. The boundary cutted helicity (figure 4.2, blue and red curves) are used from now.

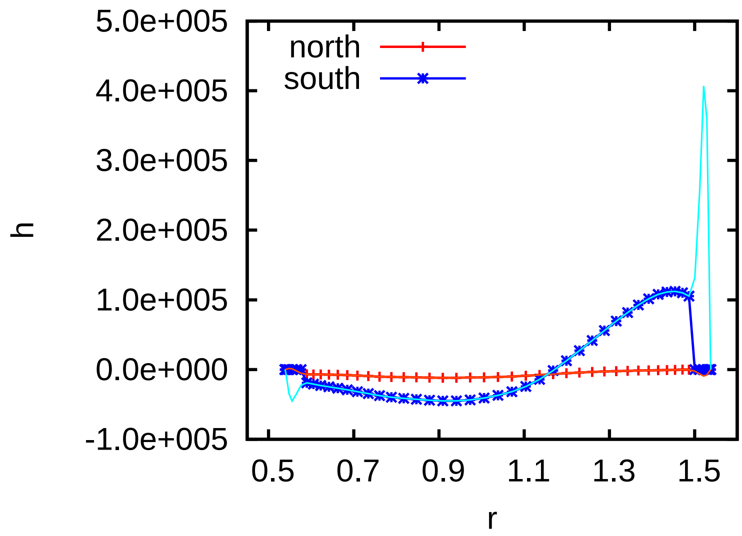

Figure 4.2: Radial profile of the helicity for northern (red) and the southern hemisphere (blue).

Interestingly, the modified kinetic helicity $h(r)$ for the southern hemisphere (same figure, red blue curve) changes the sign in the shell. Thus, we plot the radial profiles of the modified helicity for several perturbation amplitudes for the northern (figure 4.3 top plot) and southern hemisphere (same figure, bottom plot). For the homogeneous reference case ($g = 0\%$, red curves) the helicity is equatorially antisymmetric and negativ (positiv) for all radii in the northern (southern) hemisphere. An equatorially antisymmetric helicity might create an equatorially antisymmetric magnetic field, such as the dipole field for that case. If now the perturbation amplitude is increased the helicity in the northern hemisphere decreases according to the reduction of convection in the northern hemisphere (other curves in figure 4.3, top plot). For the southern hemisphere the helicity becomes more negative close to the inner core boundary with increasing g and remains positive close to the outer core boundary. Thus a hemispherical helicity creates a hemispherical magnetic field.

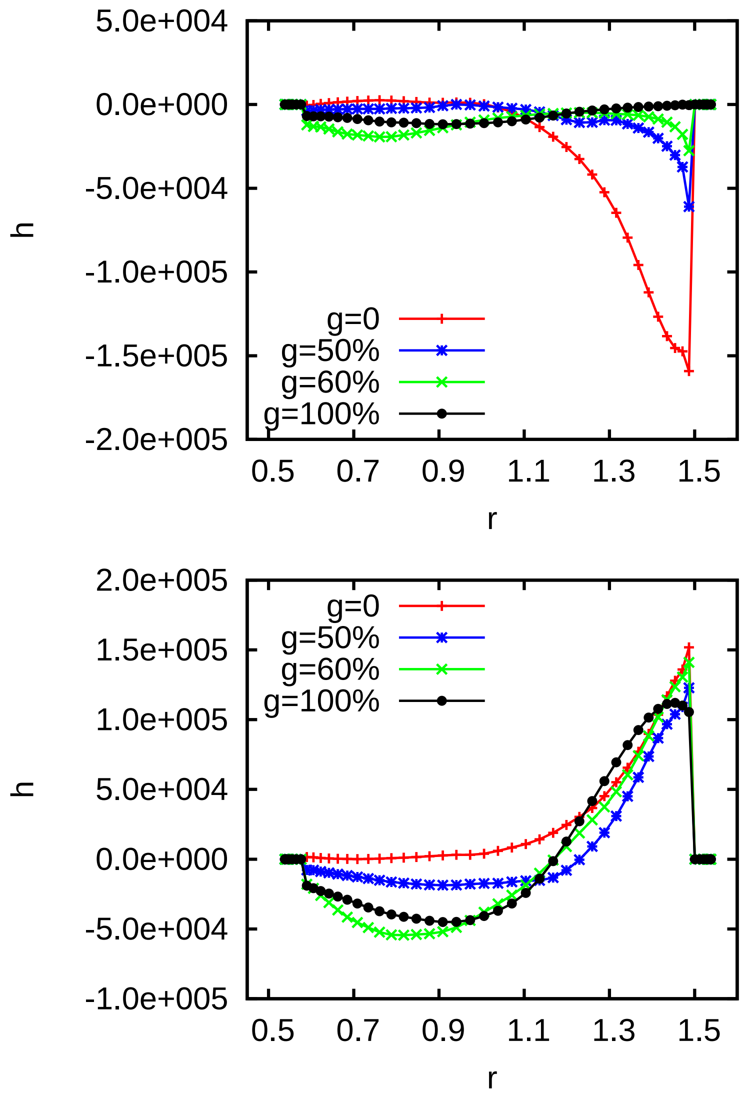

Figure 4.3: Radial profile of the helicity for northern (upper plot) and the southern hemisphere (lower plot) for different perturbation amplitudes.

Even though interesting to see, our main interest is an estimate of the total helicity on the southern hemisphere in order to work with the dispersion relations for the mean field $\alpha\omega$ and $\alpha^2\omega$ dynamos. Since the helicity changes sign, a simple integration over the radius will not provide the correct measure of the potential to induce magnetic field via the α-effect. Instead, we use the rms helicity of the southern hemisphere

$$h_{SH}^{rms} = \left[\int_{\pi/2}^{\pi} \int_{r_i+2\delta_E}^{r_o-2\delta_E} \overline{(\boldsymbol{u}' \times (\nabla \times \boldsymbol{u}'))}^2 r^2 \ \sin\vartheta \, d\vartheta \, dr \right]^{1/2} . \tag{4.40}$$

The radial integration is restricted to points which are two Ekman layer thicknesses away from the boundaries.

4.4 Application to Hemispherical Dynamos

The liability of the used assumptions can be justified, when comparing the predicted frequencies with those measured from the numerical simulations. Given the numerous approximations involved it is not expected to match the measured frequencies very accurately, the calculated dispersion should at least predict the correct order of magnitude and follow the same trend, e.g. when increasing the shearing. In the 3D simulations the transformation from classical columnar dynamo into the hemispherical solution can be studied while varying the amplitude of the relative strength of the heat flux anomaly. When the hemispherical convection mode is strong, magnetic and velocity field is strongly axisymmetric and thus more applicable to the mean field theory.

Busse and Simitev (2006) and Schrinner et al. (2011) simplified the dispersion relation further in approximating the wave number k_z and the derivatives with typical length scales. We follow that approach and evaluate the shear term $\partial u/\partial y$ such that

$$\frac{\partial u}{\partial y} \approx \frac{u}{\delta y} = \frac{Re^*}{\delta_y} , \tag{4.41}$$

where δy is the characteristic variation length scale of the shear in latitudinal direction and Re^* is the Reynolds number associated with the axisymmetric energy (as in equation 3.16, in section 3.6.4). It is reasonable that, δy is half the circumference along y-direction (ϑ before) at mid depth.

$$\delta y \approx \pi(r_i + r_o)/2 \approx \pi , \tag{4.42}$$

where $r_i = 0.54$ and $r_o = 1.54$, the nondimensional inner and outer core radii. The characteristic length scale in radial direction is then $\delta z \approx (r_o - r_i) = 1$, the shell thickness. The wave numbers k_z and k_y correspond to the 2π-th of the equivalent inverse length scale and are given by:

$$k_z = \frac{2\pi}{\delta_z} = 2\pi \tag{4.43}$$

$$k_y = \frac{2\pi}{\delta_y} = 2 \tag{4.44}$$

$$k^2 = 4 + 4\pi^2 . \tag{4.45}$$

The definition of the α quantity (equation 4.14) contains not only the helicity, but also the correlation time τ. For this we use

$$\tau = \frac{d_{con}}{Re^{con}} , \tag{4.46}$$

where d_{con} is a characteristic convective length scale. We take the mean degree $\bar{l}$ from the spectrum of the nonaxisymmetric kinetic energy to evaluate $d_{con} = 1/\bar{l}$. The frequencies predicted in a pure $\alpha\omega$ model $\nu_{\alpha\omega}$, and for the more realistic $\alpha^2\omega$ model $\nu_{\alpha^2\omega}$ are then roughly:

$$\nu_{\alpha\omega} = \sqrt{\frac{\alpha}{2}}\sqrt{k_z\frac{Re^*}{\delta_y}} \tag{4.47}$$

$$\nu_{\alpha^2\omega} = \sqrt{\frac{\alpha}{2}}\sqrt{\sqrt{(\alpha k^2)^2 + \left(k_z\frac{Re^*}{\delta_y}\right)^2} - \alpha k^2}\,. \tag{4.48}$$

Figure 4.4 tests the two different dispersion relations. It is obvious that the second α-term significantly reduces the frequencies. Furthermore, the $\alpha^2\omega$-dispersion fits slightly better the observed frequencies obtained from the time evolution of the Gauss coefficients (see figure 3.18). The misfit increases strongly at small Re^* where the system is in a non or weakly perturbed state and the ω-effect is very weak and the mean field assumptions therefore break down. The better agreement of the frequencies with the $\alpha^2\omega$ dispersion at larger Re^* indicates that the α-effect still plays a role for toroidal field production. Both dispersion relations show the same trend for increasing the shear amplitude, what is characteristic feature of the Parker waves (Parker 1955). The two dispersion relations differ only by a factor of two or three. If one takes the numerous simplifications and estimates into account we can conclude that both might fit.

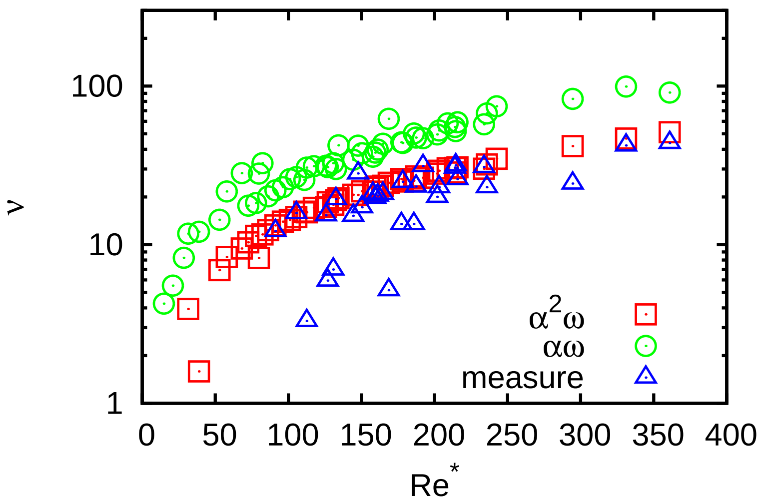

Figure 4.4: Frequencies measured from the evolution of the Gauss coefficients (blue triangles), the frequencies calculated by the $\alpha\omega$ (eq. 4.31, green circles) and the $\alpha^2\omega$ (eq. 4.36, red squares) dispersion relation as function of the zonal flow amplitude given by Re*.

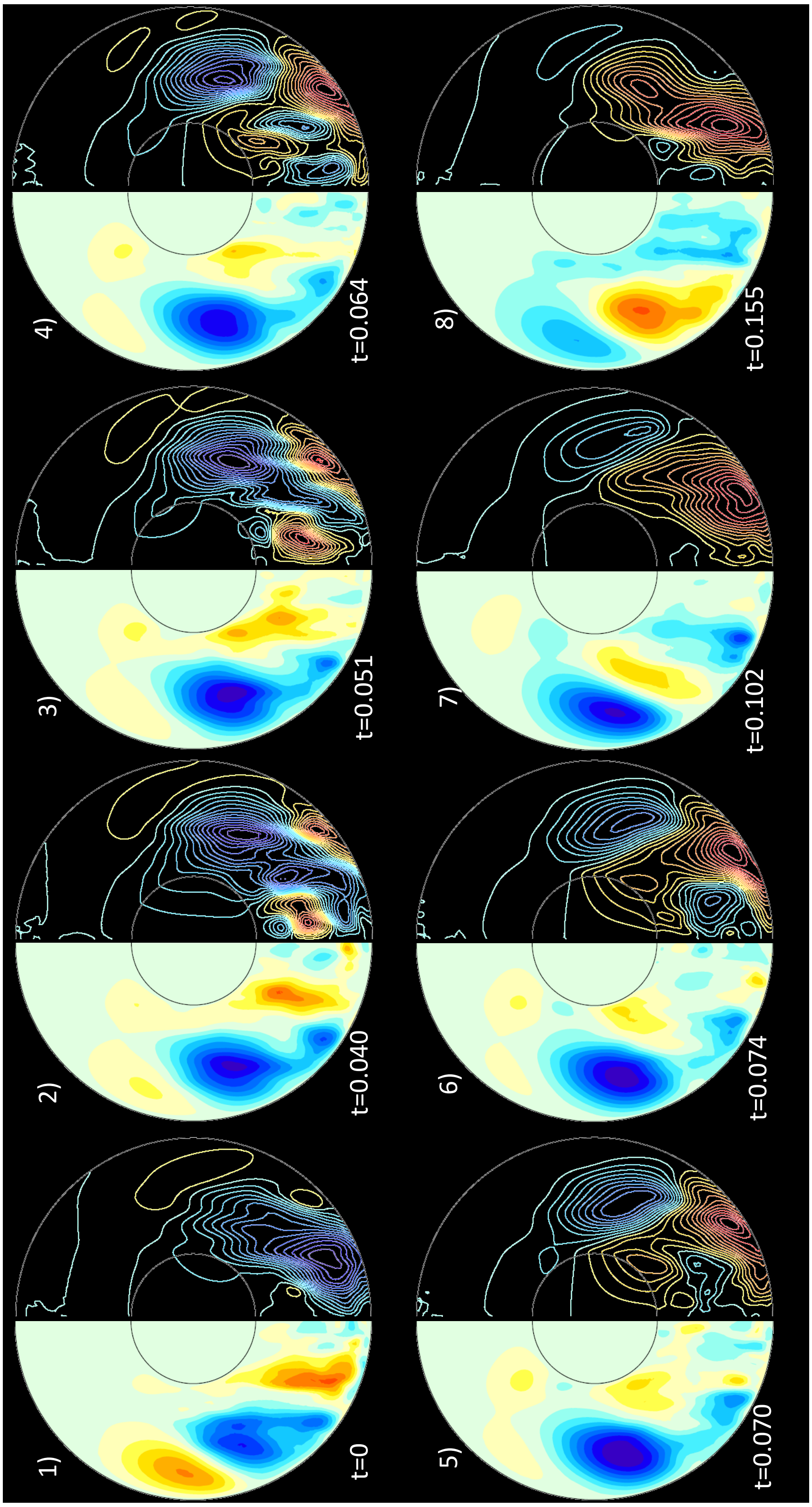

Figure 4.5: Evolution of the axisymmetric toroidal (right) and poloidal field lines (left halfs) during half a wave cycle. The time steps between two individual snapshots are non-equidistant.

Yoshimura (1976) studied the evolution of Parker waves in the solar context. There it was found that the 22-year-cycle of the solar magnetic field can be explained with a mean field dynamo approach (Stix 2002, Rüdiger and Hollerbach 2004). On the sun, the field changes polarity every 11 years, whereas periods of strong magnetic field are associated with the presence of sun spots and other magnetically driven activity on the solar surface. The sunspots show a characteristic migrating behavior, where the spots appear pairwise (but with different polarity) on either side of the solar equator in higher latitudes. Then they migrate equatorwards, describing the typical pattern of the famous butterfly diagrams. The sunspots represent the poloidal part of the magnetic field. For the sun it is believed, that a mean field model of a $\alpha\omega$-dynamo type can describe the correct reversal and migration properties of the solar magnetic field (Yoshimura 1976). The direction of the Parker dynamo wave depends on the product of α-effect and the zonal flow gradient thus the ω-effect and their signs. The ω-effect is associated with the differential rotation, where the strongest radial gradients of the angular velocity reside at the bottom of the convective zone (tachocline). It might be a difficult task, to predict the dominant sign of the α-term in the convective hemispheres of the sun. Therefore several mechanism were proposed to explain the equatorward migration of the sunspots associated with the poloidal field. Tobias and Weiss (2007), Rüdiger and Hollerbach (2004) give recent reviews on that issue.

We propose, that the dynamo waves found in the hemispherical dynamos share characteristics with the solar magnetic field and its cyclic dependence beyond the dispersion relation for the Parker waves. Therefore we firstly show a series of axisymmetric poloidal field lines and axisymmetric toroidal field during half a wave cycle in figure 4.5. The left halfs show the toroidal field and the right halfs the poloidal field lines. The cycle can be interpreted as starting a mid southern latitude at the outer boundary (compare figure 4.5, small red patch, plot 1). Here normal polarity field (red) is amplified (2), moves radially inward (3,4) and then northward (5,6) along the inner boundary. It then starts to move radially outward (7,8) and finally southward along the outer boundary to close the cycle. During the cycle cancellations and variations in the production efficiency lead to variation in the field strength.

To compare this to the migration direction predicted from mean field $\alpha\omega$ dynamos, figure 4.6 shows the isocontours of the zonal averaged angular velocity. Yoshimura (1976) showed how the signs of α-effect and differential rotation or shear, $\partial u/\partial y$ affects the propagation direction. Figure 4.6 shows isocontours of the angular velocity, what is proportional to the zonal velocity and changes from strongly westward in the northern hemisphere to eastward in the southern. This gradient in latitude (y-direction in our notation) seem to be the major source of the gradients in the angular velocity, a variation in radial direction is not clearly visible. Note, that we had neglected the shear along the radius (z-direction). The gradient $\partial u/\partial y > 0$ everywhere in the shell except for the region inside the tangent cylinder at the southern pole. The sign of the α-effect flips at half radius of the shell, as shown in figure 4.3, lower plot. Thus the product $\alpha\ \partial u/\partial y$ is negative (positive) close to outer (inner) boundary, representing an southward (northward) migration (Yoshimura 1976, Rüdiger and Hollerbach 2004). This seems to be consistent with the migration of the dynamo wave shown in figure 4.5. It should be noted, that the numerous simplifications included in the mean field model might just be marginally satisfied. Even though the main field and flow is indeed axisymmetric, we further assumed, besides other approximations, that the zonal flow gradient is only strong for the latitudinal direction. Especially close to the southern pole, this might be true. Also we assumed the α to be constant and isotropic, although we had seen that the helicity is strongly hemispherical and the turbulent convection in the southern hemisphere has strong gradients and time dependencies. Thus we expect derivations from the simplified mean field theory. But it remains an interesting fact, that if applying a simple $\alpha\omega/\alpha^2\omega$ dynamo model, the order of magnitude predictions for the frequencies of the magnetic oscillations and the migration are consistent with Parker's wave theory (Parker 1955).

Furthermore, Yoshimura (1976), Tobias and Weiss (2007) pointed out, that a $\alpha\omega$ dynamo wave migrates along isolines of constant angular velocity. This (for our case) radial motion is visible at the equator. The field migrating northward close to inner boundary (see figure 4.5, red polarity, plot 7 and 8), moves outwards and pushes the other (blue) polarity ahead and southwards.

As another agreement with the Parker dynamo waves, in some of our simulations we can observe a phase shift between the poloidal and toroidal magnetic field energy. Figure 4.7 shows the time evolution of both fields during several magnetic oscillations. Yoshimura (1976) predicted from the analysis of mean field $\alpha\omega$ waves, that the poloidal field is ahead of the toroidal field by a phase shift of $\pi/4$. Note, in the study this is used to determine the sign of of α in each hemisphere. Figure 4.7 clearly brings out a phase shift. The black bar denotes a full cycle time (representing 2π), and the phase shift of $\pi/4$ in blue color. However, the phase shift fits quite well to time evolution of the fields.

For the sun the evolution of the sunspots were used to measure the frequencies and migration behavior of the solar field. A so called 'butterfly diagram' plots the radial field at the surface or a scatter plot of the sunspots as function of the time. We use the axisymmetric poloidal field to plot a similar figure (4.8). The amplitude and direction of axisymmetric field at the CMB is shown as function of time (here real time) and latitudinal angle. The time scales of the solar cycle are roughly 22 years, where here the slowest waves in our model have oscillation periods of roughly tens of thousands years. The details of rescaling the viscous to physical time is described in section 5. In figure 4.8 the slopes of the magnetic field patches vary with latitude. The southward migration of a patch of given polarity is rather slow as shown by smaller slopes, whereas the inward migration and amplification is fast.

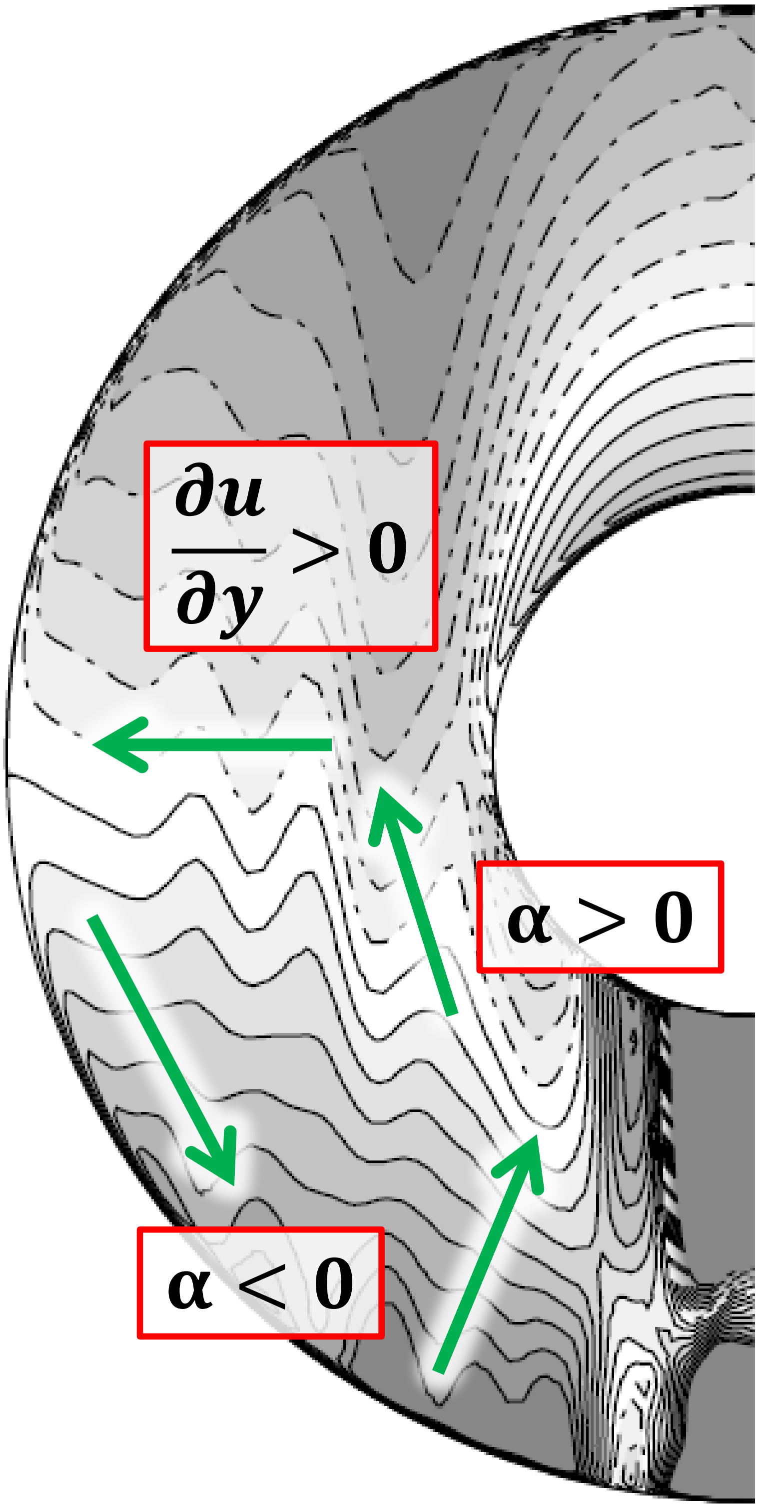

Figure 4.6: Gray-shaded isocontours of the zonal averaged angular velocity in black and white shows the main shear due to zonal flow gradients is in latitudinal direction. The shear ∂u/∂y associated with the ω-effect is positive everywhere, whereas the α-effect changes sign from $\alpha > 0$ near the inner boundary to $\alpha < 0$ close to the outer boundary (CMB). For comparison in figure 4.3, lower plot the radial profile of the helicity was discussed.

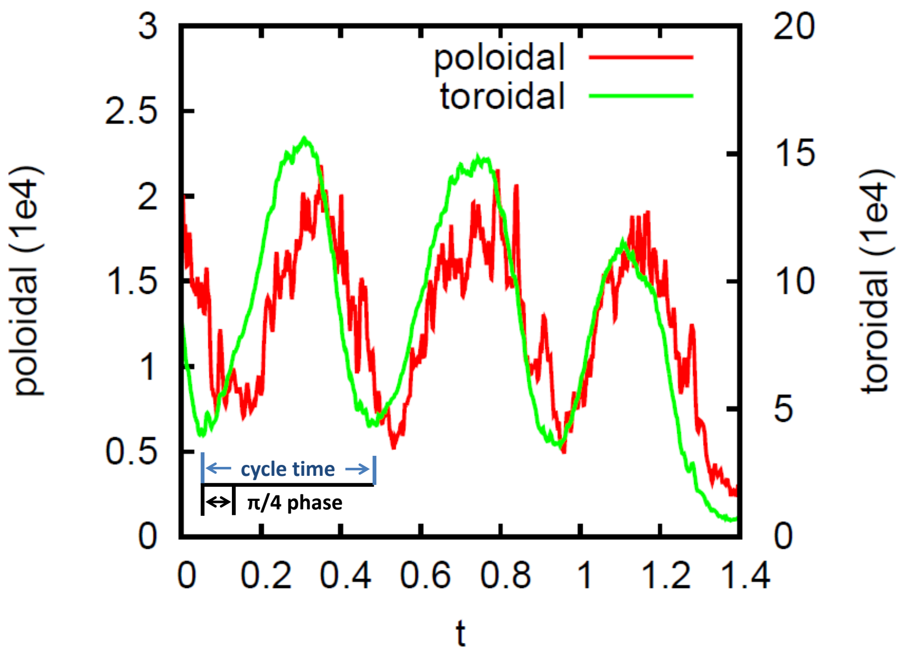

Figure 4.7: Time evolution of poloidal (red) and toroidal (green) magnetic field during several wave cycles. There seems to be a consistent phase shift between the two energies. Time scale at the left bottom denotes a full cycle and the appropriate $\pi/4$-fraction of it.

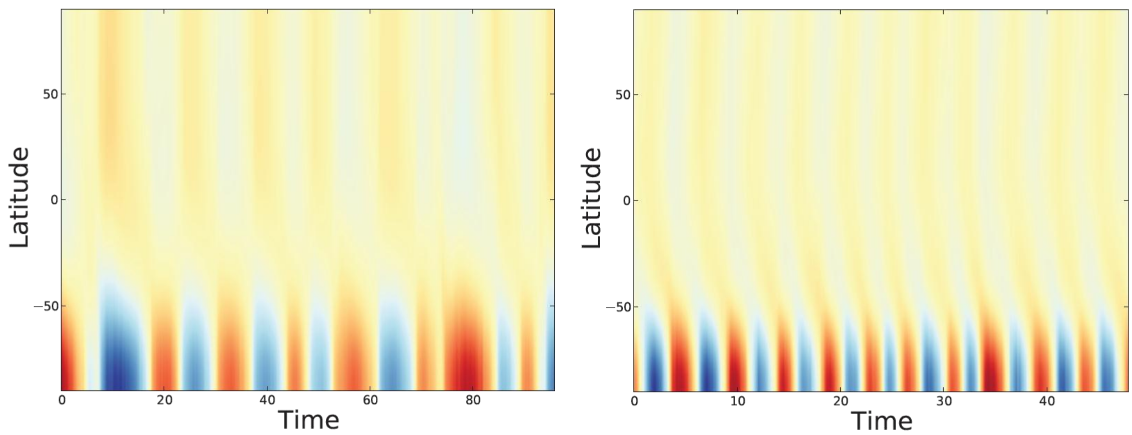

Figure 4.8: Time evolution of the poloidal CMB field as a function of latitude for two different frequencies. Note, that time scale is rescaled to kyrs and slightly different in the right plot. We refer to the section 5 for the details of the time rescaling.

5 Application to Mars and Discussion

The main research highlights of the this chapter are compiled in a publication named 'A hemispherical dynamo model: Implications for the Martian crustal magnetization' and re-submitted after moderate revision to the 'Physics of the Earth and Planetary Interiors' (PEPI).

In this section we aim to relate our findings to the crustal magnetization of Mars. Although we could show that it is indeed possible to enforce a substantial hemispherical dynamo by combining internal heating as driving mode and apply a degree-1 anomaly on the CMB heat flux, there are further constraints for using such magnetic fields as an admissible model for the hemispherical pattern of the crustal magnetization on todays Mars. To compare our numerical results to the satellite and meteorite measurements, we have to continue the magnetic fields upwards to the surface and rescale time and magnetic field strength to physical units. As mentioned in the introduction (section 1.4.2), the measured pattern of the crustal magnetization reveals a distinct hemisphericity, thus most of the magnetic anomalies are located south of the equator (Acuña et al. 1999). Figure 5.1 shows a reconstruction of the radial magnetic field according to the crustal magnetization measurements by the MGS space craft (Langlais et al. 2004). Amit et al. (2011) calculate a root mean square amplitude of the magnetic field in the northern and southern hemisphere of 8.4 and 29.5 nT, respectively.

To address whether our model provides a realistic explanation for the crustal magnetization of Mars, we compare the numerical results to the hemisphericity of the crustal field and furthermore to predictions of the ancient dynamo field strength. Estimates of the strength of the magnetizing field are based on paleomagnetic analysis of Martian meteorites (ALH 84001) and range from 5 to 50 μT (Weiss et al. 2002). Details on the laboratory investigation of that meteorite can be found in section 1.4.2 or in greater detail in Weiss et al. (2010) and Langlais et al. (2010).

In our numerical simulations magnetic field strength is given in terms of the square root of the Elsasser number $\Lambda = B^2/\mu_0\lambda\rho\Omega$. We rescale to dimensional units, by assuming a mean density of $\rho = 7000\,\mathrm{kg/m^3}$, mean rotation rate of $7.1 \times 10^{-5}\,\mathrm{s^{-1}}$, magnetic diffusivity $\lambda = 2\,\mathrm{m^2/s}$, radius of surface and CMB $r_{sur} = 3.39 \times 10^6$ m and $r_{sur} = 1.55 \times 10^6$ m, respectively. The physical parameters are taken from table 1.1 and can be found in Morschhauser et al. (2011) or Jones (2007).

An alternative way of rescaling magnetic field strength has been proposed by Christensen and Aubert (2006) and relies on the convective power available to drive the dynamo. However, our simulations show that the magnetic field strength significantly depends on the perturbation pattern and amplitude and therefore their scaling laws based on homogeneous temperature boundary conditions do no apply. Even if the convective power as given by the Rayleigh number is kept constant, the field strength varies strongly

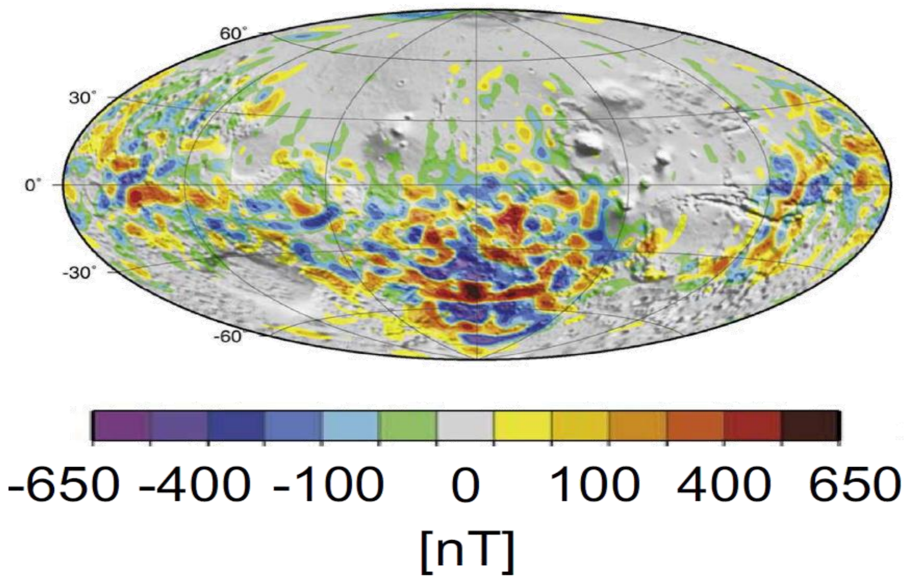

Figure 5.1: Reconstructed radial magnetic field at 200 km altitude from Langlais et al. (2004) using equivalent dipole sources.

due to the gradual change to the hemispherical magnetic field with significantly lower magnetic energy.

The rescaling of the time can be done in different ways. The nondimensional time scale used in this study is the viscous diffusion time $\tau_\nu = D^2/\nu$. However, since we are mostly interested in the dynamo process this is converted into a magnetic diffusion time scale τ_λ by multiplying with the magnetic Prandtl number Pm:

$$\tau_\lambda = \frac{D^2}{\lambda} = \tau_\nu Pm \,. \tag{5.1}$$

The time is then rescaled by setting τ_λ to a realistic planetary value. Using $D = 1.09 \times 10^6$ m we find $\tau_\lambda = 17\,\text{kyrs} \cdot Pm$. In principle each of the nondimensional numbers could be used for rescaling the time, since these numbers are defined as the ratios between time scales (see table 2.2 for details). For example the magnetic Reynolds number Rm as the ratio magnetic diffusive and advection time scale, D^2/λ and D/U, respectively, can be used as well if a characteristic velocity U is know. For the Earth, the secular variation might give this velocity scale.

5.1 Surface Extrapolation

In order to describe the field magnetizing the crustal rocks, we extrapolate the result of the hemispherical dynamo towards the planetary surface using a potential field extrapolation (equation 5.9). This approach was applied to Earth's magnetic field by Gauss and assumes an electrically isolating mantle and thus no electrical currents in the mantle. The magnetic field in the absence of currents is equivalent to a simple diffusive process. The Maxwell equation ($\nabla \times \boldsymbol{B} = \boldsymbol{j}$) then simplifies with $\boldsymbol{j} = 0$ to

$$\nabla \times \boldsymbol{B} = 0 \, . \tag{5.2}$$

The magnetic field is then a conservative vector field and can be described as the gradient of a scalar potential b

$$\nabla b = \boldsymbol{B} \, . \tag{5.3}$$

Applying a divergence operator on this equations yields the Laplace equation

$$\Delta b = 0 \, . \tag{5.4}$$

In spherical coordinates the Laplace operator is defined as

$$\left[\frac{1}{r^2}\frac{\partial}{\partial r}\left(r^2\frac{\partial}{\partial r}\right) + \frac{1}{r^2 \sin\vartheta}\frac{\partial}{\partial\vartheta}\left(\sin\vartheta\frac{\partial}{\partial\vartheta}\right) + \frac{1}{r^2\sin\vartheta}\frac{\partial^2}{\partial\phi^2}\right] b = 0 \tag{5.5}$$

One of the major inventions of Gauss was the description of such a potential field with spherical harmonics (Kono 2007). When assuming the sources are located inside the planet, Gauss proposal is

$$b = r_{sur} \sum_{l}^{\infty} \sum_{m}^{l} \left(\frac{r_{sur}}{r}\right)^{l+1} P_{lm}(\cos\vartheta) \left[g_{lm}\cos(m\phi) + h_{lm}\sin(m\phi)\right] \, , \tag{5.6}$$

where r_{sur} is the surface radius of Mars and P_{lm} are the Schmidt-normalized associated Legendre-polynoms, which are proportional to the spherical harmonics Y_{lm} like

$$Y_{lm} = \frac{1}{\sqrt{2\pi}} \sqrt{\frac{2l+1}{2}\frac{(l+m)!}{(l-m)!}} P_{lm}(\cos\vartheta) \left(g_{lm}\cos(m\phi) + h_{lm}\sin(m\phi)\right) \, . \tag{5.7}$$

Here g_{lm} and h_{lm} are named after its inventor Gauss coefficients (Kono 2007). Equation 5.6 for the magnetic potential b shows the structure of the product ansatz frequently used for solving the Laplace equation. The radial dependence is proportional $r^{-(l+1)}$, whereas the horizontal dependence is given by the spherical harmonics. For the Earth, the Gauss coefficients measured by satellites are used to investigate the temporal evolution of the geomagnetic field (Kono and Finlay 2007). Note, for the Earth the core field is only visible for degree and order $l, m < 13$, because the higher modes are biased by the crustal magnetization (Kono 2007, Purucker and Whaler 2007).

For the further investigation we want to restrict the analysis to the axisymmetric (order or azimuthal wave number $m = 0$), because the main contribution of magnetic field including the cyclic variations follow the axisymmetric field only. Figure 5.2 shows the temporal evolution of several axisymmetric (red and black) and nonaxisymmetric (other colors) Gauss coefficients. It can be seen, the regular oscillations of larger amplitude are mainly carried by the axisymmetric modes. Interestingly they show the same frequency but the signs alternate with the spherical harmonic degree l. The red (black) curve in figure 5.2 corresponds to the g_{10} (g_{20}) thus dipolar (quadrupolar) spherical harmonic mode, which has a equatorial parity of antisymmetry (symmetry). Combining both with opposite sign amplifies the magnetic field in the southern and weakens the field on the northern hemisphere. We refer here to the figure 3.18 showing that all modes belonging to a single symmetry family show same signs, where the dipolar is equatorially antisymmetric and the quadrupolar family is equatorially symmetric. The nonaxisymmetric Gauss coefficients show irregular variations of much weaker amplitude (figure 5.2, green, blue, orange curve). The investigation of the mean field induction equation yielded frequencies for the axisymmetric (mean) magnetic field contributions. We tested the resulting dispersion relation against the frequencies measured from the axisymmetric modes and found a good agreement.

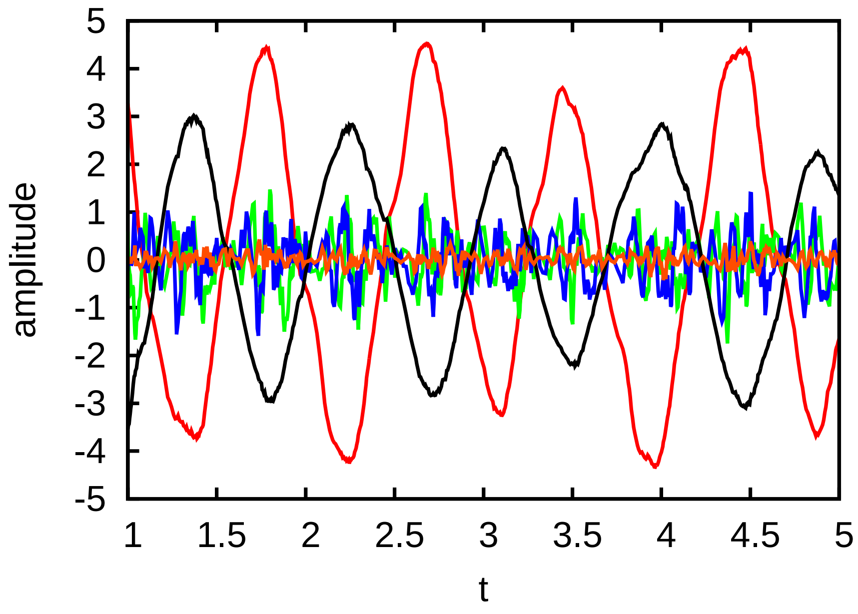

Figure 5.2: Time evolution of the several Gauss coefficients g_{lm} at the Martian surface. The axisymmetric modes (red - g_{10} and black - g_{20}) show regular oscillations with large amplitudes, whereas the nonaxisymmetric (green - g_{11}, blue - h_{11} and orange - g_{22}) have more irregular variations and are weaker in amplitude. The parameters are $E = 10^{-4}$, $Ra = 4 \times 10^7$, $Pm = 2$ and $g = 60\%$.

For the axisymmetric contributions is the azimuthal wavenumber $m = 0$ and all $h_{lm} = 0$, hence the expression for the potential field simplifies to

$$b(r, \vartheta, \phi) = r_{sur} \sum_{l}^{\infty} \left(\frac{r_{sur}}{r} \right)^{l+1} g_l P_l(\cos \vartheta) . \tag{5.8}$$

The radial field is given by the radial derivative of the magnetic potential:

$$B_r(r, \vartheta) = \sum_{l}^{\infty} (l+1) \left(\frac{r_{sur}}{r} \right)^{l+2} g_l P_l(\cos \vartheta) . \tag{5.9}$$

This equation describes the radial dependence of a set of spherical harmonics mode of degree l, where the mode decays with radius the faster the higher l is. The figure 5.3 shows this radial decay of the Gauss coefficients for the first six axisymmetric modes when extrapolating from the CMB to the surface. The heat flux anomaly strength is here $g = 100\%$, the other parameters are $E = 10^{-4}$, $Ra = 4\times10^{7}$, $Pm = 2$ and $Pr = 1$. The core mantle boundary is on the the left side at $r/r_{cmb} = 1$ in figure 5.3, the surface at the right. All modes decay depending on the degree l proportional to $r^{-(l+2)}$ for the field. Therefore the field becomes increasingly dipolar with further extrapolation. In the figure we show a hemispherical dynamo, what is dominated by $l = 4$ and $l = 5$ at the CMB, but the dipolar mode $l = 1$ has the slightly largest amplitude at the surface.

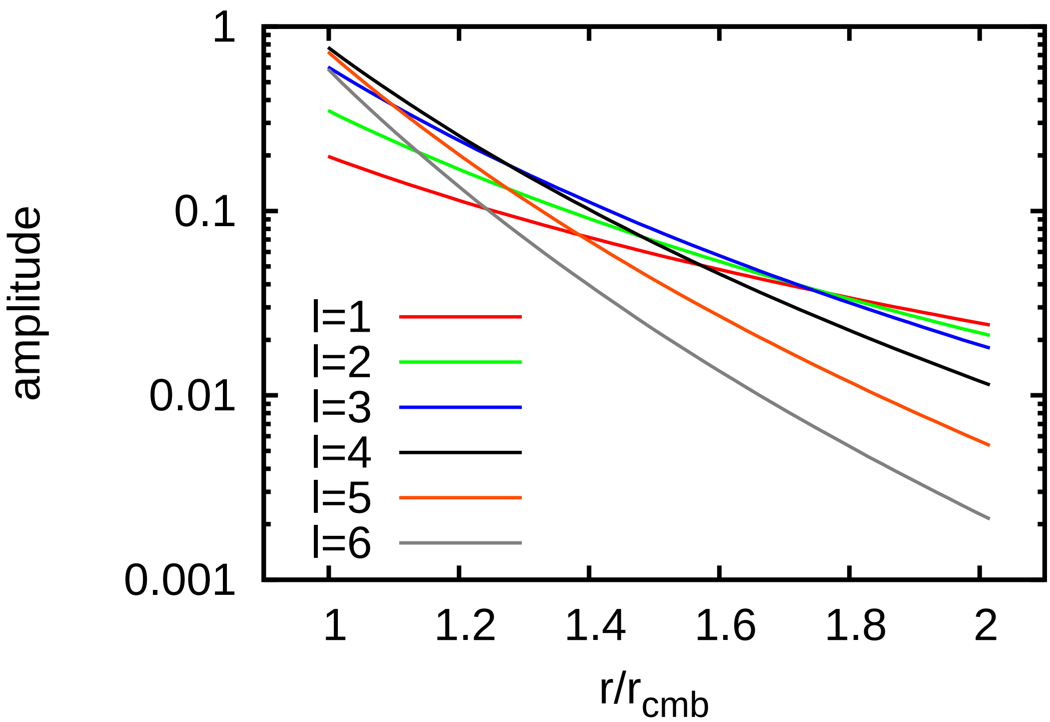

Figure 5.3: Decay of the amplitude of Gauss coefficients when extrapolating the CMB field as a potential field of a hemispherical dynamo. Parameters: $g = 100\%, E = 10^{-4}, Ra = 4\times10^{7}, Pm = 2$ and $Pr = 1$

In figure 5.4 we compare the radial field at the CMB (first plot) and the surface (second), using snapshots of the solution. The surface extrapolation damps the small scales and also the field amplitude. Thus the field at the surface is more dominated by the modes of larger degree l because of the decay proportional to $r^{-(l+2)}$. The increase in dipolarity and decrease of magnetic field amplitude with increasing extrapolation distance is controlled by the spectral distribution of the CMB field. The smaller the dominant magnetic scales at the CMB the stronger are both effects. Note, here all axisymmetric and nonaxisymmetric modes are used.

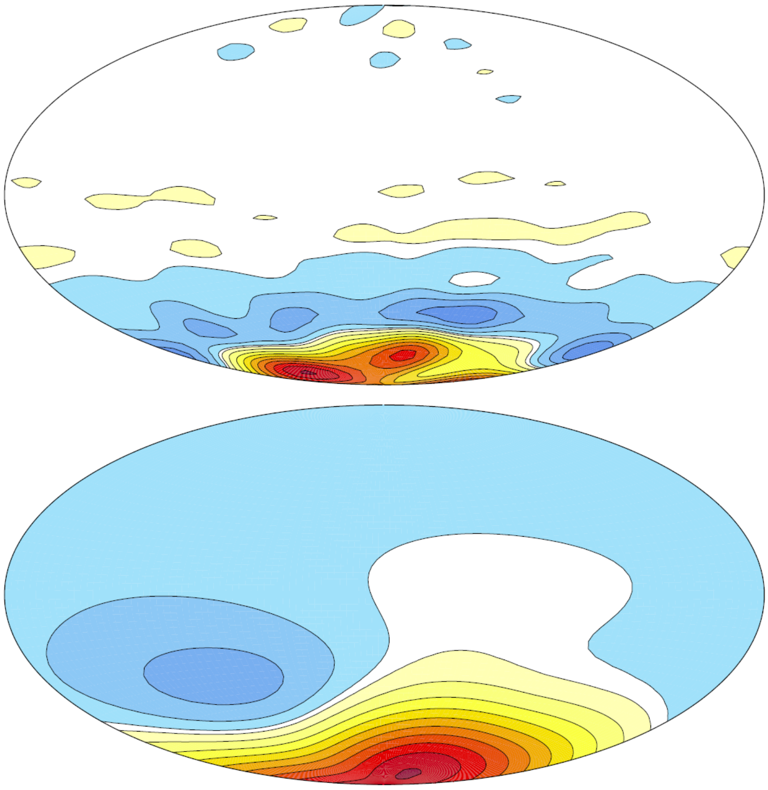

Figure 5.4: Snapshot of the radial magnetic fields taken at the CMB (upper) and at the planetary surface (lower plot) for a hemispherical dynamo. The contour steps are 45μT (upper) and 0.75μT (lower). Parameters as in figure 5.3.

5.2 Hemisphericity

The surface extrapolations of our hemispherical dynamos should match the measured dichotomy of the crustal magnetization. This implies, that there appeared no major resurfacing events altering the dichotomy significantly after magnetization because the measurements are taken 3.7 Gyrs (Langlais et al. 2010) after the magnetization process occurred. To measure the equatorial dichotomy of the magnetic field at the a given extrapolation radius, we sum the unsigned magnetic flux over each hemisphere separately:

$$B_r^{N,S}(r) = \int_0^{2\pi} \int_{0,\pi/2}^{\pi/2,\pi} |B_r(r,\vartheta,\phi)| \sin\vartheta \,\mathrm{d}\vartheta \,\mathrm{d}\phi \,. \tag{5.10}$$

Then, for example $B_r^N(r)$ denotes the surface integral of the unsigned radial field in the northern hemisphere. The hemisphericity $\mathcal{H}(r)$ is then defined as:

$$\mathcal{H}(r) = \left| \frac{B_r^N(r) - B_r^S(r)}{B_r^N(r) + B_r^S(r)} \right| \,. \tag{5.11}$$

The hemisphericity is a function of radius according to the extrapolation away from the core mantle boundary. A pure equatorial symmetric magnetic field such as a dipole, will have by definition $\mathcal{H} = 0$, whereas a magnetic field residing in only one hemisphere will have $\mathcal{H} = 1$. For the crustal magnetization of Mars, Amit et al. (2011) obtained an rms field strength of 29.5 nT in the southern hemisphere and 8.4 nT in the northern. They give an uncertainty range of $\pm\sqrt{3}$ nT. We find then for our hemisphericity measure

$$\mathcal{H}(r = r_{sur}) = 0.55 \pm 0.1 \ . \tag{5.12}$$

The strong hemisphericity of the Martian crustal magnetization puts some contraints on the spectral distribution of the involve magnetic modes (Amit et al. 2011). We therefore further investigate the spectral properties of our dynamos and calculate the hemisphericity introduced above.

5.2.1 Synthetic Spectra

In section 2.9 it was mentioned that a hemispherical magnetic field needs equal contributions of both: the dipolar (equatorially antisymmetric) and quadrupolar (equatorial symmetric) family of magnetic modes. We will investigate the spectral representation of the radial CMB and surface field regarding this property. The dipolar family are all modes where the sum of degree l and order m is odd, which means they are antisymmetric with respect to the equator. The so called quadrupolar family in turn does obey the rule that $l + m$ is even and is therefore symmetric with respect to the equator. Each family alone would yield a hemisphericity $\mathcal{H} = 0$, since the unsigned flux is always equatorially symmetric. An appropriate combination of modes of both families is required to yield a pattern of unsigned magnetic flux with equatorial asymmetry or 'hemisphericity' and values $\mathcal{H} > 0$. To test the effect of such a spectral 'whitishness', a simple test distribution of the Gaussian coefficients is taken with $g_l = 1$ for all l and $r = r_{sur}$:

$$B_r(\vartheta) = \sum_{l=1}^{l=l_{max}} (l+1) P_l(\cos\vartheta) \ . \tag{5.13}$$

The more modes are taken into account, the more the magnetic flux is concentrated towards one of the poles. When all modes have a positive sign, the peak appears on the northern pole. Whereas if the modes of quadrupolar family are multiplied with (-1), the peak is located around the southern pole. Figure 5.5 shows the latitudinal distribution of the radial field as a function of maximum number of modes l_{max}, where all modes have the same amplitude but alternating signs depending on the affiliated symmetry family (dipolar or quadrupolar). The $l_{max} = 1$-case on the left border of figure 5.5 is then a simple axisymmetric dipole field. The further l_{max} increases, the more modes are added and the more the field is concentrated at the southern pole and the more increases the hemisphericity.

In figure 5.6 we calculate the hemisphericities for 'spectral white' fields up to maximum order l_{max} of one thousand. As expected, the hemisphericity $\mathcal{H}$ increases with the maximum number of modes involved. Note, that surface hemisphericities are suggested to be $\mathcal{H}(r_{sur}) = 0.55 \pm 0.1$ (Amit et al. 2011). The 'spectral white' fields match these values from $l_{max} = 3$ and exceed the uncertainty at $l_{max} = 6$ (see figure 5.6). To obtain $\mathcal{H} > 0.8$ twenty modes are needed, whereas to reach unity a thousand seem sufficient.

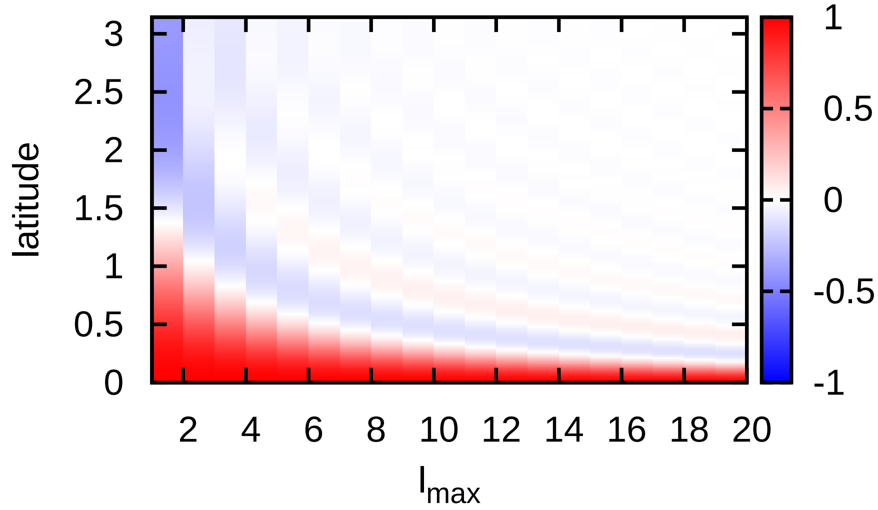

Figure 5.5: Radial field for a hypothetical axisymmetric dynamo with white spectrum up to degree l_{max} (x-axis). In the y-axis the latitude is shown, with 0 - southern pole, $\pi/2$ - equator and π - north pole. The $l_{max} = 1$ field is only an axisymmetric dipole. All fields are normalized such that the maximum peak equals unity.

Thus significant contribution of small scale energy is needed, what is unlikely to be maintained again ohmic decay.

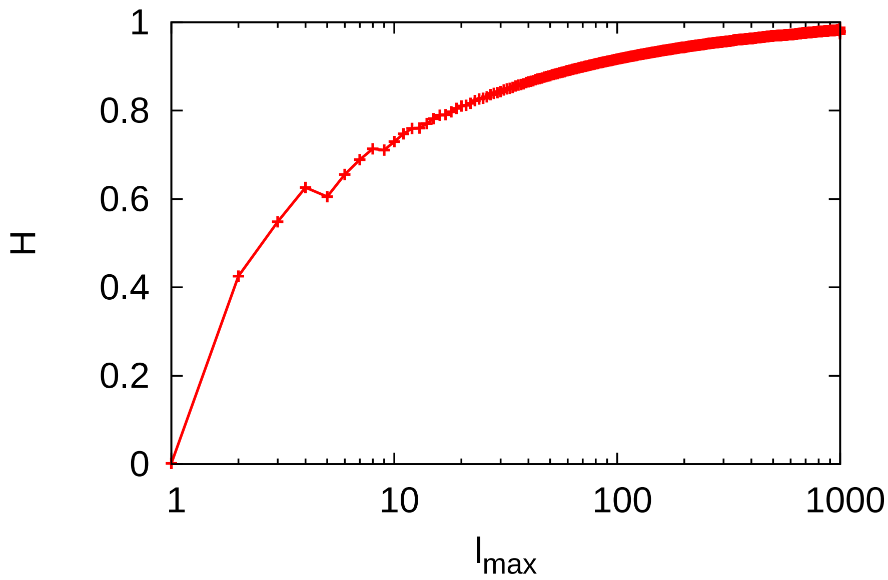

Figure 5.6: Hemisphericity $\mathcal{H}$ of a synthetic hemispherical dynamo, constructed with an exactly white spectrum of l_{max} modes.

5.2.2 Numerical Spectra

We had seen, that a flat spectral distribution ('whitishness') yields a strong hemisphericity. In figure 5.7 we show the spectrum per degree l of the time averaged poloidal magnetic energy of the full core shell. Again, the standard parameters are used here: $E = 10^{-4}$, $Ra = 4 \times 10^7$, $Pm = 2$ and $Pr = 1$, where we vary the perturbation amplitude g. The $g = 0$ reference case with homogeneous CMB heat flux (figure 5.7, red curve) is clearly dominated by the dipole mode ($l = 1$), whereas all the other modes ($l < 1$) are smaller by an order of magnitude. The spectra of the perturbed ($g < 0\%$) cases show more a whitish distribution, where the effect increases with increasing perturbation amplitude. The dipolar component is exceeded in amplitude by some of the higher modes for the strong perturbed case (light blue and yellow curve in figure 5.7). Since the magnetic field reverses in some cases the time averaged spectra rather than the spectrum of the time averaged field is taken. The total magnetic energy decreases with increasing the perturbation amplitude, whereas the spectral representation changes from clearly dipole dominated (red curve in figure 5.7) towards hemispherical (other curves). At $g = 60\%$ (pink curve) the spectrum is indeed rather flat, what interestingly coincides with the onset of the dynamo waves. In figure 3.18 the temporal evolution of the Gauss coefficients and the onset of the periodic variations are shown. Since our major interest is in the axisymmetric surface field, we computed the Gauss coefficients at the CMB associated with the poloidal spectrum discussed before. Figure 5.8 shows a simplified spectra in terms of the axisymmetric ($m = 0$) Gaussian coefficients g_l for the first 14 modes taken at the CMB. This agrees well with the energy spectra (figure 5.7), showing that in the dipolar reference case (red curve in both plots) clearly the modes of the dipolar family are promoted. For the dipolar reference case

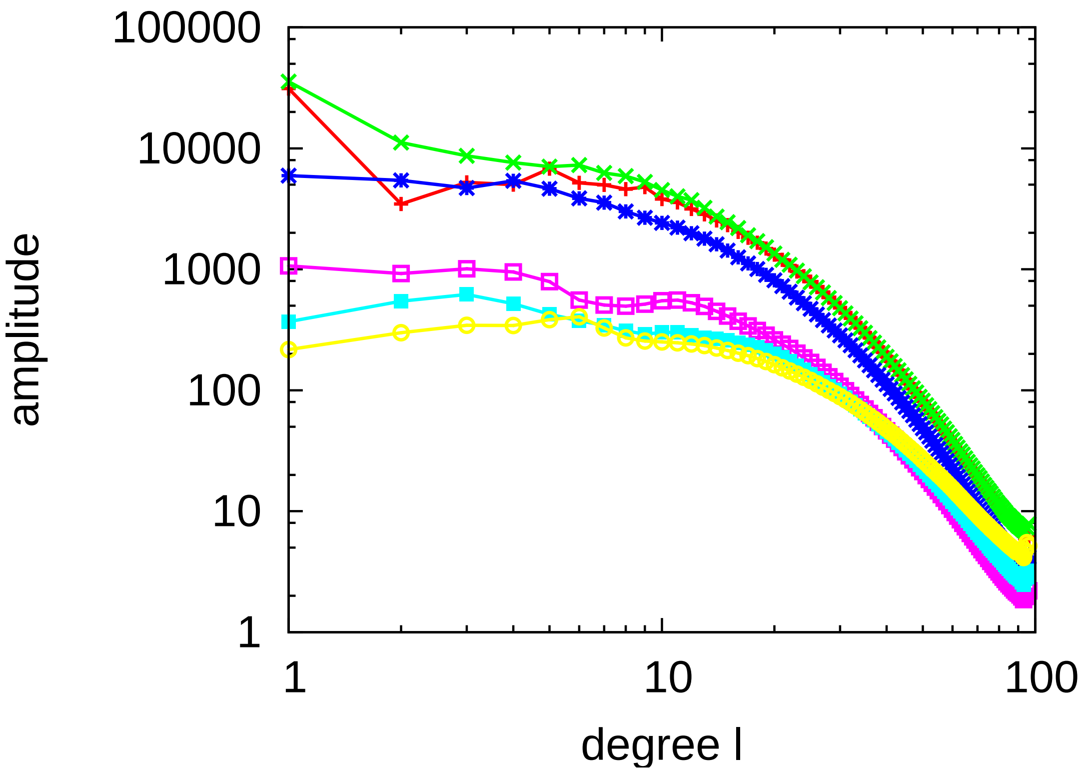

Figure 5.7: Poloidal energy spectra of full core shell by degree l for the dipolar reference case (red), and several perturbed cases. Colors: g = 20% - green, g = 50% - blue, g = 60% - pink, g = 100% - light blue g = 200% - yellow. The parameters are $E = 10^{-4}$, $Ra = 4 \times 10^{7}$ and $Pm = 2$.

(red curves) the stronger (weaker) dipole (quadrupolar) family is visible by the zig-zag pattern until $l = 6$. The hemispherical magnetic field (other curves) does not show such a clear separation into the two families. Therefore the reference case has a strong equatorially antisymmetry and weak hemisphericity, whereas the flat spectra of the perturbed case relate to a hemispherical field. For the leading modes up to $l = 7$ the distribution flattens out, and becomes 'whitish' at $g = 60\%$ (pink curve), where the oscillations set in. Higher perturbations decrease the amplitude of the first modes, therefore the maximum Gauss coefficient is around a spectral degree of $l = 5$.

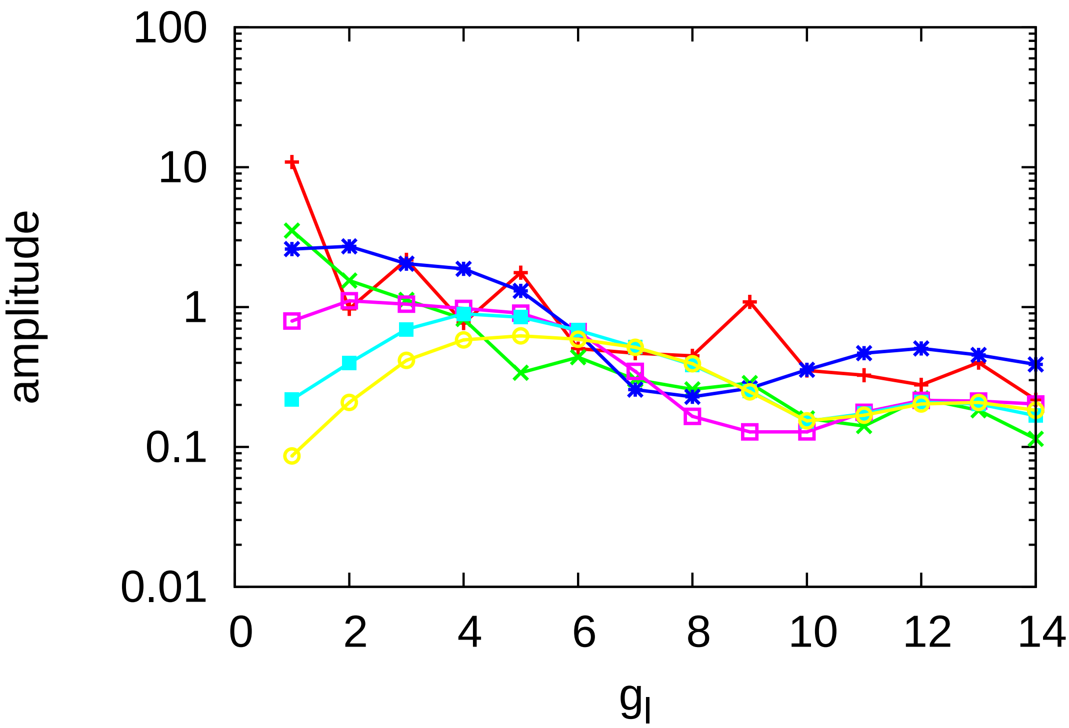

Figure 5.8: First 14 axisymmetric Gauss coefficients taken at the CMB by degree l for the dipolar reference case (red), and several perturbed cases. Colors: g = 20% - green, g = 50% - blue, g = 60% - pink, g = 100% - light blue g = 200% - yellow. Parameters as in figure 5.7.

5.2.3 Hemisphericities from the Simulations

The hemisphericity will be affected by the extrapolation procedure. In figure 5.3 we had shown the radial decay of several axisymmetric Gauss coefficients for the hemispherical $g = 100\%$ case. Furthermore, the hemisphericity tends to be high if the leading modes have a comparable amplitude. Thus the hemisphericity will be strongest if the leading modes cross each other during the extrapolation. Figure 5.9 shows the hemisphericity of the mean radial magnetic field intensity as a function of the extrapolation radius. In that figure, the extrapolation radius is extended to several Mars radii, where the martian surface is at $r/r_{cmb} = 2.1$. The higher g, the larger the hemisphericity, but all curves tend to zero, since the dipole mode is increasingly dominant with increasing extrapolation radius. Figure 5.9 shows, that the hemisphericity of a hemispherical magnetic field can be significant even at several planetary radii resulting in a deformed magnetosphere. Obviously, for a stronger perturbation the maximum hemisphericity moves further out to larger radii. For a magnetic field magnetizing rocks on the crust, the morphology at the surface is crucial. We can find, $\mathcal{H}(r = r_{sur}) > 0.5$ for a perturbation of $g = 100\%$ (light blue curve in figure 5.9) at the Martian surface, what is comparable to the lowest estimates for hemisphericity of the crustal magnetization thus the surface field of a hemispherical dynamo can indeed match the crustal hemisphericity. Even though the dipole becomes more and more important with outward extrapolation, it is indeed possible that the hemisphericity increases with r/r_{cmb}. This is the case, if the dipolar mode, or other modes of small l are weaker than the leading modes. Due to the slower decay of the dipolar mode, it then crosses the other modes at given extrapolation radius hence maximizes the hemisphericity. As an example, the $g = 100\%$ case has leading modes of around $l = 4, 5$ at the CMB (see figure 5.8 light blue curve or figure 3.18) and a CMB hemisphericity of $\mathcal{H}(r = r_{CMB}) = 0.77$. During the extrapolation towards the surface the spectral distribution changes according the figure 5.3 where the dipolar mode is the strongest at the surface. At an extrapolation radius of $r/r_{CMB} = 1.3$ the hemisphericity peaks at $\mathcal{H} = 0.85$ and drops until the surface ($r/r_{CMB} = 2.1$) down to $\mathcal{H}(r_{sur}) = 0.55$.

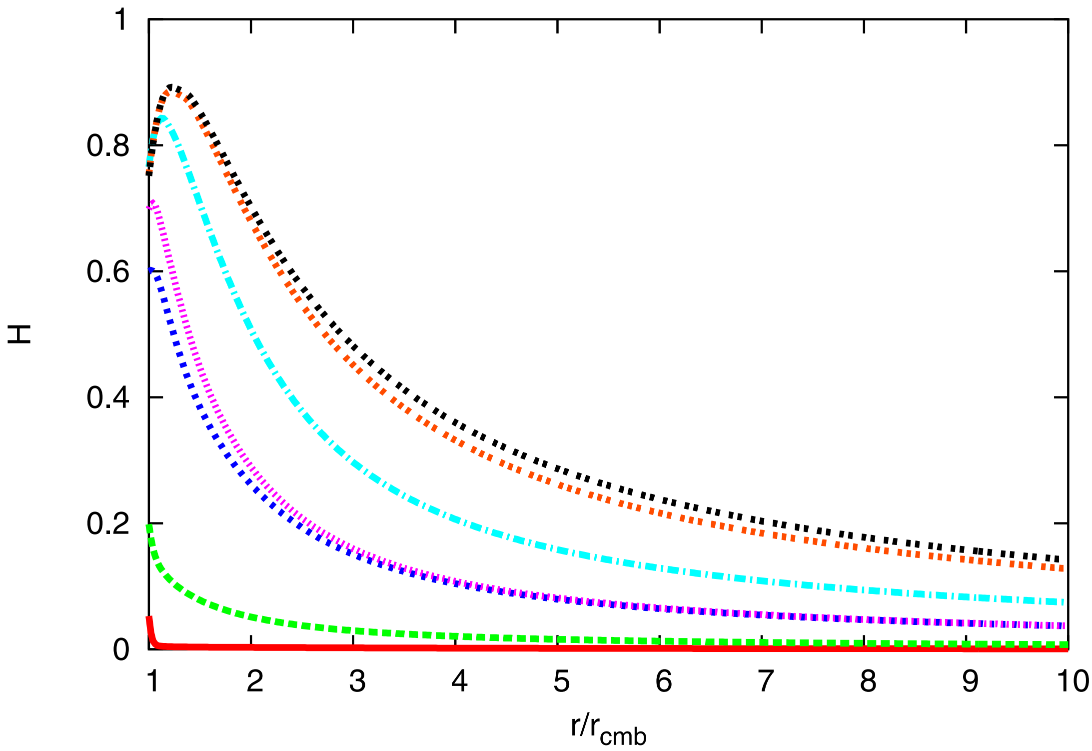

Figure 5.9: Radial dependence of the magnetic hemisphericity $\mathcal{H}$(r) for different CMB heat flux perturbation amplitudes g. All curves tend to zero for larger radii since the equatorially asymmetry decrease with decreasing small scales. But for the dipole dominated reference case, the hemisphericity is always very close to zero. Colors: red - g = 0, green - g = 30%, blue - g = 50%, pink - g = 60%, light blue - g = 100%, orange - g = 150% and black - g = 200%.

Keeping in mind the magnetic field oscillations, we study the temporal evolution of the hemisphericity in figure 5.10 at the cmb (green) and the planetary surface (red) for a hemispherical dynamo with $g = 100\%$. The time averaged value is given by the horizontal lines. The variation is surprisingly strong and oscillates at twice the variation frequency of the individual magnetic field Gauss coefficients. Since all coefficients roughly oscillate with the same period there are two instances during each each period where the hemisphericity is particularly large since axial dipole and quadrupole have the same maximal amplitude. Note, that $\mathcal{H}(r_{sur})$ (red curve) reaches maximal 0.8, what is also the maximal value for the CMB variations (see figure 5.10, green curve). On the other hand, if both are close to zero during an oscillation cycle, higher modes contribute stronger leading to weaker hemisphericity.

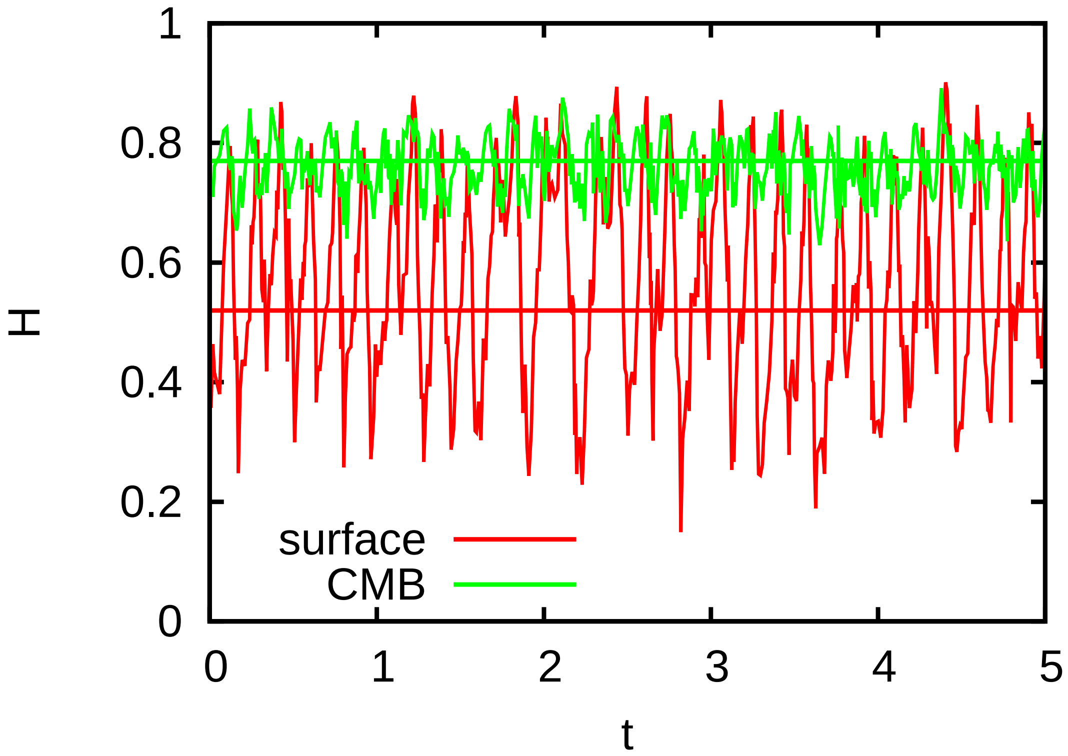

Figure 5.10: Time evolution of hemisphericity $\mathcal{H}$ at the CMB (green) and surface (red) for g = 100%. The horizontal lines are the according time averages.

We time average the hemisphericity over several viscous diffusion times to find a reasonable characteristic value independent of the temporal variations. Figure 5.11 show the hemisphericities calculated at the CMB (top plot) and the surface (bottom plot) for all model cases as a function of the Reynolds number Re^* based on the thermal winds (see equation 3.16). The colors relate the different Ekman numbers, the symbols to different Rayleigh numbers and the size of symbols is increased proportional to the square root of the perturbation amplitude g. In table 3.3 on page 100 the symbols are described in greater detail. The axisymmetric zonal flows in our model are based on the thermal wind balance. Thus we drive stronger zonal flows, if the perturbation amplitude g is larger and make the dynamo more and more hemispherical. As an example, the curve of $\mathcal{H}_{cmb}$ of $E = 10^{-4}$ (figure 5.11, empty blue squares) first increase linearly with Re^* and then saturates around $\mathcal{H}_{cmb} \approx 0.75$ for $Re* \geq 200$. This is consistent with the onset of the EAA mode since small values of Re^* denote the unperturbed reference case with homogeneous CMB heat flux (smallest symbols) characterized by weak zonal flows and strong equatorial symmetry that goes along with a weak hemisphericity. All the other curves basically show the same trend for the CMB values of $\mathcal{H}$. But it can be seen that the cases with lower Ekman number, such as $E = 3 \times 10^{-5}$ (black symbols)) and $E = 10^{-5}$ (red) do not show the clear relation as the other cases. This might be consequence of the weaker emergence of the EAA mode for comparable anomaly amplitudes (see figure 3.30). There is a trade off between g and Ra increasing either parameter leads to larger Re^* values. For $E = 10^{-5}$ $\mathcal{H}_{cmb}$ remains small at $g = 100\%$ and we could not afford to increase Ra here since larger Ra as well as lower E values both promote smaller convective and magnetic length scales and therefore require finer numerical grids.

If the poloidal field is extrapolated towards the planetary surface the hemisphericities decrease because the equatorial symmetric dipolar mode becomes increasingly more important. In the bottom panel figure 5.11 we show the surface hemisphericity as a function of Re^*. Additionally the measured surface values for the hemisphericity is marked by the dark line and gray areas as uncertainties. Interestingly, we can only find large symbols reflecting strong CMB heat flux perturbations matching gray area. The unperturbed and weaker perturbed cases are either too symmetric in unsigned magnetic flux with respect to the equator or the decay of $\mathcal{H}$ is too strong with increasing extrapolation radius. The decay of the hemisphericity is controlled by the length scales of the CMB field. A larger perturbation amplitude g (symbol size in the plot), a larger Rayleigh number or a larger magnetic Prandtl number will decrease the magnetic length scales. As an example, the green symbols referring to $E = 3 \times 10^{-4}$ are calculated with $Pm = 5$, thus the magnetic length scales are rather small. There is only little difference between the hemisphericities at the CMB (figure 5.11, upper plot) and the surface (same figure, lower plot). As a consequence, to obtain a large hemisphericity at the surface, the length scales of the leading magnetic modes need to be small enough for not being overwhelmed by the dipolar (or other larger scale modes) mode. E.g., if there would be only the dipolar and the quadrupolar mode with equal amplitude at the CMB, the hemisphericity will significantly decrease while extrapolation.

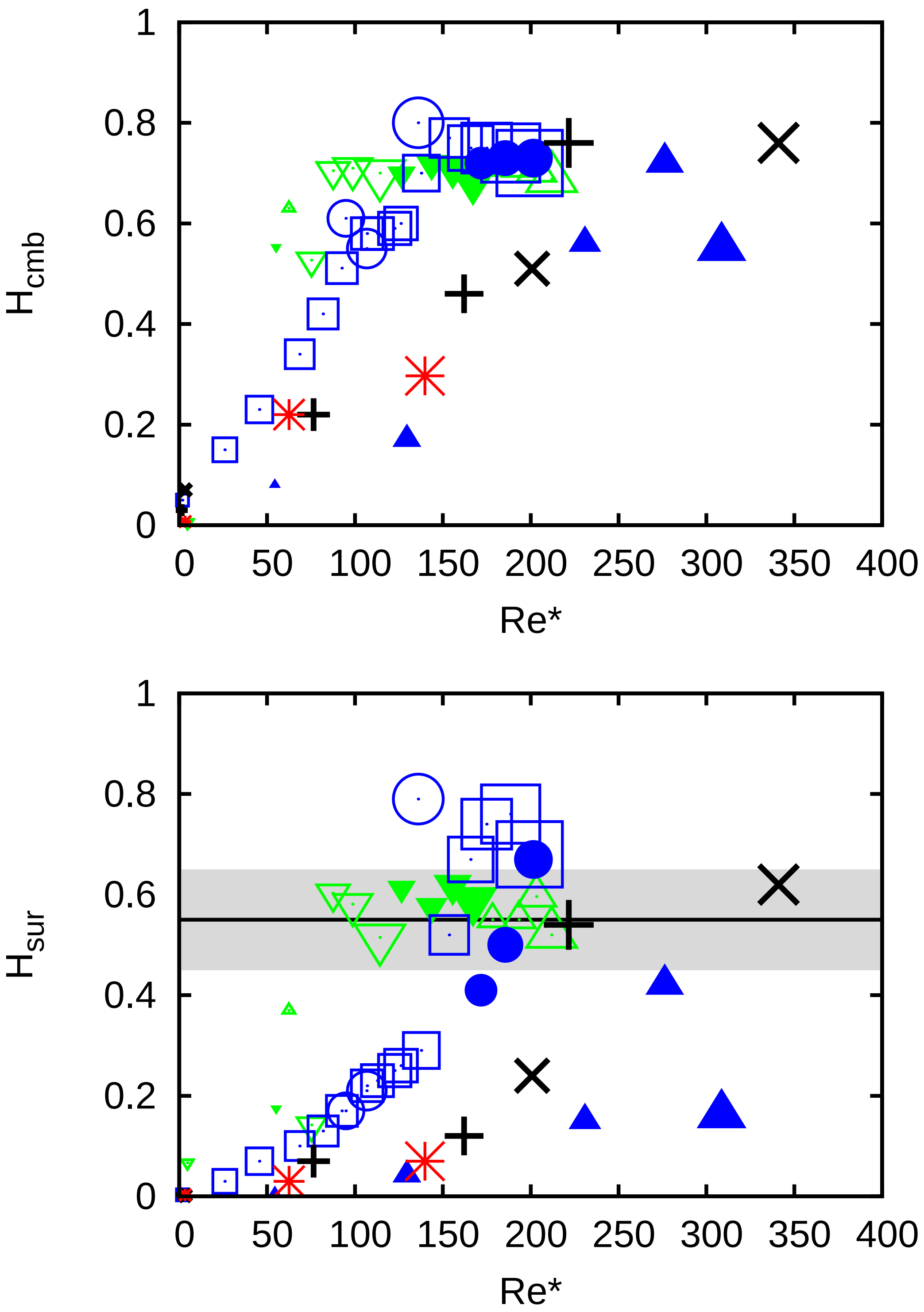

Figure 5.11: Top panel: Hemisphericity at CMB versus Re*, the Reynolds number based on the equatorially antisymmetric thermal wind.
bottom panel: Hemisphericity at the (imaginary) Martian surface.

5.3 A Simple Cooling and Magnetization Model

Our numerical results obtained so far, suggest that it is indeed possible to find hemispherical magnetic fields with appropriate hemisphericity matching the satellite measurements (Acuña et al. 1999, Amit et al. 2011). Here we want to address the question how to translate the surface magnetic field into a crustal magnetization pattern. In the introduction (section 1.4.1) it was mentioned, that a ferromagnetic rock will imprint the ambient magnetic field when it cools under the Curie temperature. Rocks with a temperature higher than the Curie temperature are heated before by impacts or volcanic activity. Furthermore Langlais et al. (2004) suggested, that the magnetization depth in the Martian crust is between 20 and 40 km. It remains an open question, if a thick magnetized layer is compatible with reversing hemispherical dynamo. The obtain an order of magnitude estimate of how fast and deep magnetization can grow if the magnetic field reverses, we investigate a strongly simplified model describing the cooling and magnetization process. We therefore analyze for the 1D heat conduction problem, as it is typically solved for the magnetization in Earth if fresh oceanic crust is created at mid-oceanic ridges. When this fresh crust is transported outwards at divergent plate boundaries and cooled down, it preserves the ambient field direction and strength when reaching the Curie temperature. If the dynamo undergoes polarity reversals, the new crust will show stripes of both polarities. This has led to the conclusion, that the magnetic field of the Earth is of reversing nature.

For the magnetization of the Martian crust the situation is different. The crust might have been magnetized without crustal spreading to a depth of 20 km or 40 km (Langlais et al. 2004). Therefore the magnetization history in the Martian crust is a function of depth and not distance from a crustal spreading zone as for the Earth. Note, the natural border of crustal magnetism in depth is given by the depth at which the Curie temperature is exceeded due to the thermal gradient. During the time of dynamo action and crustal genesis, the Curie depth was maybe rather similar to the magnetization depths proposed by Langlais et al. (2004).

Here we investigate the cooling time of a 1D-pile of crustal rock, which is initially heated up to the solidus temperature everywhere. The upper boundary is the surface of the Mars, whereas the lower describes the depth of the Curie temperature. The heat is evacuated through heat conduction, not due to convection. Thus we solve for the 1D heat conduction equation.

$$\frac{\partial T}{\partial t} = \kappa \frac{\partial^2 T}{\partial x} \, . \tag{5.14}$$

Crustal rocks a rather poor heat conductors. Assuming density ρ, specific heat C_p and thermal diffusivity k to be 2900 kg/m^3,1000 J/kgK and 3 W/mK, respectively, leads to thermal conductivity κ

$$\kappa = \frac{k}{\rho C_p} = 1.034 \times 10^{-6}\,\mathrm{m}^2/\mathrm{s} = 3.25 \times 10^{-5}\,\mathrm{km}^2/\mathrm{yr} \, . \tag{5.15}$$

The numerical values are provided in Morschhauser et al. (2011). Therefore the temperature will be nearly completely reduced through the upper boundary, where the cooling is very efficient due to radiation into space. A rough order-of-magnitude for the cooling time can be achieved, when approximating the equation 5.14, such that

$$\frac{T}{\tau} = \kappa \frac{1}{D^2} T \ . \tag{5.16}$$

The characteristic temperature time scale is given by $\tau = D^2/\kappa$. Using $D = 20$ km and 40 km gives $\tau = 12.3$ Myrs and 49 Myrs, respectively when assuming the above given value of the thermal diffusivity κ. This shows already the large difference between the oscillatory time scales (10 kyrs) and the cooling time for crustal rocks. However, since the material closer to the surface will cool much faster, the total, depth integrated, magnetization will be dominated by the upper layer. During the time of stable polarity interval of the order of 10 kyrs, a layer of $D = \sqrt{10\,\text{kyrs}\, 3.25 \times 10^{-5}\,\text{km}^2/\text{yr}} = 570$ m is magnetized. Deeper layers will cool much slower, thus the thickness of the magnetization obtained during a stable polarity interval will further decrease. Therefore the total depth integrated magnetization of a pile of 20 km or 40 km will be negligible.

To obtain the magnetization history we solve for the 1D time dependent heat diffusion equation and magnetize at a given depth when the Curie temperature is reached. Using an explicit forward time central space (FTCS) finite difference approach, leads to a discretization of heat equation 5.14:

$$\frac{T^{n+1}(i) - T^n(i)}{\Delta t} = \kappa \frac{T^n(i-1) + T^n(i+1) - 2T^n(i)}{(\Delta x)^2} \ . \tag{5.17}$$

Where n is the ordering number of the time step, i the spatial position, Δt the time step and Δx the grid spacing. Since the scheme is explicit one can find the simple equation:

$$T^{n+1}(i) = \frac{\kappa \Delta t}{(\Delta x)^2} \left(T^n(i-1) + T^n(i+1) - 2T^n(i)\right) + T^n(i) \ . \tag{5.18}$$

A stability criterion is needed to avoid numerical instabilities. It can be shown, that $\kappa\Delta t/(\Delta x)^2 < 0.5$ is sufficient for numerical stability. This criteria serves to define the time step $\Delta t = 0.4(\Delta x)^2/\kappa$, where we use 80% of the largest time step possible. The stepping in x-direction is choosen such that the time step is much smaller than the smallest frequency of the dynamo waves we obtain from the numerics. Typical oscillation periods are roughly 10 kyrs, the algorithm uses $\Delta x = 1/1000$, and therefore $\Delta t = 153.68$ yr which is sufficient to resolve the oscillations in time. For the magnetization profile of a fast reversing field a much larger resolution might be needed, because the imprinted magnetization becomes more and more compressed due to slower cooling at the lower end of the rock pile.

Firstly we concentrate on the time to reach the Curie temperature while cooling to a depth of 20 km and 40 km. We simulate the cooling of a hot pile of rock, where the rock pile has an initial temperature of 1000° C representing the solidus temperature. Further we choose the Curie temperature to be 500° C. The fast cooling through the planetary surface is taken into account when using fixed temperature condition at the outer boundary of $T = 0$. Further we distinguish between two different setup, characterized in figure 5.12. For the first model, we choose the lower boundary to be thermally isolating $\partial T/\partial x = 0$ thus all heat is exclusively lost through the upper boundary (see figure 5.12). For the second model we take the thermal gradient during the early evolution of Mars into account.

Thickness	20 km	40 km
Model 1: isolating	4.7	18.7
Model 2: thermal gradient	25	100
estimates	12.3	49

Table 5.1: Cooling time in million years.

We assume that the (linear) thermal gradient is so steep, that it crosses the Curie temperature at the lower edge of the rock pile. Thus for a 20 km anomaly, $T(20\,\text{km}) = 500°$ C and $T(40\,\text{km}) = 1000°$ C as shown in figure 5.12, blue line. Then the thermal gradients for the 20 km (40 km) model is 25 K/km (12.5 K/km), respectively. If the temperature has reached the Curie temperature at the lower edge or more precisely everywhere inside the rock pile, the time integration is stopped and we find the time it takes to magnetized a layer of a given thickness. Table 5.1 compares the cooling times for two different numerical models and the rough order of magnitude estimates. Obviously, the two numerical models differ by factor of five in the cooling time, where as the estimates reside in the middle of both. The more realistic model 2 with the thermal gradient shows far larger cooling times than the model 1 with the isolating lower boundary. However, all of the magnetization times exceed the typical reversal rate obtained from the numerics and mean field considerations by three orders of magnitude.

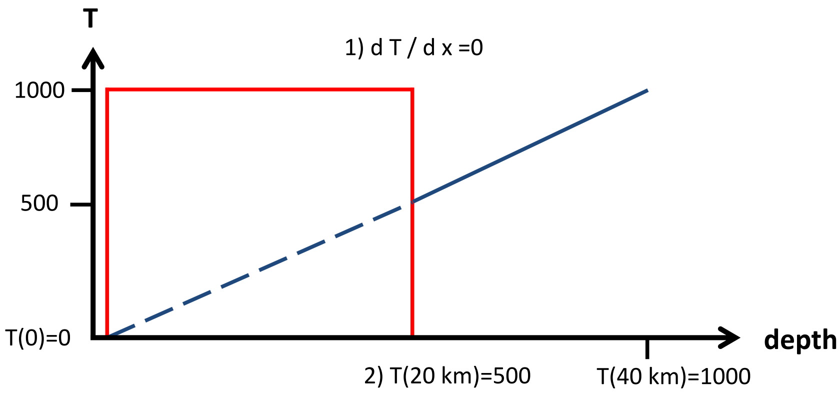

Figure 5.12: Numerical setup for the cooling model. The red box characterizes the T = 1000° C temperature anomaly, the blue line is the background profile of the thermal gradient. Here we show the setup for the 20 km thickness model. Further details see text.

The cooling is faster for the layers close to the upper surface and slower for the layers closer to the lower boundary. Naming Curie time as the time interval it takes to reach the Curie temperature, and Curie depth as the depth in which the Curie temperature during the cooling process is reached, figure 5.13 shows the Curie depth as function of the Curie time for the model 1 with isolating lower boundary (reddish colors) and for model 2 with the background thermal gradient (blue colors). The temperature anomaly mimicking the magnetizing rock pile is 20 km (red and orange) or 40 km (blue and light blue). For smaller Curie depths and times all curves agree and follow the same power law, whereas the difference between the models is only visible for the very large depths and times. The slope in the log-log plot (figure 5.13) is consistently with the diffusion equation 0.5.

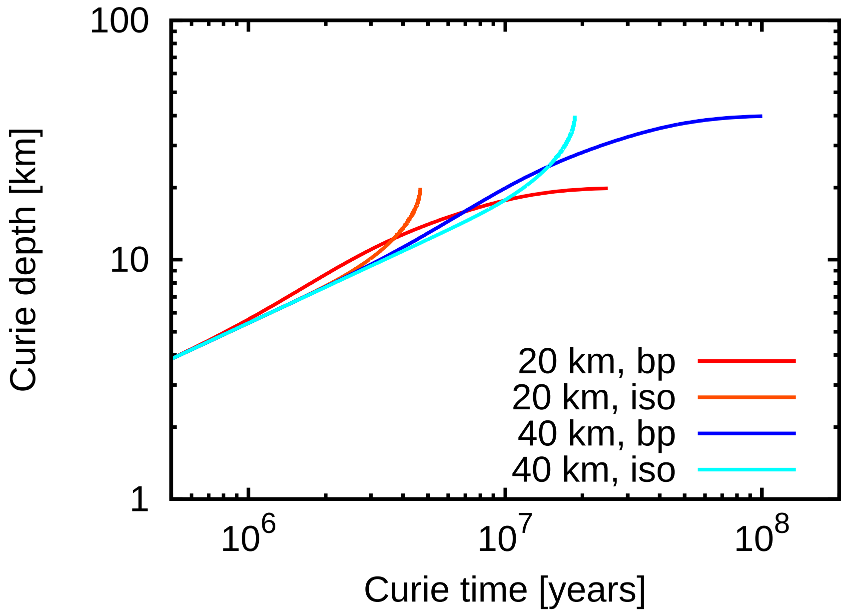

Figure 5.13: Curie depth versus Curie time for a 20 km (40 km) pile in red (blue) for the Model 2 with background profile and orange (light blue) for the isolating Model 1.

Finally the rock pile is magnetized by an oscillating field. The ambient magnetic field fluctuates according to $B(t) = \cos(t\,2\pi/P)$, where P is the oscillation period. We test to what extend the rock pile can be magnetized while changing P by from 10^4 (years) up to 10^9. The first values reflects roughly the largest oscillation periods measured from the numerical simulations, whereas the latter value is given by the time interval when the dynamo on Mars was active (Morschhauser et al. 2011). Assuming that crustal genesis and the duration of the ancient Martian dynamo agreed roughly, the maximal value then also describes a magnetic field what is rather stationary with respect to the cooling time scales. Figure 5.14 shows the obtained relative magnetization as function of depth. In the plot there is a running depth-average of the imprinted magnetic field directions and amplitudes shown. The different curves correspond to different oscillation periods P. For the very fast oscillations with $P = 10^4$ and $P = 10^5$ we cutted the curves when the first aliasing appeared. This is due to the fact that different magnetization directions becomes increasingly dense at greater depth, thus the grid resolution can not resolve an oscillation cycle appropriately anymore. In figure 5.14 it can be seen that for faster oscillation periods (smaller P) the magnetization can not penetrate into significant depth. For example, when $P = 10^6$, the magnetization will drop to the $1/e$-th of its maximal value after roughly

138 kyrs corresponding to only 4.5 km of depth are magnetized crust unidirectional. Such an oscillation period agrees to the time scales for geomagnetic reversals (Kono 2007). For any deeper magnetization the averaging effect due to the clumping of inverse polarity layers wipes out the magnetization signal seen from above.

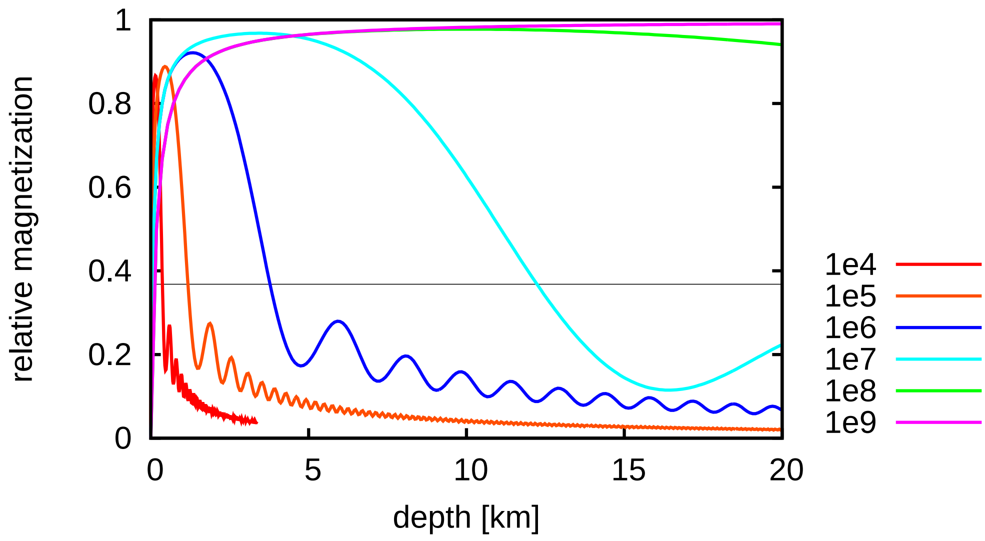

Figure 5.14: Running depth-average of the magnetization as function of depth. Different colors relate to different oscillation periods P.

As an interpretation, if the ancient Martian dynamo showed regular polarity reversals only the fast cooling upper layers can be magnetized. Any layer of depth whose cooling time is significantly larger than the oscillation period, the inverse polarities of the imprinted field averages out the magnetization. Langlais et al. (2004) stated a magnetized layer thinner than 20 km to be rather unlikely. This shows the problem with the rapidly polarity inversions of the Parker-wave-like oscillations.

The frequencies of the oscillations in the hemispherical dynamo agree very well with those obtained from the mean field theory (see section 4) for both, the $\alpha\omega$ and the $\alpha^2\omega$ model. It is possible to get an estimate for the minimum frequency (largest oscillation period P) from the $\alpha\omega$ dispersion relation. If the growth rate reaches zero, the dynamo is activated and further amplifies. For border of a zero growth rate $\gamma = 0$, equation 4.31 yields a minimum frequency of $\nu_0 = k^2/Pm$. If one takes into account dimensional units, this gives $\nu_0 = k^2\lambda$. If we assume the wave number $k = 2\pi/l_k$ corresponding the fundamental mode with length scale l_k equals to core radius and $\lambda = 2\,\mathrm{m}^2/\mathrm{s}$ we find $\nu_0 = 26$ kyrs. Interestingly, for the $\alpha^2\omega$-dynamo no such simple calculation can be made. Thus all frequencies might are possible to occur and the oscillation period can not be bordered by a maximal value. If the magnetization was acquired in a similar way, say while cooling thick layers of hot rocks, an satellite observer would measure the time average of the underlying magnetization history.

5.4 Time Averaging

Amit et al. (2011) addressed also the issue of how to relate the magnetic field from a dynamo simulation to crustal magnetization pattern. As we had seen, the typical time scales for crustal genesis and cooling exceed those from the numerical simulations by far thus the time dependence of the core field has to be taken into account and appropriate time averages need to be applied. To translate the dynamo field into a magnetization pattern, Amit et al. (2011) suggest two end-members depending on how the magnetization was acquired. The 'homogeneous' crustal growth model assumes that the crust is build up in global layers. This means the magnetization is reflected by the process we modeled above with the simple coolig model, thus a thick layer of rocks hotter than the Curie temperature cooled according to only heat diffusion. As our model suggests, the net acquired magnetization as seen by an observer would then be roughly proportional to $\tilde{B}$, the rms value of the time averaged magnetic field:

$$\tilde{B} = \left(\langle \boldsymbol{B} \rangle^2\right)^{1/2} \tag{5.19}$$

The other end member is what Amit et al. (2011) call the 'random' magnetization model, which assumes that the magnetization was acquired in regional patches without correlation in time and space. Volcanoes and small impacts create then a patchwork in space and time of smaller magnetic sites, which are thin enough to cool faster than (if any) the oscillation period of the magnetic field. The net acquired magnetization would then rather reflect the time average of the local intensity:

$$\bar{B} = \left\langle \left(\boldsymbol{B^2}\right)^{1/2} \right\rangle \tag{5.20}$$

The latter scenario ignores the temporal aspect and the constraint of a thick magnetized crust. The magnetization process records the magnetic changes happening during the periods of crust formation, whereas to build a magnetized layer of 20 km thickness it is necessary to pile up thin layers with probably inverse polarity. Both arguments yield that the local net magnetization, as seen by an observer, is always proportional to the time averaged local magnetic field, possibly slightly dominated by the outermost layers. For the geomagnetic field the magnetic time scales range from several years to tens of million years (see figure 5.14, light blue curve for $P = 10^7$). Higher field harmonics typically change on time scales of centuries while the axial dipole component is much more stable. During the last tens of million years is has reversed roughly four times per million year. Even for Earth the net local crustal magnetization is reduced by the fact that layers with opposing polarity cancel each others (Kono 2007).

Figure 5.15 and 5.16 presents extrapolations of $\tilde{B}$ and $\bar{B}$, respectively, of our models at $E = 10^{-4}$, $Ra = 4 \times 10^7$, $Pm = 2$ and for different g values as a function of the averaging time τ. The gray shaded areas reflect the suggestion of Weiss et al. (2002) for the field strength of the ancient Martian field. The time averaged intensities, shown in figure 5.16, demonstrate the for $g < 60\%$ field strengths similar to that predicted for Mars are reached. For the higher perturbations the magnetic field amplitude at the surfaces drops due to less efficient induction in the hemispherical dynamo models. The intensity of the time averaged field (figure 5.15) show similar results for $g \leq 56\%$. However, for $g > 60\%$ the dynamo becomes oscillatory and the field decays rapidly when the

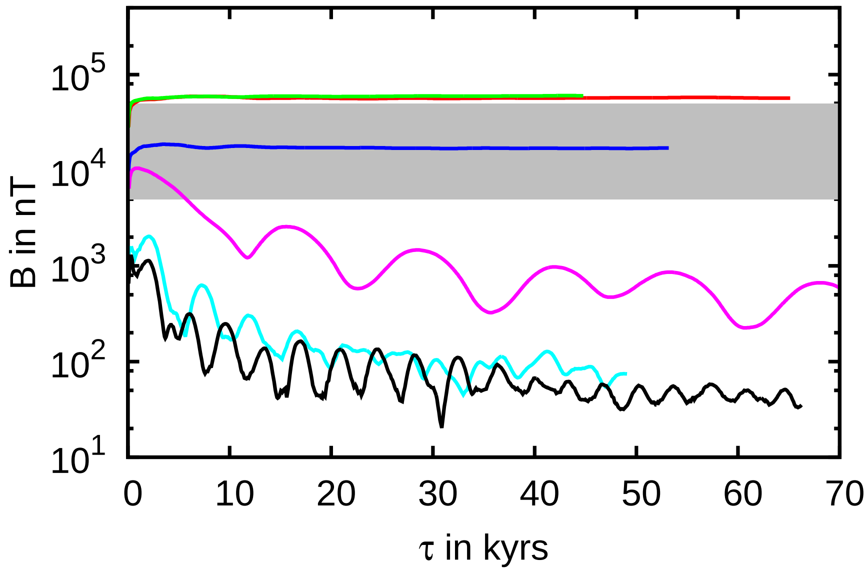

Figure 5.15: Amplitude of the time averaged surface magnetic field in nT and the according hemisphericity $\mathcal{H}$ as function of averaging time in kyrs. The gray area indicates the surface magnetic field strength suggested by Weiss et al. (2002) and the hemisphericity of the crustal magnetization (Amit et al. 2011). Red - g = 0%, green - g = 30%, blue - g = 60%, pink - g = 100%, turquoise - g = 150%.

averaging times exceed the oscillation period of roughly 10 kyr. This shows the dilemma of the hemispherical dynamos in order to count as the internal source of the dichotomous magnetization of Mars. The periods, listed in table $A.1$, are of similar order for all the oscillating hemispherical dynamos. This is much too short to build up any significant crustal magnetization. We therefore conclude that while the hemispherical dynamo can reach hemisphericities similar to that of the Martian crustal magnetization their oscillatory nature makes them incompatible with the rather strong magnetization amplitude. The scaling law for the magnetic field strength we use here, is based on the assumption that the force balance is mainly magnetostrophic (Elsasser number $\Lambda = 1$), but this approach might not be valid for the hemispherical dynamos. Scaling laws of the magnetic field strength for a homogeneous boundary are more successful (Christensen and Aubert 2006) and predict correct field strengths based on the available power (Christensen and Wicht 2007).

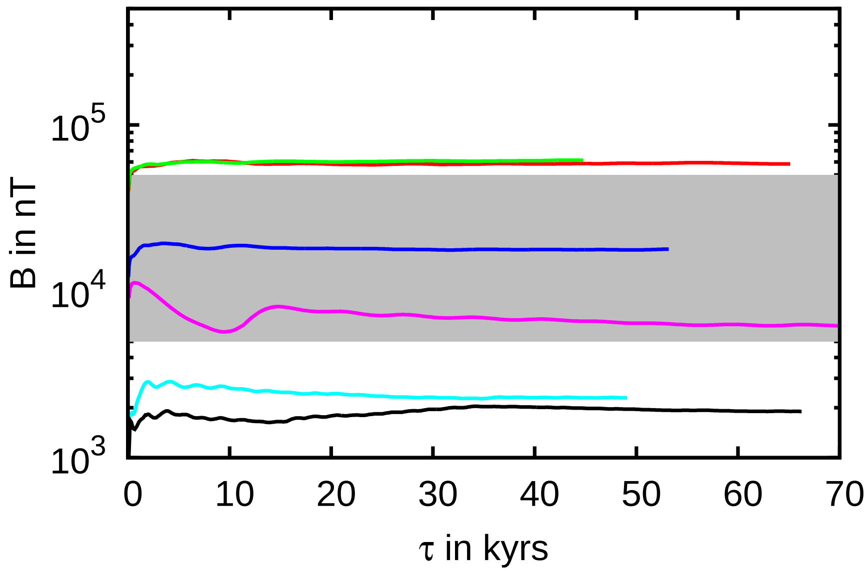

Figure 5.16: Same plot as 5.15, but for the mean field intensity.

6 Discussion

It is rather problematic to model the realistic planetary properties like viscosity, diffusivities or rotation rate, but our numerical model still offers significant insights into the dynamics and the induction mechanism of dynamos influenced by CMB heat flux anomalies. We described in detail how the convection and induction mechanisms are altered by a degree-one (sinusoidal) perturbation of the mean CMB heat flux (section 3). The major finding is the onset of an equatorially antisymmetric and axisymmetric (EAA) convective mode, which is characterized by strong thermal winds (zonal flows) and hemispherical poloidal flow and magnetic field. When this EAA mode reaches a significantly amplitude relative to the classical columnar convection, the magnetic field tends to periodically reverse (section 3.4.2). We successfully attempted to describe the oscillations with mean field dynamo models (section 4), where the dominant axisymmetry of flow and field makes the mean field theory applicable. The frequency of the polarity reversals estimated from the numerical results and those predicted from dynamo wave dispersion relations agree surprisingly well. To apply the findings to the heterogeneous magnetization pattern of Mars (Acuña et al. 1999), we tested our models against the hemisphericity of the magnetization (Amit et al. 2011) and suggested field strength (Weiss et al. 2002) by extrapolating the CMB field towards the planetary surface (section 5). We further showed that independent of the magnetization process, the crustal field represents the time average of the core field. Due to the different time scales of the oscillations and the magnetization history, a hemispherical and rapidly oscillating field seems incompatible with slowly acquired the crustal magnetization.

6.1 Validity of the Model Setup

It remains an open question to what extent the EAA mode can contribute to planetary core convection. The amount of data collected (see table A.1), does not allow a meaningful prediction for the response of the core convection affected by a large scale heat flux heterogeneity. In general a much lower Ekman number will not allow to significantly break the Taylor-Proudman constraint, therefore the magnetostrophic force balance is expected to hold. The main contribution of the forced hemispherical convective mode are the equatorially antisymmetric and axisymmetric zonal flows, which severely violate the Taylor-Proudman condition of z-independent flow. The zonal flows are driven by latitudinal temperature anomalies (thermal wind) and introduce a broad shear layer with large variation of zonal flow parallel to the axis of rotation. The few numerical runs at smaller Ekman number (such as $E = 1 \times 10^{-5}$), show already a significantly weaker effect on the convection and induction. It might be possible, that the EAA mode can not contribute to large extend to the core convection if the Taylor-Proudman theorem holds.

Both, the mechanical boundary conditions of rigid walls and the action of the Lorentz force seem to support the strength of the hemispherical convection (section 3.6.2 and 3.4.1, respectively). The thickness of the mechanical boundary layers introduced by the rigid walls scales like $E^{1/2}$ (Soward and Dormy 2007) and therefore tends to zero at realistic values of the Ekman number ($E = 10^{-15}$). We have seen in section 3.6.2, the free slip walls do not strengthen the EAA flow, even though they typically show somewhat larger kinetic energies (see also figure 3.24 and the table 3.2). In the pioneer study of Stanley et al. (2008) also free slip boundary conditions are used. The anomaly strength was taken to be three times the mean superadiabatic heat flux. Stanley et al. (2008) did not investigate the flow symmetries with respect to the EAA mode, but we believe that the EAA mode was not so much dominant as in our study. At least our simulations for free slip boundaries showed besides the ageostrophic EAA convection the emergence of geostrophic zonal flows, which can not originate from thermal winds (compare 3.6.2). Stanley et al. (2008) did not use internal heating to drive convection but used a bottom heated setup, where the CMB heat flux is balanced with a lower boundary heat flux. In section 3.6.1, we have shown that bottom driven dynamos are much less sensitive to the heat flux anomaly than the internally heated cases explored here. This might explain why Stanley et al. (2008) had to use a much larger anomaly amplitude ($g = 300\%$) to see the desired effect.

The Elsasser number Λ measures the impact of the Lorentz force relative to the Coriolis force. Λ is thought to be of order 1 in planetary dynamos (Christensen and Wicht 2007), what is consistent with our simulations. For the perturbed dynamos we find Elsasser numbers of $\Lambda \approx 0.1 - 10$. The amplitude of the magnetic field is determined by the interplay between induction and Ohmic dissipation. Section 3.4.1 gives some insights about the action of the Lorentz force. There the (toroidal) magnetic field suppresses the convective columns and thus supports the relative strength of the EAA mode. The Elsasser number may overestimate the impact of the Lorentz force since both the magnetic field and the kinetic flow have their strongest contributions in large scale axisymmetric toroidal components. The Lorentz force can not act on a flow parallel to the field and thus predominantly alters the small scale convective motions in the (southern) hemisphere.

The Rayleigh number controls the vigor and length scales of the convective motions. Landeau and Aubert (2011) have shown, that the EAA mode can also co-exist besides the columnar convective motions if the Rayleigh number is sufficiently high. They restricted the study to homogeneous heat flux boundary conditions. We also studied the impact of the Rayleigh number on homogeneous CMB heat flow, especially for an Ekman number $E = 10^{-4}$, and find that for larger Rayleigh numbers the EAA convection is a natural part of the convection. This confirms the conclusions of Landeau and Aubert (2011). However, further increasing the vigor of the convection leads also to more efficient mixing that goes along with more turbulent, three dimensional flow at even higher Rayleigh numbers. As a consequence, the EAA mode might appear in homogeneous dynamos only for a given range in supercriticality. If the supercriticality is enhanced to far, the latitudinal temperature anomaly as the source of the EAA mode is reduced due to the more efficient mixing. For this fast mixing regime a scaling law according to King et al. (2010) might be valid. Unfortunately, our data coverage is insufficient to proof this idea. Figure 3.30 in section 3.6.4 shows the dynamic response of the convection in terms of activating the EAA convection when increasing the Rayleigh number for the homogeneous and perturbed cases. For the lowest Ekman number in the figure (green symbols refer to $E = 3 \times 10^{-4}$) both curves, the homogeneous and the boundary force tend to decrease in the strength of the EAA when the supercriticality is increased.

The EAA mode is fed by latitudinal temperature gradients driving equatorially antisymmetric thermal winds. We tested this thermal wind force balance extensively in section 3.6.3 and find that this is indeed the main driver of the strong axisymmetric zonal flows. To get an order of magnitude estimate or a scaling law for the thermal wind balance, we restrict the amount of data to only axial perturbations (degree $l = 1$ and order $m = 0$) of $g = 100\%$, but take all combinations of Ekman E and Rayleigh number Ra into account. King et al. (2010) suggested a scaling for radial temperature anomalies, what we applied to the latitudinal temperature gradients. This scaling law predicts a relation between temperature anomalies and the supercriticality, such that a temperature gradient decrease as $\delta_T \propto (Ra/Ra_c)^{-6/11}$. Interestingly the scaling still holds for latitudinal temperature anomalies, such as we introduced with the CMB heat flux perturbations. Assuming this scaling law to be valid and that the thermal wind balance holds also for a realistic planet, we can estimate the characteristic zonal flow amplitude in terms of a Reynolds number $Re^* = 10^8 ... 10^9$ depending on the supercriticality of the dynamo. A realistic flux based Rayleigh number, might be on the order of $Ra_Q = 10^{28}$ (King et al. 2010), providing extremely small convective length scales, and therefore also small penetration depths of thermal anomalies. The total flow amplitude in planetary cores will not exceed the estimate of the characteristic zonal flow amplitude by far. Given a magnetic Reynolds number of $Rm = 500$ and magnetic Prandtl number $Pm = 10^{-6}$ (Jones 2011), yields $Re = Rm/Pm = 5 \times 10^8$. Note, such a simple scaling neglects a further dependence on the Ekman number. The Ekman dependence so far only appears in the supercriticality ($Ra_c \propto E^{-5/3}$). The smaller (and more realistic) the Ekman number is, the more important will be the Taylor-Proudman constraint of a z-independent (geostrophic) flow yielding an additional decrease of the EAA mode with decreasing Ekman number. The EAA mode is by definition ageostropic, thus the thermal winds might only contribute little to the total kinetic energy of a convecting planetary core.

The variation amplitude of the CMB heat flux pattern one of the main study parameters here, as well as in Amit et al. (2011). Stanley et al. (2008) choose a rather high (and fixed) amplitude of $g = 300\%$. It is thought, that anomaly amplitudes beyond $g = 100\%$ violate the Boussinesq-Approximation, since they introduce a net buoyancy flow into the core. This leads to a stable stratification and the assumption that the background state is adiabatic and well mixed may be violated. Our model equations are based on the fact, that there are only small fluctuations in temperature and density on top of the adiabatic reference state. As stated in the introductory section 1.6, the amplitude of thermal anomalies introduced by mantle features, such as hot mantle plumes, cold subdcuted slabs or by giant impacts, can easily exceed the mean superadiabatic heat flux (compare table 2.1). Therefore also the amount of heat conducted along the core adiabate will be affected strongly and should be taken into account in the models.

We also varied the orientation angle relative to the axis of rotation of the heat flux anomaly following Amit et al. (2011). They restricted there analysis to tilting angles of $\alpha = 0°, 45°, 90°$, where we covered a broader range. We could show, consistent with the findings of Amit et al. (2011) that only the equatorial anomaly of $\alpha = 90°$ provides a dynamo solution showing significant differences from the EAA mode. Interestingly there is not much of a difference between $\alpha = 0°$ and $\alpha = 80°$ in terms of activating the EAA mode and drive a north/south hemispherical dynamo. Obviously, the breaking of the equatorial symmetry has a much stronger control over the dynamics. As long as the anomaly is aligned with or has a contribution along the axis of rotation, the EAA mode emerges and the radial magnetic field is mainly restricted to the hemisphere of higher heat flux. Since the orientation of the heat flux anomaly is determined by the mantle, which has no preferred axis due to the action of Coriolis force, basically all orientations of the anomaly are possible. While in the study of Landeau and Aubert (2011) with homogeneous CMB heat flux the hemispherical dynamo can emerge in either side of the equator due to the spontaneous breaking of the equatorial symmetry, Amit et al. (2011), Aurnou and Aubert (2011) and our approach force the hemispherical field to match the crustal magnetization localized in the southern as well, by using higher heat flux in the southern and smaller in the northern hemisphere.

6.2 Hemispherical Dynamo Action

We have shown that already several tens of percent of relative CMB anomaly amplitude are sufficient to transform the stationary dipolar dynamo induced by convective columns into a hemispherical oscillating configuration mainly driven by ageostrophic thermal winds and localized convection (section 3 and figure 3.18). Large scale and as well axisymmetric meridional circulation tries to equilibrate the temperature anomaly. Consequently, these flows are deflected by the action of the Coriolis force into the azimuthal direction creating two large scale and counter directed thermal wind cells. The convective (poloidal) motions are then restricted to a cusp in the vicinity of the pole of higher heat flux. Most of the kinetic energy, as showed in the plot 3.10, is stored in the zonal flows. Note, that the zonal flow energy is added to the system and not converted, therefore the total kinetic energy in the perturbed cases exceed by far those in the homogeneous cases (figure 3.10). Typically this contribution reaches up to 90% of the total kinetic energy. Althought a larger kinetic energy goes along with a higher magnetic Reynolds number, the magnetic energy of the hemispherical dynamos are significantly smaller than for the dipolar ones. The amplitude of the kinetic poloidal energy changes only little, but becomes localized in the fast cooling (southern here) hemisphere.

The induction of the magnetic field changes from a first order α^2-dynamo in the homogeneous $g = 0\%$ case to a more or less pure $\alpha\omega/\alpha^2\omega$-dynamo in the hemispherical convective case. The induction in the convective columns is a well understood standard induction process (Wicht and Aubert 2005). Deeper investigations of the mechanism can be found at Aubert et al. (2008b), Christensen et al. (2001), Christensen and Wicht (2007). Helical motions responsible for the α-process are created by the superposition of the rotating convective columns and a secondary flow along the columns (pole- or equatorward). The ω-effect according to shearing of poloidal field into axisymmetric toroidal is thought to be of minor importance. Our numerical measurements (see figure 3.13), reveal a weak contribution of roughly $\omega^* = 10\%$ for the homogeneous dynamo model. However, the hemispherical convective mode forced by the heat flux anomaly, increases the relative amount of ω-induced toroidal field up to 85%. Whenever the ω-effect becomes dominant, oscillations including polarity reversals set in (figure 3.18). These oscillations are quite different from those of the observed magnetic field of the Earth. Reversals on the Earth typically emerge randomly and are very rare. Further details about the geomagnetic reversals in numerical dynamo simulations can be found in Amit et al. (2010). There are attempts to relate the reversal frequencies to the core evolution Driscoll and Olson (2009) or CMB heat flux disturbances of different patterns Olson et al. (2010). However, all of the Earth related studies report random reversals happening a few times per Myrs. The oscillations we observe under the influence of strong ω-effect are more related to the regular magnetic field oscillations of the Sun. Simple models of the solar convection uses mean field axisymmetric $\alpha\omega$-theory to describe the solar variability as the evolution of a dynamo wave (Parker 1955). This is basically consistent with the findings of our Mars model. To show this is indeed a magnetic wave and there is no advection involved, we computed the magnetic Reynolds number based on the axisymmetric poloidal field to be roughly $Rm_{ad} = 20 - 40$. This gives the ratio of the poloidal advective time scale to the magnetic time scale, showing that it can not be a simple magnetic field advection. Otherwise the time scales should be comparable and thus $Rm_{ad} = O(1)$. Although the significant meridional circulation transports hot fluid from the northern hemisphere to the faster coolong southern and thus its pattern matches the evolution of the poloidal magnetic field, its direction is opposite to the Parker wave. Furthermore we tested the obtained frequencies against the dispersion relation for Parker dynamo waves, and find the good match with both, an $\alpha\omega$ and an $\alpha^2\omega$ dispersion relation (section 4). Therefore the second α-effect responsible for the induction of toroidal field is of minor importance if the ω-effect is strong. Note, that in the hemispherical dynamo models the main flow and field are axisymmetric, what is a requirement for applying the mean field theory.

6.3 Application to Mars

To apply the results of the numerical model to the measurements of the crustal field on Mars, we upward continue the radial CMB magnetic field via a potential field extrapolation (section 5.1). The surface magnetic field strength of the hemispherical dynamos is much smaller than in a typical dipolar reference case. This might have several reasons. First of all, the total magnetic energy inside the dynamo region is smaller by one order of magnitude (see figure 3.13 or the table A.1) in hemispherical dynamos. This is mainly related to the reduction of helical flows, thus weaker poloidal field induction. Since the poloidal field contribution can be exclusively created in these helical flows, the contribution of poloidal field to the total magnetic energy in the dynamo shell is rather small. Secondly, the mean lengths scale of the poloidal field are much smaller in the hemispherical cases, as shown in figure 3.9. Since the decay of a single magnetic mode of degree l is proportional to $r^{-(l+2)}$ for the field, a small scale field will have a much weaker surface amplitude than a dipolar one. As a third point, we had seen that in any scenario of crustal genesis and magnetization only the time averaged field can be imprinted into crustal rocks (section 5.4). Since the magnetic field shows these fast magnetic field oscillations including polarity reversals (figure 3.18), the time averaged poloidal surface field will decay even further on the relevant time scales for crustal magnetization in the order of millions of years. Note, that the uppermost crustal layer will always have significant magnetization due to its fast cooling rate, if it cools under the Curie temperature in the presence of an ambient field.

We calculated the equatorial asymmetry of the radial field intensity in terms of the hemisphericity $\mathcal{H}$, both at the CMB and the surface by comparing the unsigned magnetic flux in each hemisphere (equation 5.11). A hemispherical magnetic is represented in a flat spectrum for the leading modes, where equatorial symmetric and antisymmetric modes cancel each other in one hemisphere and amplify in the opposing hemisphere. In section 5.2.1 we discussed the hemisphericity for a synthetic magnetic field with an artificial white spectrum. The radial dependence and time variability of the hemisphericity $\mathcal{H}$ according to the surface extrapolation was analyzed on section 5.2.3, showing that the hemisphericity at the CMB typically exceeds that at the surface. Intuitively, this statement matches the expectation, since all modes decay depending of their degree l and thus the equatorial symmetric dipole becomes increasingly more important with radius. However, we also observed that the maximum hemisphericity is not always located at the CMB, but can reside somewhere in the mantle (see figure 5.9) depending on the small-scaleness of the poloidal CMB field. This can happen, if the dipole mode is weaker than higher modes at the CMB, and the poloidal energy spectra (see figure 5.7 or distribution of Gauss coefficients (figure 5.8) becomes flatter or more 'whitish' at a certain distance away from the CMB.

Figure 6.1 tries to compile our results for a zero tilt angle by relating the cmb (top panel) and surface (bottom) hemisphericities to the magnetic Reynolds number $Rm^\star$ which is only based on the equatorially anti-symmetric part of the zonal flow and therefore useful to quantify the important ω-effect in the hemispherical dynamo cases. Compare also the table A.1 for more details. We use here the magnetic Reynolds number, instead of the hydrodynamic Reynolds number to take into account the different magnetic Prandtl number used in the study. The figure 6.1 is equivalent to figure 5.11, but the colors do not represent the Ekman numbers, but the secular variation. For all black symbols, the dynamo is stable in time and does not show polarity inversions. The red symbols denote the oscillating cases. It is clearly visible, that a sufficient strong hemisphericity goes along with the dynamo waves showing regular reversals. Note that there are also cases with high hemisphericity at the CMB $\mathcal{H}_{cmb}$ (figure 6.1, top plot), which show no oscillations (black symbols).

The ratio of $\mathcal{H}_{cmb}$ and $\mathcal{H}_{sur}$ is controlled by the length scales of the leading poloidal magnetic modes. The leading modes correspond to spherical harmonics of degree $l = 5..7$ for a typical hemispherical case. If the dipole and other modes of large length scale (smaller l) are sufficiently small, the spectral distribution of the strongest might remain flat but is shifted to higher l during the surface extrapolation. In general the length scales of the magnetic field d_m are controlled with respect to the convective length scales via the magnetic Prandtl number as the ratio between magnetic and viscous diffusion time, τ_λ and τ_ν:

$$Pm = \frac{\tau_\nu}{\tau_\lambda} = \frac{d_c^2/\nu}{d_m^2/\lambda}, \tag{6.1}$$

with the convective length scales d_c. Larger values of Rayleigh number Ra, perturbation amplitude g and smaller Ekman number E lead to smaller convective length scales, thus smaller magnetic length scales. In figure 6.1 we can easily identify this dependence for g

(e.g. filled circles) and Pm (all kinds of triangles have $Pm = 5$). For Ra and E the effect is not clearly visible and might be biased by stronger dependencies on g and Pm.

Extrapolating the CMB field geometry using the geometric decay of the single modes, leads to the lower plot of figure 6.1. The horizontal black line and the gray area shows the estimated value of the equatorial asymmetry (hemisphericity) in the crustal magnetization of Mars (Amit et al. 2011) and the uncertainties, respectively. It can be seen, that only the oscillating cases (red symbols) show sufficient hemisphericity $\mathcal{H}_{sur}$ at the planetary surface. All the symbols with very large Rm^* are those with $E = 3 \times 10^{-4}$ and $Pm = 5$. For this cases it is rather easy to force the EAA convective mode to occur and thus the amplitude of the zonal flows is rather strong. On top of that the high magnetic Prandtl number increase the magnetic Reynolds number. An appropriate model would need to match these values for the surface hemisphericity $\mathcal{H}_{sur}$ to successfully explain the crustal magnetization dichotomy with a hemispherical dynamo mechanism. All our model runs fulfilling this condition show oscillations, and therefore can not explain the observed magnetization strength reported by Acuña et al. (2001).

Note, there is some evidence for a reversing dynamo in the crustal magnetization. Connerney et al. (1999) studied the magnetic lineations in the southern hemisphere and concluded, that they could have been acquired by plate tectonics and a reversing internal magnetic field. The presence of plate tectonics, as stated by Morschhauser et al. (2011), is indeed a possible scenario during the time of an active dynamo. Maybe even a necessary condition, since plate tectonics cool the underlying mantle much faster and might have increased the CMB heat flux over the adiabatic core heat flux thus allowing for core convection and finally a dynamo at all. On the other hand plate tectonics recycle crust quickly and thus that the average thickness might not exceed a few km. That contradicts the conjecture of Langlais et al. (2004) that a unidirectional magnetization need to be at least present in the uppermost 20 km of the crust. Thinner magnetized crust is only compatible with the observed magnetic moment, if the magnetization density in terms of abundance of iron oxides or other ferromagnetic minerals is much larger than expected. If the magnetized crust would be thin enough corresponding to an anomalous density of magnetic carriers, also our reversing dynamos would again serve as proper model.

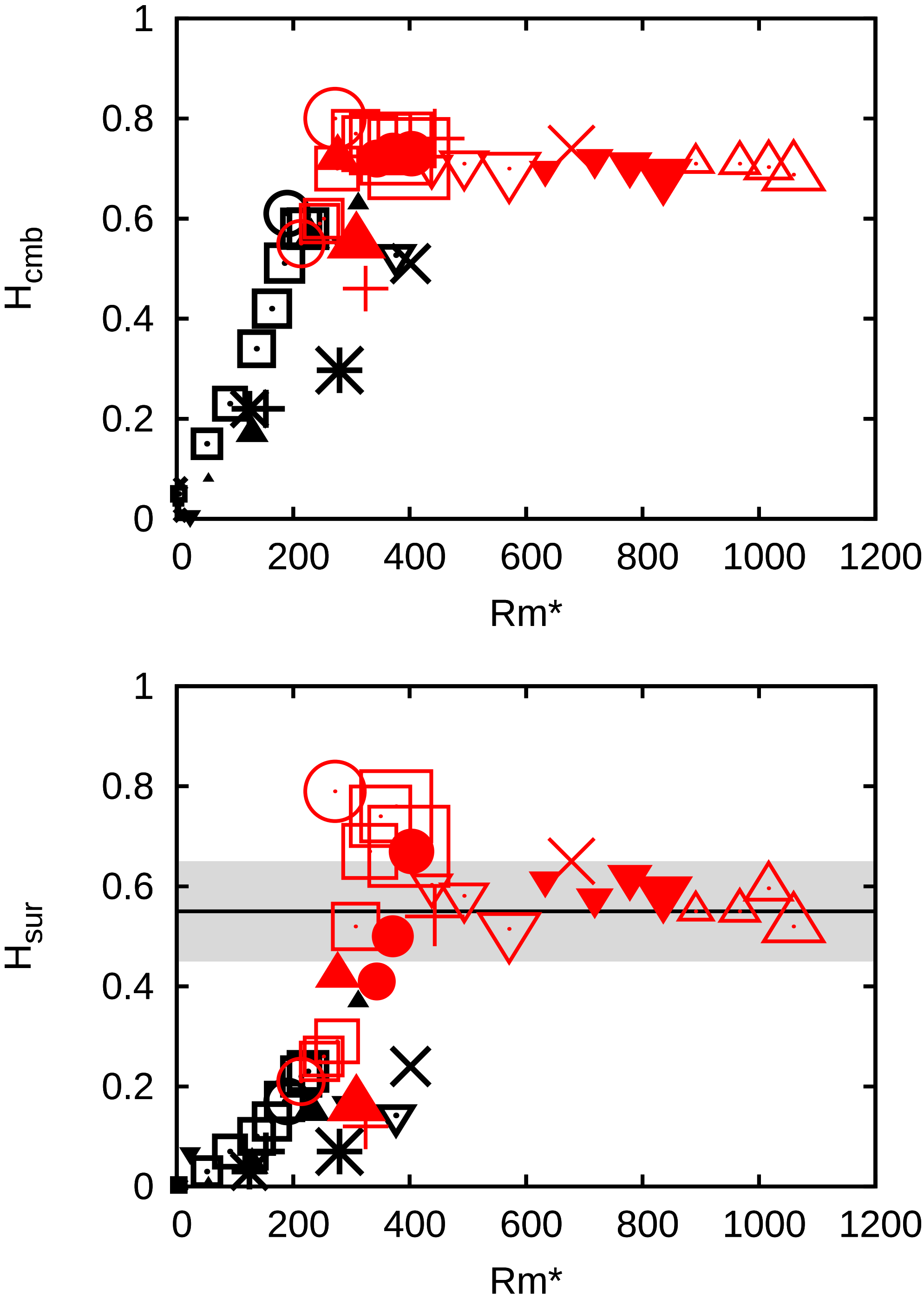

Figure 6.1: Top panel: Hemisphericity at cmb versus $Rm^{\star}$, the magnetic Reynolds number based on the equatorially antisymmetric thermal wind. bottom panel: Hemisphericity at the (imaginary) Martian surface versus $Rm^{\star}$.

7 Summary

In 1998 the space probe Mars Global Surveyor (MGS) delivered vector magnetic field measurements during orbits 185 – 400 km altitude over the Martian surface (Acuña et al. 1999). Crustal magnetization on Mars is characterized by its age of at least 3.7 Gyrs, a strong amplitude, its depth of at least 20 km and the remarkable equatorial dichotomy. In this study we therefore aim to model dynamos, which favor to concentrate the magnetic field in one (south for Mars) hemisphere. Several attempts have been made to develop numerical dynamo models which take characteristic features of the early Martian interior into account (Stanley et al. 2008, Amit et al. 2011). We are following these studies and model the ancient Martian dynamo as driven exclusively by thermal convection and vary laterally the amount of heat escaping from the core into mantle.

The so modified dynamos concentrate dynamo action in the hemisphere of higher core mantle boundary (CMB) heat flux. Indeed, the surface extrapolation of the core field matches successfully the crustal magnetization pattern. However, our results suggest that hemispherical dynamos which are boundary driven by CMB heat flux anomalies show an oscillatory behavior including polarity inversions. We suggest that the oscillatory nature originates from strong shear induced by equatorially antisymmetric and axisymmetric thermal winds. Given the distinct time scales of crustal cooling and magnetization on the one hand, and those typical for the cycle period in our hemispherical dynamos on the other hand, our results seem inconsistent with a magnetization depth of at least 20 km (Langlais et al. 2004).

Interestingly, the time dependence of the hemispherical dynamo was found to agree well with the Parker's theory of plane waves in order predict the solar cycle (Parker 1955). We compared the frequencies and evolution of the reversing hemispherical dynamos with the propagation of Parker-like dynamo waves and found a surprisingly good agreement. This might be based on the fact, that the main contributions of flow and the magnetic field in our simulations are axisymmetric and thus share characteristics with the mean field model applied to the sun.

A Table of Runs

E	Ra	Pm	g	α	Rm	$Rm^\star$	Λ	EAA	ω^*	$\bar{B}_{sur}$	$\mathcal{H}_{sur}$	$\mathcal{H}_{cmb}$	osci	freq.
3e-4	1e7	5	0	0	280.9	13.4	12.27	6.9e-3	0.208	55161	5.5e-3	6.9e-2	no	-
			40	0	442.9	77.1	7.56	0.74	0.74	16107	0.142	0.53	no	-
			60	0	497.1	90.8	2.8	0.79	0.85	2501	0.603	0.705	yes	12.19
			100	0	560.5	104.4	2.6	0.80	0.85	2242	0.581	0.708	yes	15.82
			200	0	672.5	124.5	2.1	0.72	0.84	2059	0.52	0.70	yes	15.3
	3e7	5	0	0	593.5	57	12.4	0.21	0.45	17288	0.175	0.553	yes	?
			40	0	756.2	131.2	18.7	0.71	0.69	16244	0.61	0.7	yes	19.4
			60	0	817.5	148.8	17.4	0.79	0.75	10849	0.58	0.72	yes	17.21
			100	0	896.4	162.9	8.2	0.77	0.80	5152	0.62	0.71	yes	20.91
			200	0	1020	183.8	7.2	0.68	0.82	3979	0.59	0.69	yes	13.51
	6e7	5	0	0	825.5	66.5	15	0.148	0.405	11560	0.37	0.63	yes	?
			40	0	1046	185.3	34.3	0.74	0.64	21745	0.55	0.705	yes	23.27
			60	0	1113	200.9	24.4	0.77	0.71	15201	0.55	0.71	yes	23.02
			100	0	1183	213.1	18.2	0.75	0.76	9387	0.6	0.703	yes	25.91
			200	0	1306	201.2	16.7	0.67	0.78	7268	0.52	0.69	yes	26.2
1e-4	7e6	2	0	0	54.6	0.12	-	2.24e-5	-	-	-	-	-	-
			100	0	133.5	61.3	0.1	0.85	0.32	803.2	0.1	0.21	no	-
		5	0	0	117.1	0.79	9.79	1.93e-3	0.21	62510	4e-4	3e-3	no	-
			100	0	326.9	60.3	0.97	0.85	0.66	1469	0.1	0.35	yes	?
			200	0	449.5	83.5	-	0.84	-	-	-	-	-	-
			100	90	230.8	-	2.22	5e-3	0.20	7264	-	-	yes	18.84
	2.1e7	2	0	0	105.9	3.21	4.95	3.64e-3	0.24	64635	1.0e-3	0.03	no	-
			60	0	178.1	74.89	6.24	0.72	0.63	14017	0.12	0.38	no	-
			80	0	228.3	94.85	1.06	0.74	0.53	1684	0.17	0.61	yes	10.69
			100	0	247.6	106.8	0.15	0.73	0.58	1001	0.21	0.55	yes	?
			200	0	313.3	136	0.19	0.76	0.77	689	0.79	0.8	yes	56.27
			100	90	160.2	40.2	2.64	6.6e-3	0.18	699	-	-	yes	?
	4e7	1	100	0	169.3	143.1	0.2	0.73	0.53	922	0.21	0.22	no	-
			200	0	206.5	171.5	-	0.7	-	-	-	-	(yes)	
		2	0	0	155.6	1.79	6.26	2e-3	0.18	58349	3.0e-3	0.05	no	-
			20	0	162.9	7.3	9.1	0.11	0.29	65067	0.03	0.15	no	-
			30	0	172.7	17.1	10.32	0.28	0.38	61323	0.07	0.23	no	-
			40	0	200.9	45.4	11.3	0.48	0.49	31610	0.1	0.34	no	-
			46	0	213.7	58.2	21.4	0.59	0.55	22360	0.13	0.42	no	-
			50	0	229.3	73.8	22.9	0.66	0.58	17938	0.17	0.51	no	-
			54	0	253.8	98.2	7.4	0.71	0.61	13907	0.22	0.58	no	-

			56	0	267.6	112	5.53	0.71	0.61	11877	0.23	0.58	no	-
			58	0	283.5	127.2	2.84	0.75	0.63	8259	0.25	0.59	no	-
			60	0	283.4	127.9	3.4	0.73	0.63	6154	0.26	0.6	yes	13.96
			100	0	338.1	153.6	2.64	0.78	0.76	2219	0.52	0.77	yes	40.83
			200	0	409.8	175	1.16	0.74	0.75	1628	0.74	0.75	yes	62.6
			100	90	217.3	-	1.47	8.4e-3	0.21	10071	-	-	yes	20.77
			200	90	226.5	-	5.41	4.1e-3	0.24	10934	-	-	no	-
		5	100	0	837.5	149.9	6.83	0.81	0.8	3493	0.7	0.65	yes	79.87
	8e7	2	0	0	228.7	3.2	7.06	9e-3	0.18	60036	3.3e-3	0.07	no	-
			60	0	400.2	171.8	5.5	0.74	0.65	9268	0.41	0.72	yes	26.97
			100	0	457.6	201.61	2.97	0.79	0.73	3240	0.68	0.73	yes	61.3
			100	90	297.5	-	3.73	6.4e-3	0.20	16424	-	-	yes	24.5
	2e8	1	0	0	251.8	54.4	-	0.05	-	-	-	-	-	-
			60	0	309.9	230.1	2.14	0.63	0.56	6095	0.15	0.56	no	-
			100	0	343.5	276.3	0.34	0.64	0.65	1119	0.42	0.72	yes	24.32
			100	90	270.4	-	0.77	4e-3	0.21	7954	-	-	yes	17.95
3e-5	1e8	2	0	0	137.1	1.44	7.68	5.7e-3	0.19	80508	1e-3	0.03	no	-
			60	0	210.7	24.1	12.31	0.5	0.53	25567	0.1	0.23	no	-
			100	0	360.4	162.1	5.07	0.81	0.67	5157	0.12	0.46	yes	10.34
			100	90	199.5	-	1.4	3.1e-3	0.16	10657	-	-	yes	?
3e-5	4e8	2	0	0	316.9	3.31	12.2	5.5e-3	0.26	71085	2.1e-3	0.07	no	-
			60	0	517.1	200.9	29.9	0.64	0.49	30528	0.24	0.51	no	-
			100	0	769.1	341	6.04	0.76	0.70	4584	0.62	0.76	yes	87.6
Mars														
3e-15	2e28	1e-6	?	?	500?	?	?	?	?	5000	0.45	?	no?	

Table A.1: Selection of runs performed. Rm - magnetic Reynolds number, Λ - Elsasser number of rms field in full core shell, EAA - relative equatorially antisymmetric and axisymmetric kinetic energy, ω^* - relative induction of toroidal field by shearing,$|B|_{sur}$ - time averaged field intensity at the Martian surface in nT, $\mathcal{H}_{sur}$ and $\mathcal{H}_{cmb}$ - hemisphericity at the surface and CMB, freq. - rough frequency ($2\pi Pm/\tau_{vis}$) if present. Decaying solutions are marked with '-' in the Elsasser number. If not a single frequency could be extracted '?' is used.

Bibliography

Acuña, M. H., Connerney, J. E. P., Ness, N. F., Lin, R. P., Mitchell, D., Carlson, C. W., McFadden, J., Anderson, K. A., Reme, H., Mazelle, C., Vignes, D., Wasilewski, P., Cloutier, P., 1999, Global Distribution of Crustal Magnetization Discovered by the Mars Global Surveyor MAG/ER Experiment, Science, 284, 790–793

Acuña, M. H., Connerney, J. E. P., Wasilewski, P., Lin, R. P., Mitchell, D., Anderson, K. A., Carlson, C. W., McFadden, J., Rème, H., Mazelle, C., Vignes, D., Bauer, S. J., Cloutier, P., Ness, N. F., 2001, Magnetic field of Mars: Summary of results from the aerobraking and mapping orbits, Journal of Geophysical Research, 106, 23 403–23 418

Amit, H., Leonhardt, R., Wicht, J., 2010, Polarity Reversals from Paleomagnetic Observations and Numerical Dynamo Simulations, Space Science Reviews, 155, 293–335

Amit, H., Christensen, U. R., Langlais, B., 2011, The influence of degree-1 mantle heterogeneity on the past dynamo of Mars, Physics of the Earth and Planetary Interiors, 189, 63–79

Anufriev, A. P., Jones, C. A., Soward, A. M., 2005, The Boussinesq and anelastic liquid approximations for convection in the Earth's core, Physics of the Earth and Planetary Interiors, 152, 163–190

Arkani-Hamed, J., Olson, P., 2010, Giant impact stratification of the Martian core, Geophysical Research Letters, 37, 2201–2205

Aubert, J., Amit, H., Hulot, G., Olson, P., 2008a, Thermochemical flows couple the Earth's inner core growth to mantle heterogeneity, Nature, 454, 758–761

Aubert, J., Aurnou, J., Wicht, J., 2008b, The magnetic structure of convection-driven numerical dynamos, Geophysical Journal International, 172, 945–956

Aurnou, J. M., Aubert, J., 2011, End-member models of boundary-modulated convective dynamos, Physics of the Earth and Planetary Interiors, 187, 353–363

Balogh, A., 2010, Planetary Magnetic Field Measurements: Missions and Instrumentation, Space Science Reviews, 152, 23–97

Bandfield, J. L., Hamilton, V. E., Christensen, P. R., 2000, A Global View of Martian Surface Compositions from MGS-TES, Science, 287, 1626–1630

Banerdt, W. B., Golombek, M. P., Tanaka, K. L., 1992, Stress and tectonics on Mars, pp. 249–297

Barabash, S., Fedorov, A., Lundin, R., Sauvaud, J.-A., 2007, Martian Atmospheric Erosion Rates, Science, 315, 501–503

Bisshopp, F. E., Niiler, P. P., 1965, Onset of convection in a rapidly rotating fluid sphere, Journal of Fluid Mechanics, 23, 459–469

Bloxham, J., 2000, Sensitivity of the geomagnetic axial dipole to thermal core-mantle interactions, Nature, 405, 63–65

Bloxham, J., Gubbins, D., 1987, Thermal core-mantle interactions, Nature, 325, 511–513

Braginsky, S. I., 1964, Kinematic Models of the Earth's Hydromagnetic Dynamo, Geomagnetism and Aeronomy/Geomagnetizm i Aeronomiia, 4, 572–583

Braginsky, S. I., Roberts, P. H., 1995, Equations governing convection in earth's core and the geodynamo, Geophysical and Astrophysical Fluid Dynamics, 79, 1–97

Breuer, D., Moore, W. B., 2007, Dynamics and Thermal History of the Terrestrial Planets, the Moon, and Io, in Treatise on Geophysics Volume 10: Planets and Moons, (Ed.) T. Spohn, Treatise on Geophysics, pp. 299–341, Elsevier

Breuer, D., Spohn, T., 2003, Early plate tectonics versus single-plate tectonics on Mars: Evidence from magnetic field history and crust evolution, Journal of Geophysical Research (Planets), 108, 5072

Breuer, D., Spohn, T., Wullner, U., 1993, Mantle differentiation and the crustal dichotomy of Mars, Planetary and Space Sciences, 41, 269–283

Bronstein, I. N., Semendjajew, K. A., Musiol, G., 2005, Taschenbuch der Mathematik, Deutsch (Harri)

Busse, F. H., 1970, Thermal instabilities in rapidly rotating systems., Journal of Fluid Mechanics, 44, 441–460

Busse, F. H., Simitev, R., 2007, Planetary Dynamos, in Treatise on Geophysics Volume 10: Planets and Moons, (Ed.) T. Spohn, Treatise on Geophysics, pp. 281–297, Elsevier

Busse, F. H., Simitev, R. D., 2006, Parameter dependences of convection-driven dynamos in rotating spherical fluid shells, Geophysical and Astrophysical Fluid Dynamics, 100, 341–361, 0904.4293

Cain, J. C., Ferguson, B. B., Mozzoni, D., 2003, An n = 90 internal potential function of the Martian crustal magnetic field, Journal of Geophysical Research (Planets), 108, 5008

Chandrasekhar, S., 1961, Hydrodynamic and hydromagnetic stability

Charbonneau, P., 2010, Dynamo Models of the Solar Cycle, Living Reviews in Solar Physics, 7, 3

Christensen, U. R., 2002, Zonal flow driven by strongly supercritical convection in rotating spherical shells, Journal of Fluid Mechanics, 470, 115–133

Christensen, U. R., Aubert, J., 2006, Scaling properties of convection-driven dynamos in rotating spherical shells and application to planetary magnetic fields, Geophysical Journal International, 166, 97–114

Christensen, U. R., Olson, P., 2003, Secular variation in numerical geodynamo models with lateral variations of boundary heat flow, Physics of the Earth and Planetary Interiors, 138, 39–54

Christensen, U. R., Tilgner, A., 2002, Der Geodynamo, Physik Journal, 1, 41–47

Christensen, U. R., Wicht, J., 2007, Numerical Dynamo simulations, in Treatise on Geophysics Volume 8: Core Dynamics, (Ed.) P. Olson, Treatise on Geophysics, pp. 245–282, Elsevier

Christensen, U. R., Aubert, J., Cardin, P., Dormy, E., Gibbons, S., Glatzmaier, G. A., Grote, E., Honkura, Y., Jones, C., Kono, M., Matsushima, M., Sakuraba, A., Takahashi, F., Tilgner, A., Wicht, J., Zhang, K., 2001, A numerical dynamo benchmark, Physics of the Earth and Planetary Interiors, 128, 25–34

Connerney, J. E. P., 2007, Planetary Magnetism, in Treatise on Geophysics Volume 10: Planets and Moons, (Ed.) T. Spohn, Treatise on Geophysics, pp. 243–275, Elsevier

Connerney, J. E. P., Acuna, M. H., Wasilewski, P. J., Ness, N. F., Reme, H., Mazelle, C., Vignes, D., Lin, R. P., Mitchell, D. L., Cloutier, P. A., 1999, Magnetic Lineations in the Ancient Crust of Mars, Science, 284, 794–798

Dehant, V., 2003, PLANETARY SCIENCE: Enhanced: A Liquid Core for Mars?, Science, 300, 260–261, http://www.sciencemag.org/cgi/reprint/300/5617/260.pdf

Dehant, V., Van Hoolst, T., de Viron, O., Greff-Lefftz, M., Legros, H., Defraigne, P., 2003, Can a solid inner core of Mars be detected from observations of polar motion and nutation of Mars?, Journal of Geophysical Research (Planets), 108, 5127

Desjardins, B., Dormy, E., 2007, Introduction to self-excited dynamo action, in Mathematical Aspects of Natural Dynamos, (Ed.) S. A. M. Dormy, E., The Fluid Mechanics of Astrophysics and Geophysics, pp. 1–59, Grenoble Sciences

Driscoll, P., Olson, P., 2009, Polarity reversals in geodynamo models with core evolution, Earth and Planetary Science Letters, 282, 24–33

Dziewonski, A. M., Anderson, D. L., 1981, Preliminary reference Earth model, Physics of the Earth and Planetary Interiors, 25, 297–356

Elkins-Tanton, L. T., Zaranek, S. E., Parmentier, E. M., Hess, P. C., 2005, Early magnetic field and magmatic activity on Mars from magma ocean cumulate overturn, Earth and Planetary Science Letters, 236, 1–12

Faber, T. E., 1995, Fluid Dynamics for Physicists

Frey, H., Schultz, R. A., 1988, Large impact basins and the mega-impact origin for the crustal dichotomy on Mars, Geophysical Research Letters, 15, 229–232

Frey, H. V., Roark, J. H., Shockey, K. M., Frey, E. L., Sakimoto, S. E. H., 2002, Ancient lowlands on Mars, Geophysical Research Letters, 29, 1384

Gastine, T., Duarte, L., Wicht, J., 2012, Dipolar versus multipolar dynamos: the influence of the background density stratification, ArXiv e-prints, 1208.6093

Gilbert, W., 1600, de Magnete

Glatzmaier, G. A., 1984, Numerical simulations of stellar convective dynamos. I - The model and method, Journal of Computational Physics, 55, 461–484

Glatzmaier, G. A., Coe, R. S., 2007, Magnetic Polarity Reversals in the Core, in Treatise on Geophysics Volume 8: Core Dynamics, (Ed.) P. Olson, Treatise on Geophysics, pp. 283–295, Elsevier

Glatzmaier, G. A., Roberts, P. H., 1995, A 3-Dimensional Convective Dynamo Solution with rotating and finitely conducting Inner-Core and Mantle, Physics of the Earth and Planetary Interiors, 91, 63–75, ISSN 0031-9201, 4th International Symposium of the International-Union-of-Geodesy-and-Geophysics (IUGG) Union-Committee-for-Study-of-the-Earths-Deep-Interior (SEDI), Whistler Mountain, Canada, AUG 07-12, 1994

Glatzmaier, G. A., Roberts, P. H., 1997, Simulating the geodynamo, Contemporary Physics, 38, 269–288

Glatzmaier, G. A., Coe, R. S., Hongre, L., Roberts, P. H., 1999, The role of the Earth's mantle in controlling the frequency of geomagnetic reversals, Nature, 401, 885–890

Goedbloed, J. P. H., Poedts, S., 2004, Principles of Magnetohydrodynamics

Guervilly, C., Cardin, P., 2010, Numerical simulations of dynamos generated in spherical Couette flows, Geophysical and Astrophysical Fluid Dynamics, 104, 221–248, 1010.3859

Harder, H., Christensen, U. R., 1996, A one-plume model of martian mantle convection, Nature, 380, 507–509

Hartmann, W. K., Neukum, G., 2001, Cratering Chronology and the Evolution of Mars, Space Science Reviews, 96, 165–194

Hartmann, W. K., Malin, M., McEwen, A., Carr, M., Soderblom, L., Thomas, P., Danielson, E., James, P., Veverka, J., 1999, Evidence for recent volcanism on Mars from crater counts, Nature, 397, 586–589

Hood, L. L., Young, C. N., Richmond, N. C., Harrison, K. P., 2005, Modeling of major martian magnetic anomalies: Further evidence for polar reorientations during the Noachian, Icarus, 177, 144–173

Hori, K., Wicht, J., Christensen, U. R., 2010, The effect of thermal boundary conditions on dynamos driven by internal heating, Physics of the Earth and Planetary Interiors, 182, 85–97

Hori, K., Wicht, J., Christensen, U. R., 2012, The influence of thermo-compositional boundary conditions on convection and dynamos in a rotating spherical shell, Physics of the Earth and Planetary Interiors, 196, 32–48

Hulot, G., Finlay, C. C., Constable, C. G., Olsen, N., Mandea, M., 2010, The Magnetic Field of Planet Earth, Space Science Reviews, 152, 159–222

Jones, C. A., 2007, Thermal and Compositional Convection in the Outer Core, in Treatise on Geophysics Volume 8: Core Dynamics, (Ed.) P. Olson, Treatise on Geophysics, pp. 131–185, Elsevier

Jones, C. A., 2011, Planetary Magnetic Fields and Fluid Dynamos, Annual Review of Fluid Mechanics, 43, 583–614

Keller, T., Tackley, P. J., 2009, Towards self-consistent modeling of the martian dichotomy: The influence of one-ridge convection on crustal thickness distribution, Icarus, 202, 429–443

King, E. M., Soderlund, K. M., Christensen, U. R., Wicht, J., Aurnou, J. M., 2010, Convective heat transfer in planetary dynamo models, Geochemistry, Geophysics, Geosystems, 11, Q06016

Kono, A., Finlay, C. C., 2007, Geomagnetic Secular Variation and Its Applications to the Core, in Treatise on Geophysics Volume 5: Geomagnetism, (Ed.) M. Kono, Treatise on Geophysics, pp. 147–194, Elsevier

Kono, M., 2007, Geomagnetism in Perspective, in Treatise on Geophysics Volume 5: Geomagnetism, (Ed.) M. Kono, Treatise on Geophysics, pp. 1–33, Elsevier

Krause, F., Rädler, K.-H., 1980, Mean-field magnetohydrodynamics and dynamo theory

Kulsrud, R. M., 2005, Plasma physics for astrophysics

Kutzner, C., Christensen, U. R., 2002, From stable dipolar towards reversing numerical dynamos, Physics of the Earth and Planetary Interiors, 131, 29–45

Landau, L. D., Lifshitz, E. M., 1959, Fluid mechanics by L.D. Landau and E.M. Lifshitz; translated from the Russian by J.B. Sykes and W.H. Reid, Pergamon Press ; Addison-Wesley, London : Reading, Mass. :

Landeau, M., Aubert, J., 2011, Equatorially asymmetric convection inducing a hemispherical magnetic field in rotating spheres and implications for the past martian dynamo, Physics of the Earth and Planetary Interiors, 185, 61–73

Langlais, B., Purucker, M. E., Mandea, M., 2004, Crustal magnetic field of Mars, Journal of Geophysical Research (Planets), 109, E02008

Langlais, B., Lesur, V., Purucker, M. E., Connerney, J. E. P., Mandea, M., 2010, Crustal Magnetic Fields of Terrestrial Planets, Space Science Reviews, 152, 223–249

Langlais, B., Thébault, E., Ostanciaux, E., Mangold, N., 2012, A Late Martian Dynamo Cessation Time 3.77 Gy Ago, in Lunar and Planetary Institute Science Conference Abstracts, vol. 43 of Lunar and Planetary Inst. Technical Report, p. 1231

Larmor, J., 1919, How could a Rotating Body such as the sun become a Magnet, Report of the British Asssociation for the Advancement of Science, 87, 159–160

Lee, D.-C., Halliday, A. N., 1997, Core formation on Mars and differentiated asteroids, Nature, 388, 854–857

Leweling, M., Spohn, T., 1997, Mars: a magnetic field due to thermoremanence?, Planetary and Space Sciences, 45, 1389–1400

Lillis, R. J., Frey, H. V., Manga, M., 2008a, Rapid decrease in Martian crustal magnetization in the Noachian era: Implications for the dynamo and climate of early Mars, Geophysical Research Letters, 35, 14 203–14 209

Lillis, R. J., Frey, H. V., Manga, M., Mitchell, D. L., Lin, R. P., Acuña, M. H., Bougher, S. W., 2008b, An improved crustal magnetic field map of Mars from electron reflectometry: Highland volcano magmatic history and the end of the martian dynamo, Icarus, 194, 575–596

Longhi, J., Knittle, E., Holloway, J. R., Waenke, H., 1992, The bulk composition, mineralogy and internal structure of Mars, pp. 184–208

Lyubimov, D. V., Lyubimova, T. P., Alexander, J. I. D., Lobov, N. I., 1998, On the boussinesq approximation for fluid systems with deformable interfaces, Advances in Space Research, 22, 1159–1168

Manglik, A., Wicht, J., Christensen, U. R., 2010, A dynamo model with double diffusive convection for Mercury's core, Earth and Planetary Science Letters, 289, 619–628

Marinova, M. M., Aharonson, O., Asphaug, E., 2008, Mega-impact formation of the Mars hemispheric dichotomy, Nature, 453, 1216–1219

Melosh, H. J., 1980, Tectonic patterns on a reoriented planet - Mars, Icarus, 44, 745–751

Mohit, P. S., Arkani-Hamed, J., 2004, Impact demagnetization of the martian crust, Icarus, 168, 305–317

Morschhauser, A., Grott, M., Breuer, D., 2011, Crustal recycling, mantle dehydration, and the thermal evolution of Mars, Icarus, 212, 541–558

Ness, N. F., 2010, Space Exploration of Planetary Magnetism, Space Science Reviews, 152, 5–22

Ness, N. F., Acuña, M. H., Connerney, J., Wasilewski, P., Mazelle, C., Sauvaud, J., Vignes, D., D'Uston, C., Reme, H., Lin, R., Mitchell, D. L., McFadden, J., Curtis, D., Cloutier, P., Bauer, S. J., 1999, MGS magnetic fields and electron reflectometer investigation: discovery of paleomagnetic fields due to crustal remanence, Advances in Space Research, 23, 1879–1886

Nimmo, F., 2007, Theory of Geodynamo, in Treatise on Geophysics Volume 8: Core Dynamics, (Ed.) P. Olson, Treatise on Geophysics, pp. 31–65, Elsevier

Nimmo, F., Stevenson, D. J., 2000, Influence of early plate tectonics on the thermal evolution and magnetic field of Mars, Journal of Geophysical Research, 105, 11 969–11 980

Nimmo, F., Tanaka, K., 2005, Early Crustal Evolution of Mars, Annual Review of Earth and Planetary Sciences, 33, 133–161

Olson, P., Christensen, U. R., 2002, The time-averaged magnetic field in numerical dynamos with non-uniform boundary heat flow, Geophysical Journal International, 151, 809–823

Olson, P., Christensen, U., Glatzmaier, G. A., 1999, Numerical modeling of the geodynamo: Mechanisms of field generation and equilibration, Journal of Geophysical Research, 1041, 10 383–10 404

Olson, P. L., Coe, R. S., Driscoll, P. E., Glatzmaier, G. A., Roberts, P. H., 2010, Geodynamo reversal frequency and heterogeneous core-mantle boundary heat flow, Physics of the Earth and Planetary Interiors, 180, 66–79

Ossendrijver, M., 2003, The solar dynamo, Astronomy and Astrophysics Reviews, 11, 287–367

Parker, E. N., 1955, Hydromagnetic Dynamo Models., Astrophysical Journal, 122, 293

Piel, A., 2010, Plasma Physics

Proctor, M., 2006, Dynamo action and the sun, in EAS Publications Series, (Eds.) M. Rieutord, B. Dubrulle, vol. 21 of EAS Publications Series, pp. 241–273

Purucker, M. E., Whaler, K. A., 2007, Crustal Magnetism, in Treatise on Geophysics Volume 5: Geomagnetism, (Ed.) M. Kono, Treatise on Geophysics, pp. 1195–236, Elsevier

Reese, C. C., Solomatov, V. S., 2010, Early martian dynamo generation due to giant impacts, Icarus, 207, 82–97

Roberts, J. H., Zhong, S., 2006, Degree-1 convection in the Martian mantle and the origin of the hemispheric dichotomy, Journal of Geophysical Research (Planets), 111, 6013–6035

Roberts, J. H., Lillis, R. J., Manga, M., Frey, H. V., 2008, Impact-related Heating and the Cessation of the Martian Dynamo: Early Results, in Lunar and Planetary Institute Science Conference Abstracts, vol. 39 of Lunar and Planetary Institute Science Conference Abstracts, pp. 1358–1359

Roberts, J. H., Lillis, R. J., Manga, M., 2009, Giant impacts on early Mars and the cessation of the Martian dynamo, Journal of Geophysical Research (Planets), 114, 4009–4019

Roberts, P. H., 1965, On the Thermal Instability of a Highly Rotating Fluid Sphere., Astrophysical Journal, 141, 240

Roberts, P. H., 1968, On the Thermal Instability of a Rotating-Fluid Sphere Containing Heat Sources, Royal Society of London Philosophical Transactions Series A, 263, 93–117

Roberts, P. H., 2007, Theory of Geodynamo, in Treatise on Geophysics Volume 8: Core Dynamics, (Ed.) P. Olson, Treatise on Geophysics, pp. 67–102, Elsevier

Rochette, P., Lorand, J.-P., Fillion, G., Sautter, V., 2001, Pyrrhotite and the remanent magnetization of SNC meteorites: a changing perspective on Martian magnetism, Earth and Planetary Science Letters, 190, 1–12

Rüdiger, G., Hollerbach, R., 2004, The magnetic universe : geophysical and astrophysical dynamo theory

Runcorn, S. K., 1975a, On the interpretation of lunar magnetism, Physics of the Earth and Planetary Interiors, 10, 327–335

Runcorn, S. K., 1975b, An ancient lunar magnetic dipole field, Nature, 253, 701–703

Runcorn, S. K., Collinson, D. W., O'Reilly, W., Battey, M. H., Stephenson, A., Jones, J. M., Manson, A. J., Readman, P. W., 1970, Magnetic properties of Apollo 11 lunar samples, Geochimica et Cosmochimica Acta Supplement, 1, 2369

Schrinner, M., 2011, Global dynamo models from direct numerical simulations and their mean-field counterparts, Astronomy and Astrophysics, 533, A108, `1105.2912`

Schrinner, M., Rädler, K.-H., Schmitt, D., Rheinhardt, M., Christensen, U., 2005, Mean-field view on rotating magnetoconvection and a geodynamo model, Astronomische Nachrichten, 326, 245–249

Schrinner, M., Rädler, K.-H., Schmitt, D., Rheinhardt, M., Christensen, U. R., 2007, Mean-field concept and direct numerical simulations of rotating magnetoconvection and the geodynamo, Geophysical and Astrophysical Fluid Dynamics, 101, 81–116, `arXiv:astro-ph/0609752`

Schrinner, M., Petitdemange, L., Dormy, E., 2011, Oscillatory dynamos and their induction mechanisms, Astronomy & Astrophysics, 530, A140, `1101.1837`

Schubert, G., Spohn, T., 1990, Thermal history of Mars and the sulfur content of its core, Journal of Geophysical Research, 95, 14 095–14 104

Schubert, G., Turcotte, D. L., Olson, P., 2001, Mantle Convection in the Earth and Planets

Smith, D. E., Zuber, M. T., Solomon, S. C., Phillips, R. J., Head, J. W., Garvin, J. B., Banerdt, W. B., Muhleman, D. O., Pettengill, G. H., Neumann, G. A., Lemoine, F. G., Abshire, J. B., Aharonson, O., Brown, C., D., Hauck, S. A., Ivanov, A. B., McGovern, P. J., Zwally, H. J., Duxbury, T. C., 1999, The Global Topography of Mars and Implications for Surface Evolution, Science, 284, 1495

Smith, D. E., Zuber, M. T., Frey, H. V., Garvin, J. B., Head, J. W., Muhleman, D. O., Pettengill, G. H., Phillips, R. J., Solomon, S. C., Zwally, H. J., Banerdt, W. B., Duxbury, T. C., Golombek, M. P., Lemoine, F. G., Neumann, G. A., Rowlands, D. D., Aharonson, O., Ford, P. G., Ivanov, A. B., Johnson, C. L., McGovern, P. J., Abshire, J. B., Afzal, R. S., Sun, X., 2001, Mars Orbiter Laser Altimeter: Experiment summary after the first year of global mapping of Mars, Journal of Geophysical Research, 106, 23 689–23 722

Sohl, F., Spohn, T., 1997, The interior structure of Mars: Implications from SNC meteorites, Journal of Geophysical Research, 102, 1613–1636

Soward, A., Dormy, E., 2007, Boundary and Shear Layers in Rotating Fluids, in Mathematical Aspects of Natural Dynamos, (Ed.) S. A. M. Dormy, E., The Fluid Mechanics of Astrophysics and Geophysics, pp. 119–151, Grenoble Sciences

Spiegel, E. A., 1971, Convection in Stars: I. Basic Boussinesq Convection, Annual Review of Astronomy and Astrophysics, 9, 323

Spiegel, E. A., Veronis, G., 1960, On the Boussinesq Approximation for a Compressible Fluid., Astrophysical Journal, 131, 442

Spohn, T., 2007, Overview, in Treatise on Geophysics Volume 10: Planets and Moons, (Ed.) T. Spohn, Treatise on Geophysics, pp. 1–26, Elsevier

Spohn, T., Acuña, M. H., Breuer, D., Golombek, M., Greeley, R., Halliday, A., Hauber, E., Jaumann, R., Sohl, F., 2001, Geophysical Constraints on the Evolution of Mars, Space Science Reviews, 96, 231–262

Sprenke, K. F., Baker, L. L., 2000, Magnetization, Paleomagnetic Poles, and Polar Wander on Mars, Icarus, 147, 26–34

Sreenivasan, B., Gubbins, D., 2011, On mantle-induced heat flow variations at the inner core boundary, Physics of the Earth and Planetary Interiors, 187, 336–341

Stanley, S., Elkins-Tanton, L., Zuber, M. T., Parmentier, E. M., 2008, Mars´ Paleomagnetic Field as the Result of a Single-Hemisphere Dynamo, Science, 321, 1822–

Stern, D. P., 2002, a Millennium of Geomagnetism, Reviews of Geophysics, 40, 1007

Stix, M., 2002, The sun: an introduction

Takahashi, F., Tsunakawa, H., Matsushima, M., Mochizuki, N., Honkura, Y., 2008, Effects of thermally heterogeneous structure in the lowermost mantle on the geomagnetic field strength, Earth and Planetary Science Letters, 272, 738–746

Tanaka, K. L., 1986, The stratigraphy of Mars, Journal of Geophysical Research, 91, 139

Tilgner, A., 2007, Rotational Dynamics of the Core, in Treatise on Geophysics Volume 8: Core Dynamics, (Ed.) P. Olson, Treatise on Geophysics, pp. 208–241, Elsevier

Tobias, S., Weiss, N., 2007, Linear $\alpha\omega$-Dynamos For the Solar Cycle, in Mathematical Aspects of Natural Dynamos, (Ed.) S. A. M. Dormy, E., The Fluid Mechanics of Astrophysics and Geophysics, pp. 281–312, Grenoble Sciences

Weiss, B. P., Vali, H., Baudenbacher, F. J., Kirschvink, J. L., Stewart, S. T., Shuster, D. L., 2002, Records of an ancient Martian magnetic field in ALH84001, Earth and Planetary Science Letters, 201, 449–463

Weiss, B. P., Fong, L. E., Vali, H., Lima, E. A., Baudenbacher, F. J., 2008, Paleointensity of the ancient Martian magnetic field, Geophysical Research Letters, 35, L23207

Weiss, B. P., Gattacceca, J., Stanley, S., Rochette, P., Christensen, U. R., 2010, Paleomagnetic Records of Meteorites and Early Planetesimal Differentiation, Space Science Reviews, 152, 341–390

Wetherill, G. W., 1990, Formation of the earth, Annual Review of Earth and Planetary Sciences, 18, 205–256

Wicht, J., 2002, Inner-core conductivity in numerical dynamo simulations, Physics of the Earth and Planetary Interiors, 132, 281–302

Wicht, J., Aubert, J., 2005, Dynamos in action

Williams, J.-P., Nimmo, F., 2004, Thermal evolution of the Martian core: Implications for an early dynamo, Geology, 32, 97

Yoshida, M., Kageyama, A., 2006, Low-degree mantle convection with strongly temperature- and depth-dependent viscosity in a three-dimensional spherical shell, Journal of Geophysical Research (Solid Earth), 111, 3412–3422, `arXiv:physics/0512180`

Yoshimura, H., 1976, Phase relation between the poloidal and toroidal solar-cycle general magnetic fields and location of the origin of the surface magnetic fields, Solar Physics, 50, 3–23

Zolotov, M. Y., 2007, Solid Planet-Atmosphere Interactions, in Treatise on Geophysics Volume 10: Planets and Moons, (Ed.) T. Spohn, Treatise on Geophysics, pp. 349–365, Elsevier

Zuber, M. T., Solomon, S. C., Phillips, R. J., Smith, D. E., Tyler, G. L., Aharonson, O., Balmino, G., Banerdt, W. B., Head, J. W., Johnson, C. L., Lemoine, F. G., McGovern, P. J., Neumann, G. A., Rowlands, D. D., Zhong, S., 2000, Internal Structure and Early Thermal Evolution of Mars from Mars Global Surveyor Topography and Gravity, Science, 287, 1788–1793

Publications

Refereed Publications

- Dietrich W., Wicht J.: ’A hemispherical dynamo model - Implications for the Martian crustal magnetisation’, submitted to PEPI

Conference Contributions

- Dietrich W., Wicht J., Christensen U.: ’Lateral CMB heat flux variations as a model for Martian paleomagnetic field’, EGU 2010, Vienna (Poster)
- Dietrich W., Wicht J., Christensen U.: ’Lateral CMB heat flux variations as a model for Martian paleomagnetic field’, Geodynamics Workshop, Westfälische Wilhelms-Universität Münster (Oral)
- Wicht J., Dietrich W., Hori K.: ’Equatorially anti-symmetric convection in rotating spherical shells’, Geodynamics Workshop, Westfälische Wilhelms-Universität Münster (Oral)
- Dietrich W., Wicht J., Christensen U.: ’Lateral core mantle boundary heat flux variations as a model of the Martian paleomagnetic field’, EPSC 2010, Rome (Oral)
- Christensen U., Wicht J., Dietrich W.: ’Magnetic fieldgeneration of Earth-like planets’, DLR Berlin (Oral)
- Christensen U., Wicht J., Dietrich W.: ’Magnetic fields and dynamos in terrestrial planets’, AGU 2010, San Francisco, (Oral)
- Dietrich W., Wicht J., Christensen U.: ’The convective origin of hemispherical dynamos’, EGU 2011, Vienna (Oral)
- Dietrich W., Wicht J., Christensen U.: ’A hemispherical dynamo model: Implications for the Martian crustal magnetization’, Dynamo iGdR 2011, Cargese (Oral)
- Dietrich W., Wicht J., Christensen U.: ’A hemispherical dynamo model: Implications for the Martian crustal magnetization’, AGU, San Francisco (Poster)
- Wicht J., Hori K., Dietrich W., Manglik A.: ’Numerical models for the Early Geodynamo’, AGU 2011, San Francisco (Poster)
- Dietrich W., Wicht J., Christensen U.: ’Time variability of hemispherical dynamos: An application to Mars’, EGU 2012, Vienna (Poster)

- Cao H., Russel C.T., Wicht J., Dietrich W., Christensen U., Dougherty M.K.: 'The Size of the inner Core and Magnetic Field Configuration at the Dynamo surface', EGU 2012, Vienna (Poster)

Acknowledgements

First of all, I want to thank my supervisors Prof. Ulrich Christensen and Prof. Andreas Tilgner for accepting me as a PhD student and guiding my work in all scientific questions. It was always impressive to witness, how the complex theory of MHD dynamos and geophysics can become understandable if explained properly. Furthermore, I give all my thanks to Dr. Johannes Wicht for his unwavering support and supervision during the three years of my PhD. His open mind and scientific expertise is highly appreciated. I am also grateful to be part of the IMPRS under the wise coordination of Dr. Dieter Schmitt. The Helmholtz Research Alliance "Planetary Evolution and Life" provided the financial support, what I acknowledge. I want to thank the other members of the Dynamo group at the MPS, whose untiring cooperativeness and deep knowledge of dynamo theory, fluid dynamics and visualization methods I shamelessly exploited. Special thanks here to Dr. Thomas Gastine for helpful discussions and his visualization skills that exceed mine by far. Domenico Meduri spent too much time to derive, discuss and solve problems with me on the white board - grazie mille!

I am grateful to our group secretaries Karin Peschke and Silvia Schirmer for managing the business trips, the GWDG for providing computational facilities and the planetary research group of the DLR in Berlin for organizing the productive Alliance Weeks. Among them, I want to highlight Dr. Lena Noack and Prof. Doris Breuer for their thorough knowledge of geophysics. Furthermore, many thanks go to Matthias Meyer for developing the sophisticated Vmagic tool for 3D rendering.

I am deeply indebted to (now Dr.) Daniel Verscharen for being both, a good friend and an excellent scientist. He never ceased in helping me to find, discuss, understand and solve my research challenges. I always enjoyed his company and scientific brilliance during our PhD time in the institute and our extensive evening and night activities. I want to highlight Dr. Julia Thalmann and Corinna Köpke for all the engaging discussions during our coffee and lunch breaks. Our common evenings and weekends created a cheerful social atmosphere and enriched my life.

I also would like to thank the other people at the MPS, who allowed me to enjoy my time at the MPS and in Göttingen. Tijmen, Juanjo, Peter, David, Maria D., Hannah, Ray, Megha, Karsten, Yeon Joo, Shahin, Farhad, Nafiseh and the other students, scientists and staff members who made my stay at the MPS such a wonderful experience.

Not to forget my grandparents, parents and siblings for their unquestioned support. Very special thanks to the players and trainers of my football club "SV Puma Göttingen". It was always fun and a pleasure to escape the world of physics and enjoy our refreshing team spirit.

Last but not least, I want to say thank you to my love Isabell for always staying by my side and enduring my absence during long office hours. I haven't taken it for granted.

Curriculum Vitae

Persönliche Daten:

Name:	Wieland Dietrich
Geburtsdatum:	03.10.1983
Geburtsort:	Weimar
Staatsangehörigkeit:	deutsch

Schulausbildung:

1994 - 2002 Goethegymnasium Weimar, Abschluss Abitur

Studium:

2003 - 2009	Studium an der Universität Bayreuth, Abschluss Diplom Physiker, Diplomarbeit zum Thema: Effekt lokal isolierender Randschichten auf die Mischungseigenschaften in Rayleigh-Benard-Konvektionszellen, unter Betreuung von Prof. Dr. Walter Zimmermann und Dr. Henri Samuel

Promotion

2009 - 2012	Promotionsstudium an der Georg-August-Universität Göttingen im Rahmen des Promotionsprogrammes GAUSS ProPhys sowie der International Max Planck Research School on Physical Processes in the Solar System and Beyond (Solar System School), Thema der Dissertation: Numerical Dynamo Simulations for the Ancient Mars, unter Betreuung von Prof. Dr. Ulrich Christensen, Prof. Dr. Andreas Tilgner und Dr. Johannes Wicht